Driving Influences of Ionospheric Electrodynamics at Mid- and High-Latitudes

Maimaitirebike Maimaiti

Dissertation submitted to the Faculty of the
Virginia Polytechnic Institute and State University
in partial fulfillment of the requirements for the degree of

Doctor of Philosophy
in
Electrical Engineering

John Michael Ruohoniemi, Chair
Joseph Benjamin Baker
C. Robert Clauer
Wayne A. Scales
Richard M. Buehrer
Randolph H. Wynne

November 21, 2019
Blacksburg, Virginia

Keywords: Ionospheric Electrodynamics, Magnetic Reconnection, Penetration Electric Field, Substorm Onset Prediction, Machine Learning

Driving Influences of Ionospheric Electrodynamics at Mid- and High-Latitudes

Maimaitirebike Maimaiti

(ABSTRACT)

The ionosphere carries a substantial portion of the electrical current flowing in Earth's space environment. Currents and electric fields in the ionosphere are generated through (1) the interaction of the solar wind with the magnetosphere, i.e. magnetic reconnection and (2) the collision of neutral molecules with ions leading to charged particle motions across the geomagnetic field, i.e. neutral wind dynamo. In this study we applied statistical and deep learning techniques to various datasets to investigate the driving influences of ionospheric electrodynamics at mid- and high-latitudes. In Chapter 2, we analyzed an interval on 12 September 2014 which provided a rare opportunity to examine dynamic variations in the dayside convection throat measured by the RISR-N radar as the IMF transitioned from strong By+ to strong Bz+. We found that the high-latitude plasma convection can have dual flow responses with different lag times to strong dynamic IMF conditions that involve IMF By rotation. We proposed a dual reconnection scenario, one poleward of the cusp and the other at the magnetopause nose, to explain the observed flow behavior. In Chapters 3 & 4, we investigated the driving influences of nightside subauroral convection. We developed new statistical models of nightside subauroral (52° - 60°) convection under quiet (Kp $\leq$ 2+) to moderately disturbed (Kp = 3) conditions using data from six mid-latitude SuperDARN radars across the continential United States. Our analysis suggests that the quiet-time subauroral flows are due to the combined effects of solar wind-magnetosphere coupling leading to penetration electric field and neutral wind dynamo with the ionospheric conductivity modulating their relative dominance. In Chapter 5, we examined the external

drivers of magnetic substorms using machine learning. We presented the first deep learning based approach to directly predict the onset of a magnetic substorm. The model has been trained and tested on a comprehensive list of onsets compiled between 1997 and 2017 and achieves 72±2% precision and 77±4% recall rates. Our analysis revealed that the external factors, such as the solar wind & IMF, alone are not sufficient to forecast all substorms, and preconditioning of the magnetotail may be an important factor.

Driving Influences of Ionospheric Electrodynamics at Mid- and High-Latitudes

Maimaitirebike Maimaiti

(GENERAL AUDIENCE ABSTRACT)

The Earth's ionosphere, ranging from about 60 km to 1000 km in altitude, is an electrically conducting region of the upper atmosphere that exists primarily due to ionization by solar ultraviolet radiation. The Earth's magnetosphere is the region of space surrounding the Earth that is dominated by the Earth's magnetic field. The magnetosphere and ionosphere are tightly coupled to each other through the magnetic field lines which act as highly conductive wires. The sun constantly releases a stream of plasma (i.e., gases of ions and free electrons) known as the solar wind, which carries the solar magnetic field known as the interplanetary magnetic field (IMF). The solar wind interacts with the Earth's magnetosphere and ionosphere through a process called magnetic reconnection, which drives currents and electric fields in the coupled magnetosphere and ionosphere. The ionosphere carries a substantial portion of the electrical currents flowing in the Earth's space environment. The interaction of the ionospheric currents and electric fields with plasma and neutral particles is called ionospheric electrodynamics. In this study we utilized statistical and machine learning techniques to study ionospheric electrodynamics in three distinct regions. First, we studied the influence of duskward IMF on plasma convection in the polar region using measurements from the Resolute Bay Incoherent Scatter Radar – North (RISR-N). Specifically, we analyzed an interval on Sep. 12, 2014 when the RISR-N radar made measurements in the high latitude noon sector while the IMF turned from duskward to strongly northward. We found that the high latitude plasma convection can have flow responses with different lag times during strong IMF conditions that involve IMF By rotation. Such phenomena are

rarely observed and are not predicted by the antiparallel or the component reconnection models applied to quasi-static conditions. We propose a dual reconnection scenario, with reconnection occurring poleward of the cusp and also at the dayside subsolar point on the magnetopause, to explain the rarely observed flow behavior. Next, we used measurements from six mid-latitude Super Dual Auroral Radar Network (SuperDARN) radars distributed across the continental United States to investigate the driving influences of plasma convection in the subauroral region, which is equatorward of the region where aurora is normally observed. Previous studies have suggested that plasma motions in the subaruroral region were mainly due to the neutral winds blowing the ions, i.e. the neutral wind dynamo. However, our analysis suggests that subauroral plasma flows are due to the combined effects of solar wind-magnetosphere coupling and neutral wind dynamo with the ionospheric conductivity modulating their relative importance. Finally, we utilized the latest machine learning techniques to examine the external drivers (i.e., solar wind and IMF) of magnetic substorms, which is a physical phenomenon that occurs in the auroral region and causes explosive brightening of the aurora. We developed the first machine learning model that forecasts the onset of a magnetic substorm over the next one hour. The model has been trained and tested on a comprehensive list of onsets compiled between 1997 and 2017 and correctly identify substorm onset $\sim$75% of the time. In contrast, an earlier prediction algorithm correctly identified only $\sim$21% of the substorm onsets in the same dataset. Our analysis revealed that external factors alone are not sufficient to forecast all substorms, and preconditioning of the nightside magnetosphere may be an important factor.

Acknowledgments

I would like to start by expressing my deepest appreciation to my advisors, Dr. John M. Ruohoniemi and Dr. Joseph B. H. Baker, for their continuous support and guidance throughout my Ph.D. I forever feel fortunate to have taken a radar system design course from Dr. Ruohoniemi during my first semester at Virginia Tech, which then led me to switch field from antenna and RFIC design to space science. Coming in with no space science background, I learned a lot on the topics along with a wide range of new skills such as programming and machine learning, all thanks to their support and encouragement. I would especially thank them for giving me the freedom to pursue my passion for Data Science and complete a dual Master of Arts degree in Data Analysis & Applied Statistics from the Department of Statistics. I feel so blessed to have been a student of two wonderful professors who see the value in such pursuit. I thank them for all their efforts in making the SuparDARN@VT such a wonderful place for me and others.

I am very grateful to Dr. C. Robert Clauer, Dr. Wayne Scales, Dr. R. Michael Buehrer and Dr. Randolph Wynne for serving as my committee members and for their time and efforts in reviewing this dissertation. Special thanks to Dr. C. Robert Clauer for providing me with a collaboration opportunity on studying an extremely rare event, which led to one first-authored and one co-author papers published in JGR Space Physics.

I would like to thank and acknowledge my collaborators. I thank my labmate, Dr. Bharat Kunduri, for his significant support and contributions to my research on machine learning applications to space science and Dr. A. J. Ribeiro for building the basis for my research on

subauroral convection. I also thank Dr. Stefan Eriksson at the Laboratory for Atmospheric and Space Physics at the University of Colorado Boulder for providing me with an opportunity to collaborate on a case study, whose publication gave further support to my research results on polar cap convection. I would also thank Dr. Raymond A. Greenwald and Dr. Kjellmar Oksavik for providing invaluable research insights. I would like to acknowledge Dr. Arthur D. Richmond in the High Altitude Observatory at the National Center for Atmospheric Research for providing his ionospheric electric field model code and to Dr. Daniel R. Weimer at Virginia Tech for providing his statistical electric potential model code for the high-latitude ionosphere.

I also extend my gratitude to all of my past and present labmates for their friendly support and invaluable suggestions. Special thanks to Kevin for his tireless effort on keeping the radars and data servers functioning, Nathaniel and Evan for teaching me technical skills when I first joined the group, and Shirling and Shibaji for having with me countless valuable discussions on many things. I would also like to thank Space@VT center administrators, ECE staff members and computer systems administrators for their support and assistance. Special thanks to Debbie Collins for always treating me with kindness and saying encouraging words when things became tough on me.

Last but not least, I am deeply grateful to my wife, Dilraba Abla, for her tremendous sacrifice for me by taking care of our two little ones with love and care and trying her best to make my life after work as stress-free as possible. To my parents and my two lovely sisters, I do not have words to express my thanks and gratitude to you. I could come to this stage because of your unconditional love and support throughout my life. I am extremely blessed and honored to be born to such a wonderful family.

This research was supported by the National Science Foundation under grants AGS-1341918, AGS-1259508, AGS-1243070 and AGS-1552247.

Contents

List of Figures

List of Tables

Chapter 1

Introduction

This Chapter presents background materials for this research; the solar wind-magnetosphere-ionosphere system, its coupling mechanisms and the related physical phenomena, and instruments and techniques. The Chapter ends with research objectives and the dissertation organization.

1.1 The Solar – Terrestrial Environment

In this section we separately introduce the three components of the solar-terrestrial environment; solar wind, Earth's magnetosphere and ionosphere. In the next section, we present them as a single system and discuss their coupling mechanisms.

1.1.1 The Solar Wind and the Interplanetary Magnetic Fields

The universe is not empty; It is filled with plasma, which consists of gases of ions and free electrons with approximately equal numbers. Our solar system is not an exception. The sun constantly releases a stream of plasma known as the solar wind, which consists mostly of hydrogen ($\sim$95% H^+) and helium ($\sim$5% He^{++}) ions and an equal number of electrons. The source of the solar wind is the sun's hot corona, the upper atmosphere of the Sun. The solar wind carries interplanetary magnetic field (IMF), which is the solar magnetic field dragged

out from the sun's corona. The IMF is "frozen-in" to the highly conductive solar wind, thus both travel at the same speed that ranges from 300 to 800 km/s. While light emitted from the Sun takes about 8 minutes to reach Earth, the solar wind reaches Earth in about 2-4 days. Since the sun is rotating, the solar wind and IMF emitted from the sun conform to a spiral shape known as the Parker Spiral [Parker, 1958]. Figure 1.1 shows a schematic view of the Parker Spiral.

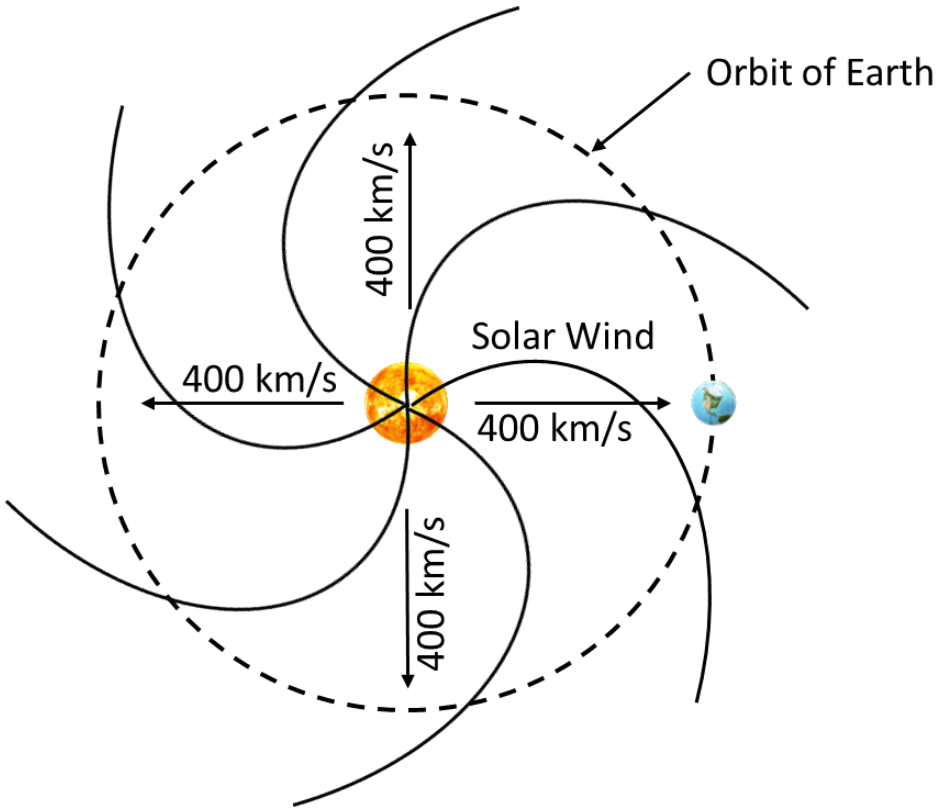

Figure 1.1: Schematic of the Parker spiral, as suggested by Parker [1958].

1.1.2 Earth's Magnetic Field and Magnetosphere

Earth's Magnetic Field

Earth is surrounded by a dipole shaped magnetic field like that of a bar magnet (Figure 1.2), directed horizontal at the magnetic equator and nearly vertical at the poles. Earth's magnetic field is generated by circulating electric currents due to the motions of molten iron in Earth's outer core [Merrill et al., 1998]. The magnetic field extends from Earth's interior out into the space, with its magnetic south and north poles located near the geographic north and south poles, respectively. The dipole axis is tilted about 11° from the spin axis of Earth, thus the magnetic poles are not exactly aligned with the geographic poles. Therefore, the pointing direction of a magnetic compass is generally different from the true geographic north. As will be explained in Section 1.2, Earth's magnetic field plays a crucial role in coupling Earth's upper atmosphere to magnetosphere and solar wind.

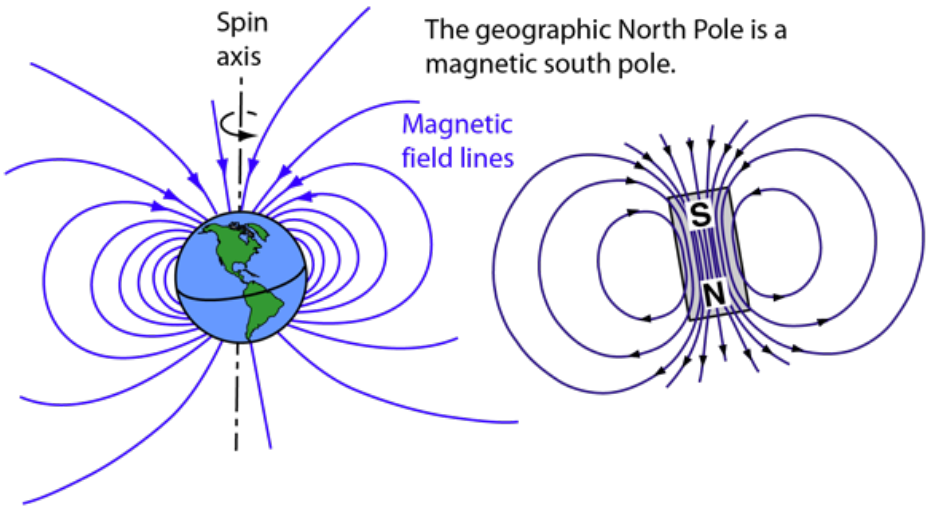

Figure 1.2: Magnetic fields of Earth (left) and an equivalent bar magnet (right) (Image source: http://hyperphysics.phy-astr.gsu.edu/hbase/magnetic/MagEarth.html).

Earth's Magnetosphere

The magnetosphere [Parks, 2015; Borovsky and Valdivia, 2018] is the region of space surrounding Earth that is dominated by Earth's magnetic field (Figure 1.3). It is formed by the interaction of the solar wind with Earth's magnetic field. The shape of the magnetosphere is highly dynamic and changes with the solar wind conditions. The constant blowing of the solar wind compresses its sunward side to ∼10 Earth Radius (RE, ∼6378 km) on the equatorial plane and stretches its nightside to much greater distances. This forms a long tail of about 200 RE, which is referred to as the magnetotail [Nishida, 2000]. The outermost layer of the magnetosphere is the bow shock [Fairfield, 1971] which forms due to the supersonic solar wind encountering Earth's magnetic field. Passing through the shock, the solar wind is slowed, compressed, and heated. The magnetopause is the boundary where the pressure from Earth's magnetic field is balanced with that from the shocked solar wind [Šafránková et al., 2002]. It moves inward (outward) in response to increase (decrease) in solar wind pressure. The region between the bow shock and the magnetopause is called the magnetosheath [Kaymaz, 1998]. Here, Earth's magnetic field is weak and irregular. The particle densities in this region are considerably lower than what are found beyond the bow shock, but greater than within the magnetopause.

Earth's magnetosphere plays a crucial role in protecting life by shielding the atmosphere from the solar wind. When the solar wind reaches the bow shock, it is deflected to either side, much like water is deflected before the bow of a ship. It decelerates and bypasses Earth along the magnetopause boundary. Thus, the magnetosphere forms an obstacle to the solar wind and protects the atmosphere being blown away by the solar wind. However, as we will explain in Section 1.2, the solar wind can still transfer a significant amount of energy to Earth's magnetosphere.

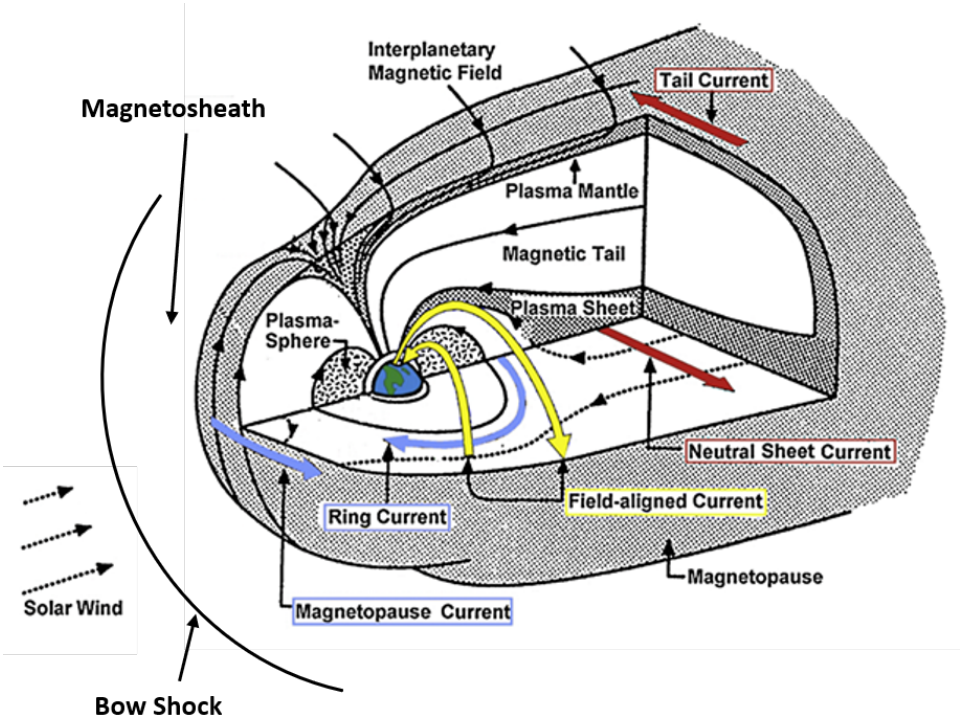

Figure 1.3: Schematic depiction of the magnetosphere (Adapted from Lühr et al. [2016]).

Now we introduce the internal structure of the magnetosphere within the magnetopause. The region inside the magnetopause may be divided into three broad regions (from outward to inward toward Earth): tail lobes, plasma sheet, and the inner magnetosphere.

Plasma Sheet and Tail Lobes

The plasma sheet [Elphic et al., 1999; Denton and Borovsky, 2009] is a thick layer of hot plasma centered on the tail's equator. It has a typical thickness of 3-7 RE, density of 0.3-0.5 ions/cm^{-3}, and typical ion energy of 2-5 keV. This region is highly dynamic, and its thickness, density and energy vary significantly with solar wind conditions. The plasma sheet has its associated electric current, called the neutral sheet current, which flows across the tail's equator from dawn flank to dusk flank and closing along the magnetopause.

The tail lobes are two regions north and south of the plasma sheet. Earth's magnetic field

lines in the northern and southern tail lobes point towards and away from Earth, respectively. This region is almost empty of plasma, with density of 0.01 ion/cm^{-3}. The volume of this space is large and can store appreciable magnetic energy that is tapped from the solar wind energy. Release of this energy triggers geomagnetic disturbances such as substorms (see Section 1.3.1).

Inner Magnetosphere

The inner magnetosphere is the region from near geostationary orbit (∼7 RE from Earth's center) inward toward Earth [Baker, 1995]. This region can be treated as a magnetic dipole in which charged particles are trapped by Earth's magnetic field [Olson and Pfitzer, 1974]. It is a relatively stable region and includes important features such as the Van Allen radiation belts, plasmasphere, and the ring current. These three features are highly overlapped in space because there are no sharp physical divisions in the particle populations. The radial range of these features on the magnetic equator plane are about 2–7 RE. Below we introduce each of three features separately.

The Van Allen radiation belts [Baker et al., 2017] are two donut-shaped belts of radiation circling Earth. The inner one (∼1.2–3 RE) is fairly stable, but the outer one (∼4–8 RE) swells and shrinks over time in response to solar wind variations. They were named after James Van Allen who discovered them in 1958 after the launch of Explorer 1, the first U.S. satellite, and the Explorer 3 [Allen, 1958; Allen and Frank, 1959]. The radiation belts are filled with highly energetic (MeV) charged particles, most of which originated from the solar wind and were captured by Earth's magnetic fields. By trapping the solar wind, Earth's magnetic field deflects those energetic particles and protects the atmosphere from destruction. However, the belts are hazardous to spacecraft and endanger the lives of astronauts. Therefore, energization of the Van Allen radiation belts has important space weather implications (see Section 1.3.3 for space weather).

The plasmasphere [Darrouzet et al., 2009] is a donut-shaped region surrounding Earth (see Figure 1.3). It consists of particles of relatively high density (10-10^3 cm^{-3}) and low energy (usually less than 1 eV). The particle population in this region decreases outwards and terminates at a relatively sharp boundary called the plasmapause (at ∼4–5 RE in the equatorial plane) where the plasma density drops by an order of magnitude. Outside the plasmapause is the outer radiation belt. Plasma in the plasmasphere is trapped on magnetic field lines that rotate with Earth, and thus, roughly corotates with the planet.

The ring current consists of energetic (10-200 keV) charged particles that are trapped on magnetic field lines. It carries substantial westward flowing current around Earth (see Figure 1.3), thus creating a magnetic field opposite to Earth's geomagnetic field in the inner region. The ring current is one of the major current systems in Earth's magnetosphere. During geomagnetic storms, which will be explained in Section 1.3.2, the ring current intensifies significantly and affects Earth's magnetic field.

1.1.3 Earth's Atmosphere and Ionosphere

The Atmosphere

Earth's atmosphere is the layer of gases that surrounds Earth's surface. Figure 1.4 (left) shows the five layers of the atmosphere and the temperature profile of these layers. Starting from the ground surface toward the space they are: troposphere, stratosphere, mesosphere, thermosphere, and exosphere. The troposphere is the innermost layer ranging between 0 - 10 km altitudes and its temperature decreases with increasing altitude. This layer is most relevant to our existence; it has enough oxygen for us to breathe. When we talk about the "weather" in our daily life, we are referring to the weather conditions in this layer. The layer on top of it is the stratosphere, covering about 10 – 50 km altitude. The very important

ozone layer, which protects us from the sun's ultraviolet variation, is in this layer. The mesosphere is located between 50 – 85 km altitude range, where the majority of the meteors dissipate and is the coldest layer. Above it is the thermosphere, ranging from 85 to 600 km altitudes. This is the layer where the International Space Station and some low Earth orbit satellites are located. The exosphere is the outermost layer of Earth's atmosphere, ranging from 600 to 10,000 km. It separates the atmosphere from the outer space.

The Ionosphere

The neutral gas molecules and atoms in Earth's upper atmosphere, i.e. the topside mesosphere and above, are ionized by high-energy X-rays and ultraviolet (UV) lights emitted from the Sun. This ionized part of the atmosphere, from about 60 km to 1,000 km altitude, is called the ionosphere [Kelley and Heelis, 1989; Kelley, 2009]. It overlaps with the thermosphere and parts of the mesosphere and the exosphere. Because the ionosphere consists of partially ionized gas, it has electrodynamic interactions with Earth's magnetic field. In particular, the charged particles in the ionosphere react to electric fields that map along the geomagnetic field lines.

The ionosphere can be divided into three layers: the D, E, and F regions. These regions do not have sharp boundaries and the altitudes at which they occur varies significantly by day and night. Figure 1.4 (right) shows the plasma profile of this layer, with solid and dashed lines corresponding to day and night, respectively. The D-region is the lowest layer at the altitude range of 60 – 90 km. It forms in the upper part of the mesosphere. Ionization in this layer is much weaker compared to the other layers. Due to a high recombination rate of ions and free electrons, this layer disappears during the night. The E-region starts from 90 km and extends up to 150 km, collocating with the lower thermosphere. At night, this layer weakens considerably due to lack of solar radiation. The F-region is the uppermost part of

the ionosphere, starting from 150 km and extending to as high as ∼1000 km altitude. It is found in the upper part of the thermosphere and the lower part of the exosphere. The peak in the altitude profile of the electron density usually occurs in this region.

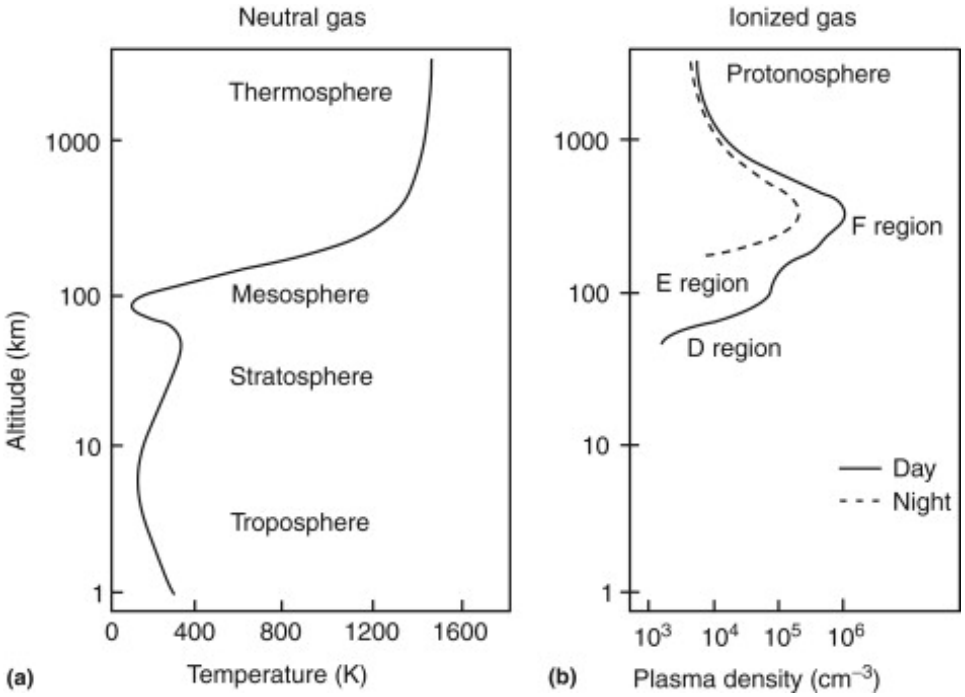

Figure 1.4: Typical height profiles of neutral atmospheric temperature (left) and ionospheric plasma density (right) with the various layers designated (from Kelley [2009]).

The ionosphere is strongly coupled to the magnetosphere through the magnetic field lines. Thus, distant points in the magnetosphere are connected to points in the ionosphere by the magnetic field lines that act as highly conductive electrical wires, which we will explain next.

Latitudinal Division of Earth's Ionosphere

The ionosphere can also be divided into distinct latitudinal regions as shown in Figure 1.5. The auroral zone (oval) is a donut-shaped region in the ionosphere whose poleward and equatorward boundaries are generally understood as the limits for electron precipitation [Feldstein and Galperin, 1985]. This is the region where one can see the aurora, which is also referred to as northern or southern lights. Aurora are the result of energetic ions (∼200

keV) ions and electrons (1-20 keV) spiraling down Earth's magnetic field lines and colliding with gas particles in Earth's upper atmosphere. Earth's magnetic field lines in the auroral region are closed, i.e., both ends are connected to Earth. They are connected to the plasma sheet region in the magnetosphere. In chapter 5, we investigate an important disturbance phenomenon called the auroral substorm which occurs in this region.

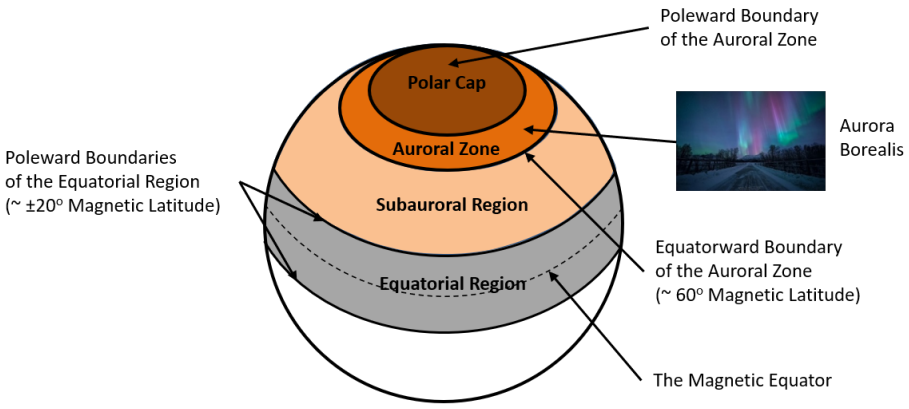

Figure 1.5: Latitudinal division of Earth's ionosphere.

The polar cap is the region poleward of the auroral oval. Here, Earth's magnetic field lines are open, that is, one end is connected to Earth and the other extends into the solar wind. The footprints of the northern and southern tail lobes in the magnetosphere reside in the northern and southern polar cap regions, respectively. The polar cap region does not produce auroral light in the ionosphere because its open field lines carry little charged particle precipitation that would trigger aurora. In this dissertation, we use the term "high latitude" to refer to the region above the equatorward auroral boundary, which includes the auroral oval and polar cap regions. In Chapter 2, we examine plasma flows in the polar cap region.

The subauroral region lies equatorward of the equatorward boundary of the auroral oval and poleward of the equatorial region that is between $\sim \pm 20^{\circ}$ magnetic latitude. The magnetic footprint of the inner edge of the plasma sheet maps to the equatorward boundary of the

auroral oval. Although the subauroral region is just next to the auroral zone, plasma flows in these two regions have very different characteristics that relate to the expected "shielding" of the subauroral ionosphere from magnetospheric electric fields (see Section 1.2.3). Plasma convection in the subauroral region is the main topic of Chapters 3 & 4.

1.2 The Solar Wind-Magnetosphere-Ionosphere Coupling

In the previous section, we separately introduced the solar wind and IMF, magnetosphere and ionosphere. These three components are in fact highly coupled and form a single system (Figure 1.6). The solar wind transfers some of its energy and momentum to the magnetosphere through a process called magnetic reconnection [Dungey, 1961] and, to a lesser extent, viscous interaction [Axford and Hines, 1961]. Since energetic ions and electrons can freely travel along magnetic field lines, Earth's magnetic field acts as highly conductive wires and transmits the solar wind energy to the ionosphere, where the transmitted energy is dissipated mainly as heat. The beautiful Aurora which we see in the polar regions is one of the manifestations of the solar wind energy being transferred to the ionosphere. Thus, variations in the solar wind and IMF lead to changes in the both the magnetosphere and ionosphere. In this section we discuss the coupling mechanisms between the three components.

1.2.1 Magnetic Reconnection and High-latitude Plasma Convection

It is widely accepted that the dominant source for the coupling of solar wind energy to the magnetosphere and ionosphere in the high-latitude regions is the magnetic reconnection

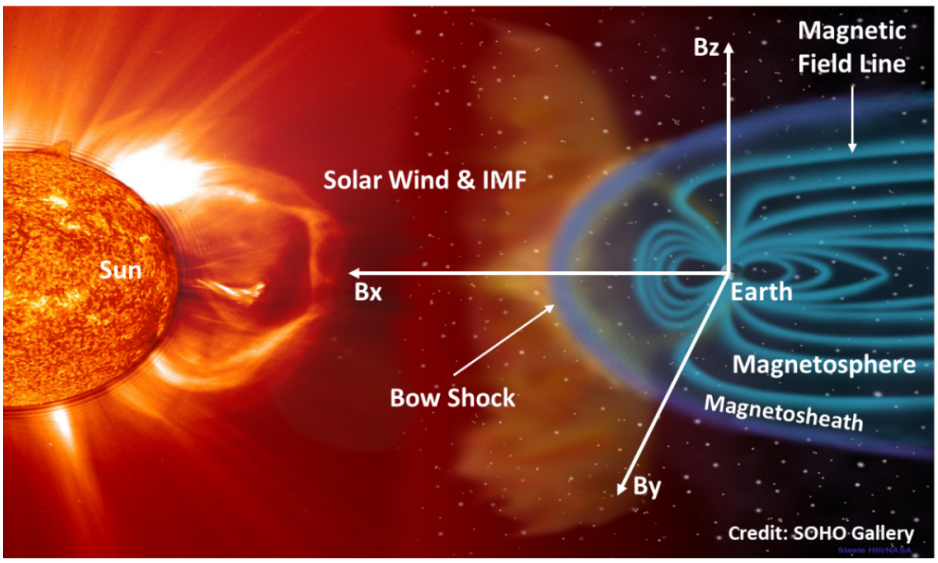

Figure 1.6: The Solar Wind - Magnetosphere - Ionosphere System (Credit: SOHO Gallery).

proposed by Dungey [1961, 1963]. When oppositely directed magnetic fields come in contact, it is possible that the two merge or reconnect.

Figure 1.7 shows the magnetic reconnection in Earth's magnetosphere under southward IMF conditions and the corresponding magnetospheric and ionospheric convection in the polar cap and auroral zone. When the solar wind carries a southward interplanetary magnetic field (IMF) to the magnetopause, as denoted by 1' in Figure 1.7, it reconnects with the northward directed Earth's closed magnetic field at the dayside magnetopause (line 1 in Figure 1.7). This leads to plasma from two different regions (i.e., the solar wind in the magnetosheath and the plasma within the magnetopause) being on the same field line and thus allows the solar wind to enter Earth's magnetosphere. The antisunward motion of the solar wind drags the newly opened field lines, 2 and 2', toward the nightside in succession (see lines 3 & 3', 4 & 4', 5 & 5', 6 & 6'), thus strengthening the two tail lobes with the addition of magnetic flux.

Dayside reconnection causes Earth's closed magnetic fields lines to open and the accumula-

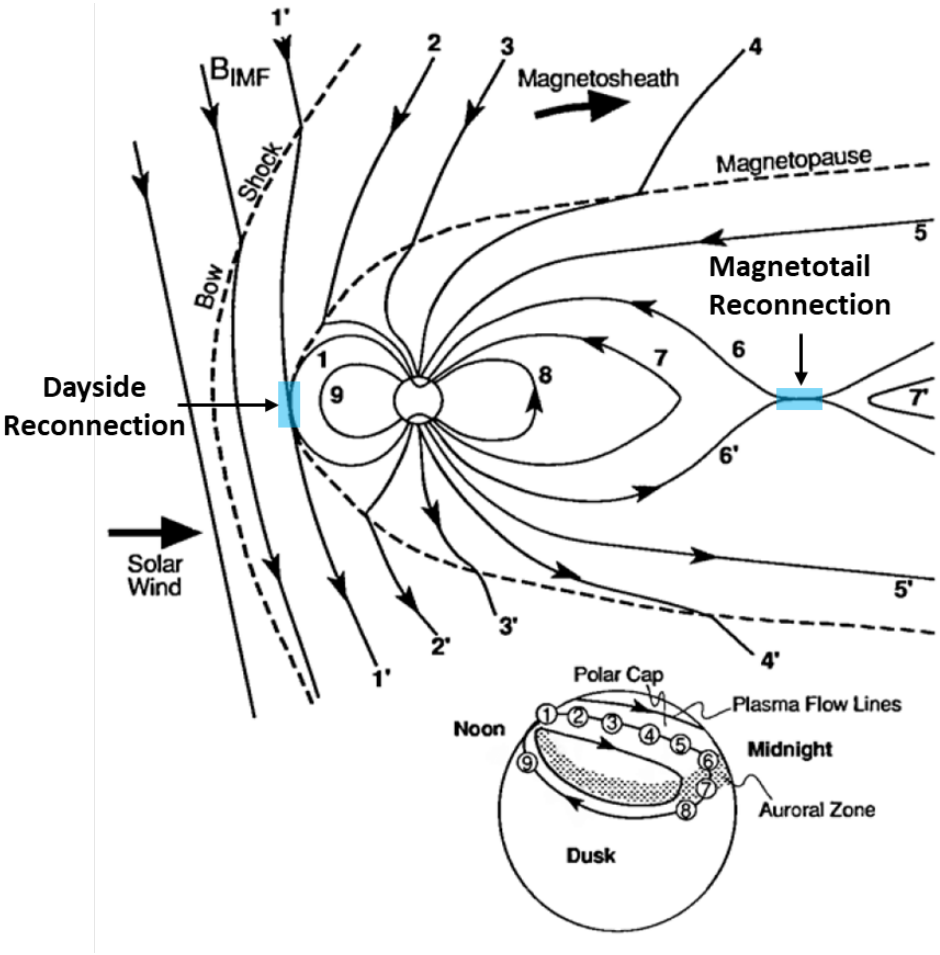

Figure 1.7: Magnetic Reconnection in the magnetosphere for Southward IMF and the associated plasma convection in the ionosphere (Adapted from [Kivelson and Russell, 1995]).

tion of these open field lines in the magnetotail causes another reconnection to occur on the nightside. That is, the oppositely directed open field lines 6 and 6' reconnect with each other and form a closed field line. Because of the magnetic tension force, which we can think of as a tension force due to a pulled string, the newly closed field line is pulled toward Earth until it returns to the dayside magnetopause (see lines 7, 8, and 9). Since the plasma is closely tied to the magnetic field, the motion of the magnetic field drives a large two-cell pattern in the magnetosphere and the ionosphere at high latitudes (Figure 1.7 bottom panel), with antisunward flows over the polar cap that return to the dayside via the dawn and dusk

flanks.

For IMF By+ (By−), the site of reconnection in the Northern Hemisphere shifts duskward (dawnward), which creates a dawnward (duskward) magnetic tension force that drives a distorted two-cell convection [Heppner and Maynard, 1987]. Under northward IMF conditions, the reconnection site shifts poleward of the cusp [Dungey, 1963; Crooker, 1979] as show in Figure 1.8 (left). Such a reconnection geometry drives a four-cell pattern depicted in the right panel in Figure 1.8, with reverse two-cell circulation constrained to a small area of the dayside polar cap and two other cells with the normal sense of circulation at lower latitudes within the polar cap and auroral zone.

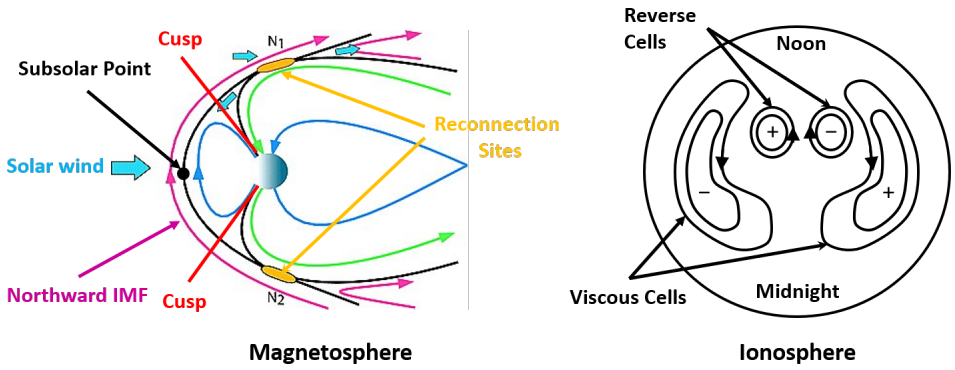

Figure 1.8: Magnetic Reconnection in the magnetosphere for Northward IMF and the associated plasma convection in the ionosphere (left panel is adapted from [Dorelli et al., 2007].

As can be seen from Figures 1.7 and 1.8, plasma convection in the ionosphere is confined to a much smaller region than that in the magnetosphere. Because the magnetosphere and ionosphere are strongly coupled through the highly conductive magnetic field lines, observations of the ionosphere can give a global picture of the magnetosphere. Thus, using the ionosphere as a map of what is happening in the magnetosphere is a very effective way of studying the behavior of reconnection in the magnetosphere. In Chapter 2, we take advantage of this method to study the IMF By influence on reconnection geometry under extreme northward IMF conditions.

1.2.2 Birkeland Currents

In addition to plasma convection at high-latitudes, the solar wind and magnetosphere interaction through magnetic reconnection drives various currents in the magnetosphere (see Figure 1.3). Among them are Birkeland currents (also known as field-aligned currents), which are a set of large-scale currents that flow along geomagnetic field lines connecting the magnetosphere to the high latitude ionosphere (Figure 1.9). They are named after the Norwegian physicist Kristian Birkeland who first predicted their existence in 1908 [Birkeland, 1908]. Birkland currents play a crucial role in transmitting electromagnetic energy from the Sun to Earth and in creating the auroras [Alfven, 1955].

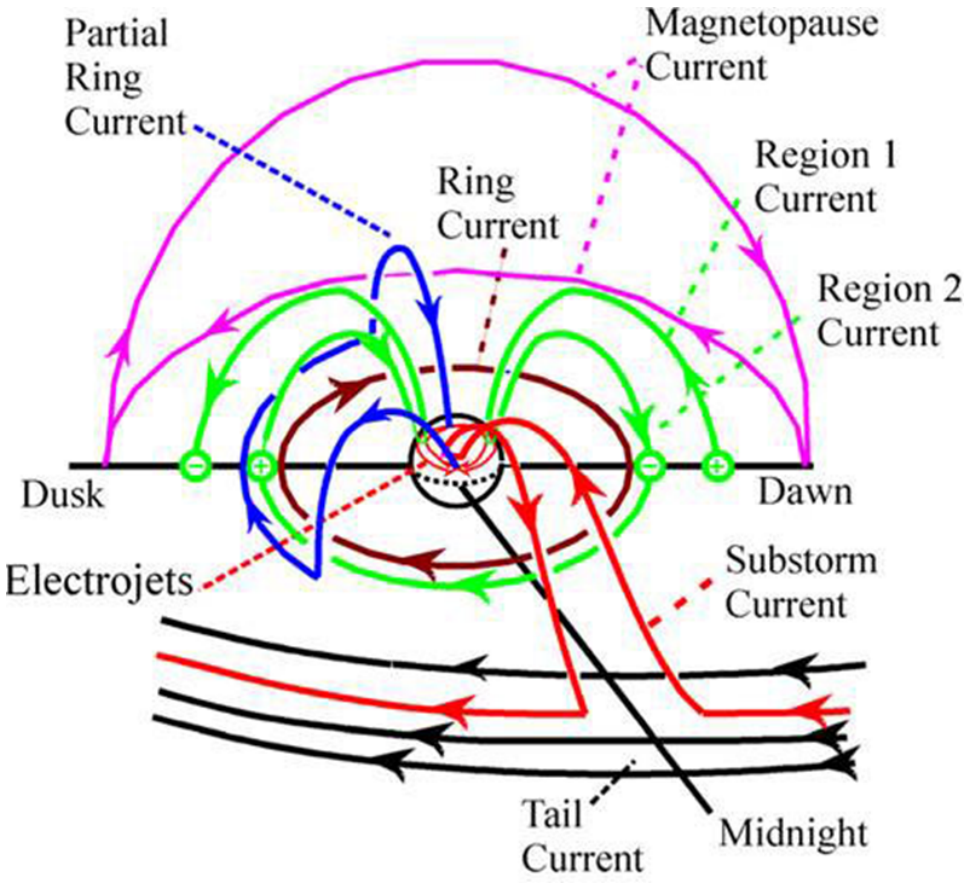

Figure 1.9: An illustration of Birkeland Currents, also known as Field-Aligned Currents (FAC)s (Credit: Robert L. McPherron, 2005 AGU Fall Meeting).

Different orientations of the IMF generate different plasma convection patterns and therefore different associated Birkeland currents. Under southward IMF condition, the Birkeland currents consist of two pairs of field-aligned current sheets; Region 1 (R1) and Region 2 (R2) currents. R1 currents flow down into the positively charged region of the high-latitude dawnside auroral zone and up from the negative region of the high-latitude duskside auroral zone, closing with the magnetopause current (see Figures 1.3 and 1.9). R2 currents have the opposite sense from region 1 in the lower-latitude regions of the auroral zone, closing with the ring currents (see Figures 1.3 and 1.9). In Chapters 3 & 4, we discuss the role of R2 currents in counterbalancing the effects of R1 currents in the inner magnetospheric region which connects to the subauroral ionospheric region through geomagnetic field lines.

Under northward IMF conditions, additional Birkeland currents, called "NBZ" currents, develop in the dayside polar cap (not shown in Figure 1.9). The NBZ currents are associated with the high latitude reverse convection cells (see Figure 1.8) in the polar cap region, with downward current into the positive reverse cell on the duskside and upward current from the negative reverse cell on the dawnside. During a substorm (see Section 1.3.1), another large-scale current system, called the Substorm Current Wedge (SCW), develops in the auroral zone. The SWC is associated with intense auroral displays and comsists of a current from the magnetotail into the ionosphere at the eastern edge and out from the ionosphere returning to magnetotail at the western edge of the auroral activity, connected by a westward horizontal current in the ionosphere [Kepko et al., 2015]. In Chapter 5 we explore prediction of the ground signature of the SWC observed by ground magnetometers during substorms.

1.2.3 Subauroral Plasma Convection

The subauroral region lies equatorward of the auroral oval (see Figure 1.5). However, plasma convection between the auroral and subauroral regions differs significantly. For example, typical plasma drift velocities in the auroral region are a few hundreds of meters per second. In contrast, the subauroral region exhibits drifts of only a few tens of meters per second. This is because the subauroral region, whose magnetic fields map to the inner magnetosphere, is shielded from the effects of the auroral zone convection electric field. How does this happen?

Figure 1.10 shows the inner magnetosphere with (right) and without (left) the dawn-dusk electric field generated through dayside magnetic reconnection (see Figure 1.7). If there is no interaction between the solar wind and Earths' magnetosphere (i.e., the dawn-dusk electric field is 0), the inner edge of the plasma sheet aligns with the contours of plasma circulation. When a dawn-dusk electric is enforced due to dayside magnetic reconnection, the plasma sheet moves earthward and its inner edge is no longer aligned with E × B plasma circulation contours. This leads a westward "partial ring current" to flow in the nightside magnetosphere, which causes the duskside to charge positive and the dawnside negative. This "shielding E-Field" drives Region 2 Birkeland currents into (out of) the ionosphere near dusk (dawn).

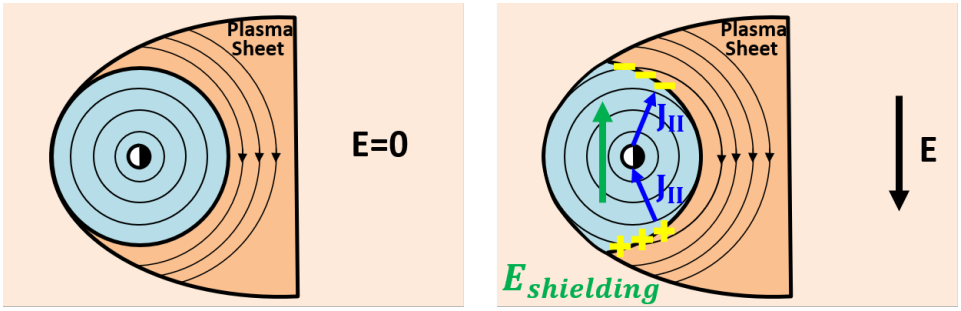

Figure 1.10: Schematic of inner magnetosphere shielding.

The subauroral convection velocity is small but not zero. It is predominantly westward during

the night in all seasons [Buonsanto et al., 1993]. This implies that there are small electric fields driving the plasma motion. Under the assumption that the inner magnetosphere is efficiently shielded by the region 2 currents, the most well-known mechanism proposed to account for electric fields in the nightside subauroral ionosphere is the neutral wind dynamo [Richmond et al., 1976; Rishbeth, 1971]. This mechanism predicts that a dynamo electric field is generated through the collision of neutral molecules with ions leading to charged particle motion across the geomagnetic field. That is, the neutral wind dynamo should entrain the plasma to follow the pattern of the background neutral winds. In Chapter 3 & 4, we discuss the role of the neutral wind dynamo in driving subauroral convection.

1.3 Geomagnetic Activities

In Section 1.2 we presented plasma convection and currents in the magnetosphere and the ionosphere under steady-state solar wind and IMF conditions. In this section, we introduce two important physical phenomena that occur because of dynamic coupling of the solar wind – magnetosphere – ionosphere system. We also introduce the concept of space weather.

1.3.1 Substorm

"A magnetospheric substorm is a transient process initiated on the night side of Earth in which a significant amount of energy derived from the solar wind-magnetosphere interaction is deposited in the auroral ionosphere and in the magnetosphere" [Rostoker et al., 1980]. Substorms occur due to the imbalance between the dayside and nightside reconnections. That is, the nightside reconnection that brings open field lines to the dayside may not be in equilibrium with the dayside reconnection. This causes more magnetic flux to be carried

to the nightside than is returned, and thus, the accumulation of magnetic energy in the magnetotail. The stored energy can then be released explosively. Compared to geomagnetic storms (see Section 1.3.2), substorms are a shorter, impulsive release of energy, and occur much more frequently [Borovsky and Yakymenko, 2017]. Multiple substorms can occur during the main phase of a geomagnetic storm. However, substorms may or may not be a major feature of a geomagnetic storm.

A typical substorm has three phases: growth, expansion, and recovery. The duration of a substorm is about 1-2 hours [Akasofu, 1964; Akasofu et al., 1965]. During the growth phase, energy is extracted from the solar wind through dayside magnetic reconnection and stored in the nightside tail of magnetosphere. Prior to the substorm onset, which is the beginning of expansion phase, magnetic field lines in the magnetotail are extremely stretched as shown in Figure 1.11. The magnetic field lines in the north and south tail lobes become antiparallel, which is a favored configuration for tail magnetic reconnection. After a certain time of growth phase starts the expansion phase, in which magnetic reconnection occurs in the nightside at ∼20 RE and the stored energy is explosively released (bottom panel in Figure 1.11). On the Earth side of the reconnection region, this causes high-speed plasma flows to appear and move toward Earth. When the flow reaches to ∼10 RE, a process called magnetic field dipolarization occurs in which the stretched magnetic field lines return to their original state. Because of dipolarization, charged particles are accelerated and precipitated to Earth's ionosphere along the closed magnetic field lines. Collision of these energetic particles with the neutral atoms and molecules in the atmosphere causes intense auroral displays. On the opposite side of the magnetotail reconnection region from Earth, a cluster of plasma called a plasmoid is formed and ejected away from Earth at a very high speed. The recovery phase starts after 20 - 30 minutes of the expansion phase. In this phase, the magnetosphere relaxes to a quiet state and the aurora begins to fade, which lasts about 30 – 60 minutes.

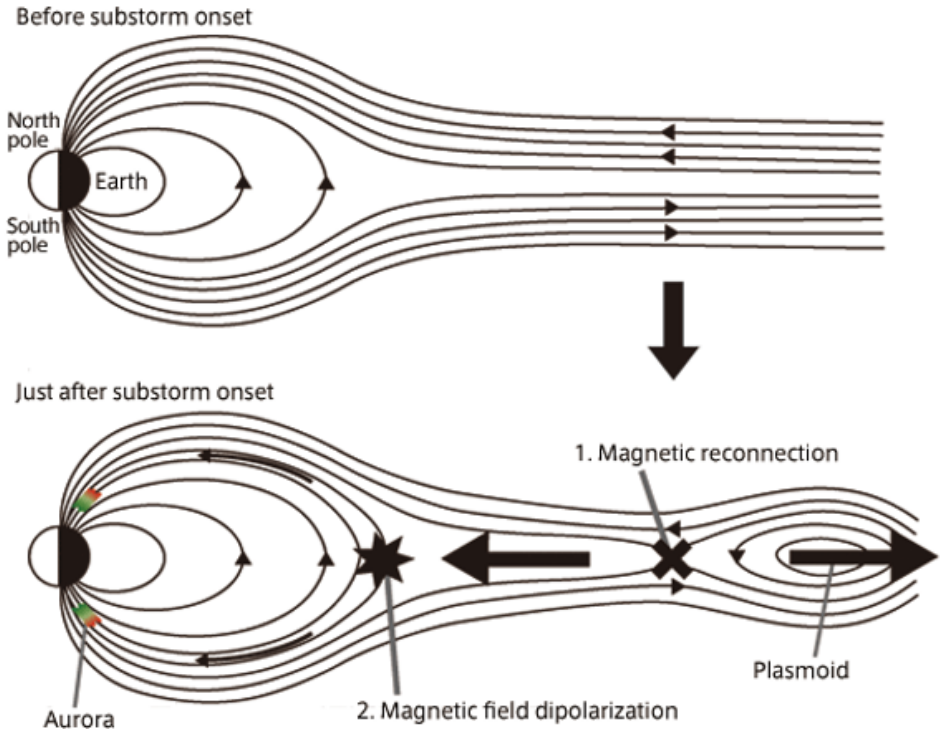

Figure 1.11: The magnetic reconnection model, which is a principal candidate for the substorm trigger (credit: JAXA).

In the auroral region ionosphere, a substorm is seen as a sudden explosive brightening and increased movement of auroral arcs on the nightside, which is known as a substorm breakup. Once a substorm breakup begins, a large amount of energy, originally from the solar wind, is deposited in the ionosphere. The substorm breakup signals the start of substorm expansion phase. Figure 1.12 shows snapshots of different phases of a substorm occurred on January 3rd, 1997, which are captured by the Ultra Violet Imager (UVI) cameras on board of Polar satellite. Panel (a) shows the nightside auroral at the time of a substorm onset, which is the moment when a substorm breakup is about to occur. The auroral intensity suddenly brightened within a minute (panel (b)), greatly intensified and expanded after 10 minutes (panel (c)) and recovered to normal after 42 minutes.

When a substorm breakup occurs, the substorm current wedge develops in the magnetosphere

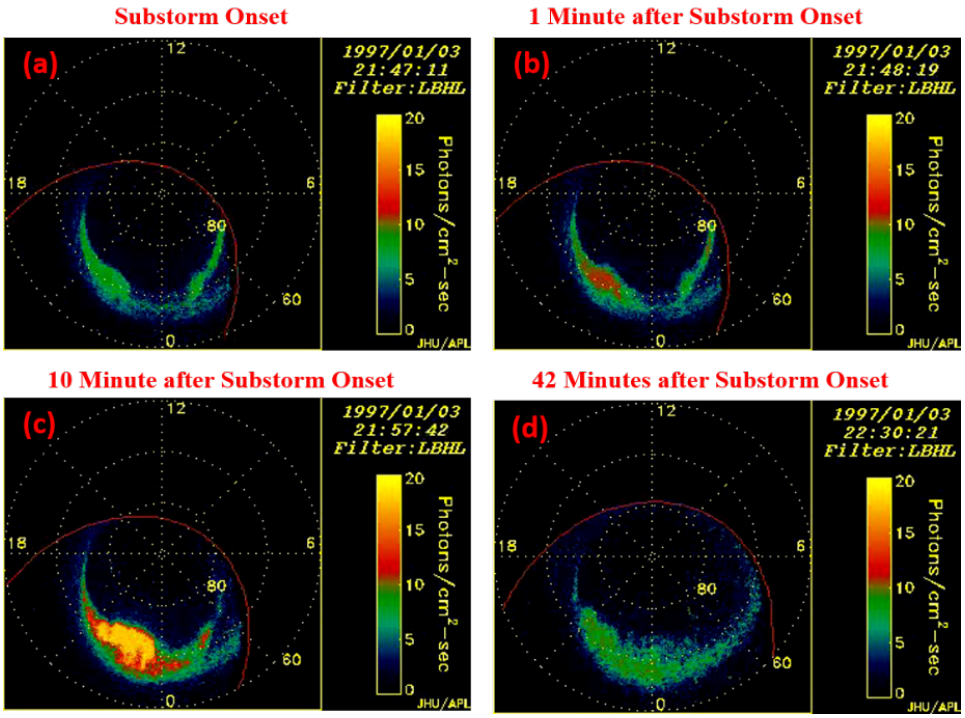

Figure 1.12: Snapshots of a substorm occurred on January 3rd, 1997 captured by the Ultra Violet Imager (UVI) cameras on board of Polar satellite.

and the auroral ionosphere (see Section 1.2.2) which may abruptly intensify in the auroral region and cause magnetic field disturbances. Such disturbances in Earth magnetic field due to an auroral substorm are called a magnetic substorm, which can be quantitatively measured by auroral electrojet indices, such as AE, AL, SME and SML, derived from ground-magnetometers (see Section 1.4.1 for indices). Figure 1.13 shows SML index that measures the magnetic substorm associated with the auroral substorm shown in Figure 1.12. The onset time of this magnetic substorm is indicated by a red vertical dashed line. SML index is provided by SuperMAG, which is a worldwide collaboration of organizations and national agencies that currently operate more than 300 ground-based magnetometers. In Chapter 5 we study the driving influences of magnetic substorms using machine learning techniques (see Section 1.4.2 for introduction to machine learning).

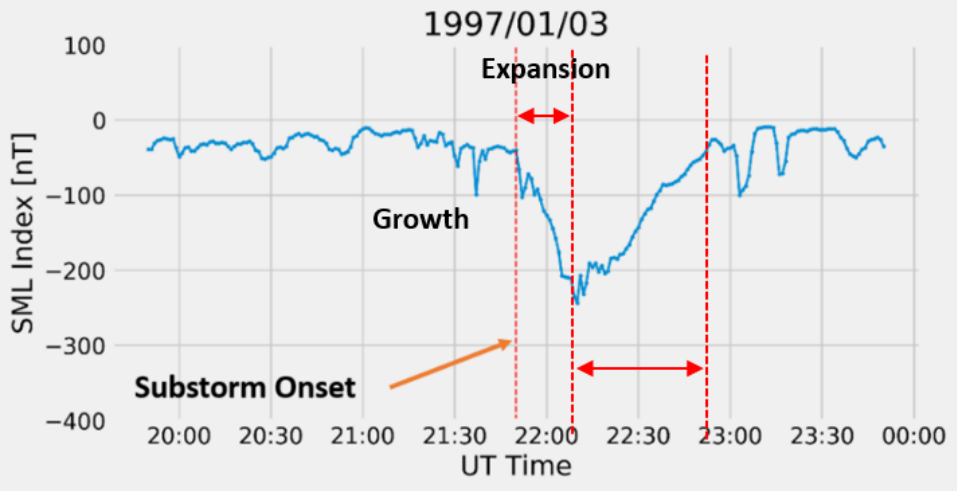

Figure 1.13: An example of a magnetic substorm occurred at 21:47 UT on January 3rd, 1997, as seen from SML index. This magnetic substorm is associated with the auroral substorm shown in Figure 1.12.

1.3.2 Geomagnetic Storm

A geomagnetic storm is a major disturbance of Earth's magnetosphere caused by a very efficient exchange of energy from the solar wind into the near-Earth space environment. It produces major changes in the magnetospheric field aligned currents and ring current, plasma convection, thermospheric temperature, and magnetic field line topology. Geomagnetic storms usually occur when there are many hours of sustained periods of high-speed solar wind, and most importantly, a southward directed IMF. As we have explained in Section 1.2.1, a southward IMF triggers magnetic reconnection at the dayside magnetopause and transports solar wind energy to the magnetotail (Figure 1.7).

A geomagnetic storm is often characterized by the one-hour disturbance storm time (Dst) index or one-minute SYM-H index, which are measures of the deviation of the H (north-south) component of the magnetic field near Earth's equator due to variations in the symmetric ring current intensity [Sugiura, 1964]. The most often used definition of a geomagnetic storm is an event wherein the minimum of the Dst index goes below a critical value, for example,

-30 nT (weak storms), -50 nT (moderate storms) or -100 nT (strong storms) [Sugiura and Chapman, 1960; Loewe and Prölss, 1997].

A typical geomagnetic storm has three phases: initial, main, and recovery. Figure 1.14 shows the Dst index during a geomagnetic storm that occurred on November 4-5, 2003, with the three phases identified. The initial phase is characterized by a brief rise in Dst (by 20 to 50 nT in tens of minutes). However, not all geomagnetic storms have an initial phase. The main phase of a geomagnetic storm is the interval of large decrease of Dst to less than a critical value. This phase generally coincides with the interval of sustained southward interplanetary field and lasts several hours. During the storm main phase, charged particles in the near-Earth plasma sheet are energized and injected deeper into the inner magnetosphere, producing the storm-time ring current. The recovery phase is when Dst recovers from its minimum value to its quiet time value. This phase is the longest and may take several hours to a few days. The recovery phase is due to loss of ring-current ions because of charge exchange with the neutral exosphere. Large geomagnetic storms can have severe adverse effects, which will be explained later in Section 1.3.3.

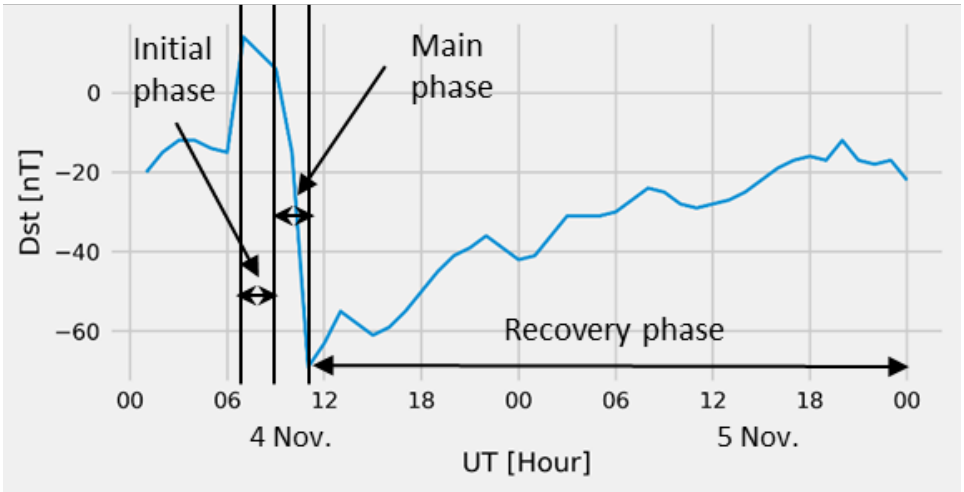

Figure 1.14: Example of a geomagnetic storm occurred on November 4-5, 2003, with the initial, main and recovery phases identified.

1.3.3 Space Weather

As we have explained in section 1.2, the solar wind, magnetosphere and the ionosphere form a single system driven by the solar wind energy. Thus, variation in the solar wind can cause changes throughout the magnetosphere, ionosphere and the ground, which we call "space weather". As defined by The National Aeronautics and Space Administration (NASA), space weather refers to the conditions on the sun, in the solar wind, and within Earth's magnetosphere, ionosphere and thermosphere that can influence the performance and reliability of space-borne and ground-based technological systems and can endanger human life or health.

Space weather events such as magnetic storms and substorms can have serious consequences. While they create beautiful aurora, they also cause damage to spacecraft through electrical charging of electronics on board [Gubby and Evans, 2002; O'Brien, 2009; Horne et al., 2013; Loto'aniu et al., 2015]. There are several hundred satellites in geosynchronous orbit and their operations can be perturbed and on occasion totally disrupted by storms and substorms. They can also disrupt navigation systems such as the Global Navigation Satellite System (GNSS) and create harmful geomagnetic induced currents (GICs) in the power grid and pipelines [Belakhovsky et al., 2019; Freeman et al., 2019]. Large storms can force the magnetopause inside geosynchronous orbit (∼6.6 RE) and cause problems for satellites that use Earth's magnetic field for orientation. Forecasting geomagnetic storms and substorms has therefore been a topic of practical as well as theoretical space weather interest. In Chapter 5, we present the first machine learning model that can forecast the occurrence probability of substorm onsets over the next one hour.

1.4 Instrumentations and Techniques

In this section we introduce the instruments and techniques used in this dissertation.

1.4.1 Instrumentations

SuperDARN Radars

The Super Dual Auroral Radar Network (SuperDARN) consists of chains of high-frequency (HF) radars in the northern and southern hemispheres that monitor ionospheric dynamics through the detection of decameter-scale field-aligned plasma irregularities in the E and F regions of the ionosphere [Greenwald et al., 1985; Chisham et al., 2007; Nishitani et al., 2019]. Figure 1.15 shows the fields of view (FOV) of currently operational SuperDARN radars. Typically, a SuperDARN radar operates between 10 and 14 MHz and has 16-24 beams, 75-100 range gates along each beam, and a 45 km range resolution. The azimuth step between beams is ∼3.3°, and an azimuthal scan across all 16-24 beams generally takes 1-2 minutes with a dwell time between 3 and 7 seconds on each beam. It is capable of detecting targets with Doppler velocities of 0 m/s up to 2 km/s.

Until 2005, the SuperDARN consisted of only high-latitude and polar cap radars (cyan and green colored FOVs in Figure 1.15) and could only monitor the regions of the ionosphere poleward of ∼60° geomagnetic latitude. The mid-latitude expansion of SuperDARN radars (red colored FOVs in Figure 1.15) over the past 15 years has provided new opportunities to study mid-latitude ionospheric convection over large areas and with unprecedented spatial resolution (see [Nishitani et al., 2019] for a comprehensive review of the accomplishments of mid-latitude SuperDARN radars). In this dissertation, the line-of-sight plasma drift velocity measurements obtained from the mid-latitude SuperDARN radars in the U.S. are used as

the primary data set for studying the driving influences of subauroral convection in Chapters 3 & 4.

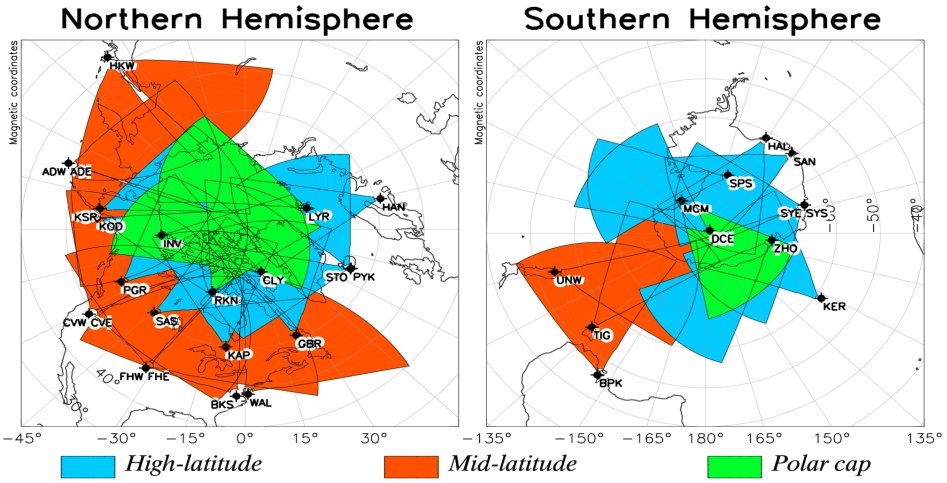

Figure 1.15: Fields of view (FOV) of currently operational SuperDARN radars from the northern (left) and southern (right) hemispheres in magnetic coordinates. Polar cap, high-latitude, and mid-latitude radar FOV are shaded in green, cyan, and red, respectively.

RISR-N

The Resolute Bay Incoherent Scatter Radar - North Face (RISR-N) is an incoherent scatter radar located at Resolute Bay, Canada (74.7° N, 94.9° W, MLAT = 82.7° N). RISR-N is a phased-array system which can electronically steer a narrow beam in any direction within its field of view (Figure 1.16). Line-of-sight ion drift measurements from multiple beam positions and range intervals are routinely combined to provide direct three-dimensional measurements of spatiotemporal variations deep within the polar cap (See [Bahcivan et al., 2010] for more details about RISR-N). The RISR-N line-of-sight ion drift velocity measurements are the primary dataset in Chapter 2 for studying polar cap plasma convection.

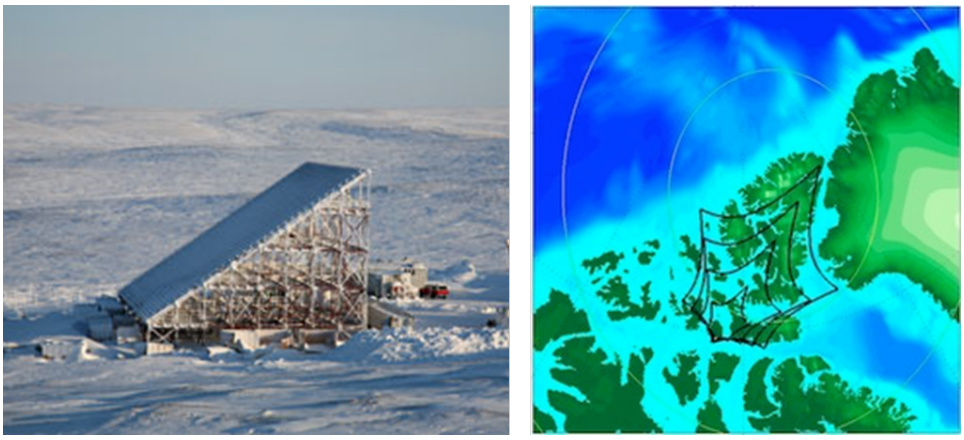

Figure 1.16: Resolute Bay Incoherent Scatter Radar – North (RISR-N) in Canada (left) and its fields of view (right). The pentagons in black show the coverage of RISR-N at 100, 200, 300, and 400 km altitudes, respectively. The white oval-shaped lines are the magnetic latitude contours.

Upstream Satellites

The Advanced Composition Explorer (ACE) and Deep Space Climate Observatory (DSCOVR) are two of several spacecraft that monitor the upstream solar wind conditions. They orbit around the Earth-Sun L1 Lagrangian point, which is one of several points in space where the gravitational attraction of the Sun and Earth are equal and opposite (Figure 1.17). The L1 point is located ∼240 RE away from Earth's center (1.5 million km) in the direction of the Sun. The solar wind that passes a spacecraft at L1 hits Earth after ∼30 - 60 min [Weimer et al., 2003].

ACE, launched in 1997, has several instruments that monitor the solar wind [Stone et al., 1998]. IMF data are from the magnetic field instrument MAG [Smith et al., 1998] while the particle data are from the Solar Wind Electron, Proton, and Alpha Monitor (SWEPAM) instrument [McComas et al., 1998]. The Deep Space Climate Observatory (DSCOVR) spacecraft is an advanced version of the ACE spacecraft and launched in 2015 to replace it.

OMNI is solar wind magnetic field and plasma data sets that are obtained from one or more

upstream satellites and have been time-shifted to Earth's bow shock nose. In Chapters 3 – 5, we use 1-min-averaged OMNI data sets to study the driving influences of subauroral plasma flows and substorms.

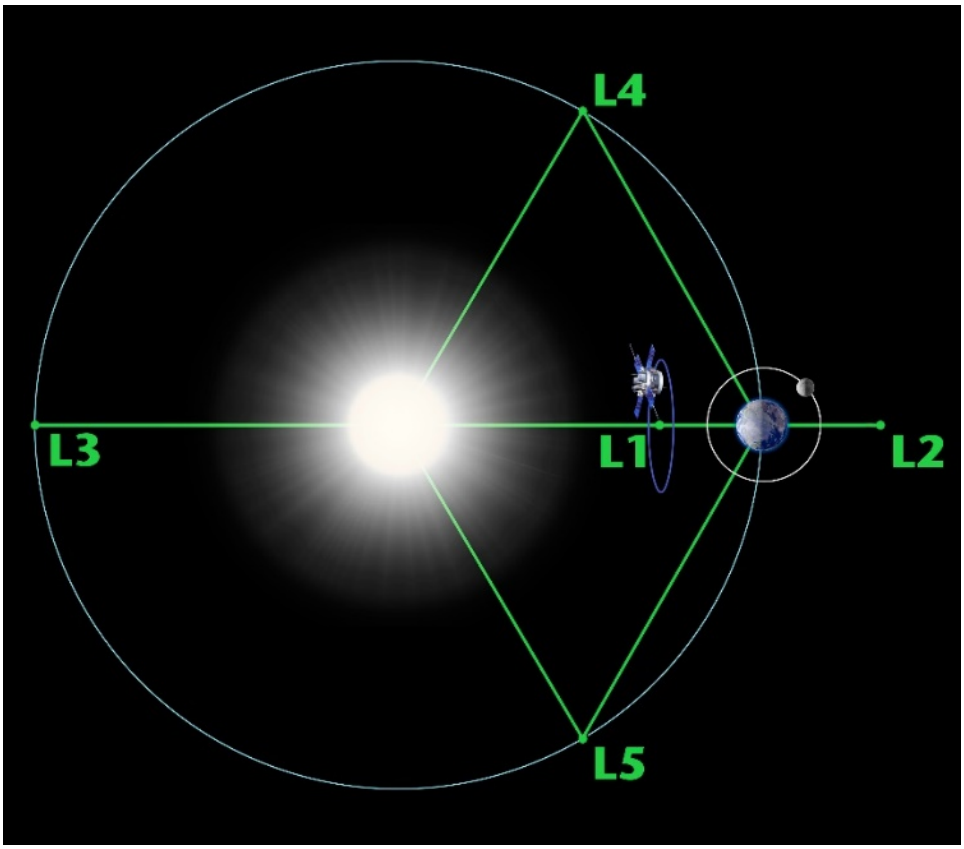

Figure 1.17: NASA's Advanced Composition Explorer (ACE) and NOAA's Deep Space Climate Observatory (DSCOVR) spacecraft orbit a point between Earth and the sun called a Lagrange point, labeled here as L1. Sitting well outside of Earth's magnetosphere, ACE/DSCOVR can observe material streaming off the sun before it enters near-Earth space (Credit: NASA/H. Zell).

Defense Meteorological Satellite Program (DMSP)

DMSP satellites are sun-synchronous polar-orbiting spacecraft with orbital height at ∼840 km (Figure 1.18). Each DMSP satellite has an orbital period of 101 minutes and takes about 20 minutes to cross the polar cap region above |50°| MLAT. Payloads on each satellite in-

clude sensors to measure precipitating auroral particles (SSJ [Hardy et al., 1984]), cold/bulk plasma properties of the ionosphere (SSIES [Heelis and Hairston, 1990], the geomagnetic field (SSM), and optical emissions in the far and extreme ultraviolet (SSULI and SSUSI). In Chapter 2, DMSP data are used to cross-validate the accuracy of the derived RISR-N ionospheric velocity vectors and provide contextual information about their proximity to the cusp. Specifically, we use Level-2 SSIES [Heelis and Hairston, 1990] cross-track ion drift velocity data at four-second cadence provided by the University of Texas Dallas and SSJ/4/5 [Hardy et al., 1984] particle data at one-second resolution provided by the Johns Hopkins University Applied Physics Laboratory.

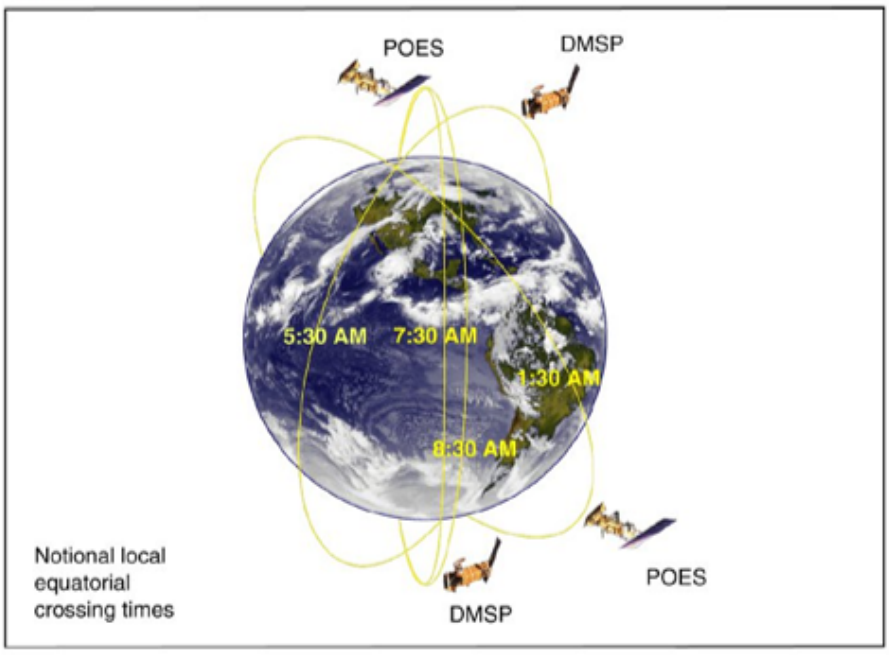

Figure 1.18: DMSP and POES Orbits (Source: NPOESS Integrated Program Office).

Polar Operational Environmental Satellites (POES)

Like the DMSP satellites, the NOAA (National Oceanic and Atmospheric Administration) POES are a series of polar-orbiting spacecraft that operates in Sun-synchronous orbits at an altitude of ∼800 km with an orbital period of 101 min (Figure 1.18). In Chapter 4, we use particle precipitation data from the Total Energy Detector (TED) instrument in the Space Environment Monitor (SEM) package [S. Evans and S. Greer, 2004] on board the POES spacecraft to estimate the equatorward auroral oval boundary.

Ground magnetometers and Geomagnetic Indices

A ground magnetometer is a device that measures the direction and strength of Earth's magnetic field. Ground magnetometers are widely distributed around the globe and have been extensively used for studying local and global scale electrodynamics. Numerous geomagnetic indices, which are measures of various magnetic activities, are derived from ground magnetometer measurements [Rostoker, 1972; Menvielle et al., 2011]. Below are the geomagnetic indices we use in this dissertation:

Dst: A measure of symmetric ring current intensity [Sugiura, 1964].

SYM-H: Same as Dst, but it has a 1-minute temporal resolution [Iyemori, 1990]

AU/AL: A measure of maximum eastward/westward auroral electrojets strength in the auroral zone [Davis and Sugiura, 1966].

AE = AU - AL: A measure of global electrojet activity in the auroral zone [Davis and Sugiura, 1966].

SMU, SML, SME: SuperMAG version of AU, AL, and AE, respectively [Newell and Gjerloev, 2011a,b].

Kp: The K-index quantifies disturbances in the horizontal component of earth's magnetic field at mid-latitudes with an integer in the range 0-9 with 1 being calm and 5 or more indicating a geomagnetic storm [Bartels et al., 1939].

F10.7: A measure of the noise level generated by the sun at a wavelength of 10.7 cm at Earth's orbit. It is an excellent indicator of solar activity [Tapping, 1987, 2013].

1.4.2 Techniques

In this subsection we give a brief introduction to machine learning, present some recent applications in our daily lives, and touch upon how space science can benefit from it.

Machine learning is a research field at the intersection of statistics and computer science. It is a subset of artificial intelligence, i.e. intelligence demonstrated by machines (see [Russell and Norvig, c2010] for various definitions of artificial intelligence). It seeks to answer the question "How can we build computer systems that automatically improve with experience, and what are the fundamental laws that govern all learning processes?" [Mitchell, 2006]. We say a machine has "learned" because machine learning algorithms can decide how to perform important tasks by generalizing from examples [Domingos, 2012]. Although the term "machine learning" was used much earlier, the concept of machine learning as we know it today was first defined by Arthur Samuel in 1959 [Samuel, 1959], who introduced the field as the subfield of computer science that gives computers the ability to learn without being explicitly programmed [Theobald, 2018].

In conventional programming, a programmer writes a set of rules or instructions into computer programs based on input data and runs them on a computer to produce a desired output. In contrast, machine learning gets computers to perform a task without relying on rules-based programming. This is done by using machine learning algorithms that can

learn and make decisions based on data (Figure 1.19). Conventional programming works best for solving problems for which we have a discreet set of direct rules governing the logic. However, there are many cases where deriving rules from input data are challenging, if not possible. For example, writing a computer problem which can identify a person in an image or video is a daunting task for a programmer, whereas modern machine learning algorithms can easily perform this task with high accuracy [Trigueros et al., 2018]. In this scenario, one may train a machine learning model to recognize a person in an image by feeding a large data set of images of different people to a machine learning algorithm. As a result, the input of the generated model would be a digital image of a person, and the output is an integer associated with a person.

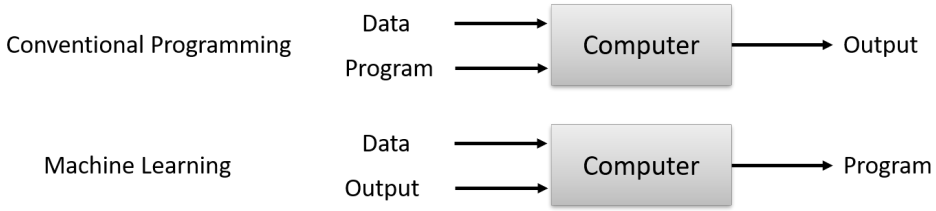

Figure 1.19: Conventional programming vs. machine learning.

Machine learning algorithms that learn from input-output pairs are called supervised learning algorithms. In supervised learning, a machine learning algorithm takes pairs of inputs and desired outputs, and learns how to produce the desired output for an input it has never seen before without any help from a human. There are two major types of supervised machine learning problems, called classification and regression. In classification, the goal is to predict a class label. For example, in spam classification, one can "train" a machine learning algorithm on historical emails and their labels (i.e., spam or non-spam). The trained algorithm will then produce a prediction for a given new email. For regression tasks, the goal is to predict a continuous number. Predicting a person's income based on input features such as education, experience, job title is an example of a regression task. In contrast, unsuper-

vised learning algorithms only take input data without preexisting labels. The goal is to draw inferences or find patterns from the unlabeled data. Unsupervised learning algorithms are suitable for tasks such as dimensionality reduction and cluster analysis.

Machine learning is powering many aspects of our modern society such as image recognition [Krizhevsky et al., 2017], speech recognition [Hinton et al., 2012], machine translation [Sutskever et al., 2014], question answering [Bordes et al., 2014], self-driving cars [Bojarski et al., 2016], reconstructing brain circuits [Helmstaedter et al., 2013], and analysis of genetic and genomic data sets [Libbrecht and Noble, 2015], etc. These applications make use of a subset of machine learning techniques called deep learning whose architecture is a multi-layer stack of simple modules or layers (Figure 1.20). Unlike conventional machine learning algorithms which require careful engineering and considerable domain expertise to extract features from the raw data (such as the pixel values of an image), deep learning methods can take the raw data as inputs and automatically discover features suitable for performing a machine learning task. With multiple layers, a deep learning system transforms features at one level (starting with the raw input) into features at a higher, slightly more abstract level. With the composition of enough such transformations, very complex functions can be learned. Thus, the key aspect of deep learning is that these layers of features are not designed by human engineers: they are learned from data using a general-purpose learning procedure [LeCun et al., 2015].

Although not widely used yet, machine learning is not new to space science. Several attempts were made to use machine learning for space weather prediction in the late 1980s and early 1990s, such as predicting solar flares [Fozzard et al., 1989], solar wind speed [Wintoft and Lundstedt, 1997], energetic electrons at geosynchronous orbit [Stringer et al., 1996], and geomagnetic indices [Lundstedt and Wintoft, 1994; Gleisner et al., 1996; Wu and Lundstedt, 1997; Hernandez et al., 1993; Gleisner and Lundstedt, 1997]. Recently, machine learning

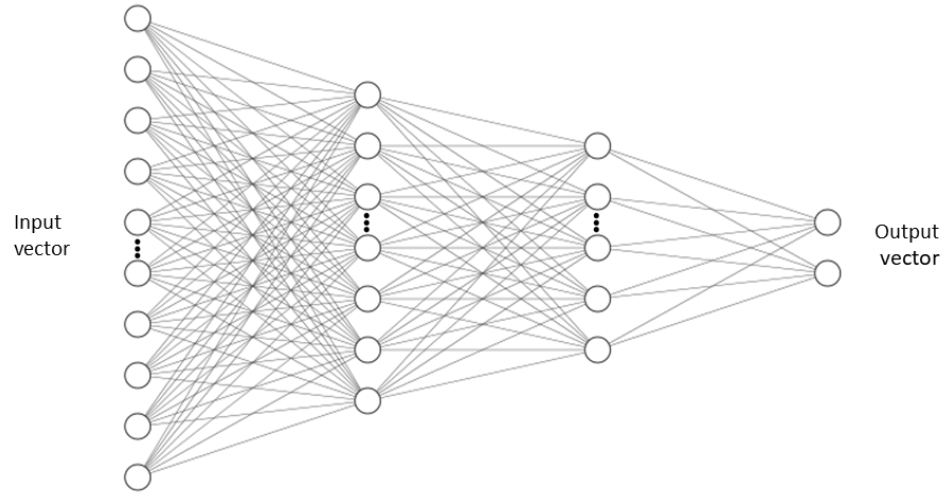

Figure 1.20: Schematic of Multilayer Perceptron (MLP), a type of deep learning architecture.

methods have been applied to segmentation of coronal holes in solar disk images [Illarionov and Tlatov, 2018], classifying auroral images [Clausen and Nickisch, 2018]; forecasting solar flares [Florios et al., 2018], geomagnetic indices [Chandorkar et al., 2017], MeV electron flux [Wei et al., 2018], and GPS signal scintillation [McGranaghan et al., 2018]; and clustering solar wind and IMF parameters [Heidrich-Meisner and Wimmer-Schweingruber, 2018], etc. However, the application of machine learning to space weather is still in its infancy compared to other fields. Some deep learning architectures that find successful applications in other fields haven't been tried on space weather problems. For example, deep learning based on convolutional neural networks (CNN), which is one of the most successful developments in machine learning [LeCun et al., 2015], has been barely touched by the space weather community [Camporeale, 2019]. In Chapter 5, we apply the latest variants of CNN models to forecast substorm onsets one hour ahead of time and to investigate the factors that impact substorms onsets.

1.5 Outstanding Research Issues

In this section we highlight outstanding research issues in ionospheric electrodynamics in the polar cap, auroral and subauroral regions. The goal is to stimulate research efforts on studying the driving influences of electric fields and currents in those regions and advancing space weather prediction. This dissertation addresses a subset of the outstanding research issues outlined here.

1.5.1 High-Latitude Convection under Dynamic Solar Wind & IMF Conditions

In Section 1.2 & 1.3 we explained how solar wind energy is coupled to Earth's magnetosphere and ionosphere through magnetic reconnection as proposed by Dungey [1961, 1963]. The Dungey mechanism incorporates a dependency on the orientation of the magnetic field carried by plasma at the point of reconnection. Based on this theory, many empirical models of ionospheric convection have been developed that are parameterized by the solar wind, IMF, and overall level of geomagnetic activity [e.g. Cousins and Shepherd, 2010; Förster and Haaland, 2015; Haaland et al., 2007; Hairston and Heelis, 1990; Heppner and Maynard, 1987; Papitashvili and Rich, 2002; Reistad et al., 2018; Ridley et al., 2000; Ruohoniemi and Greenwald, 2005; Thomas and Shepherd, 2018; Weimer, 2005; Zhang et al., 2007]. Figure 21 shows a recent statistical model of high latitude convection derived from SuperDARN radar measurements [Thomas and Shepherd, 2018].

Steady state models like that of Thomas and Shepherd [2018] are invaluable for illustrating the basic features of ionospheric convection; however, they implicitly assume quasi-static conditions, which is rarely the case. Instead, the ionospheric flows are constantly in the

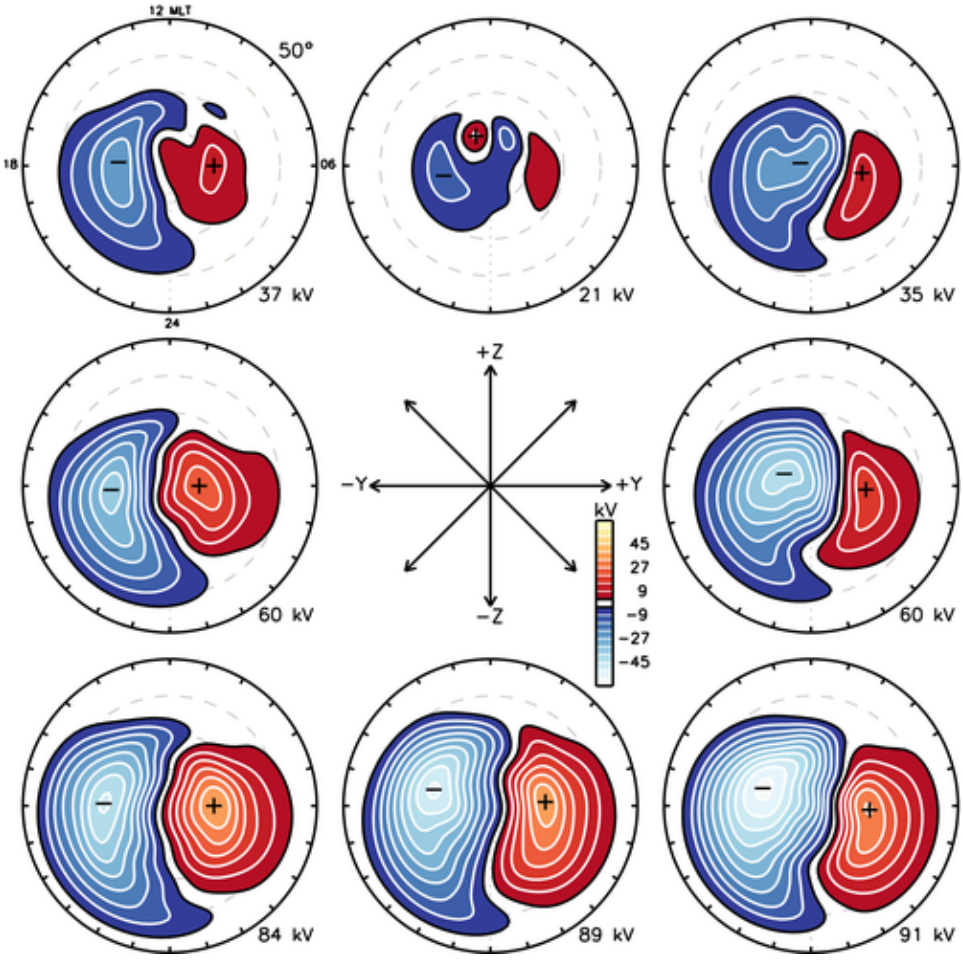

Figure 1.21: Steady-state statistical model of high latitude convection under different IMF orientations derived from SuperDARN radars measurements [Thomas and Shepherd, 2018].

process of reconfiguring to ever-changing IMF orientation and magnitude, rather than simply switching from one steady state to another [Murr and Hughes, 2007]. The temporal details of how convection transitions between two steady states are still not understood completely, especially during northward IMF conditions.

Several studies have investigated the timescales on which the global convection pattern evolves from one state to another [Ruohoniemi and Baker, 1998; Ridley et al., 1998; Lockwood and Cowley, 1999; Huang et al., 2000]. However, the corresponding reconnection geometry during the transition is not well studied. In addition, using global patterns to

examine time variation may miss some of the important mesoscale details. For example, the reverse convection cells that develop under northward IMF are constrained to lie within a small area of the high-latitude ionosphere and the emergence of sunward flow on the noon meridian in particular is inherently a mesoscale process. Thus, studying the dynamics of high-latitude convection in the ionoshpere will allow us to understand the geometry of magnetic reconnection at the magnetopause. Furthermore, it will aid us in making more realistic real-time predictions of high-latitude convection.

1.5.2 Subauroral Convection and its Driving Influences

From Figure 1.21 we can see that the high-latitude convection does not usually extend far below ∼60 MLAT. This is because, under steady solar wind and magnetospheric conditions, the inner magnetosphere and conjugate subauroral ionosphere is shielded from the effects of the dawn-dusk convection electric field across the magnetosphere by Region 2 field-aligned currents driven by pressure gradients near the inner edge of the plasma sheet [Jaggi and Wolf, 1973; Vasyliunas, 1970, 1972] (see section 1.2.3). As a result, the quiet time plasma in the nightside subauroral regions exhibits drifts of only a few tens of meters per second [Buonsanto et al., 1993; Richmond et al., 1980] in contrast to the hundreds of meters per second drifts at high-latitudes.

The most well-known mechanism proposed to account for electric fields in the nightside subauroral ionosphere is the neutral wind dynamo [Richmond et al., 1976; Rishbeth, 1971], by which a dynamo electric field is generated through the collision of neutral molecules with ions leading to charged particle motion across the geomagnetic field. The storm time version of the neutral wind dynamo mechanism is the ionospheric disturbance dynamo proposed by Blanc and Richmond [1980], by which a predominantly northward electric field is generated

at midlatitudes due to the thermospheric circulation that is driven by auroral heating during periods of high geomagnetic activity. For both types of dynamo mechanisms, it is the neutral drag force that drives the plasma motion. In the absence of geomagnetic disturbance, the thermospheric neutral winds at subauroral latitudes are generally directed eastward premidnight and westward postmidnight [Drob et al., 2015; Emmert et al., 2003, 2006; Xiong et al., 2015]. Under such conditions, we would expect the neutral wind dynamo to entrain the plasma to follow the pattern of the background neutral winds, that is, eastward premidnight and westward postmidnight at F region altitudes during quiet magnetic conditions. However, previous studies have found this to not be the case [Buonsanto et al., 1993; Fejer, 1993].

Another cause of plasma motion in the subauroral region is solar wind-magnetosphere interaction that leads to penetration of dawn-dusk convection electric field into the inner magnetosphere and ionosphere equatorward of the auroral boundary [Blanc et al., 1977; Nishida, 1968] (see Section 1.2.3). As the inner magnetosphere (subauroral region) is considered to be shielded from the effects of the dawn-dusk convection electric field, the occurrence of penetration electric fields is mostly invoked under geomagnetically disturbed conditions [e.g. Blanc et al., 1977; Buonsanto et al., 1992; Yeh et al., 1991]. However, some studies have reported the presence of penetration electric fields under quiet time conditions [e.g. Carpenter and Kirchhoff, 1975; Heelis and Coley, 1992; Lejosne and Mozer, 2016; Wand and Evans, 1981a]. Thus, the driving influences of subauroral flows are still not well understood. In Chapters 3 & 4, we examine the driving influences of nightside subauroral convection using plasma drift measurements from six U.S. mid-latitude SuperDARN radars.

1.5.3 Driving Influences of Substorm Onset

A substorm is a transient and complex phenomenon that takes place in Earth's magnetosphere and ionosphere, involving energy transfer from the magnetotail to the auroral ionosphere. Strong coupling between the solar wind, magnetosphere and the ionosphere is an important aspect of the substorm phenomenon (see Section 1.3.1). Over the past six decades, substorms have been extensively studied using observations from both space and ground-based instruments, as well as through first principles models [Akasofu, 1964; McPherron, 1979; Pudovkin, 1991; Lyons, 1995; Lui, 2000; Newell and Gjerloev, 2011b].

Determining the roles of different IMF and solar wind parameters in triggering a substorm has been a subject of interest for several decades. Several studies have focused on analyzing the impact of different solar wind and IMF parameters on the substorm growth phase [Akasofu, 1975; Caan et al., 1977; Lyons, 1995; Henderson et al., 1996; Freeman and Morley, 2004; Newell et al., 2016]. A majority of these studies find IMF Bz to be the most important factor controlling substorm activity [McPherron et al., 1973; Caan et al., 1977; McPherron, 1979; Pudovkin, 1991]. Besides IMF Bz, the solar wind velocity (Vx) [Li et al., 2007; Luo et al., 2013; Newell et al., 2016; Tanskanen, 2009] and IMF By [Troshichev et al., 1986; Petrukovich et al., 2000; Wild et al., 2009; Lee et al., 2010] were also shown to influence the occurrence of substorms.

A widely debated topic has been the mechanism that triggers substorm expansion phase onset. Some studies proposed that the onset may be externally triggered by a change in solar wind and IMF conditions, such as a northward turning of Bz [Lyons, 1995; Lyons et al., 1997; Russell, 2000], whereas recent observations contradict these findings and suggest that substorms may be internally triggered and a northward turning of Bz is not necessary [Morley and Freeman, 2007; Freeman and Morley, 2009; Wild et al., 2009; Johnson and Wing,

2014]. Furthermore, understanding the chronological sequence of events constituting the actual trigger process has been a topic of heated debate for several researchers. Specifically, opposing views have emerged on whether current disruption in the near-Earth region is followed by magnetic reconnection occurring farther out in the magnetotail or vice-versa [Lui, 1991, 1996; Baker et al., 1996]. The Time History of Events and Macroscale Interactions during Substorms (THEMIS) mission [Angelopoulos, 2008] addressed this question by demonstrating that tail reconnection happens prior to current disruption [Angelopoulos, 2008]. However, the study also raised another important question about the role of preconditioning of the magnetosphere in terms of tail reconnection during the growth phase. In Chapter 5, we investigate the driving influences of substorm onset using machine learning; we analyze the importance of different IMF and solar wind parameters in triggering a substorm and discuss the external vs. internal triggers.

1.6 Research Objectives and Dissertation Organization

The goal of this research has been to investigate the driving influence of electrodynamics in the mid- and high- latitude ionosphere. The specific science questions addressed in this dissertation are the following:

1. How does the reconnection geometry evolve when polar cap convection transitions between two steady-state? (Chapter 2)

2. What are the major driving influences on subauroral convection? (Chapters 3 & 4)

3. What ability do we have to predict substorm onset using machine learning and what is revealed about the factors that influence onset? (Chapter 5)

This dissertation is organized into six chapters. Chapter 1 has introduced the background knowledge for this dissertation, instruments and techniques, outstanding research questions and objectives of this research. In Chapter 2, we analyze an interval on 12 September 2014 which provided a rare opportunity to examine dynamic variations in the dayside convection throat measured by the RISR-N radar as the IMF transitioned from strong By+ to strong Bz+. The primary goal of this chapter is to investigate the difference in lag times of IMF By and Bz influences during this event and to understand its implications for the geometry of magnetic reconnection at the magnetopause. In Chapters 3 & 4, we investigate the driving influences of subauroral convection. Specifically, in Chapter 3 we examine the subauroral midlatitude plasma convection under quiet geomagnetic conditions using nightside line-of-sight measurements from six mid-latitude SuperDARN radars in the U.S. continent. In Chapter 4, we expand this analysis to understand the manifestations of neutral wind and penetration effects as drivers of subauroral convection with progression from quiet to relatively disturbed geomagnetic conditions. In Chapter 5 we investigate the driving influences of substorm onset using machine learning and we present the first deep learning-based time series model to directly forecast the onset of a magnetic substorm with one hour of warning. Finally, Chapter 6 summarizes the conclusions and ideas for future work.

Chapter 2

IMF By Influence on Reverse Convection During Extreme Northward IMF

M. Maimaiti [1], J. M. Ruohoniemi [1], J. B. H. Baker [1], C. R. Clauer [1], Michael J. Nicolls [2], Marc R. Hairston [3]

[1]Bradley Department of Electrical and Computer Engineering, Virginia Tech, Blacksburg, Virginia, USA.

[2]Center for Geospace Studies, SRI International, Menlo Park, CA, USA.

[3]William B. Hanson Center for Space Sciences, University of Texas at Dallas, Richardson, TX, USA.

Maimaiti, M., Ruohoniemi, J. M., Baker, J. B. H., Clauer, C. R., Nicolls, M. J., and Hairston, M. R. (2017), RISR-N observations of the IMF By influence on reverse convection during extreme northward IMF, J. Geophys. Res. Space Physics, 122, 3707– 3720, doi:10.1002/2016JA023612.

Abstract

Previous studies have demonstrated that the high-latitude ionospheric convection is strongly influenced by the interplanetary magnetic field (IMF) direction. However, the temporal details of how the convection transitions from one state to another is still not understood completely. In this study, we analyze an interval on September 12, 2014 which provided a rare opportunity to examine dynamic variations in the dayside convection throat as the IMF transitioned from strong B_y+ to strong B_z+. Between 18:00 - 20:00 UT the northward face of the Resolute Bay Incoherent Scatter Radar (RISR-N) rotated through the noon sector and directly measured strengthening reverse convection flows in the dayside throat region that peaked at $\sim 2800 m/s$. Near-simultaneous measurements from DMSP satellites confirm the magnitude of the reverse convection and its proximity to the cusp. Time-series comparison of the RISR-N north-south flows with the IMF B_z component shows a remarkably high correlation, suggestive of strong linear coupling, with no sign of velocity saturation. Likewise, the east-west flow variations were highly correlated with the changes in IMF B_y. However, time-lagged correlation analysis reveals that the IMF B_y influence acted on a time-scale 10 minutes shorter than that of the B_z component. As a consequence, the manner in which the convection transitioned from the strong B_y+ condition to the strong B_z+ condition is inconsistent with either the anti-parallel and component reconnection models. Instead, we suggest that these particular observations are consistent with two separate reconnection sites on the magnetopause driven independently by the IMF B_y and B_z components.

2.1 Introduction

Plasma convection is one of the most fundamental processes for understanding the structure of geospace and disturbance effects in the magnetosphere-ionosphere (M-I) system. It is

widely accepted that the dominant source for driving plasma convection in the high latitude regions is the magnetic reconnection proposed by Dungey [1961, 1963]. The Dungey mechanism incorporates a dependency on the orientation of the magnetic field carried by plasma at the point of reconnection. For the case of purely southward IMF, reconnection is favored at the subsolar magnetopause and drives a large two-cell pattern at high lattitudes with antisunward flow over the polar cap that returns to the dayside via the dawn and dusk flanks [e.g. Ruohoniemi and Greenwald, 2005]. For IMF B_y+ (B_y-), the site of reconnection in the northern hemisphere shifts duskward (dawnward), which creates a dawnward (duskward) magnetic tension force that drives a distorted two-cell convection [Heppner and Maynard, 1987]. Under northward IMF conditions, the reconnection site shifts poleward of the cusp [Dungey, 1963; Crooker, 1979] and drives a four-cell pattern with reverse two-cell circulation constrained to a small area of the high latitude dayside and two other cells with the normal sense of circulation at lower latitudes [Burke et al., 1979; Förster et al., 2008].

Over the years, several empirical models of ionospheric convection have been developed that are parameterized by the solar wind, IMF, and overall level of geomagnetic activity [Papitashvili and Rich, 2002; Ruohoniemi and Greenwald, 2005; Weimer, 2005; Cousins and Shepherd, 2010]. Such models are invaluable for illustrating the basic features of ionospheric convection, however, they implicitly assume quasi-static conditions, which is rarely the case. Instead, the ionospheric flows are constantly in the process of reconfiguring to ever-changing IMF orientation and magnitude, rather than simply switching from one steady state to another [Murr and Hughes, 2007]. Indeed, several studies have investigated the time-scales on which the global convection pattern evolves from one state to another [Ruohoniemi and Greenwald, 1998; Ridley et al., 1998; Lockwood and Cowley, 1999; Huang et al., 2000]. However, using global patterns to examine time-variation may miss some of the important mesoscale details. For example, the reverse convection cells that develop under northward

IMF are constrained to lie within a small area of the high latitude ionospheric and the emergence of sunward flow on the noon meridian in particular is inherently a mesoscale process. Local measurements well within the polar cap are thus needed to resolve the direct response of ionospheric convection to variable northward IMF.

In this study, we examine a period of extreme northward IMF which occurred at 18:00 - 20:00 UT on September 12, 2014 when the northward face of the Resolute Bay Incoherent Scatter Radar (RISR-N) was located in the noon sector and thus ideally situated to monitor dynamic changes in the dayside reverse convection throat for an extended period of time. As we will discuss, time-series comparison of the north-south flows measured by RISR-N with the IMF B_z component shows a remarkably high correlation, with no sign of velocity saturation despite extremely high (> 20 nT) B_z+. A previous study by Clauer et al. [2016] studied the saturation aspect in detail and offered an explanation. Although not discussed by Clauer et al. [2016], the event also featured a strong and highly variable IMF B_y component which was likewise correlated with the east-west flows measured by RISR-N, but not on the same time-scale as the B_z influence. The primary goal of this paper is thus to investigate the difference in IMF B_y and B_z time-scales during this event and to understand its implications for the geometry of magnetic reconnection at the magnetopause.

2.2 Instrumentation and Data Processing

The datasets utilized in this study were obtained from RISR-N, DMSP-SSIES, DMSP-SSJ/4/5, ACE-MAG and ACE-SWEPAM. In this section, we briefly review these instruments and describe the pre-processing steps used to prepare the RISR-N raw data for subsequent analysis.

2.2.1 Resolute Bay Incoherent Scatter Radar - North Face (RISR-N)

The primary dataset is line-of-sight (LOS) ion drift velocity measurements obtained from the RISR-N incoherent scatter radar located at Resolute Bay, Canada (74.7° N, 94.9° W, MLAT = 82.7° N). RISR-N is a phased-array system which can electronically steer a narrow beam in any arbitrary direction within its field of view. LOS ion drift measurements from multiple beam positions and range intervals are routinely combined to provide direct three dimensional measurements of spatiotemporal variations deep in the polar cap (See Bahcivan et al. [2010] for more details about RISR-N). During the period of interest (September 11-15, 2014) RISR-N ran the "World Day66m" mode in coordination with all other US incoherent scatter radars. This mode collects long-pulse LOS data with 72 km range resolution and 62 sec time resolution, which is specially designed for F region studies. Figure 2.1 shows the beam configuration in (a) azimuth versus elevation format (top panel), and (b) magnetic longitude versus latitude (bottom panel). It can be seen that beams 1, 2, 6, and 10 all look towards magnetic north and extend beyond 85° MLAT. Figure 2.2 shows raw LOS ion velocities measured on September 12, 2014 in the magnetic northward (beams 2 and 10), northwest (beam 5), and northeast (beam 7) directions. Positive (blue) velocities indicate motion towards the radar. The most striking feature is a period of strong positive velocities measured on all beams starting at around 18:30 UT corresponding to sunward convection in the dayside throat region.

The primary objective of this study is to analyze how the strength and direction of the reverse convection flows seen by RISR-N in Figure 2 are modulated by variations in the IMF B_z and B_y components. The procedure for processing the multi-beam LOS data to produce a single vector characteristic of the horizontal flows in the dayside throat is as follows. First, the

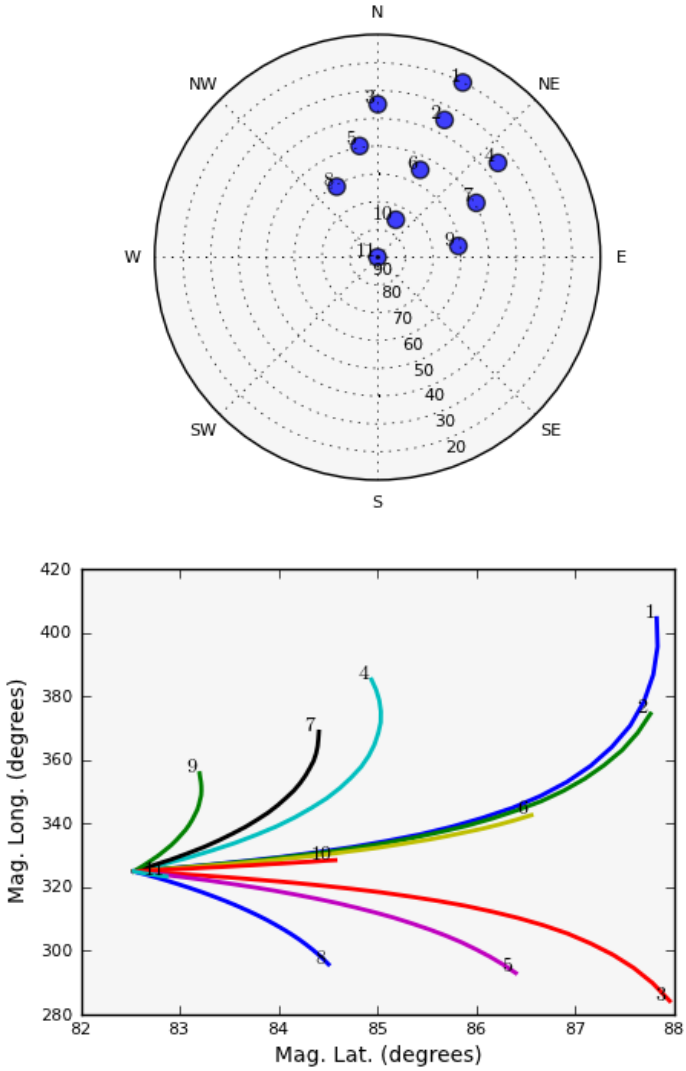

Figure 2.1: RISR-N beam configuration on September 12, 2014 in (a) geographic azimuth versus elevation format, and (b) magnetic longitude versus latitude format.

data on each beam are filtered by altitude to exclude echoes from the E-region ($< 150\ km$) and above the main F-region ($> 500\ km$). Next, the LOS velocities are filtered by velocity error ($< 50\ m/s$) and projected to the horizontal plane using the elevation angle of each beam and then resampled to 1-minute resolution. Finally, the magnitude and direction of

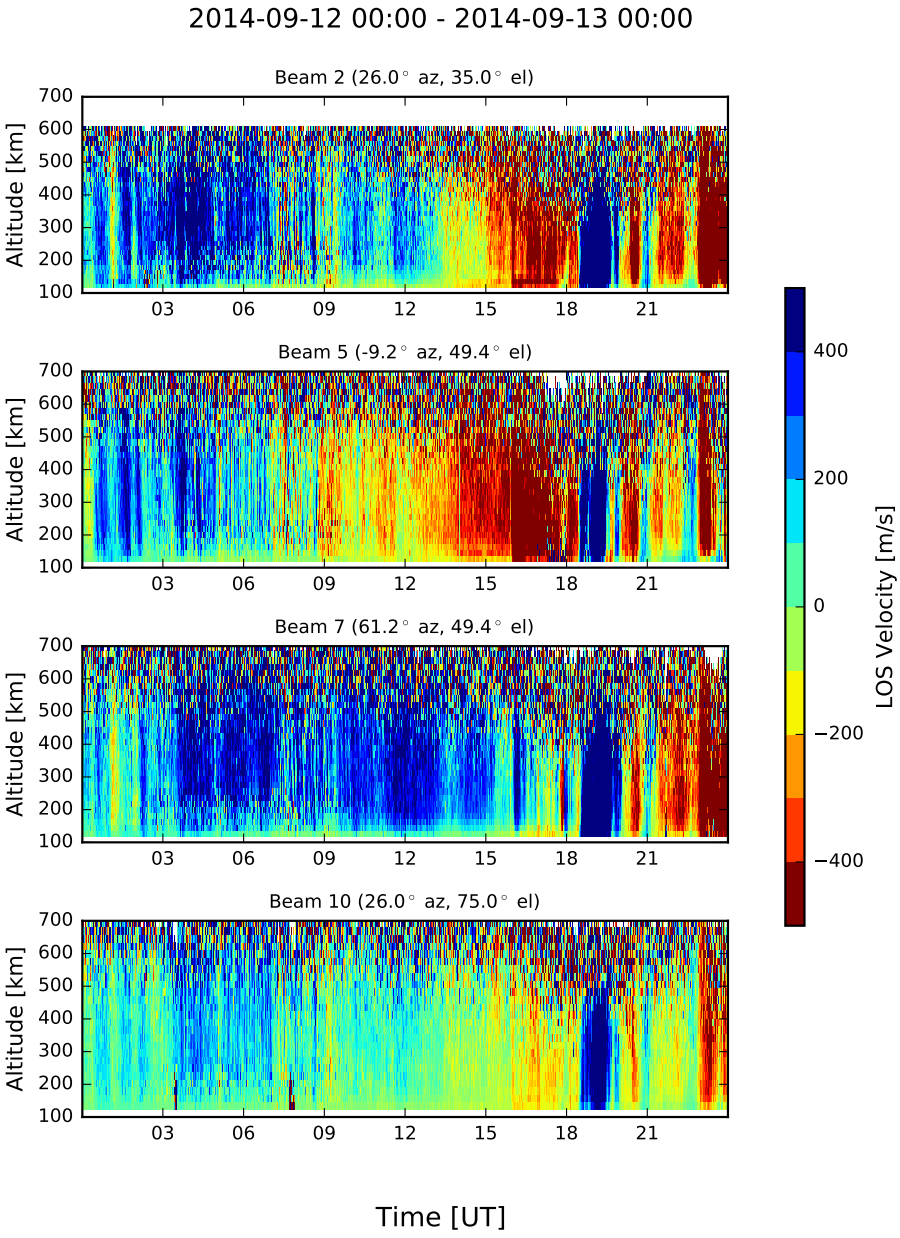

Figure 2.2: Raw RISR-N line-of-sight velocities measured on September 12, 2014 in the magnetic northward (beams 2 and 10), northwest (beam 5), and northeast (beam 7) directions. Positive (blue) velocities indicate motion towards the radar.

the horizontal velocity vector is calculated by fitting a cosine function to the variation in convection velocity versus angle with respect to magnetic north. It should be noted that this procedure assumes a uniform horizontal flow across the entire field of view. This assumption

was verified for RISR-N data collected during this particular period of interest by carefully examining the quality of the individual fittings.

2.2.2 DMSP SSIES and SSJ/4/5

Data from the Defense Meteorological Satellite Program (DMSP) satellites were used to cross-validate the accuracy of the derived RISR-N ionospheric velocity vectors and provide contextual information about their proximity to the cusp. Each DMSP satellite is in a sun-synchronous polar orbit at $\sim$ 840 km altitude corresponding to an orbital period of 101 minutes and about 20 minutes to cross the polar cap region above $|50°|$ MLAT. In this study, we use Level-2 SSIES [Heelis and Hairston, 1990] cross-track ion drift velocity data at four-second cadence provided by the University of Texas Dallas and SSJ/4/5 [Hardy et al., 1984] particle data at one-second resolution provided by the Johns Hopkins University Applied Physics Laboratory.

2.2.3 ACE MAG and SWEPAM

Solar wind and IMF data were obtained from the Advanced Composition Explorer (ACE) spacecraft in orbit around the Earth-Sun L1 lagrangian point. IMF data is from the magnetic field instrument MAG [Smith et al., 1998] and has 16 *sec* resolution while the solar wind data is from the Solar Wind Electron, Proton, and Alpha Monitor (SWEPAM) instrument [McComas et al., 1998] and has 64 *sec* resolution. Both datasets were converted to one-minute resolution by averaging (MAG) and resampling (SWEPAM). During the interval of interest, the ACE spacecraft was located near (224.7, -27.5, -22.3) R_e in GSE coordinates.

2.3 Observations

2.3.1 Solar Wind and Geophysical Conditions

Figure 2.3 shows an overview of the interplanetary and geomagnetic conditions from 14:00 - 22:00 UT on September 12, 2014. The panels from top to bottom are: (a) solar wind speed; (b) solar wind dynamic pressure; (c) IMF B_x (black), B_y (green), and B_z (red) components (GSM coordinates); (d) IMF clock angle (black) and magnitude of the transverse component B_t (blue); (e) Sym-H index; (f) AE index; (g) RISR-N southward, V_s (black), and westward, V_w (blue) components of the ionospheric convection derived using the procedure described in Section 2.2; and (h) one standard deviation errors of RISR-N fitted velocities. Dashed vertical lines identify: (I) first detection of an interplanetary shock by ACE at 15:26 UT; (II) Sym-H signature of shock arrival at the magnetosphere at 15:55 UT; and (III) the start of an extended period of northward IMF from 16:57-19:00 UT (gray shading in the upper four panels). Gray shading in the lower three panels from 17:51-20:00 UT identifies the corresponding period of northward IMF at the magnetosphere using a transit time of 54 minutes calculated by matching the sharp northward turning seen by ACE at 16:57 UT with the first onset of reverse convection observed by RISR-N at 17:51 UT (see Figure 2.2). During this period the time evolution of the RISR-N V_s component (panel g) shows a remarkable similarity with the IMF B_z variation (panel c) indicative of strong linear coupling, as argued by Clauer et al. [2016]. However, another interesting feature, not analyzed by Clauer et al. [2016], is the dynamics in the V_w component which are likewise highly correlated with IMF B_y variations. Taken together, the periods shaded in gray can thus be seen to mark a gradual transition between the following IMF conditions: (I) strong B_y+ and B_z+, (II) dominant B_y+, and finally, (III) dominant B_z+. Understanding the precise manner in which the dayside ionospheric convection transitions between these states is the primary purpose of

this study.

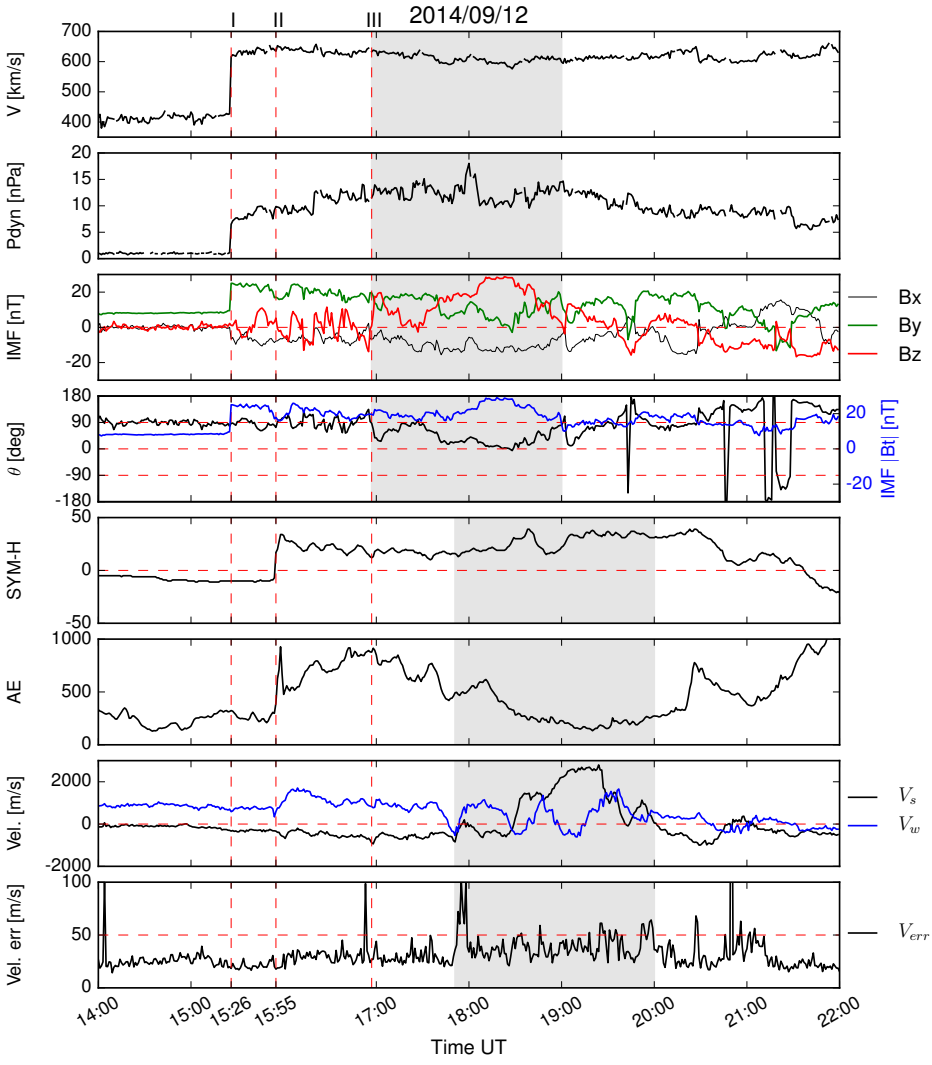

Figure 2.3: Interplanetary and geomagnetic conditions from 14:00 - 22:00 UT on September 12, 2014. From top to bottom: (a) solar wind speed; (b) solar wind dynamic pressure; (c) IMF B_x (black), B_y (green), and B_z (red) components (GSM coordinates); (d) IMF clock angle (black) and magnitude of transverse component B_t (blue); (e) Sym-H index; (f) AE index; (g) RISR-N southward, V_s (black), and westward, V_w (blue), components of the ionospheric convection; and (h) one standard deviation errors of RISR-N fitted velocities. Dashed vertical lines identify: (I) first detection of an interplanetary shock by ACE at 15:26 UT; (II) Sym-H signature of shock arrival at the magnetosphere at 15:55 UT; and (III) the start of an extended period of northward IMF from 16:57-19:00 UT (gray shading).

2.3.2 DMSP Observations

Data from the DMSP F15 and F18 satellites provide useful contextual information about the width of the reverse convection channel measured by RISR-N and its proximity to the cusp. Figure 2.4 shows an MLT-MLAT map of cross-track ion drifts from polar passes of the F15 and F18 satellites at 18:56-19:09 UT and 19:01-19:14 UT, respectively. Figure 2.5 shows energy spectrograms of the particle precipitation measured by F18. The dashed vertical red lines on Figure 2.5 identify a prominent V-shaped ion precipitation signature which is indicative of the cusp [Reiff et al., 1980; Burch et al., 1980]. The location of this cusp signature is identified on Figure 2.4 as the red circle. Also shown on Figure 2.4 is the location of RISR-N (blue dot) along with the 2D sunward convection velocity vector measured at 19:02 UT (blue) and its component in the F15 cross-track direction (cyan). Grey dots indicate the pierce points of the RISR-N beams at 19:02 UT. It is important to note that F15 flew directly over RISR-N at 19:02 UT, so the velocity comparison shown in Figure 2.4 is simultaneous, and the correspondence is quite good. Furthermore, it can be seen that RISR-N was situated well within a wide channel of reverse convection flow seen by both F15 and F18. The overall conclusion that can thus be drawn from these two figures is that RISR-N was in an ideal position to measure the strength and direction of flows in the dayside throat region, equatorward of the cusp, for an extended period of time.

2.3.3 RISR-N Observations

Recall, that Figure 2.3 provided qualitative evidence that the RISR-N V_s and V_w flow components were highly correlated with IMF B_z and B_y, respectively, during the extended period of northward IMF from 18:00 - 20:00 UT. This was further verified using time-lagged cross correlation analysis and the results are shown in Figure 2.6. The upper panel shows RISR-N

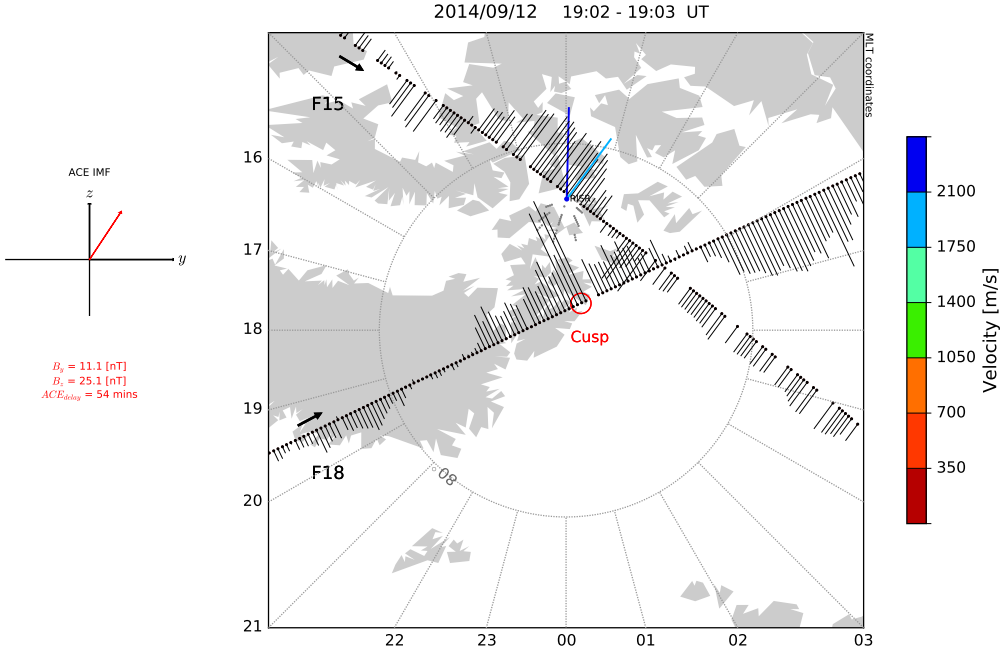

Figure 2.4: MLT-MLAT map of cross-track ion drift measurements from polar passes of the DMSP F15 and F18 satellites at 18:56-19:09 UT and 19:01-19:14 UT, respectively. Locations of a cusp precipitation signature seen by F18 (red circle) and RISR-N (blue dot) are identified along with the 2D sunward convection velocity vector measured by RISR-N at 19:02 UT (blue) and its component in the F15 cross-track direction (cyan). Grey dots indicate the pierce points of the RISR-N beams at 19:02 UT.

V_s and ACE IMF B_z lagged by 54 minutes, corresponding to a maximum correlation coefficient $C_{max} = 0.85$. The lower panel shows RISR-N V_w and IMF B_y lagged by 44 minutes corresponding to $C_{max} = 0.70$. Gray shading identifies the interval when the rate of increase in the magnitude of the sunward convection was particularly high, while the dashed vertical red line (I) identifies the time when DMSP F18 traversed the cusp (see Figure 2.5). There are two features worth emphasizing. First, there is no evidence of saturation in the ionospheric convection, as might be expected from application of extreme B_z+. Instead, as the IMF turned northward and steadily increased in strength to a maximum value of 28 nT, the north-south ionospheric flows responded quasi-linearly, peaking at 2800 m/s. This lack of

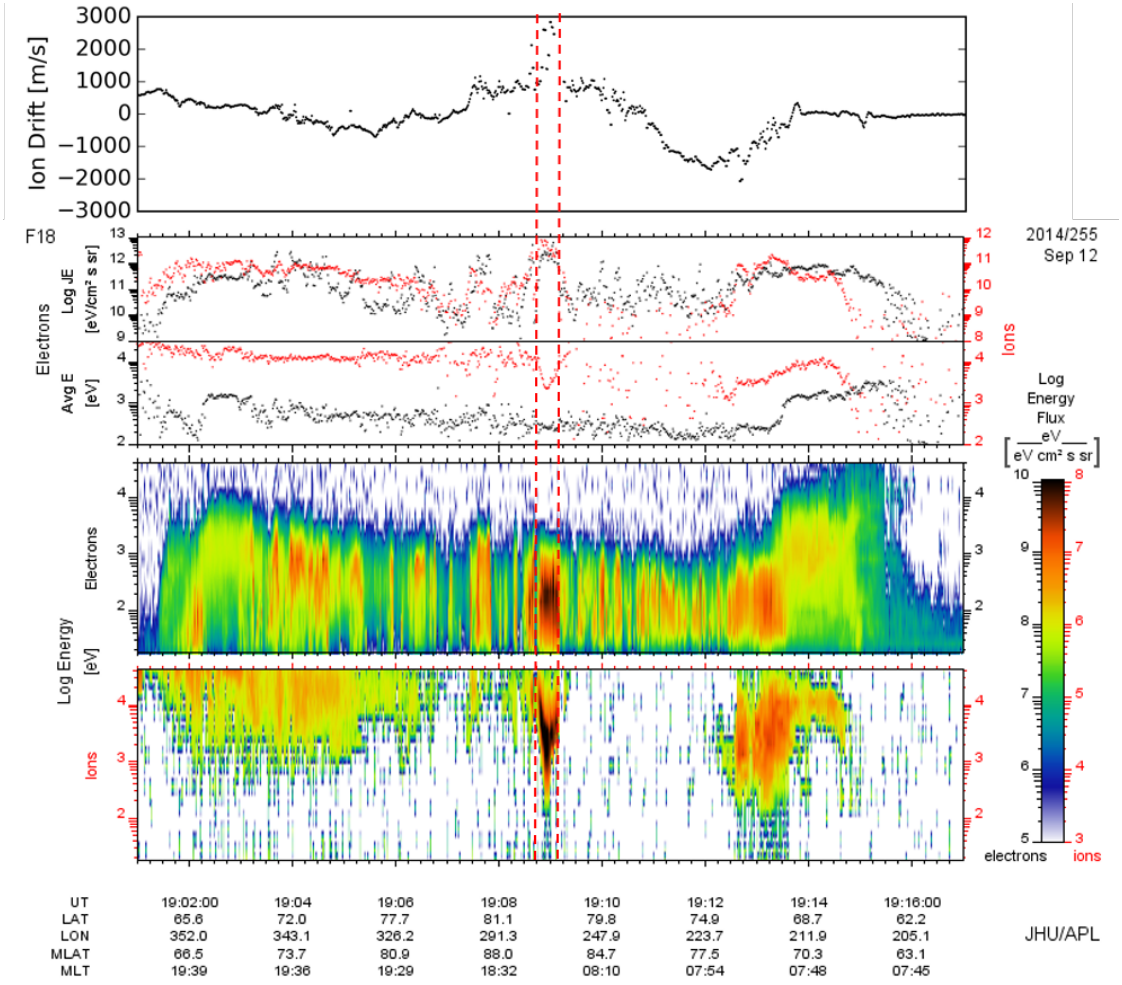

Figure 2.5: Cross-track ion drift velocity and particle precipitation data measured by DMSP F18 during its northern polar pass at 19:01 - 19:17 UT. Panels from top to bottom show: (a) sunward cross-track ion drift, (b) ion (red) and electron (black) energy flux, (c) average ion (red) and electron (black) energy, (d) electron energy spectrogram, and (e) ion energy spectrogram. Dashed vertical red lines identify a prominent V-shaped ion precipitation signature indicative of the cusp.

saturation was discussed extensively by Clauer et al. [2016]. The second noteworthy feature in Figure 2.6 is the difference in optimal correlation lag times, 54 minutes for B_z/V_s versus 44 minutes for B_y/V_w.

Figure 2.7 shows time-series of the optimal V_s-B_z (red) and V_w-B_y (green) correlation coefficients (upper panel) and corresponding lag times (lower panel) during the 18:00 - 19:00 UT

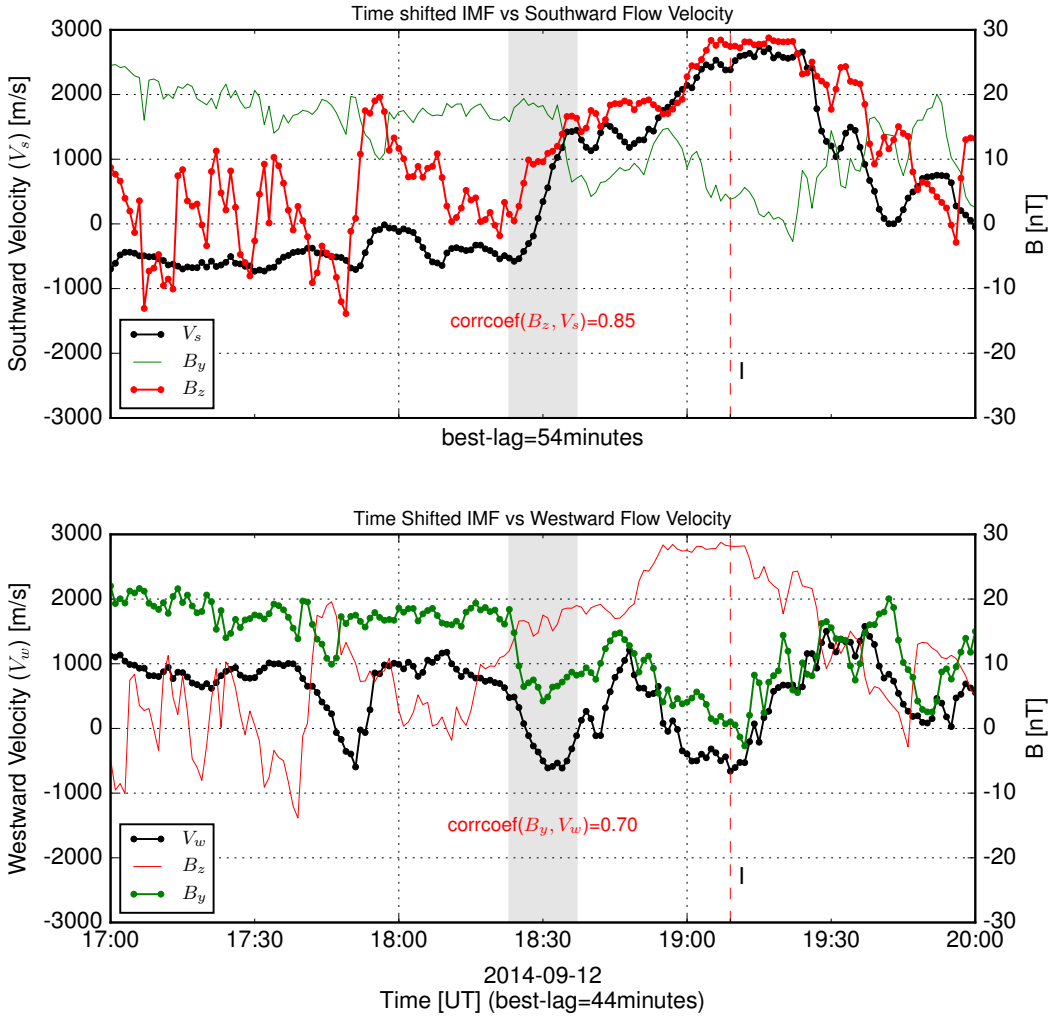

Figure 2.6: Time series plots of RISR-N V_s and ACE IMF B_z lagged by 54 minutes (upper panel) and RISR-N V_w and IMF B_y lagged by 44 minutes (lower panel). The lag times correspond to maximum cross correlation coefficients of 0.85 and 0.70, respectively. Gray shading identifies an interval when the rate of increase in the magnitude of the sunward convection was particularly high, while the dashed vertical red line (I) identifies the time when DMSP F18 traversed the cusp (see Figure 2.5)

interval. The values at each UT time were calculated by correlating 40 minutes of RISR-N data centered at that particular time against the IMF components delayed in minute increments up to a maximum of 70 minutes. The maximum correlation coefficient and cor-

responding lag time were then identified as the optimal values which are shown in Figure 2.7. It can be seen that the correlation coefficients (upper panel) are both remarkably high, and relatively stable, particularly after 18:15 UT. Likewise, the lag times are both relatively stable, with the B_y component having a lag time which is consistently shorter than that associated with B_z by about 5-10 minutes. Figure 2.8 provides additional statistical evidence for a systematic difference in the IMF B_y and B_z lag times. In this case, the mean correlation coefficient (solid) and its standard deviation (dashed) are plotted against lag time using all of the correlation data which contributed to Figure 2.7. Consistent with Figure 2.6, we again see remarkably high average correlation coefficients and a systematic 10 minute offset in lag times such that the two correlation peaks are well separated.

Taken together, Figures 2.6 - 2.8 provide strong evidence that the IMF B_y and B_z components were both highly correlated with the dayside convection during the 18:00 - 19:00 UT interval, but with a systematic difference in lag times of $\sim$ 10 minutes. This behavior suggests that both IMF components exerted a strong driving influence on the dayside flows but were essentially decoupled from each other. How is this behavior manifested in the flows? To answer this question, it's useful to examine the dynamics of the convection in the dayside throat not as a time-series of individual components, but rather, as a time series of two-dimensional vector flows. This is done in Figure 2.9 for the period 18:22 - 18:37 UT shaded gray in Figure 2.6. The left panel shows the vector time series of two-dimensional flows measured by RISR-N in the dayside throat, and the right panel shows a hodograph of the corresponding time-lagged hybrid IMF, which is a vector merging of IMF B_y lagged by 44 minutes and IMF B_z lagged by 54 minutes. Each vector in the left panel indicates the magnitude and direction of the flow measured by RISR-N during a one-minute interval, the MLAT-MLT format has sunward directed upward. Starting at 18:22 UT, the flow is initially antisunward but has a substantial dawnward component corresponding to the dominant

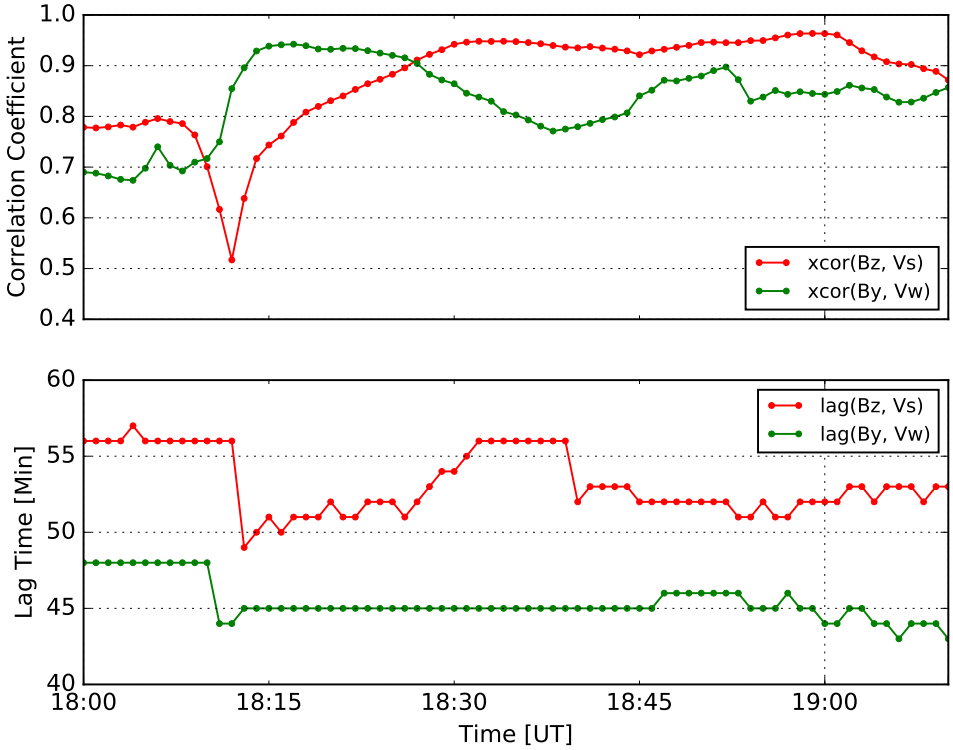

Figure 2.7: Time-series of optimal RISR-N V_s versus IMF B_z (red) and RISR-N V_w versus IMF B_y (green) correlation coefficients (upper panel) and corresponding lag times (lower panel) during the 18:00 - 19:00 UT interval using a 40-minute sliding window (see text for details).

B_y+ condition at this time. Then, in response to the northward turning of the IMF at 18:23 UT and weakening in the magnitude of the IMF B_y component, the flow vector starts to rotate in a clockwise sense becoming essentially sunward by 18:37 UT. The interesting aspect of this behavior is that it is not consistent with a simple transition from a dominant B_y+ state to a dominant B_z+ state. If that were the case, the dawnward component of the flow would simply decrease as the sunward component increased and the sense of rotation of the flow from antisunward/dawnward to sunward would be counter-clockwise. Instead, the velocity vector rotates in a clockwise sense through the larger angle which necessitates passing through a transitional state of duskward flow corresponding to a dominant B_y- condition

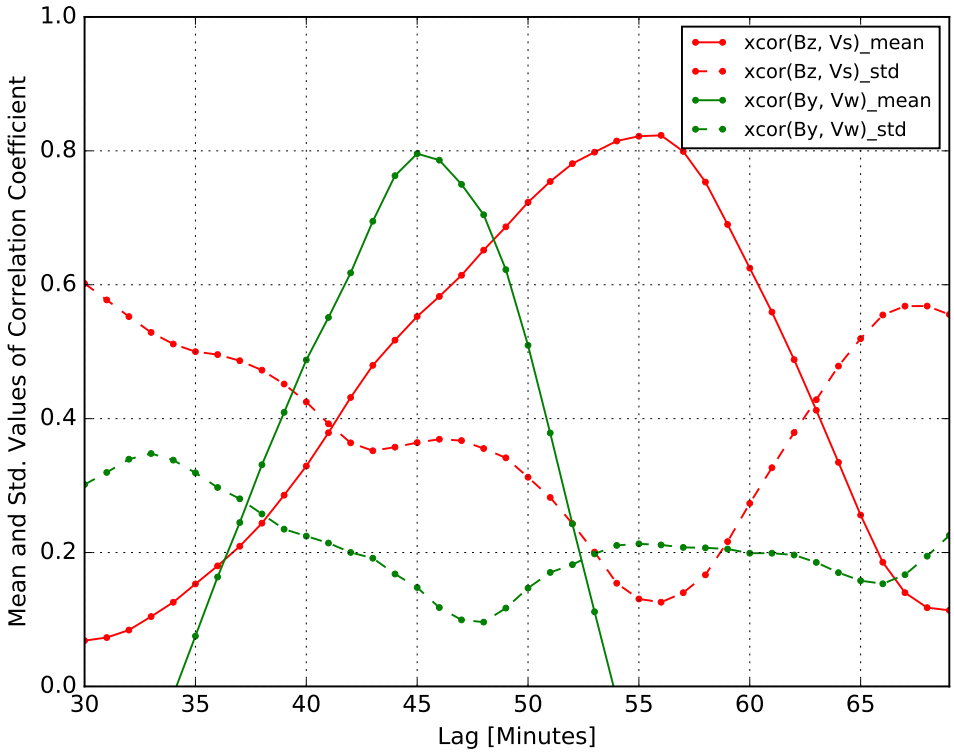

Figure 2.8: Mean (solid) and standard deviation (dashed) correlation coefficients for RISR-N V_s versus IMF B_z (red) and RISR-N V_w versus IMF B_y (green) plotted against optimal lag time using all of the correlation data which contributed to Figure 2.7 (see text for details).

despite the fact that the B_y component was positive throughout. Is there a magnetopause reconnection scenario that can possibly explain this behavior? This is discussed in the next section.

2.4 Discussion

In this study we have analyzed the interval between 18:00 - 20:00 UT on September 12, 2014 when RISR-N rotated through the noon sector while the IMF transitioned from a strong B_y+ condition to strongly northward. Near-simultaneous measurements from DMSP

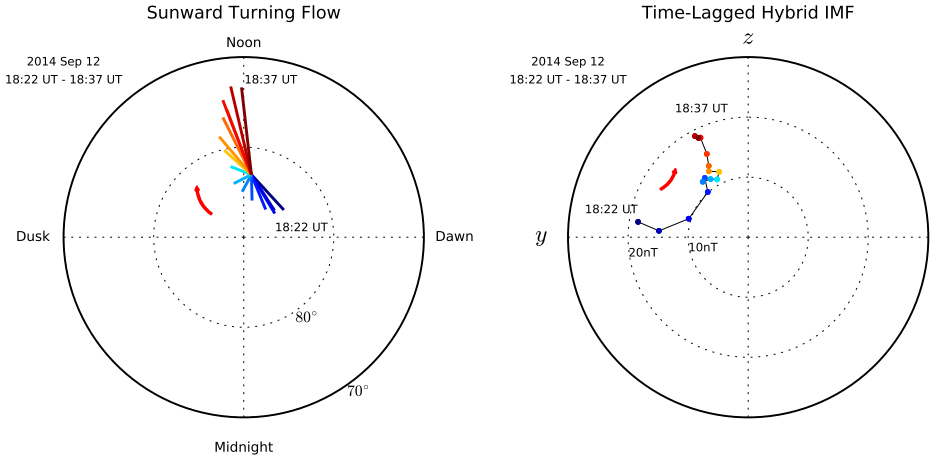

Figure 2.9: Vector time series of two-dimensional flows measured by RISR-N in the dayside throat (left) and a hodograph (right) of the corresponding time-lagged hybrid IMF (vector merging of IMF B_y lagged by 44 minutes and IMF B_z lagged by 54 minutes for the period shaded gray in Figure 2.6) at 1-minute intervals from 18:22 - 18:37 UT on September 12, 2014. The flow vectors and the IMF points are color coded by their corresponding UT times.

satellites (Figure 2.4) shows that RISR-N was in an ideal position to measure the strength and direction of flows in the dayside throat region, equatorward of the cusp, for an extended period of time. Time-lagged cross correlation analysis (Figures 2.6 - 2.8) revealed that both the RISR-N V_s and V_w flow components were highly correlated with IMF B_z and B_y, respectively, but with a systematic difference in lag times of $\sim$ 10 minutes. This behavior is manifested in the flows such that, in response to the northward turning of the IMF at 18:23 UT and weakening in the magnitude of the IMF B_y component, the flow vector starts to rotate through a greater angle path in a clockwise sense becoming essentially sunward by 18:37 UT (Figure 2.9), which is not consistent with a simple transition from a dominant B_y+ state to a dominant B_z+ state.

The results presented in this study are consistent with magnetic reconnection being the dominant influence for driving ionospheric convection in the dayside throat region during

this particular event. The strong correlation between IMF B_z and the V_s component of the dayside convection is consistent with newly opened magnetic flux tubes experiencing a sunward directed magnetic tension force which drives sunward ionospheric flows equatorward of the cusp when the IMF is northward. Likewise, the strong correlation between B_y and V_w is consistent with a dawnward magnetic tension force driving dawnward flows in the cusp when IMF B_y is positive [Senior et al., 2002]. This aspect of the results is relatively straightforward to understand, and not at all surprising. However, the manner in which the dayside convection transitions from the dominant B_y+ condition to the dominant B_z+ condition (Figure 2.9) is counter to what might be expected for a transition between quasi-steady IMF states. What does this anomalous behavior tell us about the geometry of reconnection at the magnetopause?

There are two standard models for describing the configuration of magnetic reconnection at the dayside magnetopause: the so-called "antiparallel" and "component" (subsolar) reconnection paradigms. The antiparallel model predicts that reconnection occurs in regions where the magnetic field in the magnetosheath is nearly antiparallel to the geomagnetic field. The locus of points where this applies then constitutes the reconnection line(s) on the magnetopause [Crooker, 1979; Luhmann et al., 1984]. By contrast, the component reconnection model requires only that components of the two merging field lines be antiparallel and places the reconnection site in the subsolar region where the solar wind plasma first encounters the magnetopause [Cowley, 1973, 1976; Moore et al., 2002]. Antiparallel and component reconnection models lead to significantly different reconnection sites and plasma transfer rates. Both merging models have been applied to observational studies, with Gosling et al. [1991]; White et al. [1998] and Trattner et al. [2005] favoring the antiparallel reconnection model, and Gosling et al. [1990]; Chandler et al. [1999] and Pu et al. [2005] favoring the component reconnection model.

According to the antiparallel merging model, the northern hemisphere reconnection site for dominant B_y+ conditions is on the duskward flank of the magnetopause. As the IMF clock angle decreases from 90° to 0° (i.e. duskward to northward) the reconnection site should gradually move northward and westward, eventually becoming poleward of the cusp. The magnetic tension force produced by such a change in reconnection site should rotate the flows in the dayside throat from antisunward with a substantial dawnward component to pure sunward. Figure 2.10 shows the direction of RISR-N ionospheric flows (bottom row) predicted by the antiparallel reconnection model corresponding to IMF clock angles of 90°, 45° and 0° (top row). The middle row shows schematics of the corresponding convection patterns (adapted from Figure 6 in [Crooker, 1988]) with the center of the RISR-N field-of-view identified by red circles. (Note that this is our best evaluation of where the red circles should be placed to be consistent with the MLT location of RISR-N field-of-view and the initial and final states of the observed flow vectors. It should also be noted that the flow vectors can be affected by the relative location of RISR-N between the two cells. If the larger dusk cell in Figure 2.10 (left) decreases in size enough then the sunward side of the elongated cell would move poleward. Since RISR-N is on the edge of one of the reconnection cells, any minor changes to the assumed cell shape and size will affect the RISR-N direction vector and may even cause the sunward flow turning shown in Figure 2.9 were the RISR-N field-of-view to encounter the velocity shear of the elongated cell. However, visual inspection of the LOS velocities argues against this cause and the fitted velocity errors (panel h in Figure 2.3) during the event period remained low (< 50 m/s) and steady. Had the RISR-N field-of-view encountered the velocity shear then it is to be expected that this would be apparent in the time series of LOS velocities and resulted in degraded fitting quality. It is thus reasonable to conclude that the RISR-N field-of-view stayed within the flow channel throughout the event period.) Comparing this prediction to the behavior of the RISR-N flows shown in Figure 2.10 we can see that the flow velocity predicted by the model has

the same initial and final states as the observations, but the sense of rotation in the flow vector is opposite. A similar analysis applied to the component merging model predicts the same sense of rotation (e.g. see Figure 4 in [Moore et al., 2002]). We thus conclude that the manner in which the convection reconfigured is not consistent with the straightforward progression of the reconnection site across the magnetopause that would be expected on the basis of quasi-static analysis.

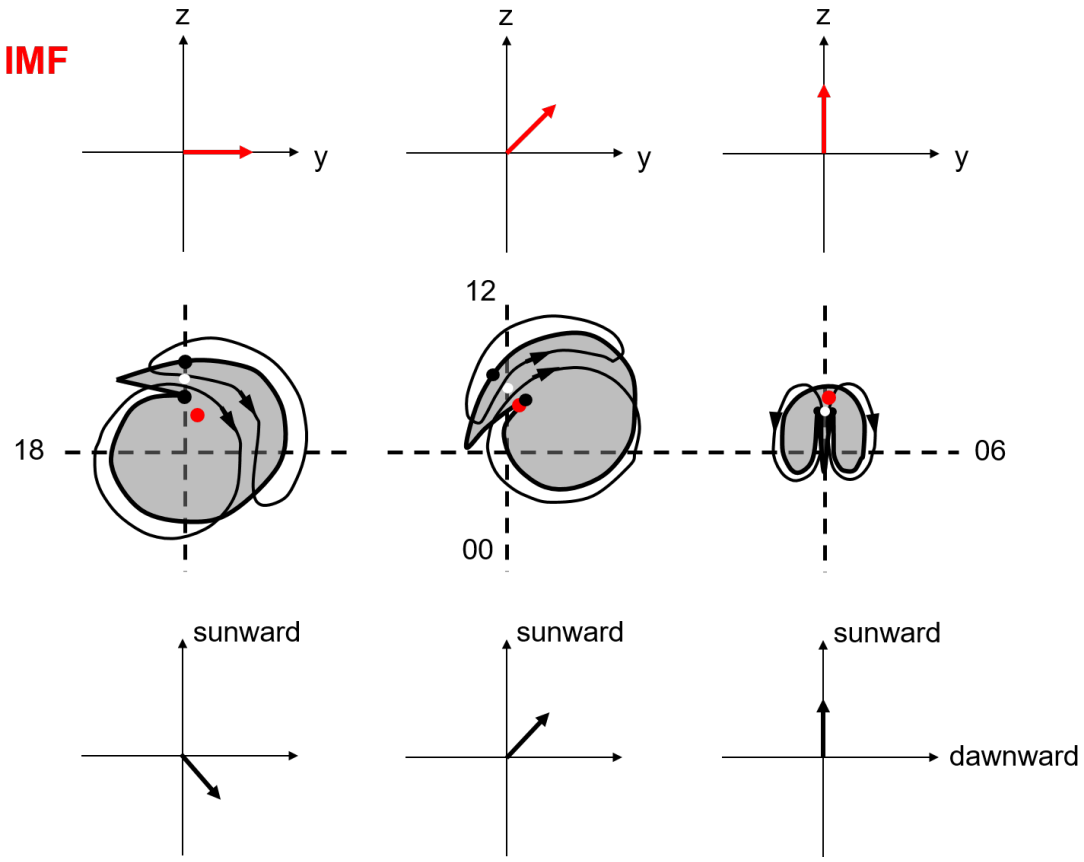

Figure 2.10: Direction of RISR-N ionospheric flows (bottom row) predicted by the antiparallel reconnection model corresponding to IMF clock angles of 90°, 45° and 0° (top row). The middle row shows schematics of the corresponding convection patterns (adapted from Figure 6 in [Crooker, 1988]) with the center of the RISR-N field-of-view identified by red circles.

Another interesting aspect of this event is the 10-minute difference in correlation lag times associated with the two IMF components. One possible explanation could be that the IMF

B_y and B_z components measured at the ACE satellite arrived at the bowshock at different times. However, given the frozen-in condition of the IMF in the solar wind plasma, this would require a mixing of dissimilar plasmas or structures in the solar wind that would tend to disrupt the expected ordering of the solar wind plasma into planar fronts. If the IMF B_y and B_z components were to arrive at the bowshock at different times then we would expect the quality of the solutions for the phase front normals and delay times in the OMNI solar wind dataset to be degraded. The ACE-specific 1min-resolution OMNI dataset includes certain metrics that speak to the quality of the fitting, e.g., the root mean squared errors of the estimated phase front normals and delay times. During the time interval examined in this study these errors are found to be very small indicating that the quality of the fitting is high. In addition, the minimum variance analysis technique, MVAB-0, which is one of the main techniques OMNIweb uses for time-shifting the upstream solar wind data to the bowshock nose, was implemented with various tuning parameters and the time-shifted results for the solar wind and IMF were found to be very similar and insensitive to the choice of parameters. These findings indicate that the assumption of co-arrival of the IMF B_y and B_z changes at the bowshock holds during the event period and therefore any difference in lag times is possibly due to different reconnection sites on the magnetopause and other temporal factors related to geometry or to the type of reconnection. The solar wind on this day had an average speed of $\sim 620\ km/s$ (Figure 2.3) meaning that it took around 36-37 minutes to travel from ACE to the bow shock nose. It then takes an additional 3-4 minutes to transit the bow shock and reach the subsolar magnetopause. Adding another 2-3 minutes for the Alfven wave to travel from the subsolar magnetopause to the ionopheric cusp, the total delay is expected to be around 44 minutes, which matches the response time of the V_w flow component to the IMF B_y. In addition, the solar wind dynamic pressure enhancement (as shown in the second panel in Figure 2.3) is also well correlated with the westward flow, V_w for the period of 18:10 - 19:15 UT. The best correlation coefficient is 0.70 at a lag time of 45 mins, which

is a similar time scale as the lag time of IMF B_y. Previous studies have shown that, under northward IMF, high solar wind dynamic pressure facilitates the component reconnection at the subsolar region [Fuselier et al., 2000]. It is therefore reasonable to conclude that the electric field driving the V_w flow was mapped down into the ionosphere from the subsolar magnetopause or a nearby region, which is the preferred site for component reconnection.

Now consider the IMF B_z component. Given the fact that a strong and sustained reverse convection was observed, it is reasonable to conclude that reconnection was occurring poleward of the cusp; we conjecture that the location was displaced from the bow shock nose by 10-15 R_e in the negative GSE x-direction and 10-14 R_e from the Earth center in the positive GSM z-direction based on magnetic field line tracing using the Tsyganenko T96 model. The sheath flow thus needs to travel 4-6 minutes (using $\Delta t = \Delta x/V_{sw}/3$, [Petrinec, 2013]) to reach the location poleward of the cusp. Assuming the usual variation in plasma density and magnetic field over this extended region we estimate that the Alfven wave takes anywhere from 4 to 12 minutes to travel through the tenuous lobe region to reach the ionosphere. A greater variations for lag time was in fact observed for B_z/antiparallel reconnection compared to B_y/component reconnection in Figure 2.7. Although modeling of the exact delay time is beyond the scope of this report and is left to future work, a delay of 10 minutes seems reasonable based on the delay times expected of propagation through the magnetospheath and Alfven wave travel time. It is thus our contention that the difference in IMF B_y/B_z correlation lag times is due to additional delays within the magnetospheric system associated with two spatially separated B_y/B_z dependent reconnection sites. Further support for this hypothesis is provided by the fact that the sense of rotation in the ionospheric convection is contrary to what is expected for antiparallel reconnection transitioning between these particular B_y/B_z states. Instead, the sense of the reconfiguration in ionospheric flows is consistent with B_y component reconnection at the subsolar magnetopause plus antiparallel reconnec-

tion poleward of the cusp. We further note that simultaneous occurrence of antiparallel and component reconnection is not unprecedented, having previously been reported by [Trattner et al., 2004; Fuselier et al., 2011].

It is interesting to consider the degree to which the strong dynamic variations in IMF couple to the convection. In this event, the systematic time-lag difference exists for a long time ($>$ 1h) during large changes in the IMF ($\sim$ 25 nT). The relative steadiness of the time-lag difference could reflect in that the reconnection sites are well-separated and variations at either site have a relatively minor impact on the overall difference. In addition, the IMF variations during this event period were relatively gradual and smooth, perhaps limiting the scope for sudden dramatic changes at either site.

We can also consider the temporal limit for variations in IMF below which the IMF effect does not register in the polar cap convection. Figure 2.11 shows the coherence of IMF B_y (lagged by 44 mins) and B_z (lagged by 54 mins) components with the westward and southward ionospheric flow components, respectively, for the period 17:40-20:00 UT when the IMF is northward. A coherence measures the degree of linear dependency of two signals by testing for similar frequency components, and the magnitude of coherence takes the value between 0 and 1. A coherence level of 1 indicates that two signals correspond to each other perfectly at a given frequency. As seen from Figure 2.11, the cut-off period for both (B_z,V_s) and (B_y, V_w) is 15 minutes at a coherence level of 0.6 and it is very sharp. A previous study by Murr and Hughes [2007] reported a statistical cut-off period of 20 minutes at the same coherence level of 0.6. Taking 15 minutes as a threshold it can be concluded that in the case of strong dynamic IMF conditions where variations in IMF have periods lower than 15 minutes the IMF does not effectively register its influence on the ionospheric convection due to the low pass-filter characteristic of the Magnetosphere-Ionosphere system.

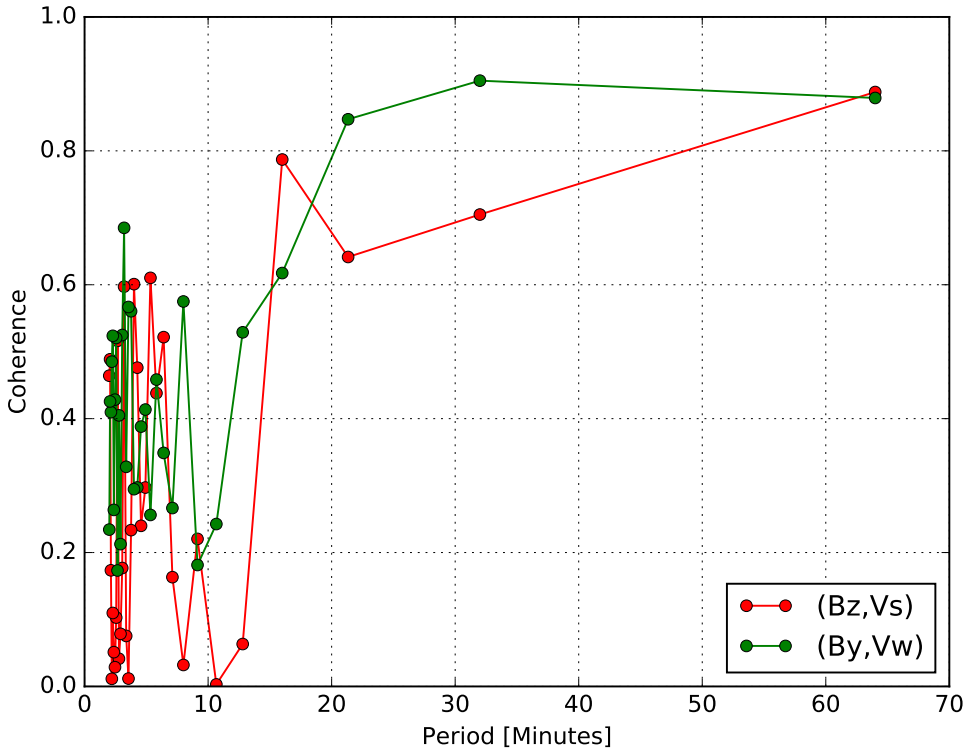

Figure 2.11: Coherence of IMF B_y (lagged by 44 mins) and B_z (lagged by 54 mins) components with the westward and southward ionospheric flow components, respectively, for the period 17:40-20:00.

2.5 Summary and Conclusions

This paper examined the dynamic response of ionospheric flows in the dayside convection throat measured by RISR-N during a period on September 12, 2014 when the IMF transitioned from a dominant B_y+ condition to strongly northward. Correlation analysis shows that the IMF B_y and B_z components were highly correlated with the westward and southward ionospheric flow components, respectively, but the sense of rotation in the RISR-N flows in response to the changing IMF was opposite to that expected from either the antiparallel or component reconnection models applied to quasi-static conditions. Furthermore, the IMF B_y influence acted on a lag time which was 10 minutes faster than that of the B_z

component. This difference in lag time is consistent with the propagation delay expected for mapping electric fields along the magnetic field from two separate reconnection sites on the magnetopause: antiparallel reconnection with the B_z component poleward of the cusp and component reconnection with the B_y component in the vicinity of the magnetopause nose. Further analysis with global MHD modeling is needed to elucidate the precise manner in which the reconnection geometry changes during periods of strong dynamic IMF.

Acknowledgments

We thank the National Science Foundation for support under grant AGS-1341918. We wish to acknowledge the use of the NASA/GFSC Space Physics Data Facility's OMNIWeb and CDAWeb service. We also gratefully acknowledge the Center for Space Sciences at the University of Texas at Dallas and the US Air Force for providing the DMSP thermal plasma data. The DMSP particle detectors were designed by Dave Hardy of AFRL, and data obtained from JHU/APL. The Resolute Incoherent Scatter Radar (RISR-N) is operated by SRI International on behalf of the U.S. National Science Foundation under NSF Cooperative Agreement AGS-1133009. The RISR-N data are available in the Madrigal Archival Database (madrigal.haystack.mit.edu) or directly from SRII in Menlo Park, CA. The majority of analysis and visualization was completed with the help of free, open-source software tools such as matplotlib [Hunter, 2007], IPython [Pérez and Granger, 2007], pandas [McKinney, 2010], and others [e.g. Millman and Aivazis, 2011].

Chapter 3

Subauroral Convection and its Major Driving Influences - Part 1

M. Maimaiti [1], J. M. Ruohoniemi [1], J. B. H. Baker [1], A. J. Ribeiro [1,2]

[1]Bradley Department of Electrical and Computer Engineering, Virginia Tech, Blacksburg, Virginia, USA.

[2]Uber Technologies Inc., San Francisco, California, USA.

Maimaiti, M., Ruohoniemi, J. M., Baker, J. B. H., & Ribeiro, A. J. (2018). Statistical study of nightside quiet time midlatitude ionospheric convection. Journal of Geophysical Research: Space Physics, 123, 2228– 2240. https://doi.org/10.1002/2017JA024903

Abstract

Previous studies have shown that F region mid-latitude ionospheric plasma exhibits drifts of a few tens of m/s during quiet geomagnetic conditions, predominantly in the westward direction. However, detailed morphology of this plasma motion and its drivers are still not well understood. In this study, we have used two years of data obtained from six mid-latitude SuperDARN radars in the North American sector to derive a statistical model of quiet-time mid-latitude plasma convection between 52° and 58° magnetic latitude (MLAT). The model is organized in MLAT-MLT (magnetic local time) coordinates and has a spatial resolution of $1° \times 7$ min with thousands of velocity measurements contributing to most grid cells. Our results show that the flow is predominantly westward (20 - 55 m/s) and weakly northward (0 -20 m/s) deep on the nightside but with a strong seasonal dependence such that the flows tend to be strongest and most structured in winter. These statistical results are in good agreement with previously reported observations from Millstone Hill incoherent scatter radar (ISR) measurements for a single latitude but also show some interesting new features, one being a significant latitudinal variation of zonal flow velocity near midnight in winter. Our analysis suggests that penetration of the high-latitude convection electric fields can account for the direction of mid-latitude convection in the premidnight sector but postmidnight mid-latitude convection is dominated by the neutral wind dynamo.

3.1 Introduction

It is widely accepted that high latitude ionospheric convection is primarily driven by the magnetic reconnection process [Dungey, 1961] and, to a lesser extent, viscous interaction [Axford and Hines, 1961]. Typical plasma flow velocities at these latitudes are a few hundred to a few thousand m/s. The quiet-time drifts in the mid-latitude regions, however, exhibit

drifts of only a few tens of m/s, and the driving mechanisms are still not well understood. Two primary candidates are: (1) the neutral wind dynamo [Rishbeth, 1971; Richmond et al., 1976] and (2) penetration of high latitude convection electric fields [Nishida, 1968; Blanc et al., 1977; Yeh et al., 1991; Buonsanto et al., 1992]. The storm-time version of the neutral wind dynamo mechanism is the ionospheric disturbance dynamo proposed by Blanc and Richmond [1980], by which a predominantly northward electric field is generated at mid-latitudes due to the thermospheric circulation that is driven by auroral heating during periods of high geomagnetic activity. In the absence of geomagnetic disturbance one might naively expect the F region ion convection to follow the pattern of the background neutral winds, however, previous studies have not found this to be the case [Buonsanto et al., 1993]. Likewise, the occurrence of penetration electric fields is mostly invoked under geomagnetically disturbed conditions [e.g., Blanc et al., 1977; Yeh et al., 1991; Buonsanto et al., 1992], but some studies have also reported the presence of penetration electric fields under quiet-time conditions [e.g., Carpenter and Kirchhoff, 1975; Wand and Evans, 1981a; Heelis and Coley, 1992; Lejosne and Mozer, 2016]. Understanding the relative importance of these two mechanisms in driving plasma convection in the mid-latitude region has been an important topic of ongoing research for decades and this study is part of that effort, focusing on the subauroral mid-latitude plasma convection under quiet geomagnetic conditions.

A number of studies have used measurements from satellite-based ion drift meters or incoherent scatter radars to categorize the average pattern of mid-latitude ionospheric plasma drifts. Heelis and Coley [1992] examined magnetic local time distributions of average zonal ion drifts at different latitudes observed by DE 2 during magnetically quiet and disturbed periods defined by Kp. They found that, at $\sim 55^{\circ}$ invariant latitude under quiet conditions, westward flow persists at all local times except for a 2 hour period near local noon. Richmond et al. [1980] produced a model of the middle and low-latitude electric fields for solar

minimum conditions using seasonally averaged quiet-day F region ionospheric E × B drift observations from several incoherent scatter radars. This model predicts diurnally varying zonal flow and semi-diurnally varying meridional flow at the Millstone Hill location, with the flow predominantly westward at night. Wand and Evans [1981b], using the Millstone Hill incoherent scatter radar (ISR), described the average ionospheric electric field in both the magnetic north-south and east-west directions for three seasons during quiet magnetic conditions, as well as the annual average during magnetically disturbed conditions. They found that the electric field is northward through the night corresponding to westward flow and the north-south component has a stronger seasonal dependence than the east-west component. Buonsanto et al. [1993] and Buonsanto and Witasse [1999], also using the Millstone Hill ISR radar, constructed average quiet-time E × B drift patterns for three seasons for both solar cycle maximum and minimum conditions. They found that the daily variation of east-west flow during quiet conditions shows daytime eastward drifts and nighttime westward drifts except in summer when the usual daytime eastward maximum near 1200 LT is suppressed. These studies all agree on general features such as the quiet-time flow being predominantly westward through the night and the presence of seasonal factors. However, they have produced somewhat contradictory pictures of how mid-latitude convection is ordered by MLT and season. Some of the inconsistencies could be due to limited statistics.

The Super Dual Auroral Radar Network (SuperDARN) consists of chains of HF radars in the northern and southern hemispheres that monitor ionospheric dynamics through the detection of decameter-scale field-aligned plasma irregularities in the E and F regions of the ionosphere [Greenwald et al., 1985; Chisham et al., 2007]. Typically, a SuperDARN radar has 16-24 beams, 75-100 range gates along each beam, and a 45 km range resolution. The azimuth step between beams is around 3.3°, and an azimuthal scan across all 16-24 beams generally takes 1-2 minutes with a dwell time between 3 and 7 seconds on each beam. It is

capable of detecting targets with Doppler velocities of 0 m/s up to 2 km/s. The mid-latitude expansion of SuperDARN radars over the past ten years has provided new opportunities to study mid-latitude ionospheric convection over large areas and with unprecedented spatial resolution and statistical significance. However, most studies of mid-latitude convection using the midlatitude SuperDARN radars have focused on features that occur during geomagnetically disturbed conditions such as the high-speed subauroral polarization streams (SAPS) [Oksavik et al., 2006; Clausen et al., 2012; Kunduri et al., 2012, 2017]. Only a handful of studies have focused on quiet-time mid-latitude convection [Baker et al., 2007; Zou and Nishitani, 2014]. The purpose of this paper is to examine the morphology of nightside mid-latitude convection under quiet-time conditions and to investigate its driving mechanisms. Specifically, we have used two years of data obtained from the six mid-latitude SuperDARN radars in the North American sector to derive a new statistical model of mid-latitude plasma convection between 52° and 58° magnetic latitude. The features of the model are in general agreement with previously reported observations from the Millstone Hill ISR but also show significant differences and several interesting new features. In the subsequent sections, we describe the derivation of the model, analyze its most prominent features, and discuss our findings in terms of possible driving mechanisms for nightside quiet-time mid-latitude convection.

3.2 Data Selection and Processing

The primary dataset consists of line-of-sight (LOS) plasma drift velocity measurements obtained from 2011-2012 by six U.S. mid-latitude SuperDARN radars. The fields of view of these radars are shown in Figure 3.1 in AACGM coordinates. The mid-latitude region that we focus on in this study lies between 52° and 58° magnetic latitude and is bounded by the

two red circles. The lower boundary was chosen because it is approximately the lowest latitude at which the radars generate measurements in the F region ionosphere while the upper boundary was chosen to be below the usual equatorward limit ($\sim 60^\circ$ Λ) of the auroral zone during quiet conditions [Holzworth and Meng, 1975; Heppner and Maynard, 1987]. (Note that not all the beams, especially the polar looking ones, of the six radars can reach the F region ionosphere at the lower boundary of 52° MLAT due to the close distance between the radars and the lower red arc. However, the more eastward/westward looking beams can still reach the F region and are the main contributors to the 52° MLAT grid cells.). Thus, leaving a 2 degree latitude gap increases the likelihood that the observed plasma drifts are subauroral and not due to the expansion of the high latitude two-cell convection. The two years selected spanned a period of low solar flux (average F10.7 = 115) during the ascending phase of Solar Cycle 24 so solar activity was increasing.

The SuperDARN radars observe backscatter primarily from plasma density irregularities in the ionosphere at E and F region heights (ionospheric scatter), reflections from the meteor trails in the lower E region (meteor scatter), and from the Earth's surface after reflection from the ionosphere (ground scatter). The data selection starts by first identifying mid-latitude ionospheric scatter, which is primarily confined to local night. (The target scatter in F region ionosphere is confined to nightside because a highly conducting E region shorts out the electric fields during the daytime as speculated by Greenwald et al. [2006]). This step is essential because the traditional method of distinguishing between scatter types in SuperDARN data was developed for high latitudes and depends solely on the Doppler velocity and Doppler spectral width of each data point. We have used the classification algorithm of Ribeiro et al. [2011], which was specifically developed to identify ionospheric scatter events in the nightside mid-latitude region with high confidence. Much like a human expert, it analyses the data by looking at a long time series of data and identifies clusters of backscatter on the

basis of temporal and spatial characteristics of the velocity distribution as either an "event" (ionospheric scatter) or a "non-event" (ground scatter). The search for ionospheric scatter is limited to range gates 7 and higher (> 450 km from the radar) in order to exclude meteor scatter and ionospheric E region scatter, which tend to arise from nearer ranges. A previous study by de Larquier et al. [2013] demonstrated that the most likely source region of this type of quiet-time nightside mid-latitude ionospheric scatter is the bottom-side F region between 220 and 320 km altitude. Then we selected for low-velocity events as was done by Ribeiro et al. [2012] to target scatter which is subauroral in origin and not due to auroral processes or SAPS. Furthermore, the data were filtered by Kp to select for geomagnetically quiet periods (Kp $\leq$ 2+).

Here we clarify our definition of "midlatitude" and "subauroral". The geomagnetic midlatitude ionosphere is typically defined as a buffer zone between the equatorial and auroral regions, with boundaries that vary with geomagnetic activity. The type of mid-latitude ionospheric scatter we have selected for has been shown by Ribeiro et al. [2012] to lie equatorward of both the auroral region and the ionospheric projection of plasmapause boundary. Therefore, we consider the region of interest (52° - 58° MLAT) under these quiet conditions to be subauroral, and henceforth use the terminology "subauroral" instead of "mid-latitude" to describe the convection.

Figure 3.2 illustrates how the LOS velocity data were processed to obtain two-dimensional ion drift vectors at each MLAT/MLT location. Panel (a) shows a two-minute scan plot of LOS velocities observed by the Christmas Valley West and Christmas Valley East (Oregon) radars over the 6:30 - 6:32 UT interval on December 13, 2012. (Note that the fields of view of the two radars overlap slightly and leave no gap.) Positive (blue) velocities indicate motion towards the radar. The two red arcs indicate the same magnetic latitudes shown in Figure 3.1. The background grids are MLAT/MLT grid cells with spatial resolution

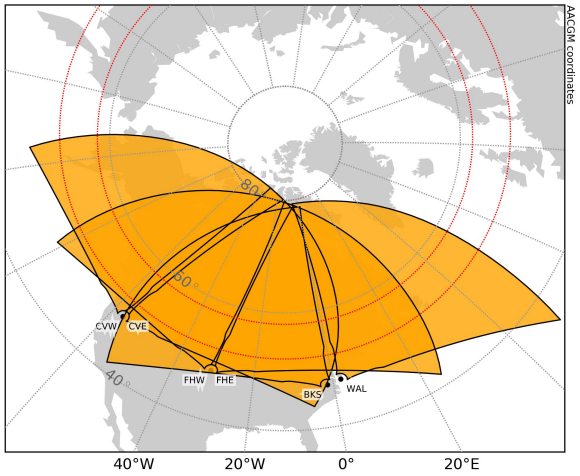

Figure 3.1: Fields of view of the six North American mid-latitude SuperDARN radars used in this study displayed in AACGM coordinate (from west to east): Christmas Valley West (CVW), Christmas Valley East (CVE) (Oregon), Fort Hays West (FHW), Fort Hays East (FHE) (Kansas), Blackstone (BKS), and Wallops Island (WAL) (Virginia). The mid-latitude region of interest lies between 52° and 58° magnetic latitudes bounded by the two red circles.

of 1° MLAT × 7 min MLT and the inset is an expanded view of the 10° azimuth bins within each MLAT/MLT grid cell, which are used to bin the LOS data. (For example, the LOS vectors located within the MLAT/MLT grid cell filled with black all share the same MLAT/MLT location and their directions are binned into the azimuth bin filled with black in the inset.) 7 min of MLT resolution was chosen because it makes an MLAT/MLT grid cell roughly square. In this panel, the smooth variation in raw LOS velocity with radar azimuth indicates a westward flowing plasma with a drift magnitude measured in tens of m/s. Panel (b) shows how the magnitude and direction of the prevailing flow vector can be obtained by fitting a cosine to the LOS-azimuth variation. Note that panel (a) corresponds to a particular time, whereas panel (b) is for data collected over an entire season from 2011-2012. Specifically, panel (b) shows an example cosine fit for all LOS data collected by all radars within a single MLAT/MLT spatial grid cell centered on MLAT=55.5° and MLT=0.0

h for winter (November-February). The median Doppler velocities for each azimuth are plotted as black circles and the size of the circle is proportional to the square root of the number of measurements within the azimuth bin. The error bars are taken as the standard deviation values of the LOS data within each azimuth bin. The best-fit cosine curve is shown in yellow and the point on the curve corresponding to measurement of the full magnitude of the velocity vector is indicated by the red star. In this example, the fitting results in a magnitude of 40.4 m/s and an azimuth of $-80.3°$ (westward, slightly northward). The flow magnitude in particular can be contrasted with auroral convection where velocity is typically measured in the hundreds of m/s.

The LOS velocities associated with the nightside subauroral ionospheric scatter are rather low in magnitude ($<$ 60 m/s) compared to the high latitude ionospheric scatter. We now comment briefly on the manner in which the velocity is determined. Analysis of the auto-correlation function renders an estimate of the variation of phase with lag time on the basis of the echo returns from a multipulse sequence [Greenwald et al., 1985]. Allowing for 2 π phase ambiguities, the slope of the phase variation produces a LOS velocity estimate [Ribeiro et al., 2013]. The velocity magnitudes can be measured from 0 m/s to a maximum value that is set by aliasing considerations and is usually greater than 2 km/s. The uncertainty available in these measurements is very low ($<$ 10 m/s) for the cases of ground scatter (due to vertical movement of ionospheric layers) and low-velocity subauroral ionospheric scatter that is demonstrated in the example of Figure 3.2a where gradual transitions in LOS velocity consistent with weak westward flow are resolved at the level of 1 m/s. For this analysis we have averaged many hundreds of LOS velocity measurements within each MLAT/MLT/azimuth bin (e.g., Figure 3.2b) and determined that the typical variability of the LOS velocity about its mean is around 15 m/s.

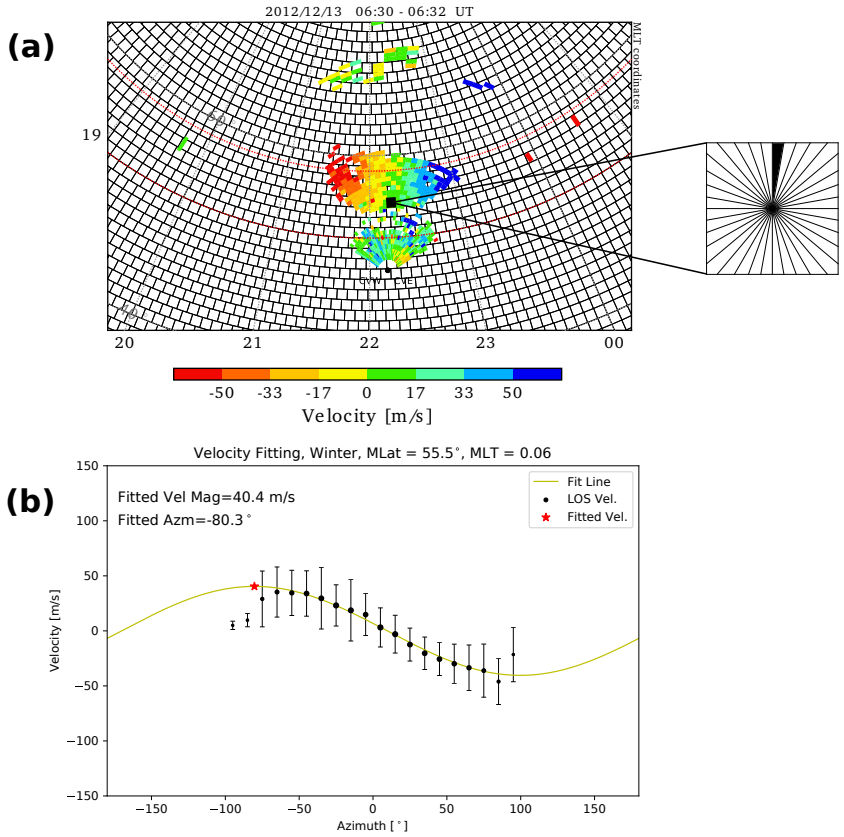

Figure 3.2: An overview of data processing procedures. (a) Two-minute scan plot of line-of-sight velocities observed by Christmas Valley West and Christmas Valley East (Oregon) radars at 6:30-6:32 UT on December 13, 2012 (the positive velocities indicate motion towards the radar). The background grids are MLAT/MLT grid cells and the inset is an expanded view of the 10° azimuth bins within each MLAT/MLT grid cell, which are used to bin the LOS data. (b) An example cosine fit to the line-of-sight velocities collected in azimuth bins within a single MLAT/MLT grid cell for winter (November-February). (See the text for details)

3.3 Results

We present three sets of plots that summarize our results for nightside subauroral convection ordered by season. Figure 3.3 shows the 2-D convection vectors derived for winter (November-February), summer (May-August), and equinox (March-April, September-October). These vectors have been produced by performing the LOS azimuth fitting analysis illustrated by Figure 3.2 for every MLAT/MLT grid cell. The coverage is limited to the nightside by the

availability of subauraral ionospheric backscatter which is confined to the hours of darkness [Ribeiro et al., 2012]. Figures 3.4 and 3.5 show, respectively, the number of measurements and the fitted velocity error ratio in each MLAT/MLT grid cell. The number of measurements (Figure 3.4) follows a similar distribution in each season such that it is relatively low near dusk and increases rapidly as midnight is approached, reaching a peak early in the dawn sector and then decreases rapidly again towards dawn. Most grid cells between 20 and 4 MLT have at least 2000 data points. The fitting quality shown in Figure 3.5 is calculated by dividing the one standard deviation errors on estimated flow magnitudes by the fitted flow magnitude. This error tends to be lower in winter and somewhat higher in summer but is mostly less than 20 %.

Now we examine the morphology of the convection (Figure 3.3) in detail. During the equinoctial seasons (bottom panel) the flow has relatively lower magnitude with an overall average of 21 m/s ($\sim$ 1 mV/m) throughout the night (i.e., 20 - 4 MLT) and is predominantly westward except near dawn where it turns equatorward. In the middle of the night, the flow is almost entirely westward and shows little variation with MLT or MLAT. This can be contrasted with high-latitude convection, which typically turns from westward to eastward near midnight and has a pronounced latitudinal shear [Ruohoniemi and Greenwald, 2005; Weimer, 2005]. The pattern for summer (middle panel) shows similar features but the convection is somewhat weaker (average of 15 m/s), particularly approaching dusk at higher latitudes. The pattern for winter (top panel) is dramatically different from the other seasons. While the flow is still predominantly westward, the flow magnitude is much higher with an average of $\sim$ 32 m/s ($\sim$ 1.6 mV/m) through the night. Approaching dawn the flow turns northward, rather than southward. There are also more pronounced variations with MLT and MLAT such as a pronounced latitudinal gradient in speed between 20 and 2 MLT.

In summary, the important features to note from Figure 3.3 regarding quiet-time subauroral

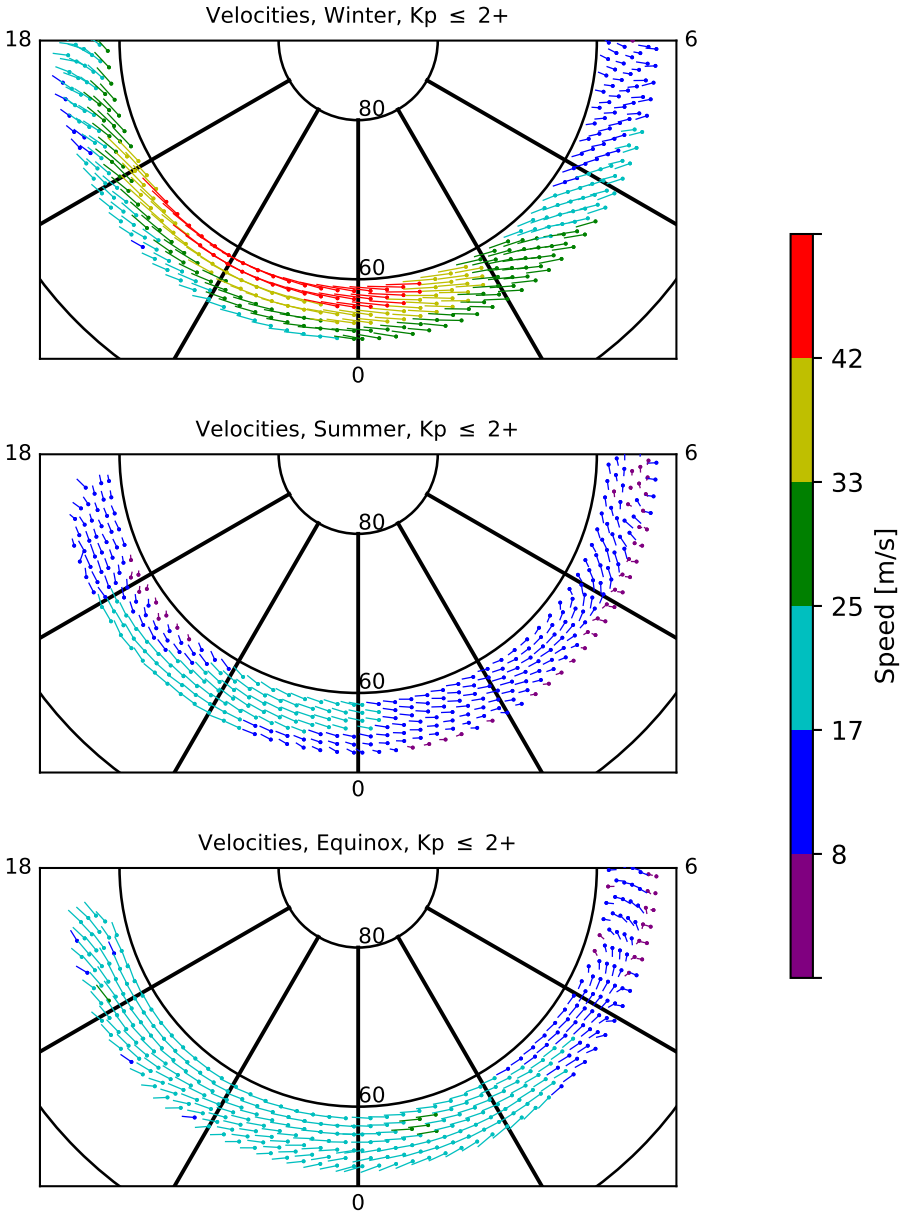

Figure 3.3: 2-D convection vectors calculated for (top to bottom) winter, summer and equinox for the region between 52° and 58° magnetic latitude centered at zero MLT, respectively. All patterns correspond to quiet geomagnetic conditions (Kp $\leq$ 2+).

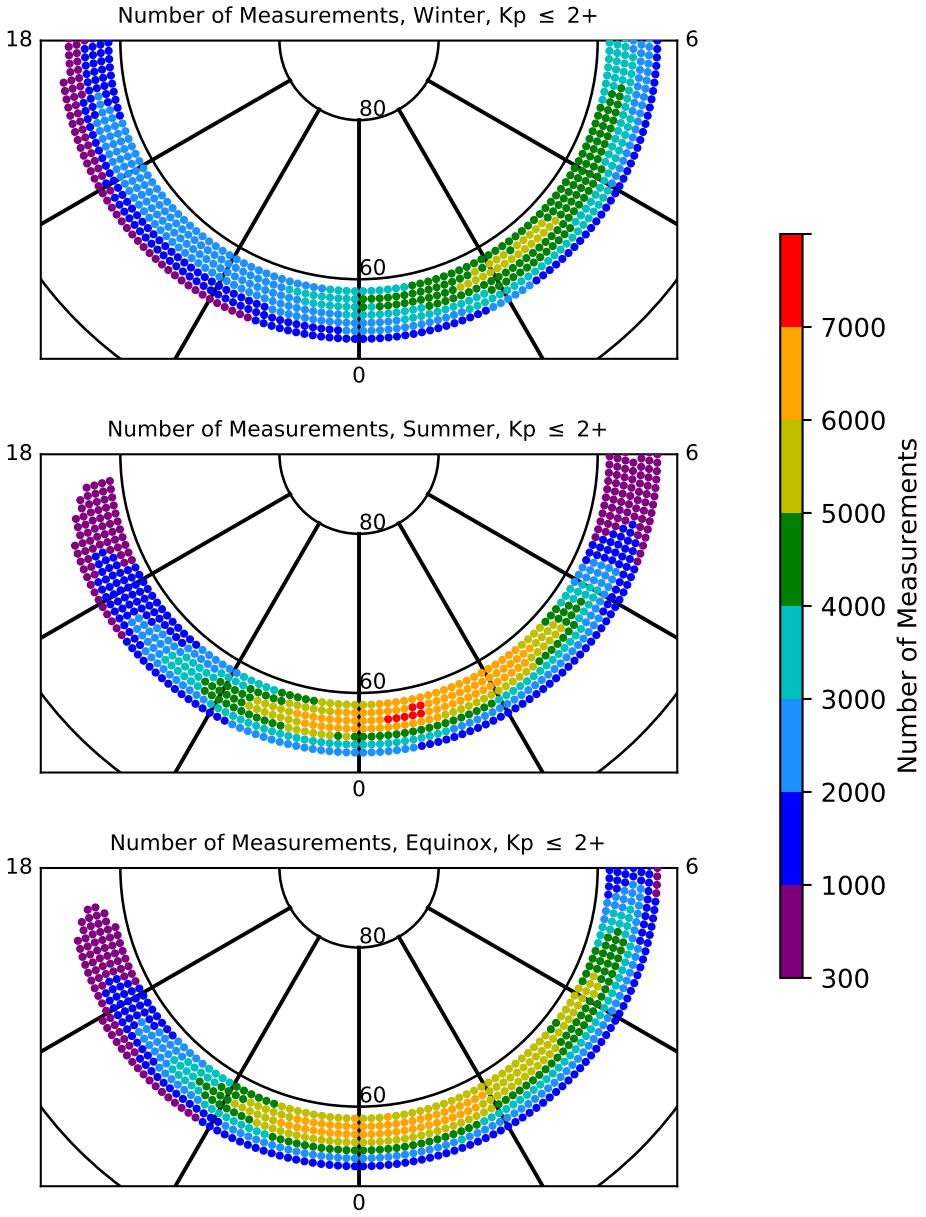

Figure 3.4: Number of line-of-sight measurements in each MLAT/MLT grid cell used to calculate the 2-D convection vectors shown in Figure 3.3.

plasma flow are the following: (1) unlike plasma drifts at high latitudes, the flow has low magnitude (20 - 50 m/s) and remains predominantly westward throughout the night, and

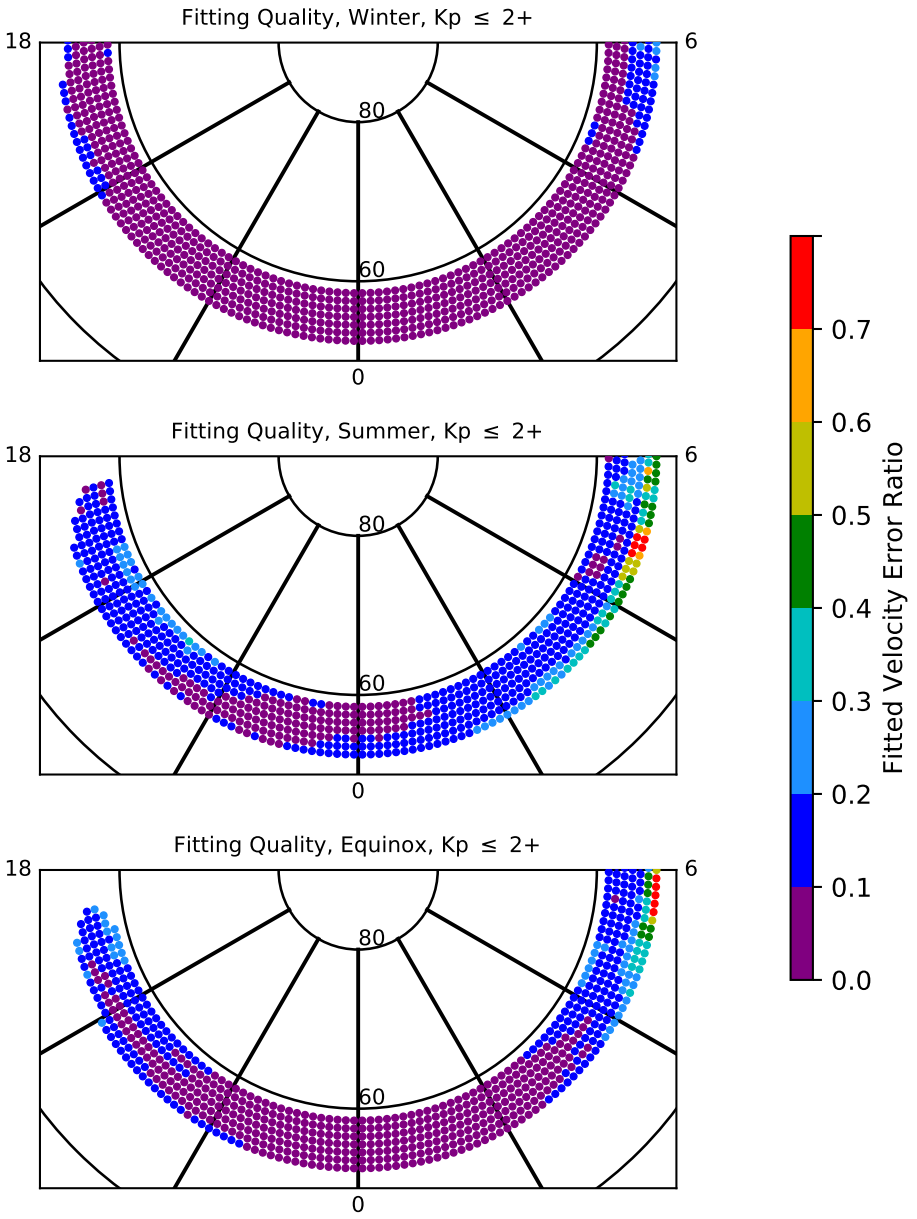

Figure 3.5: Fitted velocity error ratio in each MLAT/MLT grid for the 2-D convection vectors shown in Figure 3.3.

(2) seasonal factors are pronounced with the strongest and most spatially variable flows occurring in winter. Near midnight, the flow velocity during winter is double that of the

flow in the other seasons and there is a pronounced latitudinal gradient in flow speed.

3.4 Data Comparison: Millstone Hill ISR

We now compare the SuperDARN results derived here with those from comparable Millstone Hill radar studies. Figure 3.6 shows a comparison of the zonal plasma drifts extracted from this study for MLAT=57° (red dots with error bars) with the Millstone Hill measurements reported by Richmond et al. [1980] (blue dots with error bars) and by Buonsanto et al. [1993] for solar minimum period that covers F10.7 up to 135.0 (green triangles with error bars). We have also included the calculated empirical model drifts (smooth blue curve) reported by Richmond et al. [1980]. Figure 3.7 depicts the meridional drifts in the same format as Figure 3.6.

Figure 3.6 shows there is generally good agreement in both the strength and direction of the zonal flows. All datasets show westward flows through the night with similar magnitudes. Pronounced seasonal dependence is also evident in the zonal flows from all the datasets, with the strongest and most spatially variable flows occurring in winter. The dramatic rotation of flows with MLT from strongly westward to slightly eastward in the winter post-midnight sector is reproduced in all the radar datasets. However, there are some noticeable differences as well. Specifically, the SuperDARN results show less variation with MLT, especially during summer and equinox, and the zonal flow magnitude in summer is smaller than that specified by the Millstone Hill radar and the empirical model. By contrast, Figure 3.7 shows much less consistency between the meridional flows such that the flows seen by SuperDARN tend to be weaker, less variable, and sometimes reversed in direction from those seen at Millstone Hill. During summer and equinox, we find the meridional velocities to be very low (< 5 m/s) throughout the night, except for an equatorward turning near dawn hours; whereas

the two ISR datasets show stronger and more variable meridional drifts during the night. In fact, our results are more consistent with the empirical model than the actual measurements from the Millstone Hill radar. It is worth noting that the two ISR studies show comparable differences with each other as well.

In summary, the SuperDARN measured zonal flows are in reasonable agreement with the Millstone Hill ISR results at a single value of latitude. The situation in the meridional flows is less consistent. Specific differences are: (1) SuperDARN results show less variability, especially during summer and equinox; (2) The zonal flow magnitudes in summer are smaller than those reported in previous studies; (3) During summer and equinox, we find the meridional velocities to be very small (< 5 m/s) throughout the night, except for an equatorward turning near dawn hours.

3.5 Latitudinal Dependence: Zonal and Meridional Flows

One advantage of the SuperDARN dataset is that it covers a substantial latitudinal interval within the mid-latitude region and thus can be applied to study the latitudinal factors. Figures 3.8 and 3.9 respectively show the fitted zonal (positive eastward) and meridional (positive northward) velocities versus MLT with color-coding by MLAT. This format provides an easy way of comparing the magnitudes of the flows as functions of both MLAT and MLT and highlights the more nuanced details that are not easily seen in Figure 3.3.

Figure 3.8 illustrates the significant seasonal variation in the zonal component. During equinox, the zonal flow is steadily westward ($\sim$ 20 m/s) and has very little latitudinal and MLT variations through the night until about 3 MLT when it starts to decrease in magnitude and shows some weak variation with MLAT. During summer, the zonal flow is westward throughout the night; between 23 and 3 MLT hours it has a relatively steady

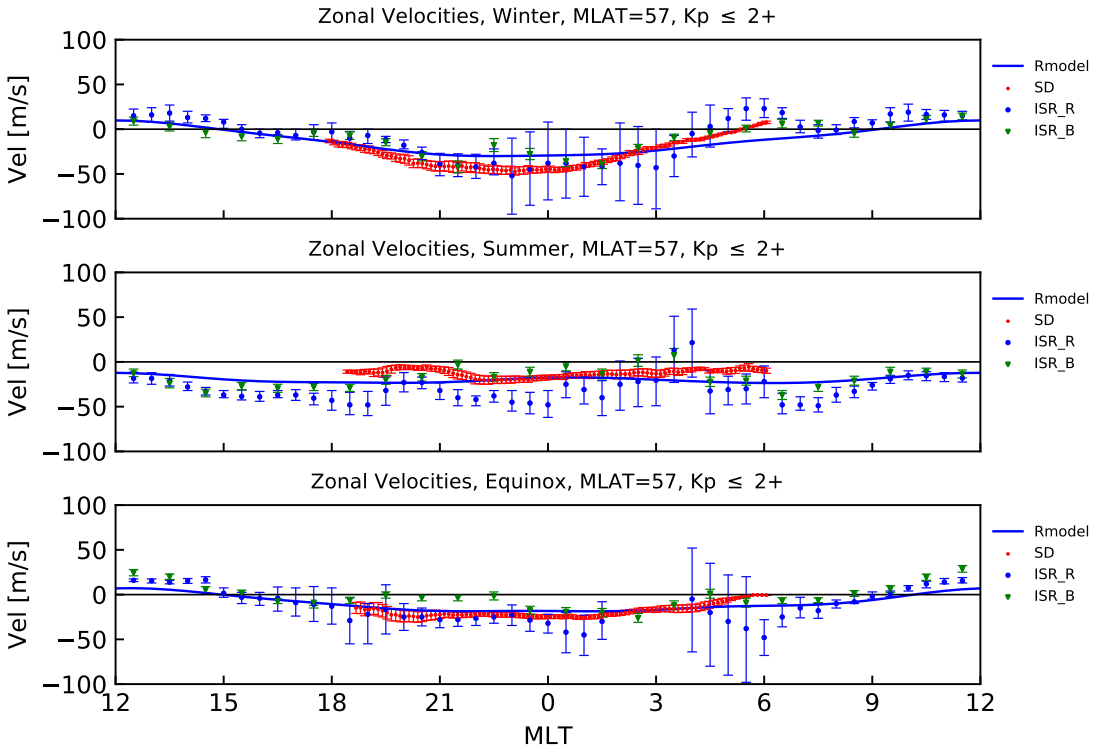

Figure 3.6: Comparison of zonal plasma drifts at 57° MLAT seen by SuperDARN (red dots with error bars) and Millstone Hill ISR measurements reported by Richmond et al. [1980] (blue dots with error bars) and Buonsanto et al. [1993] (Green triangles with error bars), as well as the Richmond et al. [1980] empirical model (smooth blue curve).

magnitude of ∼ 15 m/s (∼ 0.75 mV/m) and small dispersion with latitude. Between 19 and 22 MLT it shows a significant latitudinal variation with velocity deceasing with latitude. In winter, the zonal flow is also westward but much stronger with a dependence on MLT such that it increases in strength from ∼ 0 m/s at both dawn and dusk to ∼ 55 m/s (∼ 3 mV/m) towards midnight. However, the most striking feature in Figure 3.8 is the pronounced latitudinal variation in the winter zonal flow such that the velocity magnitude increases with latitude between 18 and 2 MLT. The sense of this variation is opposite that noted in summer in the 19 - 22 MLT interval. The dispersion of zonal speed with latitude disappears by 2 MLT. Possible reasons for this behavior will be discussed in Section 6.

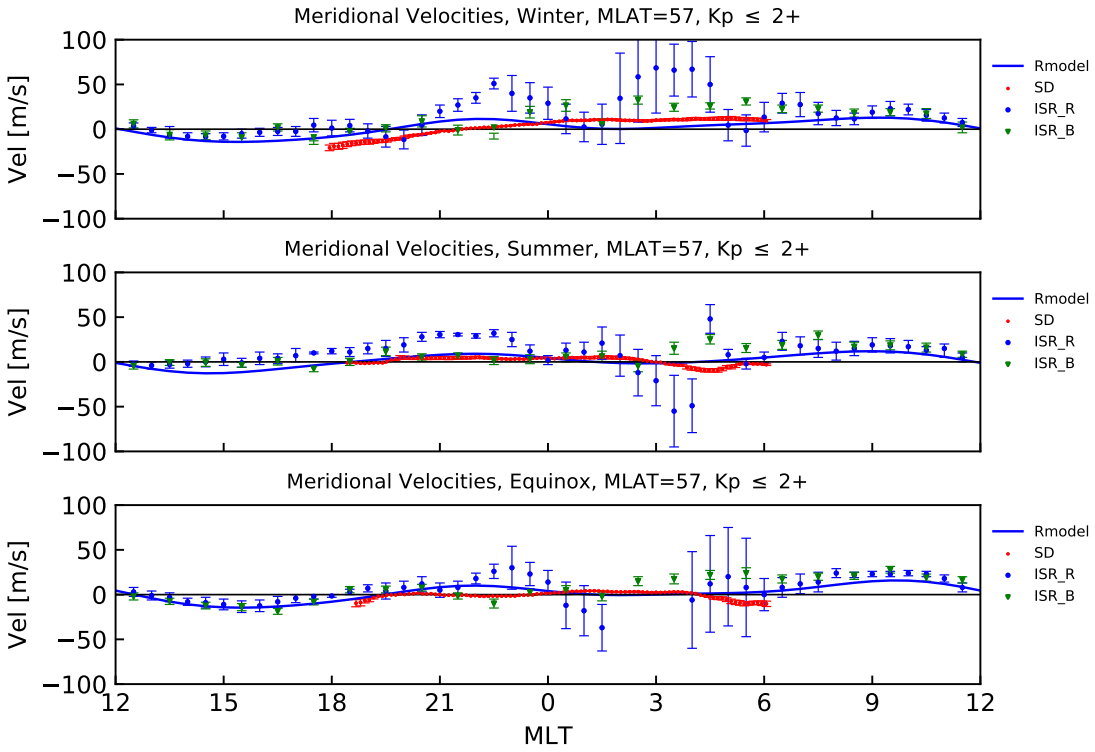

Figure 3.7: Comparison of meridional plasma drifts (similar format to Figure 3.6).

Figure 3.9 shows that the meridional component is also strongly influenced by season. During equinox and summer, the meridional flow is no more than a few m/s throughout the night but becomes significantly southward, $\sim$ 15 m/s, towards dawn and dusk. It is uniform across all latitudes (less so in equinox) and has very little variation with MLT across the nightside. In winter, however, the meridional flow is very different and shows strong variations with MLT such that the magnitude varies from 20 m/s equatorward at dusk to 20 m/s ($\sim$ 1 mV/m) poleward at dawn. In contrast to the zonal flow component, the meridional flow does not show large latitudinal variations. The meridional component in winter is equatorward at dusk and poleward at dawn. The transition from equatorward to poleward occurs between 21 and 24 MLT with the flows at higher latitudes turning earlier than those at lower latitudes.

In summary, the most prominent features from Figures 3.8 and 3.9 are as follows. (1) The flow is predominantly westward (20 - 55 m/s) and weakly northward (0 -20 m/s) between 21 and 3 MLT, which corresponds to a northward electric field ($\sim$ 1 - 3 mV/m) and a weak eastward electric field ($\sim$ 0 - 1 mV/m). (2) Both zonal and meridional flows exhibit strong seasonal dependencies with strongest flows in winter. (3) There is a significant latitudinal variation in winter zonal flow between 18 and 2 MLT. The zonal flow also shows some latitudinal variation near 21 MLT in summer of the opposite sense but not during equinox. By contrast, the meridional flow does not show much latitudinal variation irrespective of season.

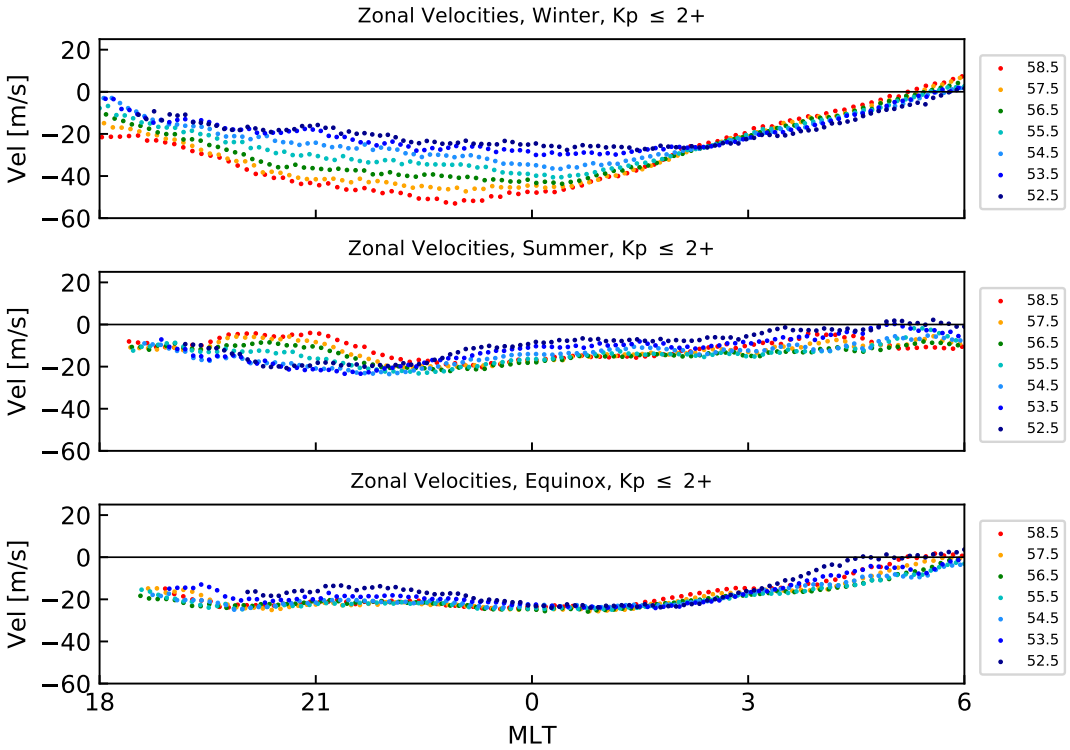

Figure 3.8: Fitted zonal velocities (positive eastward) by magnetic latitude versus MLT. The three panels, from top to bottom, are results for winter, summer, and equinox, respectively.

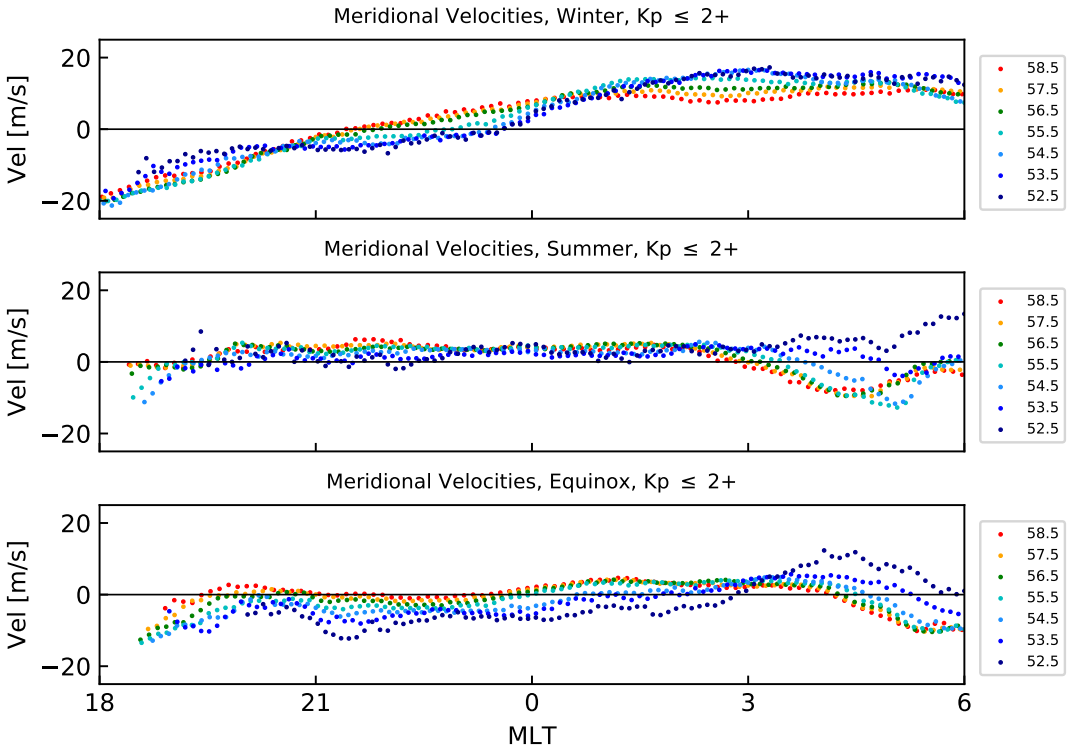

Figure 3.9: The same as in Figure 3.8 but for meridional velocities. Note that the Y-axis scale is expanded by a factor of two for clarity.

3.6 Discussion

In this study we have used SuperDARN measurements to derive statistical patterns of the nightside subauroral plasma convection under quiet-time conditions over the latitude interval 52° and 58° MLAT (Figure 3.3). These patterns have unprecedented spatial resolution and statistical significance (Figure 3.4) and the quality of the fitted velocities is good (Figure 3.5). Figures 3.6 - 3.7 show that the new results are in generally good agreement with previously reported observations from the Millstone Hill ISR while Figures 3.8 - 3.9 show that the improved latitudinal coverage reveals interesting new features, such as a significant latitudinal variation in zonal flow velocity between 18 and 2 MLT in winter. In this section, we

discuss these features in light of the possible mechanisms for driving subauroral convection.

Under geomagnetically quiet conditions the F region dynamo is believed to be the dominant mechanism for producing electric fields at night when the upper thermospheric winds are large and the E region conductivity is small. The induced electric fields cause the F region plasma to drift in the same direction as the neutral atmosphere [Rishbeth, 1971; Burnside et al., 1983; Rishbeth, 1997]. Accordingly, we would expect, in the absence of other factors, the plasma flow to follow the neutral winds. However, detailed comparison of the flow components presented in Figures 3.8 and 3.9 with wind vectors derived from the latest horizontal wind model (HWM14 model [Drob et al., 2015]) under similar conditions (results not shown) finds very little similarity during the premidnight hours, when the plasma flows predominantly westward (except for the predominantly southward flow near dusk in winter) while the neutral wind is directed eastward and southward. This difference in zonal components of wind and plasma motions was also reported by Buonsanto et al. [1993]. During the postmidnight hours, however, the neutral wind is westward and southward and ion convection is predominantly westward (except for the predominantly northward flow near dawn in winter). So, the local F region dynamo could account for the westward plasma motion in the postmidnight sector but not in the premidnight sector.

The neutral wind dynamo could also be felt through conjugacy to the southern hemisphere. Under the assumption of equipotential geomagnetic field lines, the local electric field can be influenced by conditions in the conjugate hemisphere, especially if the Pedersen conductivity there is larger [Burnside et al., 1983; Buonsanto et al., 1993; Fejer, 1993]. The conjugacy effect could be particularly significant during the dawn and dusk hours of winter because the conjugate E region in the southern hemisphere would then be strongly sunlit. However, quantifying the extent to which this may or may not be happening requires detailed knowledge of E and F region conductivities and the neutral wind patterns in both hemispheres

and is beyond the scope of the present study. Future work could investigate the conjugacy effect using the SuperDARN Hokkaido East (HOK) and Hokkaido East (HKW) radars in the northern hemisphere which have overlapping conjugate points with the Tiger (TIG), Unwin (UNW), and Buckland Park (BPK) radars in the southern hemisphere.

Next, we consider the extent to which penetration of high latitude convection electric fields might be manifested in the subauroral convection. Previous studies have shown that the plasmasphere is shielded from the magnetospheric convection electric field by charge buildup at dawn and dusk near the inner edge of the ring current [Vasyliunas, 1970, 1972; Southwood, 1977]. This shielding effect, however, is not perfect. Senior and Blanc [1984], after considering the distributions of ionospheric conductivity and field-aligned currents, showed that the shielding efficiency had been overestimated in previous studies. Kelley et al. [2003] found in one magnetic storm event that the ratio of the dawn-to-dusk component of the interplanetary electric field (IEF) to the dawn-to-dusk electric field in the equatorial ionosphere for periods less than about two hours is 15:1 (about 6.6%). Huang et al. [2007], based on a statistical study of rapid southward turnings of IMF, derived an empirical value of 9.6% for the efficiency of penetration to the dayside equatorial ionosphere, where the efficiency is defined as the ratio of the change of the equatorial ionospheric electric field to the change of the IEF. They further concluded that the IEF can continuously penetrate to the low-latitude ionosphere without significant attenuation for many hours during the main phase of magnetic storms. Although the results of Kelley et al. [2003] and Huang et al. [2007] are derived under storm time conditions, these recent studies suggest that the effect of penetration electric field is more significant than was previously understood.

If penetration of the convection electric field dominates, the observed subauroral convection should exhibit some of the gross characteristics of the high latitude convection and hence we would expect to see a roughly symmetric MLT distribution of zonal flow with westward

flow premidnight and eastward flow postmidnight. As shown in Figure 3.8, however, the subauroral flow is westward throughout the night. This indicates that penetration most likely cannot explain the flows postmidnight. But the emergence of eastward flow towards dusk suggests that the subauroral westward flow may gradually transition to two-cell convection towards higher latitudes. To explore this possibility we examine the zonal flow over the latitude interval 58° and 64° MLAT under quiet conditions corresponding to passage from the subauroral to the auroral zone. The upper limit of 64° was chosen because it is the highest latitude where fit vectors could be determined reliably on the basis of data availability. Figure 3.10 shows the fitted zonal velocities (positive eastward) between 58° and 64° MLAT. Note that the plasma flow in this higher latitude interval of 58° - 64° MLAT was not extended to the subauroral latitude interval of 52° - 58° MLAT in Figure 3.8 because both the statistical significance and the fitting quality start to degrade for the region above 60° MLAT due to limited coverage. For the summer and equinoctial seasons the zonal flow at 62° MLAT and above in fact reverses direction to eastward at around midnight MLT consistent with passage into the auroral zone. The reversal is delayed until 3 MLT in winter. (Note that the velocity at this latitude is lower than what would be expected for auroral zone flows because we selected for only low-velocity events as described in Section 3.2). In the premidnight MLT sector, however, all latitudes exhibit the westward return flow of the two-cell convection pattern. This suggests that penetration of the high latitude two-cell convection into the subauroral zone could be dominating the neutral wind effect in the premidnight MLT sector. The eastward turning that emerges in the flows at higher latitudes ($\geq$ 62° MLAT) around midnight MLT (later in the winter season) perhaps indicates penetration of the postmidnight high-latitude electric fields that is not sufficient to dominate the neutral winds there.

Penetration of the high latitude convection electric fields is usually invoked to account for electric fields seen at lower latitudes under geomagnetically disturbed conditions [e.g., Blanc

et al., 1977; Kelley et al., 1979; Yeh et al., 1991; Buonsanto et al., 1992; Kelley et al., 2003]. However, the consistency in the flow direction in the premidnight sector indicates that penetration is taking place at middle latitudes even under relatively quiet magnetic conditions. This conclusion was also reached by [Carpenter and Kirchhoff, 1975] through their examination of the electric field variations at Millstone Hill and Chatanika ($\Lambda = \sim 65.5°$). Wand and Evans [1981a] concluded that, during quiet-time conditions the evening southward electric field (eastward drift) at Millstone Hill could be due to the penetration electric field but the eastward electric field (poleward drift) represents the dynamo electric field only. Lejosne and Mozer [2016], using Van Allen Probe measurements, also attributed the quiet-time westward zonal plasma drifts at L shell values of L = 2 - 2.8 (MLAT = 45° - 53°) to penetration of solar-wind driven convection electric fields.

We consider the possibility that imperfect shielding is the cause of penetration of electric fields to the subauroral region. According to the shielding theory, the polarization charges at the inner edge of the ring current do not react effectively to an electric field that changes faster than the shielding time constant, which is the time it takes for charges at the inner edge of the ring current to re-arrange themselves to cancel out an applied electric field. Theoretical and modeling studies have provided widely varying estimates of the shielding time constant, ranging from $\sim$ 30 min ([Senior and Blanc, 1984]) to a few hours ([Southwood, 1977; Siscoe, 1982]) and up to 5 hours ([Jaggi and Wolf, 1973]). Although we selected for quiet-time conditions with Kp $\leq$ 2+, the high-latitude convection electric fields can still vary considerably during a three-hour Kp period due to variable IMF conditions. We would expect as much overshielding as undershielding which would lead to both westward and eastward flows with comparable rates of occurrence. However, the persistent westward flow during the night that was observed in all seasons suggests that undershielding is more prevalent. One possible explanation is that the polarization charges at the inner edge of the ring current

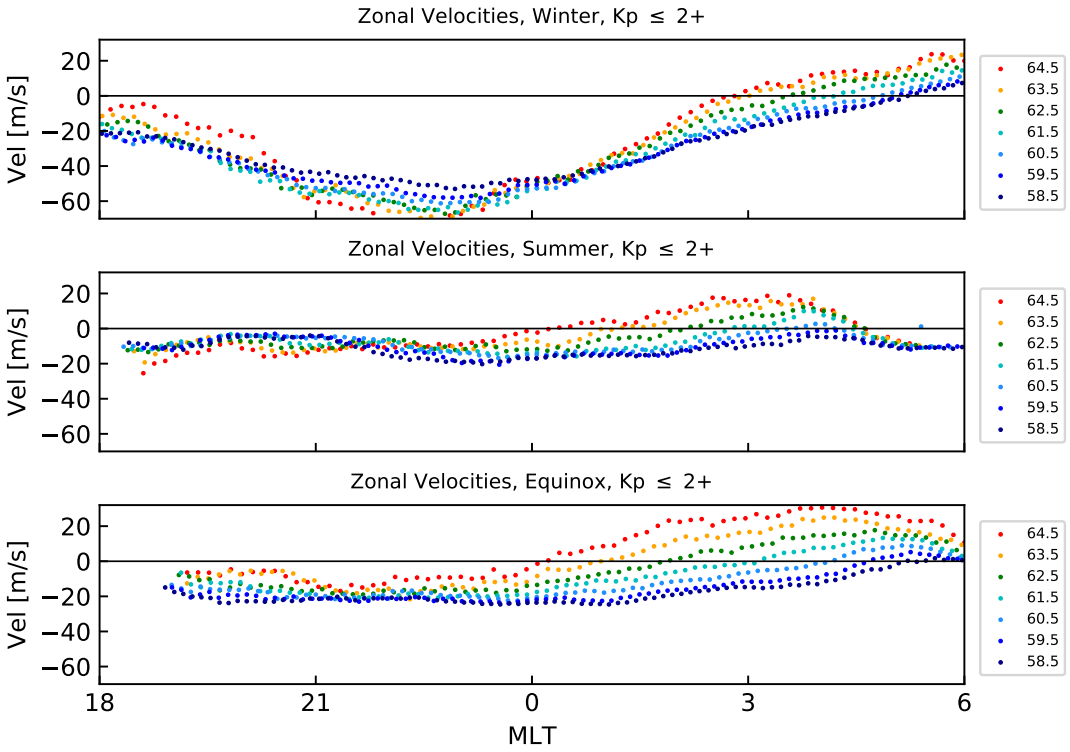

Figure 3.10: The same as in Figure 3.8 but for the region between 58° and 64° magnetic latitudes.

accumulate more slowly for an increased dawn to dusk electric field than they dissipate for a decreased electric field, which could mean that the shielding time constant is longer for undershielding than for overshielding. This hypothesis is not very far-fetched because the morphology of the field-aligned currents and the strength of the auroral precipitations under the two cases can be quite different and hence could modulate the shielding time constant.

The dependence of shielding on ionospheric conductivity is another factor that needs to be considered. Senior and Blanc [1984] found that penetration of magnetospheric electric fields equatorward of the auroral zone in the presence of a realistic mid-latitude conductance distribution produces an asymmetric potential pattern with northward electric fields (westward flows) across midnight until $\sim$ 3 MLT [Senior and Blanc, 1984; Senior and Blanc,

1987]. This is consistent with the existence of postmidnight westward flow seen in Figure 3.8. Our observation of the strongest westward flow (northward electric fields) in winter and the weakest in summer is also an indication of ionospheric conductivity playing an important role in shielding. Furthermore, the significant latitudinal variation observed between 18 - 2 MLT in winter (with increasing flow magnitude towards higher latitude between 52° - 58° MLAT) and that between 19 - 22 MLT in summer (but in opposite sense, with decreasing flow magnitude towards higher latitude between 52° - 58° MLAT) could also be a result of seasonal variations in ionospheric conductivity. The influence of ionospheric conductivity on reducing the amount of shielding provides a plausible explanation for the latitudinal dispersion of the westward flow and its seasonal variations.

IMF control is yet another factor that needs to be considered. If penetration of the high latitude convection electric fields can indeed dominate subauroral convection, then the observed subauroral plasma drifts should also be influenced by the IMF conditions. Here we show a preliminary analysis of winter convection organized by IMF B_z conditions. The OMNI IMF dataset was used to select periods for which the IMF B_z polarity was stable for at least 40 minutes. (Note that various time windows of up to 80 minutes have been tested and all rendered similar results. 40 minutes was chosen to guarantee a reasonable statistical significance and a good fitting quality.) Figure 3.11 shows the 2-D convection patterns calculated for winter under IMF B_z^+ (top) and B_z^- (bottom) conditions for the region between 52° and 58° magnetic latitudes. Both panels show similar convection features such as (1) predominantly westward flow throughout the night and meridional flow during the dawn and dusk hours and (2) a pronounced latitudinal gradient in speed between 18 and 2 MLT, which are also present in Figure 3.3. However, the convection for IMF B_z^- is significantly stronger than that for IMF B_z^+, especially in the premidnight sector. These observations were found to be true for other seasons as well (figures not shown). Note that the changed

flow conditions for IMF B_z^+ are not due to a simple expansion of auroral flows to these latitudes as the dawn sector convection remains westward. Although reduced, the emergence of an IMF dependence in subauroral convection provides further evidence that the penetration of high-latitude convection electric fields is a significant factor. More detailed exploration of IMF control of subauroral convection warrants a separate study and is left to future work.

3.7 Summary and Conclusions

In this study, we have derived a new model of nightside quiet-time subauroral convection using two years of data obtained from six mid-latitude SuperDARN radars in the North American sector. The model is organized in MLAT-MLT coordinates and features high spatial resolution ($1^\circ \times 7$ min) and unprecedented statistical significance. The results show that the flow is predominantly westward (20 - 55 m/s) and weakly northward (0 - 20 m/s) deep on the nightside and that a seasonal factor is prominent such that the flows tend to be strongest and most variable in winter. These statistical results are in general agreement with previously reported observations from the Millstone Hill ISR but our results also show interesting new features thanks to the latitudinal coverage of the SuperDARN measurements. One such new feature is a significant latitudinal variation in the zonal flow velocity near midnight in winter. Comparison with the neutral winds extracted from the HMW14 has shown that local F region neutral wind dynamo does not account for the observed sense of convection in the premidnight sector. Neglecting conjugacy effects, examination of the electric field variations between 52° and 64° magnetic latitude suggests that a considerable contribution to the subauroral electric fields comes from the high latitude regions, especially in the premidnight MLT hours, and hence penetration through undershielding is indicated as a primary driver for subauroral convection under even quiet conditions. Penetration of

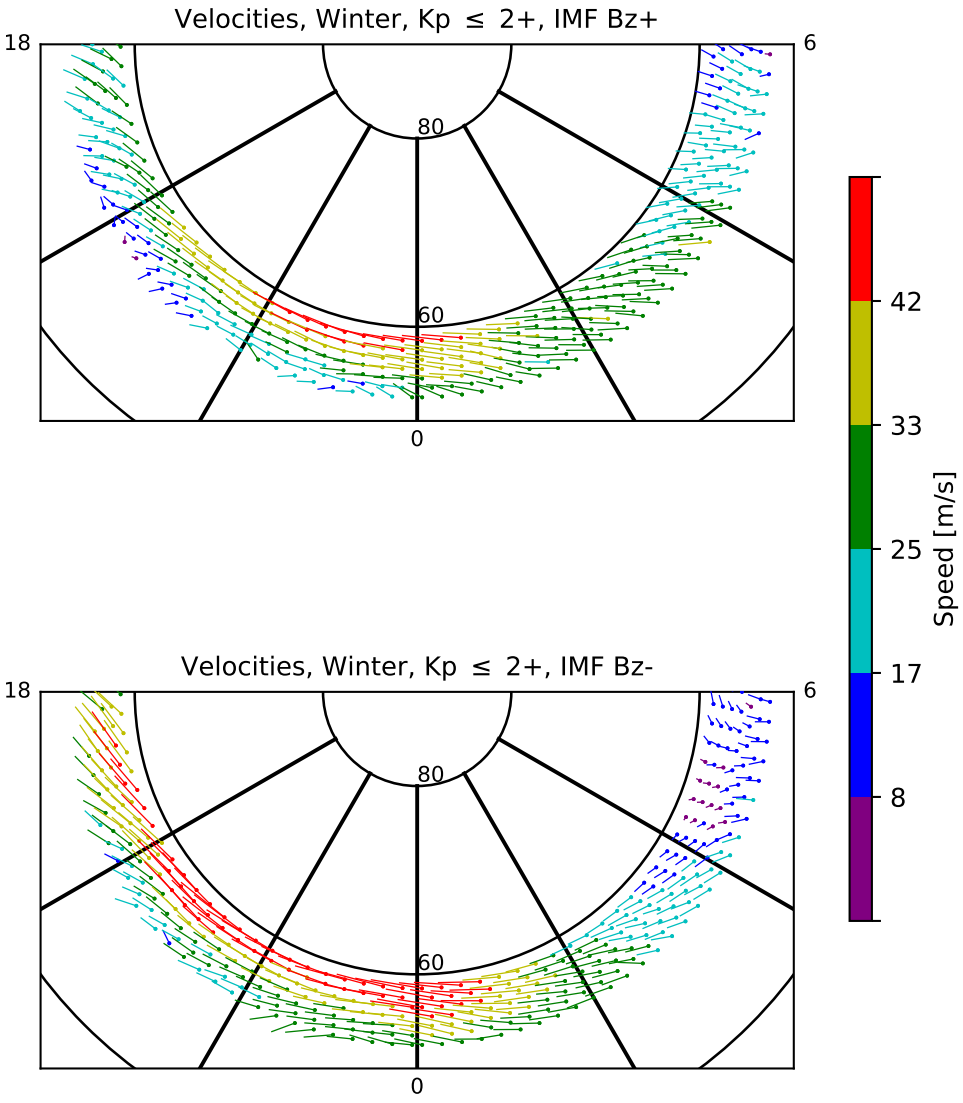

Figure 3.11: 2-D convection patterns calculated for winter under the IMF B_z^+(top) and B_z^- (bottom) conditions for the region between 52° and 58° magnetic latitudes.

the post-midnight high-latitude convection may be present but is less effective in controlling the direction of subauroral convection.

Acknowledgments

We thank the National Science Foundation for support under grants AGS-1341918, AGS-1259508 and AGS-1243070. We also thank all participants in the worldwide SuperDARN collaboration for the distribution of SuperDARN data via http://vt.superdarn.org/tiki-index.php?page=Data+Access. Special thanks to Dr. Arthur D. Richmond in the High Altitude Observatory at the National Center for Atmospheric Research for providing the code for his ionospheric electric field model. We wish to acknowledge the use of the NASA/GFSC Space Physics Data Facility's OMNIWeb and CDAWeb service. The planetary three-hour-range Kp index data are obtained from GFZ-Potsdam FTP server via ftp://ftp.gfz-potsdam.de/pub/home/obs/kp-ap/wdc/. The majority of analysis and visualization were completed with the help of free, open-source software tools such as DaViT-py (https://github.com/vtsuperdarn/davitpy), matplotlib [Hunter, 2007], IPython [Pérez and Granger, 2007], pandas [McKinney, 2010], and others [e.g. Millman and Aivazis, 2011].

Chapter 4

Subauroral Convection and its Major Driving Influences - Part 2

M. Maimaiti [1], J. B. H. Baker [1], J. M. Ruohoniemi [1], B. Kunduri, [1]

[1]Bradley Department of Electrical and Computer Engineering, Virginia Tech, Blacksburg, Virginia, USA.

Maimaiti, M., Baker, J. B. H., Ruohoniemi, J. M., & Kunduri, B. S. R. (2019). Morphology of nightside subauroral ionospheric convection: Monthly, seasonal, Kp, and IMF dependencies. Journal of Geophysical Research: Space Physics, 124, 4608– 4626.
https://doi.org/10.1029/2018JA026268

Abstract

In this study we have used seven years (2011-2017) of quiet (Kp $\leq$ 2+) to moderately disturbed (Kp = 3) time nightside line-of-sight measurements from six mid-latitude Super Dual Auroral Radar Network (SuperDARN) radars in the U.S. continent to characterize the subauroral convection in terms of magnetic latitude (MLAT), magnetic local time (MLT), month, season, Kp, and the interplanetary magnetic field (IMF) clock angle. Our results show that (1) the quiet-time (Kp $\leq$ 2+) subauroral flows are predominantly westward (20 - 90 m/s) in all months and become meridional (-20 - 20 m/s) near dawn and dusk, with the flows being the strongest and most structured in December and January. (2) The Kp dependency is prominent in all seasons such that for higher Kp the premidnight westward flow intensifies and the post-midnight eastward flow starts to emerge. (3) Sorting by IMF clock angle shows Bz+/Bz- features consistent with lower/higher Kp conditions, as expected, but also shows distinct differences that are associated with By sign. (4) There is a pronounced latitudinal variation in the zonal flow speed between 18 and 2 MLT in winter (November to February) that exists under all IMF conditions but is most pronounced under IMF Bz- and higher Kp. Our analysis suggests that the quiet-time subauroral flows are due to the combined effects of solar-wind/magnetosphere coupling leading to penetration electric field and the neutral wind dynamo with the ionospheric conductivity modulating their relative dominance.

4.1 Introduction

The plasma convection at high-latitude regions is primarily driven by the magnetic reconnection process [Dungey, 1961] and, to a lesser extent, viscous interaction [Axford and Hines, 1961]. Typical plasma flow velocities at these latitudes are a few hundred to a few thousand m/s. The high-latitude convection patterns have been studied extensively and there are

many statistical convection models developed using a variety of observations and techniques [e.g., Heppner and Maynard, 1987; Hairston and Heelis, 1990; Papitashvili and Rich, 2002; Weimer, 2005; Haaland et al., 2007; Förster and Haaland, 2015; Ridley et al., 2000; Zhang et al., 2007; Ruohoniemi and Greenwald, 2005; Reistad et al., 2018; Thomas and Shepherd, 2018]. The recent model of Thomas and Shepherd [2018] characterizes the high-latitude convection as a function of solar wind, interplanetary magnetic field (IMF), dipole tilt angle, and Kp index using line-of-sight velocity measurements from the Super Dual Auroral Radar Network (SuperDARN) radars for the years 2010-2016.

By contrast, the quiet-time plasma in the nightside subauroral regions exhibit drifts of only a few tens of m/s [Richmond et al., 1980; Buonsanto et al., 1993] and the driving mechanisms are still not well understood. The most well-known mechanism proposed to account for electric fields in the nightside subauroral ionosphere is the neutral wind dynamo [Rishbeth, 1971; Richmond et al., 1976], by which a dynamo electric field is generated through the collision of neutral molecules with ions leading to charged particle motion across the geomagnetic field. Under geomagnetically disturbed conditions the neutral wind dynamo takes the form of the ionospheric disturbance dynamo proposed by Blanc and Richmond [1980], by which an equatorward thermospheric wind is driven by auroral heating during periods of high geomagnetic activity. This wind gains westward momentum due to the Coriolis force and causes subcorotation of ionospheric plasma (i.e. westward motion with respect to the Earth), first at subauroral latitudes and progressively later at lower latitudes, by the same dynamo mechanism that takes place during quiet times. For both types of dynamo mechanisms, it is the neutral drag force that drives the plasma motion.

The neutral wind is a 3D velocity field and a significant vertical transport can take place, e.g. in the dayside cusp region, in response to magnetosphere-ionosphere coupling [Lühr et al., 2004; Crowley et al., 2010]. However, the plasma convection is primarily horizontal

and the horizontal component of the neutral wind is of primary interest when considering the neutral wind effect on plasma convection. In the absence of geomagnetic disturbance, the thermospheric neutral winds at subauroral latitudes are generally directed eastward premidnight and westward post-midnight as inferred from the recently updated horizontal wind model 2014 (HWM14) [Drob et al., 2015] and from the statistical thermospheric wind patterns based on ground-based Fabry-Perot interferometer measurements [Emmert et al., 2003, 2006] and the CHAllenging Minisatellite Payload (CHAMP) satellite's cross-track accelerometer measurements [Xiong et al., 2015]. Under such conditions, we would expect the neutral wind dynamo to entrain the plasma to follow the pattern of the background neutral winds, i.e. eastward premidnight and westward post-midnight at F region altitudes during quiet magnetic conditions. However, previous studies have found this to not be the case [Buonsanto et al., 1993; Fejer, 1993].

Another cause of plasma motion in the subauroral region is solar wind-magnetosphere interaction that leads to penetration of electric field to the region equatorward of the auroral boundary (i.e., earthward of the inner magnetosphere) [Nishida, 1968; Blanc et al., 1977]. Under steady solar wind and magnetospheric conditions, the inner magnetosphere (subauroral region) is considered to be shielded from the effects of the dawn-dusk convection electric field via region-2 field-aligned currents driven by pressure gradients near the inner edge of the plasma sheet, or the so-called "shielding layer" [Vasyliunas, 1970, 1972; Jaggi and Wolf, 1973]. The shielding breaks down when a sudden change in the dawn-dusk electric field occurs (e.g. sudden IMF Bz turnings), leading to penetration/leakage of the dawn-dusk electric field into the inner magnetosphere. Penetration may continue for a few tens of minutes [Senior and Blanc, 1984] up to several hours [Kelley et al., 2003; Huang et al., 2007; Maruyama et al., 2007] before the inner edge of the plasma sheet re-establishes shielding. In contrast to the neutral wind dynamo, where the drag from the neutral wind acts on ionospheric plasma,

it is the penetration electric field that drives the plasma flow which then drags the neutral molecules through collisions and transfers energy to them. Although the penetration effect is direct and prompt, distinguishing it from the disturbance dynamo effect at the subauroral region during geomagnetically active conditions can be difficult because both processes can exist simultaneously with similar plasma flow signatures. The occurrence of penetration electric field has mostly been reported under geomagnetically disturbed conditions [e.g., Yeh et al., 1991; Buonsanto et al., 1992], but some studies have also reported the presence of penetration electric field under quiet conditions [e.g., Carpenter and Kirchhoff, 1975; Wand and Evans, 1981a; Heelis and Coley, 1992; Lejosne and Mozer, 2016; Maimaiti et al., 2018].

A number of studies have used measurements from satellite-based ion drift meters or incoherent scatter radars (ISRs) to characterize the average pattern of subauroral ionospheric plasma drifts in terms of magnetic latitude (MLAT), magnetic local time (MLT), season, Kp, and solar cycle dependencies [e.g., Richmond et al., 1980; Wand and Evans, 1981b; Buonsanto and Witasse, 1999; Scherliess et al., 2001]. The subauroral flows measured by the different instruments all agree on general features, such as the quiet-time flow being predominantly westward through the night and season being an important factor, but somewhat disagree on how the subauroral flows are organized in terms of MLT and season (see [Maimaiti et al., 2018] for comparisons between different models). This could be because some other factors are missing in those models. Most of the previous models of quiet-time subauroral plasma flows were developed under the assumption that the flows are mainly driven by the neutral winds [Richmond et al., 1980]. If penetration of the high-latitude convection electric fields is also significant, then the subauroral plasma drifts should be influenced by IMF conditions. Maimaiti et al. [2018] showed preliminary results of the IMF Bz influence on subauroral convection. However, the authors were unable to parameterize their statistical patterns by any IMF clock angles other than IMF Bz+ and Bz- due to the limited data set they

used. The statistical model of Thomas and Shepherd [2018] includes measurements from mid-latitude SuperDARN radars that we have used in this study and also characterizes the plasma convection by IMF clock angles. However their derived convection patterns under weak solar wind driving conditions or Kp $<$ 3 conditions only reach down to 60° MLAT (See Figures S16-S18 in the supporting information in [Thomas and Shepherd, 2018]), which could be due to their method of determining the Heppner-Maynard boundary [Heppner and Maynard, 1987] based on a velocity threshold of 150 m/s. This warrants developing a quiet time model that characterizes the subauroral convection below 60° MLAT under various IMF clock angle conditions.

In a previous study, Maimaiti et al. [2018] characterized the subauroral convection in terms of MLAT, MLT, seasonal, and IMF Bz (northward vs southward) dependencies using two years (2011-2012) of data from six mid-latitude SuperDARN radars distributed across the U.S. mainland. The primary focus was to investigate the driving influences of subauroral convection under quiet (Kp $\leq$ 2+) conditions. The main conclusion was that the neutral wind dynamo alone can not explain the subauroral convection and penetration through undershielding could be an important factor even during quiet conditions. In this study we expand to seven years (2011-2017) of data collected under quiet to moderately disturbed conditions to also resolve the dependencies of subauroral convection on IMF clock angle (8 bins in the IMF Y-Z plane), geomagnetic disturbances as measured by Kp (0 - 3), and time of year at one-month resolution. We aim to understand the manifestations of the neutral wind and penetration effects as drivers of subauroral convection with progression from quiet to relatively disturbed geomagnetic conditions. To account for dynamic behaviour of the auroral oval, we apply particle precipitation measurements from Polar Operational Environmental Satellites (POES) to determine the location of the equatorward auroral boundary. Among other findings, there is evidence of disturbance dynamo effect with increasing disturbance

level and evidence of IMF By influence, indicative of electric field penetration.

The paper is organized as follows. Section 4.2 describes the data sets used in this study, the selection of subauroral ionospheric radar backscatter and the processing of radar line-of-sight velocities. Section 4.3 presents the monthly, seasonal, Kp, and IMF clock angle dependencies of the subauroral convection. Section 4.4 discusses the results in terms of ionosphere-thermosphere coupling and the penetration of high-latitude convection electric fields to the nightside subauroral ionosphere.

4.2 Data Sets and Data Processing

4.2.1 Data Sets

SuperDARN Radars: The Super Dual Auroral Radar Network (SuperDARN) consists of chains of HF radars in the northern and southern hemispheres that monitor ionospheric dynamics through the detection of decameter-scale field-aligned plasma irregularities in the E and F regions of the ionosphere [Greenwald et al., 1985; Chisham et al., 2007]. The primary data set for this study consists of line-of-sight (LOS) plasma drift velocity measurements obtained over the years 2011 - 2017 by six U.S. mid-latitude SuperDARN radars. The fields of view of these radars are shown in Figure 4.1a in altitude-adjusted corrected geomagnetic (AACGM) coordinates [Baker and Wing, 1989; Shepherd, 2014]. The 7 years selected include the peak of Solar Cycle 24. The subauroral region in this study extends down to 52° MLAT, which was chosen because it is approximately the lowest latitude at which the radars generate measurements in the F region ionosphere.

Here we clarify our definitions of ”auroral”, ”subauroral”, ”high-latitude” and ”mid-latitude”. The ”auroral oval” (or the ”auroral zone”) is a donut-shaped region in the ionosphere whose

poleward and equatorward boundaries are generally understood as the limits for electron precipitation. The positions of these two boundaries vary with geomagnetic activity. Poleward of the auroral oval is the "polar cap" ionosphere and equatorward of it is the "subauroral" ionosphere. In this study we use the terms "auroral" and "subauroral" to refer to ionospheric scatter measurements classified according to their locations relative to the equatorward auroral boundary determined from Polar Operational Environmental Satellites particle precipitation measurements. We use the term "high-latitude" to refer to ionosphere above the equatorward auroral boundary, which includes the auroral oval and polar cap regions. The six SuperDARN radars we use in this study are part of an array of "mid-latitude" radars, which were constructed near 50° MLAT to measure plasma drifts in both the subauroral and auroral regions of the ionosphere. In this study we thus use the term "mid-latitude" to refer to radar locations.

Polar Operational Environmental Satellites (POES): Mid-latitude SuperDARN radars measure scatter from both the subauroral and high-latitude regions due to large radars fields of view. It is necessary to know the equatorward boundary of the auroral oval in order to select for subauroral flows. In this study we use particle precipitation data from the Total Energy Detector (TED) instrument in the Space Environment Monitor (SEM) package [S. Evans and S. Greer, 2004] on board the National Oceanic and Atmospheric Administration (NOAA) Polar Operational Environmental Satellites (POES) spacecraft to estimate the equatorward auroral oval boundary. POES spacecraft operates in Sun-synchronous orbits at an altitude of ∼800 km with an orbital period of 101 min. The equatorward boundary of the auroral oval is determined by (1) identifying data from all available POES spacecraft in the Northern Hemisphere within +/- 30 minutes of a given time, (2) locating the MLAT and MLT of the equatorward precipitation boundary for each available POES spacecraft pass, and (3) fitting a circular curve to the data to determine the boundary distributed at all local

times. This method has also been used by Kunduri et al. [2017, 2018a] in their statistical characterization of the large-scale structure of the subauroral polarization stream (SAPS). Several previous studies have found that a circle is a good approximation for the shape of the night side equatorward auroral oval boundary [Holzworth and Meng, 1975; Gussenhoven et al., 1983; Hardy et al., 1989]. Figure 4.1b shows an example of identifying subauroral ionospheric scatter using electron number flux measurements from POES spacecraft. The dashed red circle shows the equatorward auroral oval boundary estimated on the basis of the satellite data and the color-coded polygons show the SuperDARN LOS velocities (blue-green indicates motion towards the radar, red-orange-yellow, away). The larger part of the backscatter is generated at latitudes extending equatorward from the oval boundary, i.e., from the subauroral region.

OMNI IMF: We have used 1-min-averaged OMNI field/plasma data sets shifted to the Earth's bow shock nose to characterize the subauroral plasma flows in terms of 8 different IMF clock angle conditions. The IMF clock angle bins are centered on 0°(IMF Bz+), 45°(IMF Bz+/By+), 90°(IMF By+), 135°(IMF Bz-/By+), 180°(IMF Bz-), etc., with 60° width each. The selection of 60° wide bins ensures sufficient statistics in all convection patterns since there are much less data in IMF Bz bins compared to IMF By bins. We have applied a bias vector filtering method proposed by Haaland et al. [2007] and used by Förster et al. [2007, 2008] to select for relatively stable IMF clock angle intervals. A bias vector is defined as the average of normalized IMF vectors within a time interval in the geocentric solar magnetospheric (GSM) Y-Z plane. The angle between the bias vector and the GSM-Z axis defines the clock angle, and its magnitude is a measure of IMF clock angle stability with 1 indicating a perfectly stable IMF clock angle for that time interval. IMF clock angle is considered to be stable if the bias vector for a certain time interval is above a certain threshold. In this study, a running 60-min interval (+50 min/-10 min around the time of

radar measurements) of the 1-min OMNI IMF is used to calculated the bias vector. Since the time resolution of OMNI IMF is 1 min, the bias vector is thus based on 60 individual normalized IMF vectors in the GSM Y-Z plane. Any 60-min interval with less than 55 IMF clock angle points is discarded. We have used a threshold of 0.85 for the bias vector magnitude and restricted its clock angle to fall within a 60° wide bin. We have tested runs with various bias vector thresholds up to 0.96 and the results were nearly the same, while the statistics for IMF Bz+ and Bz- bins become poor near dusk at latitudes <55°. We think the 60-min time window should be sufficient while taking into account uncertainties in the solar wind propagation in the magnetosheath and an additional ∼10 min needed to set up the global plasma convection [Ridley et al., 1998].

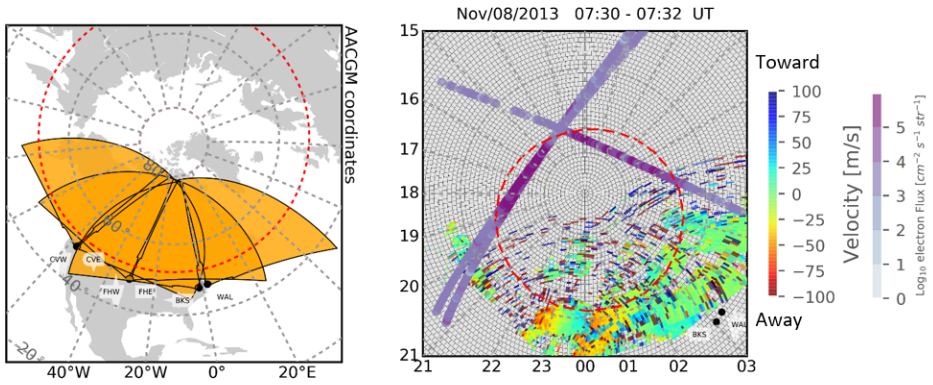

Figure 4.1: Radar fields of views and an example of identifying subauroral ionospheric scatter using electron number flux measurements from POES spacecraft. The two panels are: (a) fields of view of the six North American mid-latitude SuperDARN radars used in this study displayed in AACGM coordinate (from west to east): Christmas Valley West (CVW), Christmas Valley East (CVE) (Oregon), Fort Hays West (FHW), Fort Hays East (FHE) (Kansas), Blackstone (BKS), and Wallops Island (WAL) (Virginia). The dotted red circle indicates the 52° magnetic latitude, and (b) SuperDARN LOS data for 07:30 - 0732 UT on November 08th, 2013 and close POES satellite passes in time. The red circle shows the estimated equatorward boundary of the auroral oval.

4.2.2 Data Processing

The SuperDARN radars observe backscatter primarily from plasma density irregularities in the ionosphere at E and F region heights (ionospheric scatter), reflections from the meteor trails in the lower E region (meteor scatter), and from the Earth's surface after reflection from the ionosphere (ground scatter). The data selection starts by first identifying subauroral ionospheric scatter, which is primarily confined to local night [Greenwald et al., 2006]. This step is essential because the traditional method of distinguishing between scatter types in SuperDARN data was developed for high latitudes and depends solely on the Doppler velocity and Doppler spectral width of each data point. We have used the classification algorithm of Ribeiro et al. [2011], which was specifically developed to identify ionospheric scatter events in the nightside subauroral region with high confidence. The algorithm analyzes the data by looking at a long time series of data and identifies clusters of backscatter on the basis of temporal and spatial characteristics of the velocity distribution. It then classifies a cluster as either an "event" (ionospheric scatter) or a "nonevent" (ground scatter) based on empirical thresholds imposed on the velocity profile and duration of that cluster. It discards clusters with duration of less than 1 hr, which may potentially introduce some bias to our results in favor of long-lived events. (A previous study by de Larquier et al. [2013] demonstrated that the most likely source region of this type of quiet-time nightside subauroral ionospheric scatter is the bottom-side F region between 220 and 320 km altitude.) Finally, we selected for the SuperDARN measurements located equatorward of the estimated equatorward boundary of the auroral oval (Figure 4.1b). Data for time intervals that do not have good estimates of the boundary are discarded, which consists of ∼35% of all time intervals (We have examined that including the discarded data has negligible effect on the distribution of line-of-sight measurements in the region of interest). The remaining LOS vectors are then binned into 10° azimuth bins within each 1° MLAT × 7 min MLT grid cell in AACGM coordinates. The

median vector in each azimuth bin at 10-min UT step is extracted as representative of that time and azimuth. Most grid cells between 20 and 4 MLT have at least 1,000 ten-minute median vectors when sorted by month or Kp and at least 300 ten-minute median vectors when sorted by the IMF clock angle. Grid cells that contains less than 100 measurements are discarded. 2-D convection vectors are derived by performing a fitting of the variation of LOS velocity with viewing angle within individual MLAT-MLT bins (see Figure 2 in [Maimaiti et al., 2018] for details).

4.3 Results

In this section we present subauroral flow patterns characterized by month, season, Kp, and IMF clock angle.

4.3.1 Monthly Dependency

Maimaiti et al. [2018] examined the seasonal dependencies of quiet-time subauroral convection using two years of data. Here we examine its monthly variation.

Figure 4.2 shows the monthly variation of the two-dimensional subauroral convection vectors under Kp $\leq$ 2+ conditions calculated for the region between 52° and 60° magnetic latitudes. The three columns, from left to right, are the results for winter, equinoctial and summer months, respectively. These vectors have been produced by performing the LOS azimuth fitting analysis for every MLAT/MLT grid cell. The coverage is limited to the nightside by the availability of subauroral ionospheric backscatter which is largely confined to the hours of darkness [Ribeiro et al., 2012]. The flows shown in Figure 4.2 exhibit significant monthly variation with the flows being the strongest in December and January, i.e., in midwinter.

The month-to-month variability is largest in the winter season and smallest in the summer. In all months, however, the flows are predominantly westward during the night and become more meridional near dawn and dusk.

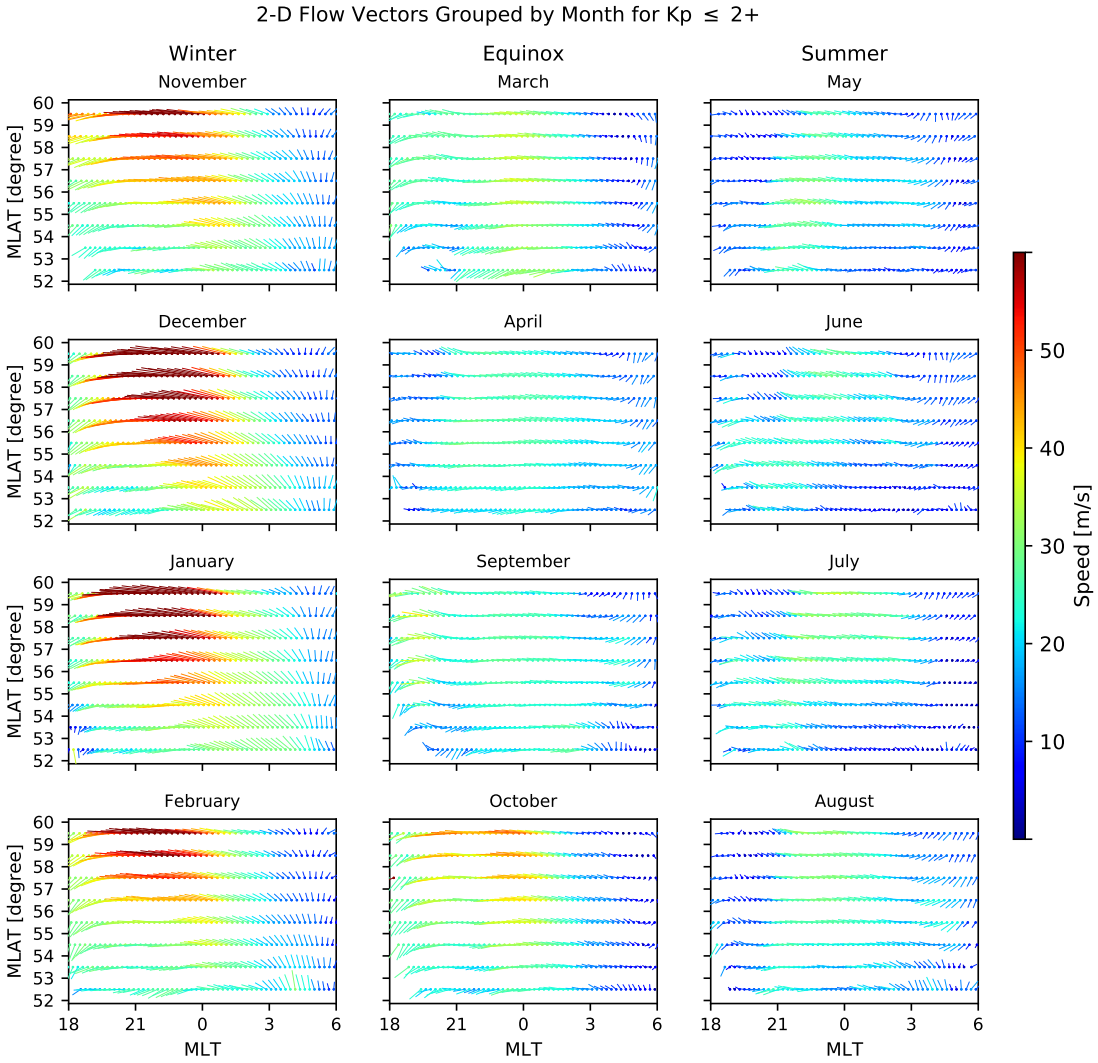

Figure 4.2: Two-dimensional subauroral convection vectors calculated for the region between 52° and 60° magnetic latitude centered at zero magnetic local time. The 12 panels show the results sorted by month during quiet geomagnetic conditions (Kp $\leq$ 2+). The three columns refer to winter months (left) , equinox (middle), and summer (right)

.

Now we examine the zonal and meridional components of the 2-D flows presented in Figure 4.2. Figure 4.3 shows the fitted zonal (positive eastward) velocities versus MLT with color

coding by MLAT. Similar to Figure 4.2, the columns of Figure 4.3 correspond to winter, equinox, and summer. It can be seen from Figure 4.3 that the variation of zonal flow is pronounced across seasons. The zonal flow in winter months is the strongest with a dependence on MLT such that it is minimum near dawn and dusk and reaches its maximum magnitude between 22 - 24 MLT. There is also a month-to-month variation within seasons that is most pronounced in winter. However, the most striking feature is the monthly dependence of the latitudinal variation in the premidnight zonal flow such that the velocity magnitude increases with latitude between 18 and 2 MLT. The latitudinal variation emerges in October, is most pronounced in December and disappears in March. In the summer months of May - August, there is a noticeable latitudinal variation of the opposite sense in the premidnight zonal flow, i.e., velocity decreases with latitude mainly between 18 and 22 MLT. The latitudinal variation of zonal flow was also reported by Maimaiti et al. [2018], but only crudely characterized at the seasonal level. Figure 3 elaborates the month by month evolution of this feature. We will further discuss the characteristics of its monthly variation in section 4.

Figure 4.4 shows the fitted meridional (positive northward) velocities versus MLT with color coding by MLAT, in the same format as Figure 4.3 (Note that the y-axis scale here is different from that in Figure 4.3). It can be seen from Figure 4.4 that the variation of meridional flow is also pronounced across seasons. The winter meridional flow shows strong variations with MLT such that the magnitude varies from 20 m/s equatorward at dusk to 20 m/s poleward at dawn, transitioning from equatorward to poleward between 21 and 24 MLT. A similar transition has also been reported in [Buonsanto et al., 1993; Scherliess et al., 2001] for winter using other techniques. The meridional flow between March and September is no more than a few meters per second throughout the night between 21 - 3 MLT but becomes significantly southward ($\sim$ 15 m/s, less so in May - July) toward dawn and dusk. In contrast

to the zonal flow component, the meridional flow does not show large latitudinal variations. It is generally uniform across all latitudes and, other than winter months, it has very little variation with MLT across the main part of nightside.

In summary, the subauroral flows are predominantly westward in all months and become meridional near dawn and dusk. Both zonal and meridional flows exhibit strong monthly dependencies with the strongest flows in December and January. There is a pronounced latitudinal gradient in the premidnight zonal flows in the winter months (November to February), which emerges in October and disappears in March. A latitudinal gradient opposite to that of winter emerges in May and lasts until August.

4.3.2 Kp Dependencies

Now we examine the Kp dependence of the subauroral flows by sorting the data according to Kp values of 0, 1, 2, and 3 separately for the winter, summer, and equinoctial seasons. Each Kp bin includes the adjacent intermediate +/- values. For example, the Kp=2 bin includes 2-, 2, and 2+.

Figure 4.5 shows the two-dimensional convection vectors calculated for the region between 52° and 60° magnetic latitudes under various Kp conditions. The 4 rows, from top to bottom, respectively, show the results for Kp = 0, 1, 2, and 3. The 3 columns, from left to right, respectively, show the results for winter, equinox, and summer. It can be seen from Figure 4.5 that a Kp dependency is noticeable in all seasons but is most pronounced in winter. Except for MLT $<$ 21 in summer, the premidnight westward flow enhances with increasing Kp. Figure 4.6 shows the corresponding fitted zonal (positive eastward) velocities versus MLT with color coding by MLAT (Note that the scale in y-axis here is different from that in Figure 4.3). As Kp increases, the enhancement of premidnight westward zonal flow is apparent in

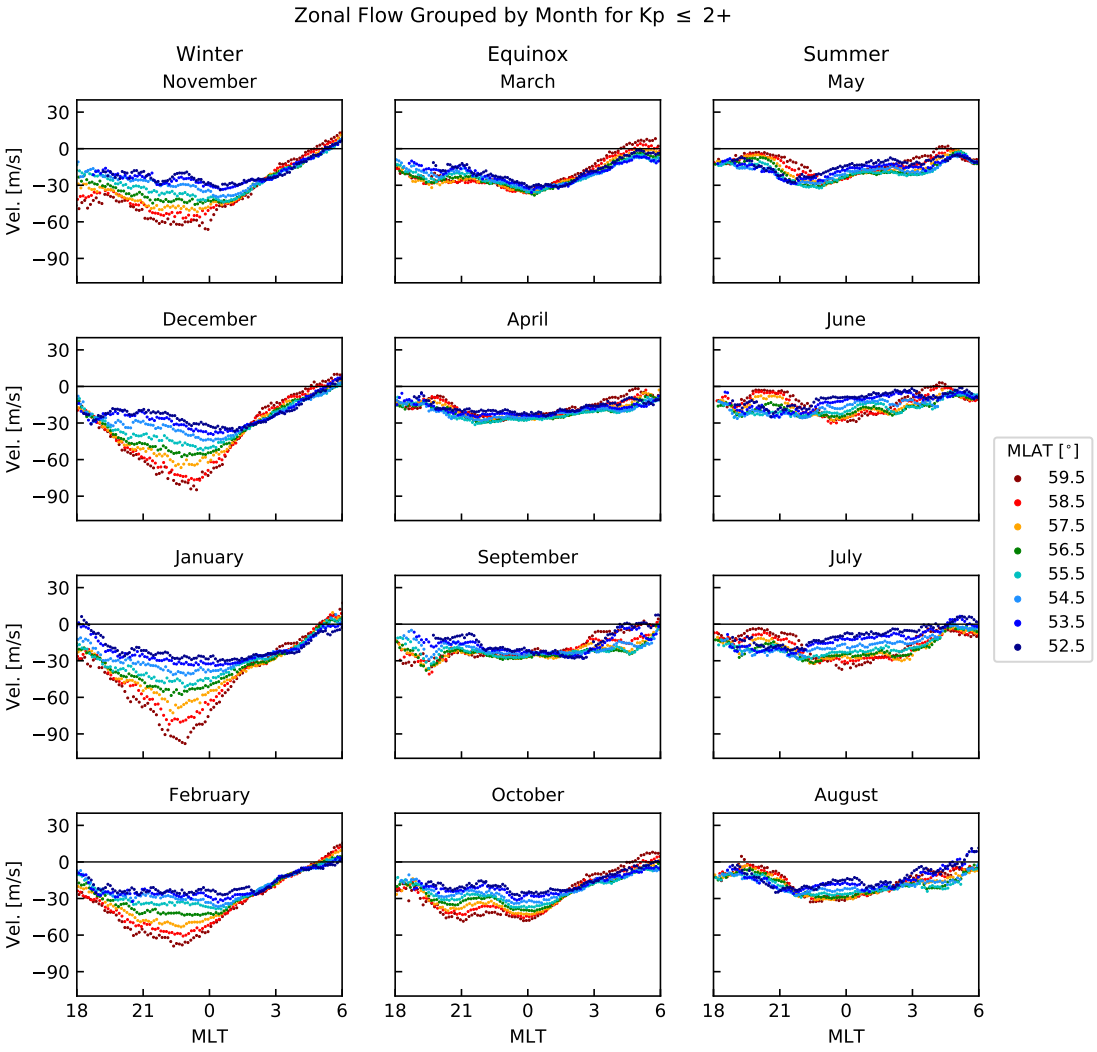

Figure 4.3: Fitted zonal velocities (positive eastward) by magnetic latitude versus magnetic local time for each of the 12 months.

all seasons but is most significant in winter. An eastward flow emerges after ∼2 MLT in all seasons when Kp reaches 3. An interesting feature to note here is that, for a given Kp, the location of the maximum zonal speed in winter shifts towards earlier MLTs with increasing magnetic latitude. For example, for Kp = 2 the location of the maximum zonal speed at MLAT=52.5° is ∼0.5 MLT, which moves to ∼23 MLT for MLAT=59.5°. Figure 4.7 shows the meridional (positive northward) velocities in the same format as Figure 4.6 but with

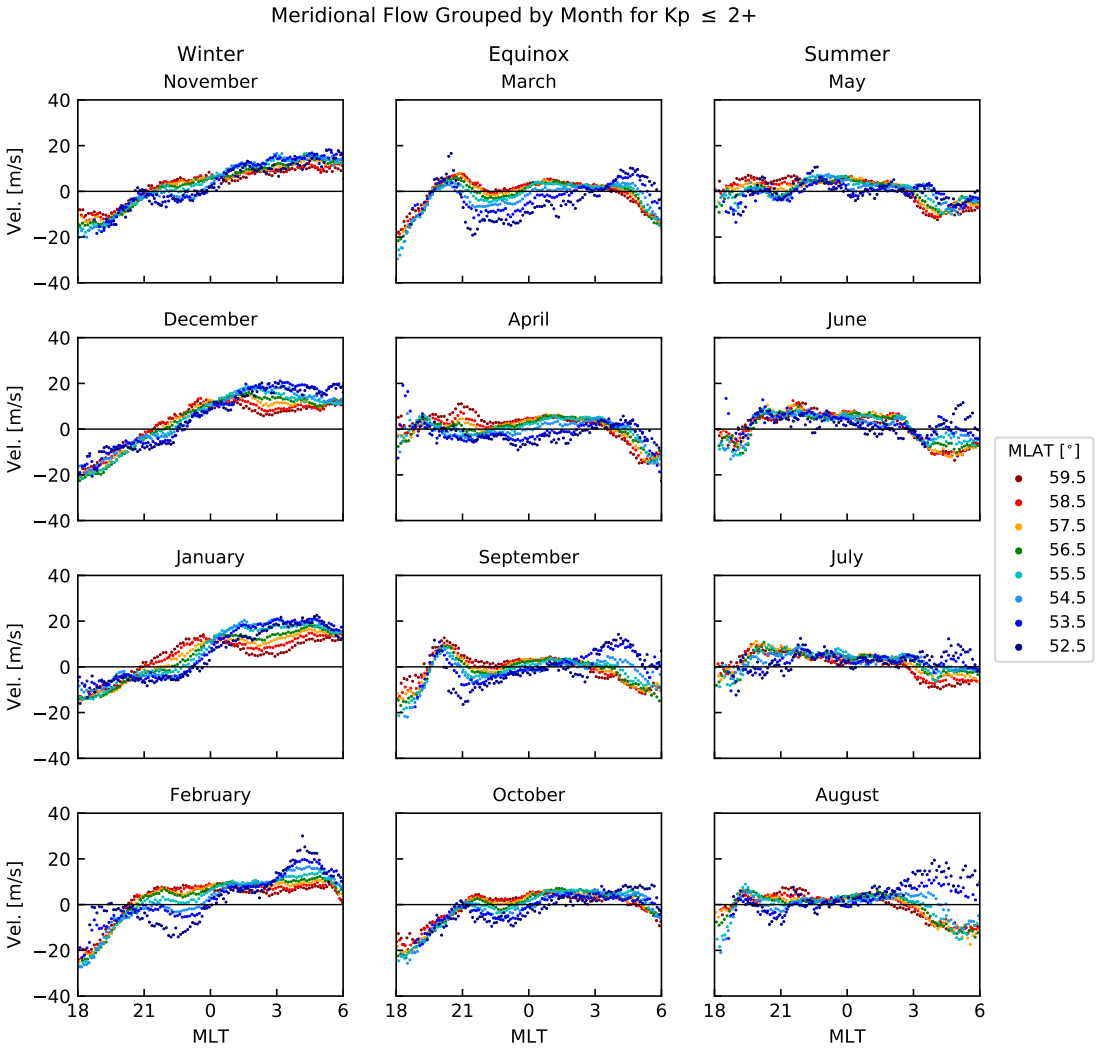

Figure 4.4: The same as in Figure 4.3 but for meridional velocities (positive northward). Note that the y-axis scale here is different from that in Figure 4.3

a different y-axis scale. In contrast to the zonal flow, increased magnetic activity leads to smaller magnitudes both in the premidnight equatorward flow and post-midnight poleward flow in winter but has little effect in equinox and summer (except for the noticeable increase in the premidnight poleward and post-midnight equatorward flow magnitudes in summer when Kp reaches 3).

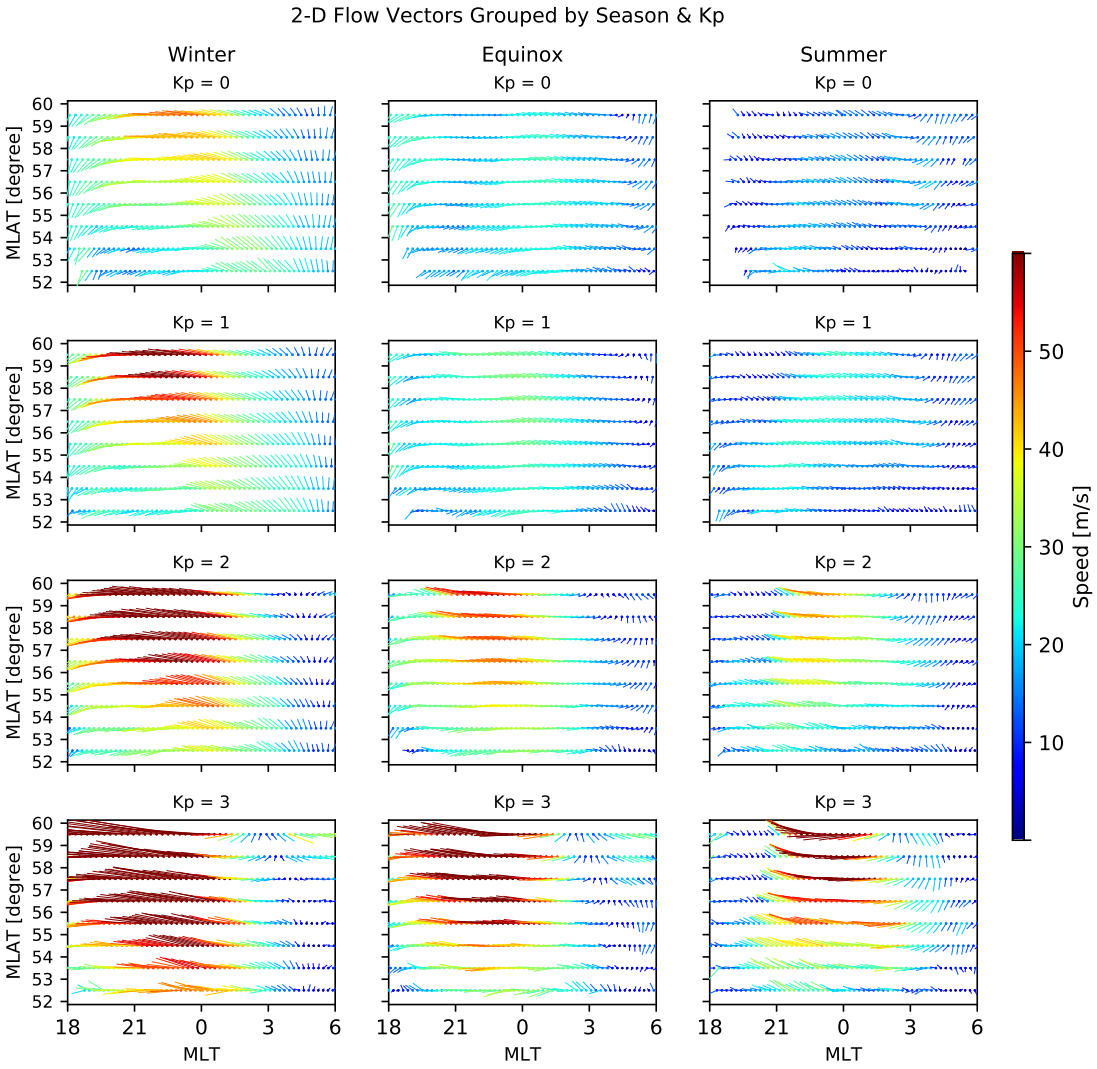

Figure 4.5: Two-dimensional subauroral convection vectors calculated for the region between 52° and 60° magnetic latitude centered at zero magnetic local time. The 4 rows, from top to bottom, are the results for Kp = 0, 1, 2, and 3, respectively. The 3 columns, from left to right, are the results for winter, equinox, and summer, respectively

4.3.3 IMF Clock Angle Dependency

The high-latitude convection is well organized by the IMF, which is not generally thought to be the case for the subauroral flows. The influence of IMF Bz on the subauroral flows was presented by Maimaiti et al. [2018] as a preliminary result and the authors concluded

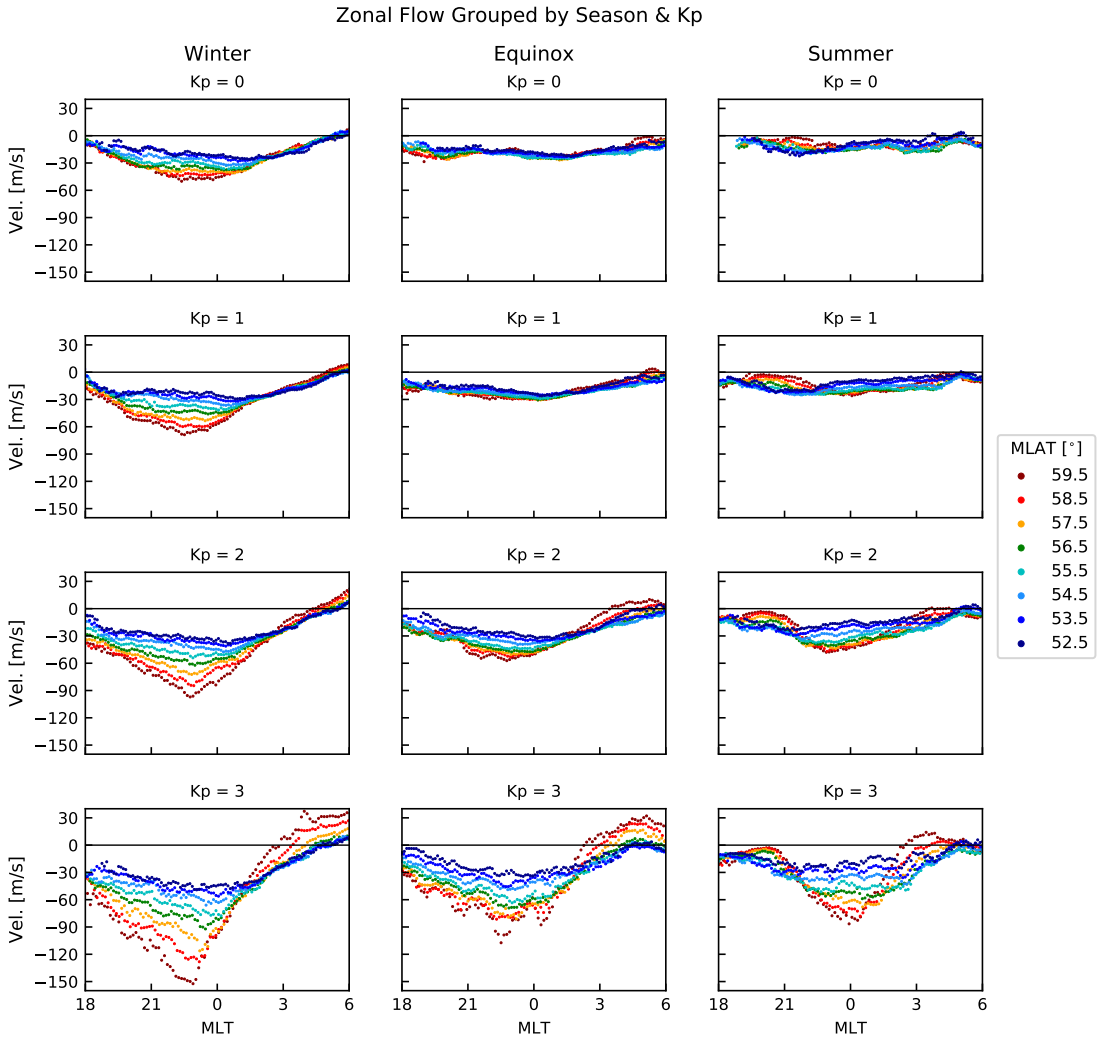

Figure 4.6: Fitted zonal velocities (positive eastward) by magnetic latitude versus magnetic local time. The 4 rows, from top to bottom, are the results for Kp = 0, 1, 2, and 3, respectively. The 3 columns, from left to right, are the results for winter, equinox, and summer, respectively. Note that the scale in y-axis is different from that in Figure 4.3.

that the IMF is an important factor. Here we show an expanded analysis of the IMF factor in the subauroral flow pattern in winter under quiet (Kp $\leq$ 2+) conditions. IMF influence also exists in summer and equinox but not as prominent as in winter (See Figures A.2-A.10 in Appendix A).

Figure 4.8 shows the two-dimensional quiet-time (Kp $\leq$ 2+) convection vectors in winter

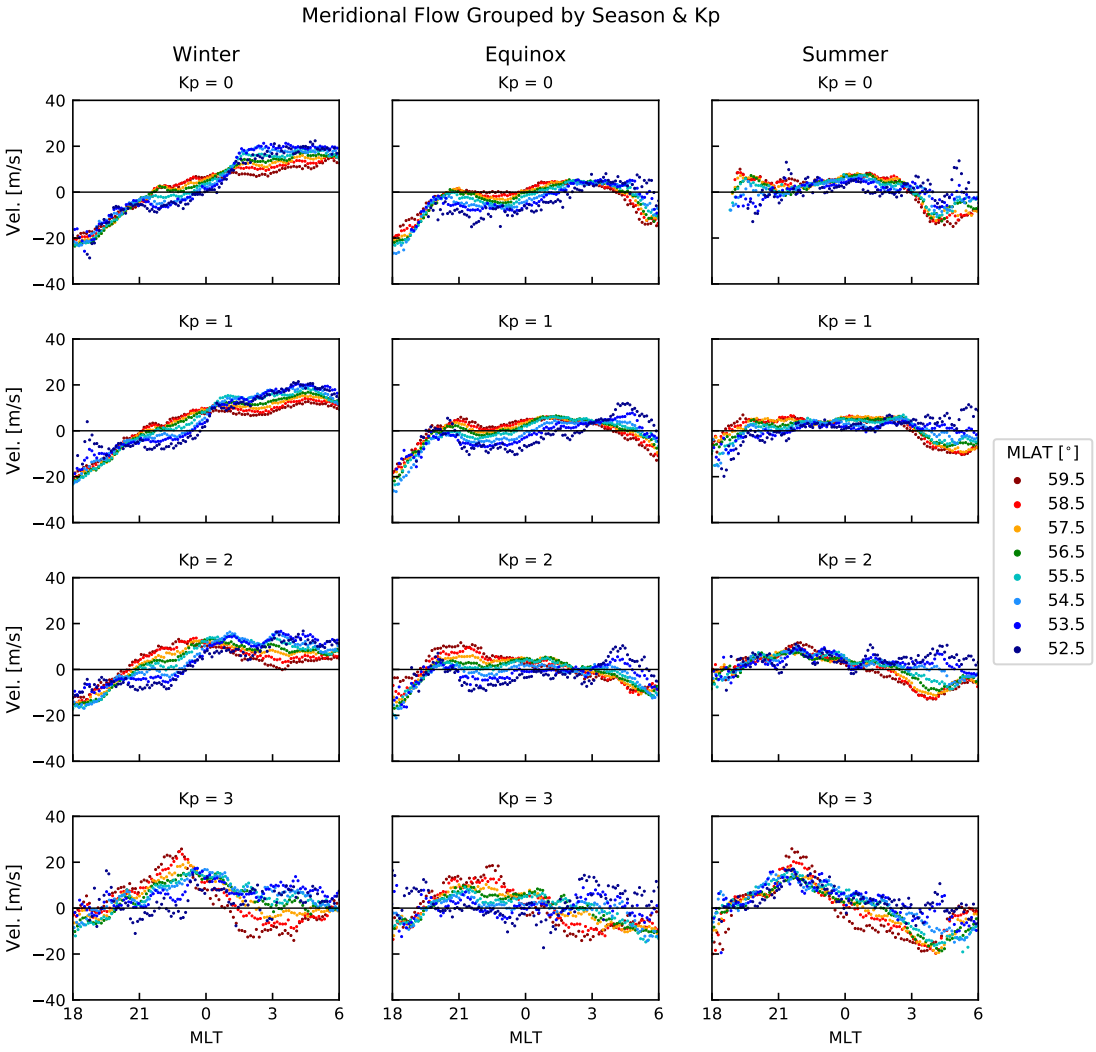

Figure 4.7: The same as in Figure 4.6 but for meridional velocities (positive northward). Note that the y-axis scale here is different from that in Figure 4.6.

months (November - February) calculated for the region between 52° and 60° magnetic latitudes under 8 IMF clock angle conditions as described in Section 4.2. (The corresponding IMF clock angle histograms are provided in Appendix A as Figure A.1.) It can be seen from Figure 4.8 that the influence of the IMF clock angle is very pronounced in winter. The pre-midnight flows are weakest under IMF Bz+ (upper-center), similar to what is seen under low Kp conditions in Figure 4.5, and gradually intensify when IMF clock angle rotates

clockwise and reaches maximum under IMF Bz- (lower-center) conditions, similar to the situation under higher Kp conditions. It then gradually weakens until the IMF turns purely northward. The trend for the post-midnight flows, however, is the opposite, where stronger meridional flows are seen for northward IMF compared to southward IMF, also consistent with the winter Kp dependence seen in Figure 4.7. Figure 4.9 shows the corresponding fitted zonal (positive eastward) velocities versus MLT with color coding by MLAT. The zonal flow is predominantly westward under IMF Bz+ but an eastward flow emerges after 2.5 MLT at higher latitudes when IMF is purely southward. The maximum zonal flow magnitude at MLAT=59.5° for IMF Bz+ is ∼60 m/s near 0 MLT but reaches 140 m/s and shifts to ∼22 MLT for IMF Bz-. The latitudinal dispersion in the pre-midnight zonal flow weakens for IMF Bz+ and intensifies for IMF Bz-. An IMF By influence is also present such that the latitudinal dispersion disappears near 1 MLT for IMF By+ (middle-right) but is delayed until after 2 MLT for IMF By- (middle-left). This is indicative of a dusk convection cell extending further across midnight for IMF By- than By+ during northern winter [Reistad et al., 2018]. Figure 4.10 shows the fitted meridional (positive northward) velocities in the same format as in Figure 4.9 but with a different scale in y-axis. In contrast to the zonal flow in Figure 4.9, the pre-midnight meridional flow is less influenced by the IMF clock angle compared to the post-midnight meridional flow. In pre-midnight, the meridional flow is ∼ -20 m/s at 18 MLT and gradually turns poleward at ∼ 21 MLT under all IMF clock angle conditions. In post-midnight, however, the poleward meridional flow at higher latitudes is suppressed from ∼ 20 m/s for IMF Bz+ to near 0 m/s for IMF Bz-. Unlike the zonal flow, the latitudinal dispersion in meridional flow is weak pre-midnight and is not significantly affected by IMF clock angle. But a small IMF By influence is present in the post-midnight meridional flow such that the latitudinal dispersion is weaker for IMF By+ than for IMF By-. The implication of the IMF clock angle influence on the subauroral plasma flow will be discussed in the Discussion Section.

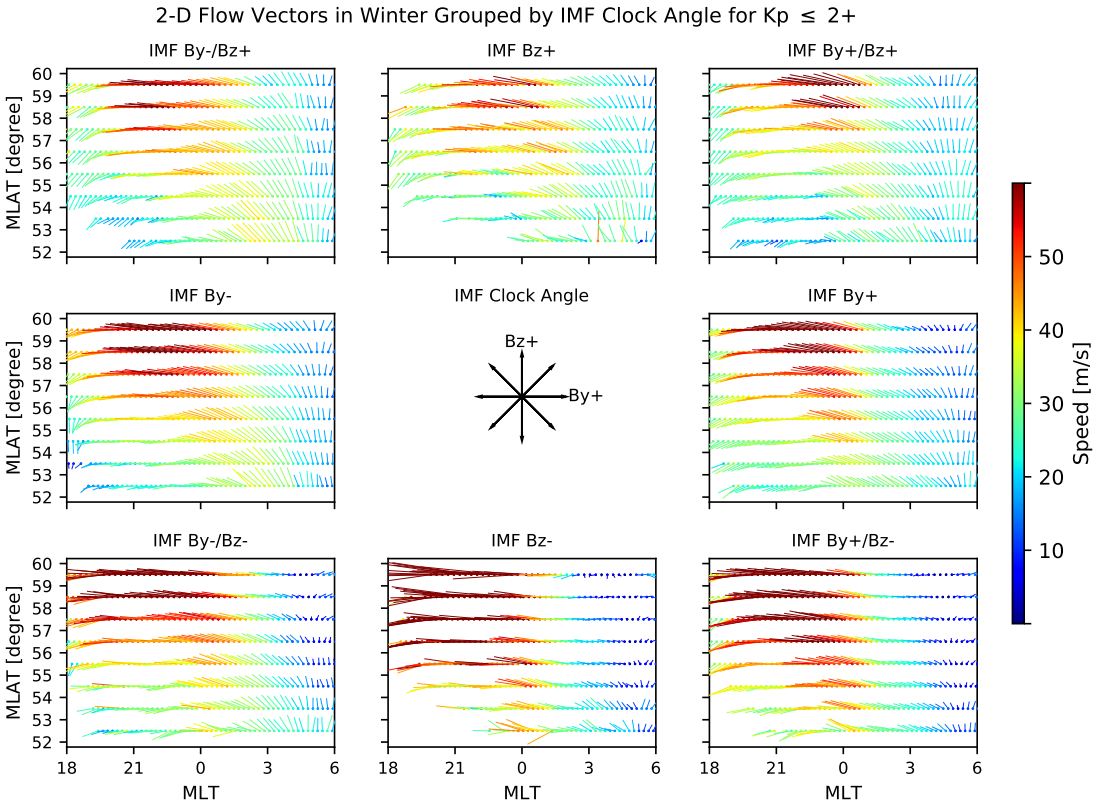

Figure 4.8: Two-dimensional quiet-time (Kp $\leq$ 2+) subauroral convection patterns calculated for winter under 8 different IMF clock angle conditions for the region between 52° and 60° magnetic latitudes.

4.4 Discussion

In this study we have used seven years of SuperDARN line-of-sight measurements to derive statistical patterns of the nightside subauroral plasma convection under quiet (Kp $\leq$ 2+) to moderately disturbed (Kp = 3) conditions over the latitude interval 52° to 60° MLAT. These climatological patterns are organized by month, season, Kp, and the IMF clock angle. Figures 4.2-4.4 show that monthly variation in the subauroral flow is pronounced across seasons. Figures 4.5-4.7 show that the Kp dependency is also noticeable in all seasons but is most pronounced in winter, while Figures 4.8-4.10 show that the IMF influence is prominent in the subauroral flows even under quiet Kp $\leq$ 2+ conditions. The improved latitudinal

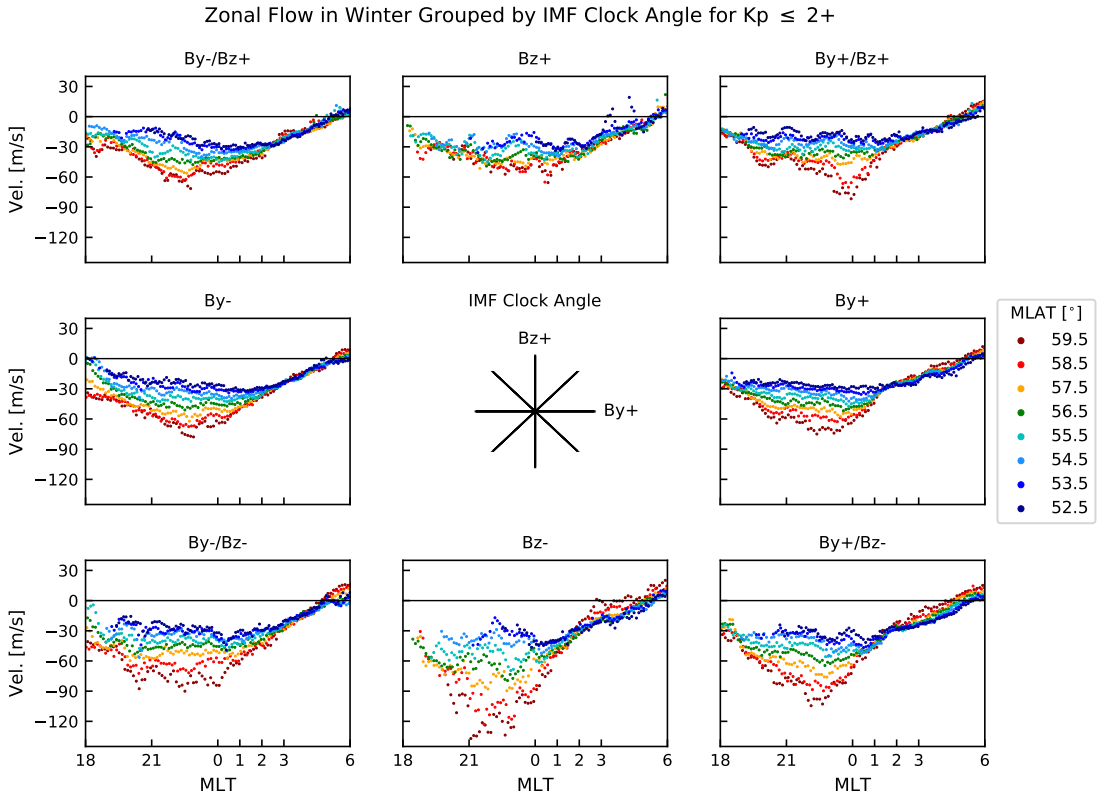

Figure 4.9: Fitted zonal velocities (positive eastward) by magnetic latitude versus MLT for 8 IMF clock angle bins. Note that extra tick marks were placed at every 1 hour between 3 - 6 MLT to aid in comparing the distinct IMF By influence on subauroral zonal flows.

coverage provided by SuperDARN compared to ISR measurements reveals interesting new features, such as a significant latitudinal variation in zonal flow velocity between 18 and 2 MLT in winter, which enhances under IMF Bz- and for higher Kp conditions. The latitudinal variation in zonal flow was first pointed out by Maimaiti et al. [2018] but not discussed in detail. In this section, we compare the results with other statistical models from comparable studies, quantitatively characterize the monthly variation of the latitudinal variation in the premidnight zonal flow, and discuss certain prominent features in light of the possible mechanisms for driving subauroral convection.

First we compare the Kp dependency of subauroral plasma flows derived here with other

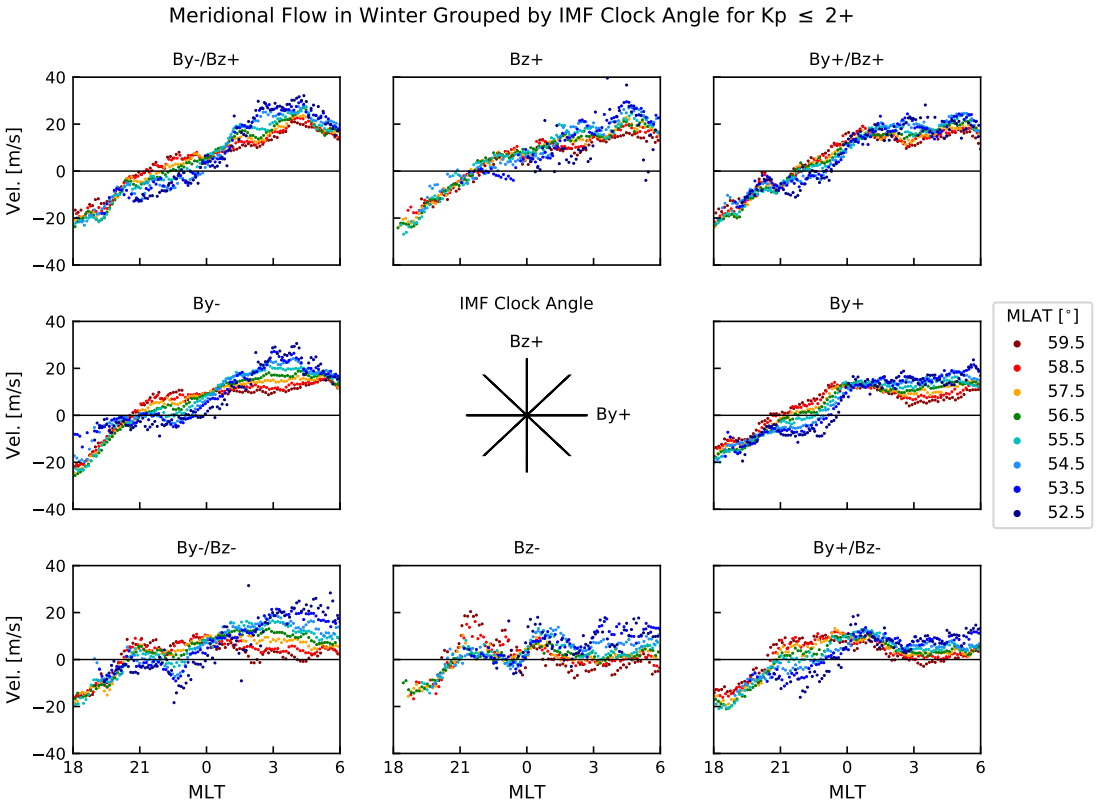

Figure 4.10: The same as in Figure 4.9 but for meridional velocities (positive northward). Note that the y-axis scale here is different from that in Figure 4.9

.

statistical models of subauroral convection from comparable Millstone Hill radar and satellite studies. Figure 4.6 shows that, as Kp reaches 3, the premidnight westward flow enhances and a post-midnight eastward flow emerges. This is consistent with comparisons between yearly averaged quiet (Kp $\leq$ 2) and relatively disturbed (Kp $\geq$ 3) times reported in previous Millstone Hill radar studies [e.g. Wand and Evans, 1981b; Buonsanto et al., 1993; Heelis and Coley, 1992], and with the Kp-dependent empirical model results reported in [Wand and Evans, 1981a]. Recently, Lejosne and Mozer [2018] studied the correlation between Kp and the electric drift measurements from the Van Allen probes and found that at L=3 (MLAT=55°) in the magnetosphere the zonal flow becomes increasingly westward in the nightside sector with increase in Kp, which lasts until ∼1 MLT and then decreases in

magnitude (see Figure 2b in [Lejosne and Mozer, 2018]). Although their results are yearly averaged, the trend is qualitatively consistent with the zonal flow at MLAT=55.5° depicted in Figure 4.6 for all seasons in the conjugate ionosphere. Figure 4.7 shows that increased magnetic activity leads to smaller magnitudes in both the premidnight equatorward flow and post-midnight poleward flow in winter. There is a noticeable increase in the premidnight poleward and post-midnight equatorward flow magnitudes in summer when Kp reaches 3. Lejosne and Mozer [2018] found that, as Kp increases, the electric drift for L = 2.5 - 3 (MLAT=51° - 55°) becomes progressively more outward (poleward) in the premidnight sector and inward (equatorward) in the post-midnight sector. Note that their results are yearly averaged and there are large variations in the correlation for meridional flows, but still the trend is consistent with the winter and summer meridional flows in Figure 4.7. The Kp dependence in winter meridional flow shown in Figure 4.7 is qualitatively consistent with model results reported in [Wand and Evans, 1981b,a; Buonsanto et al., 1993], but the meridional flow direction for Kp = 0 reported in [Wand and Evans, 1981b,a] is somewhat opposite to our observations, which could be partially due to the paucity of useful measurements between midnight and 6 MLT as mentioned in their paper. Note that meridional flow components reported in previous studies do not agree with each other (see Figure 7 in [Maimaiti et al., 2018] for comparisons between different statistical models).

Maimaiti et al. [2018] reported a significant latitudinal variation of zonal flow velocity near midnight in winter and a weaker variation in summer (but in opposite sense). This feature is elaborated on a monthly basis in Figure 4.3 which shows that the pronounced latitudinal gradient in the premidnight zonal plasma flow in the winter months (November to February) emerges in October and disappears in March. A noticeable latitudinal gradient opposite to that of winter emerges in May and lasts until August. Here we quantitatively characterize this feature by examining the monthly variation of the peak velocity gradient in the

premidnight zonal flow shown in Figure 4.3, where the velocity gradient is defined as the difference between the zonal velocities at 59.5° and 52.5° MLAT. Figure 4.11 shows the peak velocity gradient versus month (red line) and the corresponding MLT location (black line). We can see that there is a clear asymmetry in the monthly variation of the peak velocity gradient centered at January. That is, the velocity gradient is at its minimum value of ∼-70 m/s in January and quickly turns positive in April. It stays at ∼15 m/s until August and then gradually decreases to the minimum values of ∼-70 m/s in January. There is also an interesting pattern in the monthly variation of the corresponding MLT location. The peak velocity gradient in the winter months (November to February) occurs at around ∼23 MLT and moves to earlier MLTs by ∼1.5 - 3 hours in the equinoctial and summer months. This monthly variation of the velocity gradient in the premidnight zonal plasma flow could be a result of the monthly variation in ionospheric conductivity modulating the two driving mechanisms (i.e. neutral wind dynamo and penetration electric fields), which we will discuss next. This intriguing feature in the premidnight zonal convection could be a useful benchmark for modeling studies of conductivity effect on subauroral plasma convection.

Now we discuss subauroral flow features in light of the possible mechanisms for driving subauroral convection. Figures 4.2-4.3 show the quiet-time subauroral zonal flows are predominantly westward throughout the night in all months. By contrast, Xiong et al. [2015], using the CHAllenging Minisatellite Payload (CHAMP) satellites data, found that the average subauroral quiet-time (Kp < 2) zonal wind is generally directed eastward from postnoon to early morning and westward for the other local times maximizing near dawn. The two flows have little similarity during the premidnight hours, but have the same westward components during the post-midnight hours. However, the two flows again decouple from each other toward dawn with the plasma flow becoming increasingly meridional (Figures 4.3-4.4) while the neutral wind being predominately westward [Drob et al., 2015]. This seems to sug-

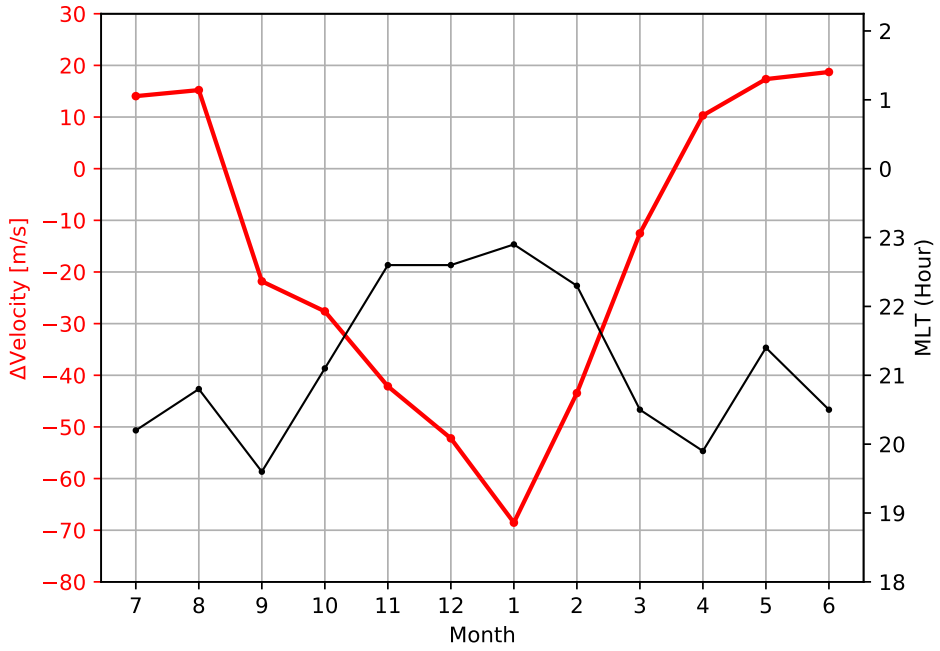

Figure 4.11: Monthly variation of the peak velocity gradient (red) in the premidnight zonal plasma flow shown in Figure 4.3 and its corresponding MLT location (black). The velocity gradient is defined as the difference between the zonal velocities at 59.5° and 52.5° MLAT.

gests that the local F region dynamo may account for some portion of the westward plasma motion in the post-midnight sector but not in the premidnight sector. Previous studies [e.g. Buonsanto et al., 1993; Maimaiti et al., 2018] also found very little similarity during the premidnight hours, with the plasma flows predominantly westward while the neutral wind is directed eastward and southward ([Emmert et al., 2003, 2006]).

Figures 4.5-4.6 show that the premidnight westward flow intensifies with increasing Kp in all seasons. The zonal flow at MLAT $\geq 57°$ turns eastward after ∼2 MLT when Kp = 3. Xiong et al. [2015] reported that under moderate disturbances (2 < Kp < 4) eastward enhancement of zonal winds appear near dawn at subauroral latitudes while westward disturbance zonal neutral winds dominate at subauroral latitudes from noon to midnight. Förster et al. [2008], in their study on IMF dependence of high-latitude thermospheric wind pattern using the CHAMP satellites data during the geomagnetically active year of 2003, observed a large

clockwise thermospheric neutral wind pattern in the dusk region extending to subauroral latitudes and a smaller anticlockwise circulation in the dawn region. The authors explained their observations as the result of both centrifugal and Coriolis forces acting on the wind in the same direction as ion-drag in the dusk region but in the opposite direction in the dawn region. Equatorward expansion of these two-cell neutral wind patterns due to increased geomagnatic activities could cause eastward enhancement of zonal winds near dawn and westward disturbance zonal neutral winds at subauroral latitudes as reported by Xiong et al. [2015]. Thus, the premidnight enhancement of westward plasma flow with increasing Kp seems to suggest that the disturbance dynamo may account for some portion of the disturbed westward subauroral flows in the premidnight sector. This is because a predominantly northward electric field (westward drift) can be generated at subauroral to equatorial latitudes by the disturbance dynamo due to the equatorward thermospheric wind gaining westward momentum by the Coriolis force [Blanc and Richmond, 1980; Fuller-Rowell et al., 2002; Fejer et al., 2017]. In the post-midnight sector, the eastward enhancement of zonal winds near dawn at subauroral latitudes reported by Xiong et al. [2015] may also play a role in the emergence of eastward plasma flows after $\sim$2 MLT for Kp = 3 shown in Figure 4.6. However, the total zonal wind, although reduced in magnitude, remains westward near dawn under moderate disturbances ($2 < \text{Kp} < 4$) as shown in [Xiong et al., 2015] Figure 4. This suggests that the disturbance dynamo can not fully explain the disturbance in zonal plasma flows under Kp = 3 conditions. Lejosne and Mozer [2018], using the Van Allen Probes measurements, also found that an increase in Kp leads to a decrease in the azimuthal drift (i.e. an increase in the westward drift magnitude), especially on the nightside. The authors attributed their finding to the ionospheric disturbance dynamo.

Next, we consider the extent to which penetration of high-latitude convection electric fields might be manifested in the subauroral convection. If penetration dominates under geomag-

netically quiet conditions, we would expect to see a roughly symmetric MLT distribution of subauroral zonal flow with westward flow premidnight and eastward flow post-midnight. As shown in Figure 4.3, however, the quiet-time subauroral flow is westward throughout the night in all months. This indicates that penetration may account for the flows premidnight, where the zonal wind during magnetically quiet periods (Kp $<$ 2) is eastward (see Figure 1 in [Xiong et al., 2015]), but most likely cannot explain the flows post-midnight. Figures 4.8-4.10 show that the IMF influence is prominent in the subauroral flows even under quiet (Kp $\leq$ 2+) conditions. The premidnight zonal flows are strongest in magnitude under IMF Bz- and weakest under Bz+. Eastward flows emerge after 2.5 MLT at higher latitudes when IMF Bz is negative (Figure 4.9). The poleward meridional flow post-midnight is suppressed to very low values for IMF Bz- and even becomes slightly equatorward at higher latitudes (Figure 4.10), suggesting an equatorward expansion of the high-latitude dusk cell. Thus, the observed subauroral convection under IMF Bz- exhibits some of the gross characteristics of the high latitude convection (i.e. westward flow premidnight and eastward flow post-midnight, and equatorward expansion of high-latitude convection patterns). This could be due to some direct effect of the penetration electric fields on subauroral convection because the penetration/leakage could continue for a few tens of minutes [Senior and Blanc, 1984] up to several hours [Kelley et al., 2003; Huang et al., 2007; Maruyama et al., 2007] before the inner edge of the plasma sheet re-establishes shielding. That is, the penetration electric field could still be the dominant driver during the 60-minute stable IMF Bz- time intervals (+50 min/-10 min around the time of radar measurements) analyzed in this study. However, the disturbance dynamo could also play a role here as we have discussed above because IMF Bz- is often associated with higher Kp. This presents a challenge that when examining the driving influences of subauroral convection under steady-state conditions, as was the focus of this study, the continuation of penetration/leakage makes it difficult to distinguish penetration electric field and disturbance dynamo effects because both processes

can exist simultaneously with similar plasma flow signatures. Further study on the response of subauroral flows to sudden IMF Bz southward/northward turning preceded by sustained IMF Bz+/IMF Bz- under quiet conditions could help separate the two mechanisms and also quantify the lasting effect of other transient phenomena such as over-shielding (i.e., the opposite of under-shielding) on steady-state subauroral convection. Another interesting feature is the signature of high-latitude dusk convection cell further extending across midnight for IMF By- than By+ during northern winter ([Reistad et al., 2018]) is also present at subauroral zonal flows as shown in Figure 4.9. Thus, the emergence of the IMF By dependence in subauroral convection provides additional evidence that the penetration of high-latitude convection electric field is a significant factor. The presence of penetration electric fields under quiet-time conditions has been suggested in previous studies [e.g., Carpenter and Kirchhoff, 1975; Wand and Evans, 1981a; Heelis and Coley, 1992; Lejosne and Mozer, 2016].

The dependence of F-region neutral wind dynamo on ionospheric conductivity is another factor that needs to be considered. One of the critical parameters in determining the importance of F-region polarization fields is the ratio of F and E region height-integrated Pedersen conductivities denoted as γ [Harper and Walker, 1977]. A low γ prevents the full buildup of F region polarization electric fields as they are shorted out by the E region conductivity [Rishbeth, 1971]. The fact that the premidnight subauroral flow is westward while the neutral wind is eastward during very low geomagnetic activity (Kp < 2) [Xiong et al., 2015] suggests that F region polarization electric fields due to the winds are partially shorted out by the E region or conjugate hemisphere due to a low γ. In the post-midnight sector, however, Fejer [1993] noted that, at Arecibo, the descent of the F-region after midnight and the decay of the E-region through the night causes an increase in the ratio γ and consequently leads to stronger coupling between the F region neutral wind and plasma drifts. Assuming that a similar situation holds in the post-midnight sector at subauroral latitudes, a higher γ

in the post-midnight sector is one explanation for the better coupling between the F region neutral wind and the plasma drifts as implied by the zonal drifts and the neutral winds both having the westward components.

Now we consider the effect of the ionospheric conductivity on shielding. One of the most striking features in Figure 4.3 is the significant latitudinal variation observed between 18 - 2 MLT in the winter months of October-February (with increasing flow magnitude towards higher latitude between 52° - 60° MLAT). The latitudinal variation disappears in March and reappears between 19 - 22 MLT during May - August but with the opposite sense (with decreasing flow magnitude towards higher latitude between 52° - 60° MLAT). The monthly variation of this feature is quantitatively characterized in Figure 4.11. The latitudinal variation could be a result of penetration being modulated by seasonal variations in ionospheric conductivity. Under steady solar wind and IMF conditions, the inner magnetosphere is shielded from the effects of the magnetospheric convection electric field by charge buildup at dawn and dusk near the inner edge of the ring current [Jaggi and Wolf, 1973; Southwood, 1977; Vasyliunas, 1970, 1972]. The shielding efficiency, however, depends on the auroral ionospheric conductance [Jaggi and Wolf, 1973; Senior and Blanc, 1984], which varies by season. Liou et al. [2001] showed observationally that the nightside auroral precipitation is stronger in winter than in summer, which implies enhanced conductance in the winter, and hence, more leakage of the convection electric fields. Senior and Blanc [1984], in their simulation, demonstrated that the enhancement of auroral conductivities by electron precipitation in the auroral zone significantly enhances both the typical duration and the absolute amplitude of the penetration of convection electric fields to subauroral latitudes (see Figure 6 in [Senior and Blanc, 1984]). The simulation results of Senior and Blanc [1984] also show that the penetration electric fields decay by latitude. Combined together, the impact of ionospheric conductivity on penetration provides an explanation for the large latitudinal

gradient in winter. It can also explain the westward premidnight flow being the strongest in winter and, together with the disturbance dynamo, can account for the emergence of penetration signatures (enhanced westward flows premidnight, emergence of eastward flows post-midnight) for Kp = 3 because a larger value of Kp corresponds to more intense auroral precipitation (i.e., enhanced auroral conductance) [Hardy et al., 1985]. The opposite velocity gradient in summer (Figure 4.11) is rather puzzling. Our explanation for this is that solar illumination of the nightside ionosphere in summer increases with latitude and there is a change in background conductivity, perhaps a reversal from winter conditions, that impacts the velocity gradient. A modeling study is needed to shed light on the complex nature of ion-neutral coupling in the subauroral region influenced by the ionospheric conductivity. In summary, the above analysis suggests that the seasonal, Kp, MLAT and MLT dependences of the subauroral flows are the combined effects of the solar-wind/magnetospheric interaction leading to penetration electric field and the neutral wind dynamo, with modulation by the ionospheric conductivity.

4.5 Summary and Conclusions

In this study, we have characterized the morphology of the subauroral (52° - 60° MLAT) convection pattern in terms of MLAT, MLT, month, season, Kp, and the IMF clock angle. The results show that the quiet-time (Kp $\leq$ 2+) subauroral flows are predominantly westward (20 - 90 m/s) in all months and become meridional (-20 - 20 m/s) near dawn and dusk. Kp dependencies are noticeable in all seasons and are most pronounced in winter such that, for higher Kp, the premidnight westward flow intensifies and the post-midnight eastward flow starts to emerge. The disturbance in the zonal plasma flow for higher Kp could be a combined effect of the disturbance dynamo and the penetration electric fields. IMF was also

found to be an important factor in shaping the morphology of subauroral flows. Compared to northward IMF Bz conditions, westward subauroral convection under southward IMF is significantly enhanced in the premidnight sector and is weakened in the post-midnight sector (even turning eastward near dawn at higher subauroral latitudes), consistent with the expected signature of electric fields penetrating from high latitudes. One of the most striking features is a latitudinal variation of zonal flow speed between 18 and 2 MLT in winter (November to February). It exists under all IMF conditions but is most pronounced under Bz- and higher Kp. Under dominant IMF By conditions, the latitudinal gradient in zonal flows disappears at earlier MLT for IMF By+ compared to IMF By-. The emergence of an IMF dependence in subauroral convection provides further evidence that the penetration of high-latitude convection electric field is a significant factor. Considering the role of ionospheric conductivity, our analysis suggests that the quiet-time subauroral flows are due to the combined effects of the solar-wind/magnetospheric coupling and the neutral wind dynamo, with the ionospheric conductivity modulating their relative dominance. That is, the premidnight westward flow is most likely due to a persistent leakage of the high-latitude convection electric fields while the post-midnight subauroral convection is dominated by the neutral wind dynamo as determined by conductivity factors.

Acknowledgments

We thank the National Science Foundation for support under grants AGS-1341918, AGS-1259508 and AGS-1552247. B. S. R. Kunduri thanks and acknowledges the support of NSF under grants AGS-1822056. We also thank all participants in the worldwide SuperDARN collaboration for the distribution of SuperDARN data via http://vt.superdarn.org/tiki-index.php?page=Data+Access. We wish to acknowledge the use of the NASA/GFSC Space Physics Data Facility's OMNIWeb and CDAWeb service. The planetary three-hour-range Kp index data are obtained from GFZ-Potsdam FTP server via

ftp://ftp.gfz-potsdam.de/pub/home/obs/kp-ap/wdc/. POES satellite data were accessed through the National Geophysical Data Center (NGDC) of the National Oceanic and Atmospheric Administration (NOAA), Boulder. The majority of analysis and visualization were completed with the help of free, open-source software tools such as DaViT-py (https://github.com/vtsuperdarn/davitpy), matplotlib [Hunter, 2007], IPython [Pérez and Granger, 2007], pandas [McKinney, 2010], and others [e.g. Millman and Aivazis, 2011].

Chapter 5

Investigation of External Triggers of Substorm Onsets Using Machine Learning

M. Maimaiti [1], B. Kunduri [1], J. M. Ruohoniemi [1], J. B. H. Baker [1], Leanna L. House [2]

[1]Bradley Department of Electrical and Computer Engineering, Virginia Tech, Blacksburg, Virginia, USA.

[2]Department of Statistics, Virginia Tech, Blacksburg, Virginia, USA

Maimaiti, M., Kunduri, B., Ruohoniemi, J. M., Baker, J. B. H., and House, L. L. (2019), A deep learning based approach to forecast the onset of magnetic substorms. Space Weather, 17. https://doi.org/10.1029/2019SW002251.

Abstract

The auroral substorm has been extensively studied over the last six decades. However, our understanding of its driving mechanisms is still limited and so is our ability to accurately forecast its onset. In this study, we present the first deep learning-based approach to predict the onset of a magnetic substorm, defined as the signature of the auroral electrojets in ground magnetometer measurements. Specifically, we use a time history of solar wind speed (Vx), proton number density, and IMF components as inputs to forecast the occurrence probability of an onset over the next one hour. The model has been trained and tested on a dataset derived from the SuperMAG list of magnetic substorm onsets and can correctly identify substorms ∼75% of the time. In contrast, an earlier prediction algorithm correctly identifies ∼21% of the substorms in the same dataset. Our model's ability to forecast substorm onsets based on solar wind and IMF inputs prior to the actual onset time, and the trend observed in IMF Bz prior to onset together suggest a majority of the substorms may not be externally triggered by northward turnings of IMF. Furthermore, we find that IMF Bz and Vx have the most significant influence on model performance. Finally, principal component analysis shows a significant degree of overlap in the solar wind and IMF parameters prior to both substorm and non-substorm intervals, suggesting that solar wind and IMF alone may not be sufficient to forecast all substorms, and preconditioning of the magnetotail may be an important factor.

5.1 Introduction

A substorm, often referred to as the magnetospheric substorm or an auroral substorm, is a complex phenomenon involving energy transfer from the magnetotail to the auroral ionosphere. Strong coupling between the solar wind, magnetosphere and the ionosphere is an

important aspect of the substorm phenomenon and its signatures can be observed in several different instruments ranging from satellites in the magnetotail to ground-based all-sky imagers and magnetometers. The duration of a substorm is about 1-2 hours [Akasofu, 1964; Akasofu et al., 1965; McPherron et al., 1973] and is typically categorized into three phases: a growth phase in which energy is extracted from the solar wind and stored in the nightside tail of the magnetosphere; an expansion phase in which stored energy is explosively released; and a recovery phase in which the magnetosphere relaxes to a quiet state [McPherron, 1979].

In all-sky imaging data, a substorm appears as a sudden explosive brightening followed by a poleward expansion of the aurora on the nightside [Akasofu, 1964]. This expansion is often associated with a westward ionospheric current flowing across the bulge of the expanding aurora. This westward current forms the ionospheric component of a 3D current system called the Substorm Current Wedge (SCW), flowing in from the magnetotail on the dawn side, and out on the dusk side [McPherron et al., 1973; McPherron and Chu, 2016]. The westward ionospheric component of the SCW leads to an increase in the westward auroral electrojet which is measured by the ground magnetometers and is usually observed as a depression in the auroral electrojet indices, such as AL (Auroral Lower) [Davis and Sugiura, 1966] and SML (SuperMAG version of AL index) [Newell and Gjerloev, 2011a]. In this study, we define these signatures of the auroral substorm in ground magnetometers and auroral indices as the magnetic substorm.

Substorms have been extensively studied over the last several decades [Akasofu, 1964; McPherron, 1979; Pudovkin, 1991; Lyons, 1995; Lui, 2000; Newell and Gjerloev, 2011b; Newell et al., 2016] using observations from both space and ground-based instruments, as well as through first principles-based models. In particular, several studies have focused on analyzing the impact of different solar wind and IMF parameters on the substorm growth phase [Akasofu, 1975; Caan et al., 1977; Lyons, 1995; Henderson et al., 1996; Freeman and Morley, 2004;

Newell et al., 2016]. A majority of these studies find IMF Bz to be the most important factor controlling substorm activity. Specifically, a southward directed Bz was considered to be crucial to enable energy transfer between the IMF and the magnetosphere [McPherron et al., 1973; Caan et al., 1977; McPherron, 1979; Pudovkin, 1991]. More recently, Newell et al. [2016] used several years of substorm onsets compiled by SuperMAG [Newell and Gjerloev, 2011a] and showed that solar wind velocity (Vx) could be the most important factor in driving substorms. While the growth phase of substorms was typically associated with periods of elevated solar wind driving, a few studies reported observations of substorms occurring during relatively quiet conditions [Kullen and Karlsson, 2004; Lee et al., 2010; Miyashita et al., 2011]. The growth phase of such substorms was thought to be driven by IMF By reconnection or a previous southward Bz interval. In summary, while substorms are generally thought to occur during periods dominated by strong geomagnetic acitivity, a subset have been reported to occur even during quiet conditions.

A widely debated topic has been the mechanism that triggers substorm expansion phase onset. Some studies proposed that the onset may be externally triggered by a change in solar wind and IMF conditions, such as a northward turning of Bz [Lyons, 1995; Lyons et al., 1997; Russell, 2000], whereas recent observations contradict these findings and suggest that substorms may be internally triggered and a northward turning of Bz is not necessary [Morley and Freeman, 2007; Freeman and Morley, 2009; Wild et al., 2009; Johnson and Wing, 2014]. Furthermore, understanding the chronological sequence of events constituting the actual trigger process has been a topic of interest for several researchers. Specifically, opposing views have emerged on whether current disruption in the near Earth region is followed by magnetic reconnection occurring farther out in the magnetotail or vice-versa [Lui, 1991, 1996; Baker et al., 1996]. The Time History of Events and Macroscale Interactions during Substorms (THEMIS) mission [Angelopoulos, 2008] addressed this question by demonstrating that tail

reconnection happens prior to current disruption [Angelopoulos et al., 2008]. The study also raised important questions about the role of preconditioning of the magnetosphere in terms of tail reconnection during the growth phase.

Over the last few decades, our reliance on satellites for communications, navigation, positioning, meteorology, Earth observation, science, technology, security, and defense has increased significantly. Currently, there are several hundred satellites in geosynchronous orbit and their operations can be perturbed and on occasion totally disrupted by substorms. For example, substorm-injected energetic particles can lead to surface charging in satellites which can damage surface materials and underlying components [Gubby and Evans, 2002; O'Brien, 2009; Horne et al., 2013]. Substorms can also produce geomagnetically induced currents that adversely impact electric supply networks [Belakhovsky et al., 2019; Freeman et al., 2019]. Forecasting substorm activity has therefore been a topic of practical as well as theoretical space weather interest. Early efforts utilized neural networks with 1-2 hidden layers (each layer composed of a few units) to predict the AE index over the next time step, as a proxy for substorm activity, using limited IMF and solar wind data as inputs [Hernandez et al., 1993; Gleisner and Lundstedt, 1997; Gavrishchaka and Ganguli, 2001]. More recently, support vector machines were trained on a limited dataset (197 data points comprising 98 onsets and 99 non onset intervals) and achieved 78% accuracy in predicting substorm onsets [Tanaka et al., 2015] (Note that, in contrast to the current study in which we report both precision and recall rates, only accuracy is reported in [Tanaka et al., 2015]). Traditional machine learning algorithms have often been successful in modeling functions between input and output data. However, a drawback associated with those algorithms is the necessity to manually extract features from the dataset, a tedious and sometimes impractical task when working with large and complex datasets. In contrast, while deep learning methods require extensive computational resources, they have been successful in modeling complex mappings

between input and output variables without the necessity for manual feature engineering, especially in large datasets [LeCun et al., 2015]. Finally, a majority of the earlier neural network based models were trained to predict the auroral indices [Hernandez et al., 1993; Gavrishchaka and Ganguli, 2001] and such models cannot be directly employed to forecast a substorm onset. We believe it would be useful to develop a deep learning model trained specifically for a binary classification task: forecasting whether a substorm will occur over the next hour.

In this study, we present the first deep learning based approach to predict the onset of a magnetic substorm, as defined by the SuperMAG SML index [Gjerloev, 2012]. Specifically, we use a time history of solar wind bulk speed (Vx), proton number density (Np), and interplanetary magnetic field (IMF) components (Bx, By, Bz) in the geocentric solar magnetospheric (GSM) coordinate system as inputs to forecast the occurrence probability of an onset over the next one hour. The magnetic substorms used for model development comprises of a comprehensive SuperMAG list of ∼35000 magnetic onsets compiled between 1997 and 2017. The paper is organized as follows. Section 2 describes the datasets used in this study, gives the definitions of technical terms, and, explains model development and data preprocessing. Section 3 presents model prediction results and Section 4 discusses some important findings and relates them to other published works on substorms. Section 5 gives the summary and conclusions of this study.

5.2 Datasets and Model architecture

5.2.1 Datasets and Data Reprocessing

Solar Wind & IMF: The solar wind and IMF data were primarily obtained from the Advanced Composition Explorer (ACE) spacecraft in orbit around the Earth-Sun L1 Lagrangian point, which is $\sim$ 240 Earth Radius away from the Earth's center. IMF data are from the magnetic field instrument MAG [Smith et al., 1998] and has 16 s resolution, while the solar wind data are from the Solar Wind Electron, Proton, and Alpha Monitor (SWEPAM) instrument [McComas et al., 1998] and has 64 s resolution. We used 1-min-averaged OMNI SW & IMF observations, which were shifted in time to the bow shock nose see

https://omniweb.gsfc.nasa.gov/html/ow_data.html#time_shift for details.

Magnetic Substorm Onset List & SuperMAG SML Index: We use the comprehensive list of $\sim$35000 substorm onsets compiled between 1997-2017 using the SML index [Gjerloev, 2012] to create our dataset. The substorm onsets were identified based on the SML index using the substorm identification criteria proposed by Newell and Gjerloev [2011a]. We discard outliers and undesirable data from this list by limiting our analysis to onsets occurring between 19:00 and 05:00 magnetic local time and, 55° and 75° magnetic latitude (the nightside auroral zone). Moreover, we consider substorms where the SML index drops below -3000 nT or the SME exceeds 3000 nT as outliers (334 events) and discard them. As a result, the number of onsets used from the SML list is reduced to $\sim$29000.

The substorm onset identification algorithm of [Newell and Gjerloev, 2011a] is as follows: The SML data were considered at a 1 min cadence in a sliding 30 min buffer. An onset was

identified at t_0 when four conditions are satisfied:

$$SML(t_0+1) - SML(t_0) < -15\ nT \tag{5.1}$$

$$SML(t_0+2) - SML(t_0) < -30\ nT \tag{5.2}$$

$$SML(t_0+3) - SML(t_0) < -45\ nT \tag{5.3}$$

$$\sum_{i=4}^{i=30} SML(t_0+i)/26 - SML(t_0) < -100\ nT \tag{5.4}$$

Thus the drop must be sharp (Equations 5.1-5.3, i.e. 45 nT in 3 min), and sustained (Equation 5.4, i.e. must be 100 nT below the initial value for the remainder of the half hour on average). The SML onset is then placed at t_0, the last minute before a 15 nT drop. Once an onset is identified, the algorithm advances ahead 20 min, which is thus the minimum permitted time between two consecutive onsets.

In this study we formulate the substorm onset prediction as a binary classification problem. Simply put, our goal is to forecast the occurrence probability of a substorm over the next 60 minutes, using a 120-minute time history of solar wind and IMF parameters (Bx, By, Bz, Vx, Np). Specifically, each data point used to train the model consists of a 120×5 input matrix of the solar wind and IMF, and an output which is a label indicating the presence (labeled as 1) or absence (labeled as 0) of an onset over the next 60 minutes. (A 120-minute time history was chosen to sufficiently cover the trend in Bz prior to the prediction time.) Figure 5.1a shows an example of a data point used to train the deep learning model which we present later. The 2D input array is shaded in gray and the output binary label is determined based on the presence/absence of a substorm within the next 60 minutes of the prediction time marked by the first vertical dotted black line from the left. The SML index is shown to confirm the presence of substorm activity, the vertical dotted red line indicates

the actual onset time identified using the procedure described in [Newell and Liou, 2011]. A data point is discarded if there are more than 20 missing values (out of 120 minutes) in any of the five input parameters, otherwise gaps were filled using linear interpolation. A uniform 10-minute delay is added to OMNI solar wind and IMF data to account for the propagation time of solar wind through the magnetosheath, the time for the effect of the external trigger at the magnetopause to affect the magnetotail and trigger substorm onset, and the time for the substorm onset to be detected by ground magnetometers. (Note that we have tried delay times between 0 - 20 minutes and found our model performance to be robust to uncertainties in delay time estimation). Following a standard practice in machine learning to improve the performance of the model, we normalized each of the input solar wind & IMF variables by subtracting the mean and dividing by its standard deviation, where the mean and standard deviation were calculated using all the measurements between 1997 - 2017. Figure 5.1b illustrates the conversion of prediction times, spanning from the year 1997 to 2017 with a step of 30 minutes, into binary labels based on the presence/absence of a substorm within the next 60 minutes. This conversion process results in a 1:6 ratio in the number of onsets vs. non-onsets. We balanced the class labels by randomly selecting an equal number of non-onset intervals before training the model. The final dataset has a total number of 60678 data points, with 30339 for each label.

5.2.2 Technical Definitions

In this section we list technical terms and model performance metrics [e.g., Lee, 2019] that we use in the later parts of this report to evaluate model performance.

True positive (TP) = correctly identified, i.e. a substorm onset occurs and the model predicts it correctly.

False positive (FP) = incorrectly identified, i.e. a substorm onset does not occur but the model incorrectly predicts it as a substorm onset.

True negative (TN) = correctly rejected, i.e. a substorm onset does not occur and the model correctly predicts it as a non-substorm event.

False negative (FN) = incorrectly rejected, i.e. a substorm onset occurs but the model does not predict it.

$$\text{Accuracy} = \frac{TruePositives+TrueNegatives}{True\ Positives+True\ Negatives+False\ Positives+False\ Negatives}$$

$$\text{Recall (True positive rate)} = \frac{True\ Positives}{True\ Positives+False\ Negatives}$$

$$\text{False negative rate} = \frac{FalseNegatives}{True\ Negatives+False\ Positives}$$

$$\text{Precision} = \frac{True\ Positives}{True\ Positives+False\ Positives}$$

$$\text{F1-Score} = \frac{2}{\frac{1}{Precision}+\frac{1}{Recall}} = 2 \times \frac{Precision \times Recall}{Precision+Recall}$$

The F1-score is the harmonic average of the precision and recall, where an F1-score reaches its best value at 1 (perfect precision and recall) and worst at 0.

5.2.3 Model Development

In this study, we train a convolution neural network (CNN) model to forecast the occurrence probability of a substorm onset, P_{onset}, over the next one hour using a 120 minute history of IMF and solar wind parameters. CNNs, first proposed by Cun et al. [1990], are a special kind of multi-layer neural network. Unlike conventional machine-learning techniques, which are limited in their ability to process image data in their raw form, CNNs were designed to recognize visual patterns directly from pixel images with minimal preprocessing. They were shown to be very effective in hierarchically capturing complex spatial and temporal

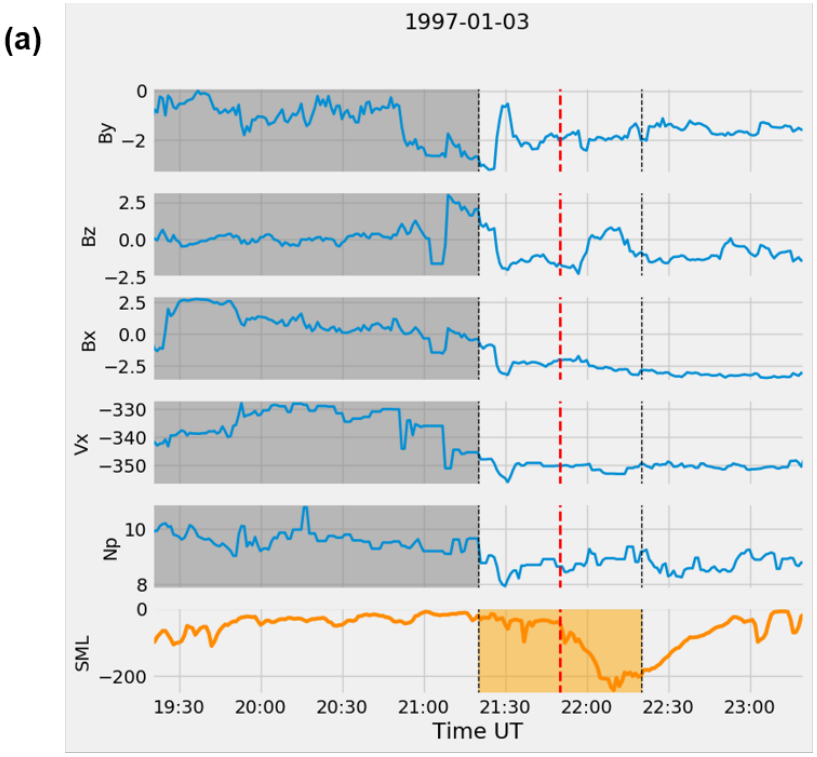

(b)

Onset Time
1997-01-01 20:16:00
1997-01-01 23:36:00
●
●
2017-12-29 19:21:00
2017-12-30 03:06:00

Prediction Time	Next 60 min
1997-01-01 19:00:00	0
1997-01-01 19:30:00	1
1997-01-01 20:00:00	1
1997-01-01 20:30:00	0
●	
●	

Figure 5.1: (a) An example of data point classification to a deep learning mode. The 2D input array is shaded in gray and the output binary label is determined based on the presence/absence of substorm within the next 60 minutes of the prediction time marked by the first vertical dotted black line from the left. The red dotted line indicates the actual onset time. In this example, the output label is 1, corresponding to presence of substorm onset in the 60-minute time interval shaded in orange and marked by the two vertical dotted black lines (b) Conversion of prediction times into binary labels based on the presence/absence of a substorm within the next 60 minutes.

relations in the dataset [Cun et al., 1990]. Since the 2D input arrays in this problem (see Figure 5.1a for an example data point) can essentially be treated as 2D images, CNNs are therefore ideally suited for capturing the dynamics of solar wind and IMF parameters that can eventually drive substorms.

Model Architecture

We developed three CNN models based on the latest variants of CNNs, such as ResNet (residual network)[He et al., 2016], FCN (fully convolutional network) [Wang et al., 2017], and MLSTM-FCN (multivariate long short-term memory coupled with fully convolutional network) [Karim et al., 2018]. A recent study [Fawaz et al., 2019] tested 9 recently developed deep learning classifiers over 12 multivariate time series classification datasets and ranked ResNet and FCN as the best in terms of average accuracy over 10 runs of each implemented model. After an extensive amount of model tuning we observed that all three variants of the CNNs showed very similar performance; no model had a clear advantage over the others. The ResNet CNN, however, is relatively easier for model tuning and is less prone to adverse effects of adding more layers [Glorot and Bengio, 2010]. We therefore decided to adopt the ResNet architecture and analyze its forecasts in greater detail.

Figure 5.2a shows the schematic of ResNet CNN architecture we have used for our application. The input layer takes a 2D array with 120 (minutes time history) $\times$ 5 (solar wind and IMF) parameters (see Figure 5.1a for an example data point). The first two convolution layers (i.e., the layers that have a set of independent filters which perform convolution operations to nodes in preceding layers) and the subsequent max pooling layer (i.e., a down-sampled version of the preceding layer) were added to reduce the input dimension while capturing some low-level features from the input data, unlike the implementation of the ResNet model by Fawaz et al. [2019]. After the max pooling layer are two Resnet Units,

each consists of three identical convolution layers stacked in series. There is an additional "shortcut connection" between the input and output of each ResNet Unit that simply performs identity mapping and its output is added to the output of the stacked layers. Resnet Units serve two purposes: (1) to make the architecture deeper so that the later convolution layers can capture the complex relationship between different input features, and (2) to overcome the problem of vanishing/exploding gradients through the "shortcut connection" [He et al., 2016]. The issue of vanishing/exploding gradients arises when training deeper networks because, as the gradients (with respect to the loss function) are back-propagated to earlier layers, repeated multiplication may make the gradients infinitely small/large and thereby prevent the network from training further [Glorot and Bengio, 2010]. We tested this ResNet CNN with different numbers of ResNet units, varying between 1 and 10, and found that a CNN model with two ResNet units performs the best on a validation dataset (see the next subsection for definition) in terms of F1-score. A max-pooling layer is applied to the output of the second ResNet Unit, which is then flattened to form a long 1D layer, connected to the output layer after one more 1D layer. The output layer has two nodes - one for the substorm class and the other for the non-substorm class. A SoftMax activation function, a normalized exponential function that maps the preceding vector into a normalized probability distribution, is applied to these two nodes to obtain probability estimates for the two classes. In summary, for any given time instant, the model is designed to accept a 120 minute history of the 5 solar wind and IMF parameters as inputs and output the probability of an onset over the next 60 minutes. The basic rationale in this ResNet CNN architecture, or CNN in general, is that it first looks for low level features and then gradually builds up more abstract concepts through a series of convolution layers.

Model Training

The ResNet architecture shown in Figure 5.2a is implemented in Keras [Chollet et al., 2015] with Tensorflow backend and trained using multi-GPUs on the High-Performance Computing (HPC) system available at Virginia Tech. Each model was trained using a back-propagation algorithm [Rumelhart et al., 1986], a widely used learning algorithm which minimizes the training loss by adjusting the weights according to a gradient descent. The objective of training is to minimize the difference between the output and target pairs (i.e., the loss value) by optimizing the weights of the network. Equation 5.5 shows the expression of binary cross-entropy loss which our model tries to minimize. The variables y and p in Equation 5.5, respectively represent, the actual label (i.e., 1 for substorm onset or 0 for non-onset) and the substorm onset probability predicted by the model. We used "Adam" optimizer [Kingma and Ba, 2014], which is a method for efficient stochastic gradient descent optimization. The adjustable parameters of "Adam" used in this study are: learning rate $\alpha = 0.00001$, learning rate decay $= 0.0$, exponential decay rates $\beta_1 = 0.9$ and $\beta_2 = 0.999$. See [Kingma and Ba, 2014] for the definitions of these adjustable parameters. We split the data into three different data sets while keeping the date points in chronological order. Such a split prevents the model from overfitting as the test and validation time periods are completely independent of the training time period.: training (70%), validation (15%) and test (15%) datasets. training dataset was used for model training, validation dataset was used for model tuning and model selection, and test dataset was used for evaluating model performance [Ripley, 1996; Russell and Norvig, c2010]. Figure 5.2b and 5.2c respectively show the loss and accuracy versus number of epochs for the ResNet CNN model with red color for training data and blue for validation data. An Epoch is a complete iteration over the entire training data. Both the training and validation losses sharply decrease in the first 15 epochs and then gradually reach their own asymptotic values; 200 epochs are enough

for the loss to converge. More importantly, the loss curves show no sign of over-fitting, indicated by the loss and accuracy curves for the validation dataset not diverging from those for training dataset after a certain epoch.

$$Loss = -\ (y\ log(p) + (1 - y)\ log(1 - p)) \tag{5.5}$$

5.3 Results

In the previous sections, we focused on data processing, model architecture and training. We formulated the problem as a binary classification task and developed a ResNet CNN model that can be used to forecast the onset of a magnetic substorm over the next 60 minutes, using solar wind and IMF as inputs. In the current section, we present the model forecasts, analyze its performance on a statistical scale, and discuss the role of different input parameters in driving the predictions. It is important to note that all the analysis presented in this section uses the test subset of the data and excludes all intervals from the training and validation subsets.

5.3.1 Model Predictions

As a first step, we present four example forecasts made by the model in Figure 5.3; one forecast from each of the TP, FP, FN and TN categories is shown. The figure presents the inputs (By, Bz, Bx, Vx and Np) fed to the model along with SML index which is indicative of substorm activity. The time period shown in each plot is centered around the prediction interval (one hour) and spans five hours, including the two-hour input period. The prediction interval in each of the plots is indicated by the shaded-regions, and the inputs to the model are

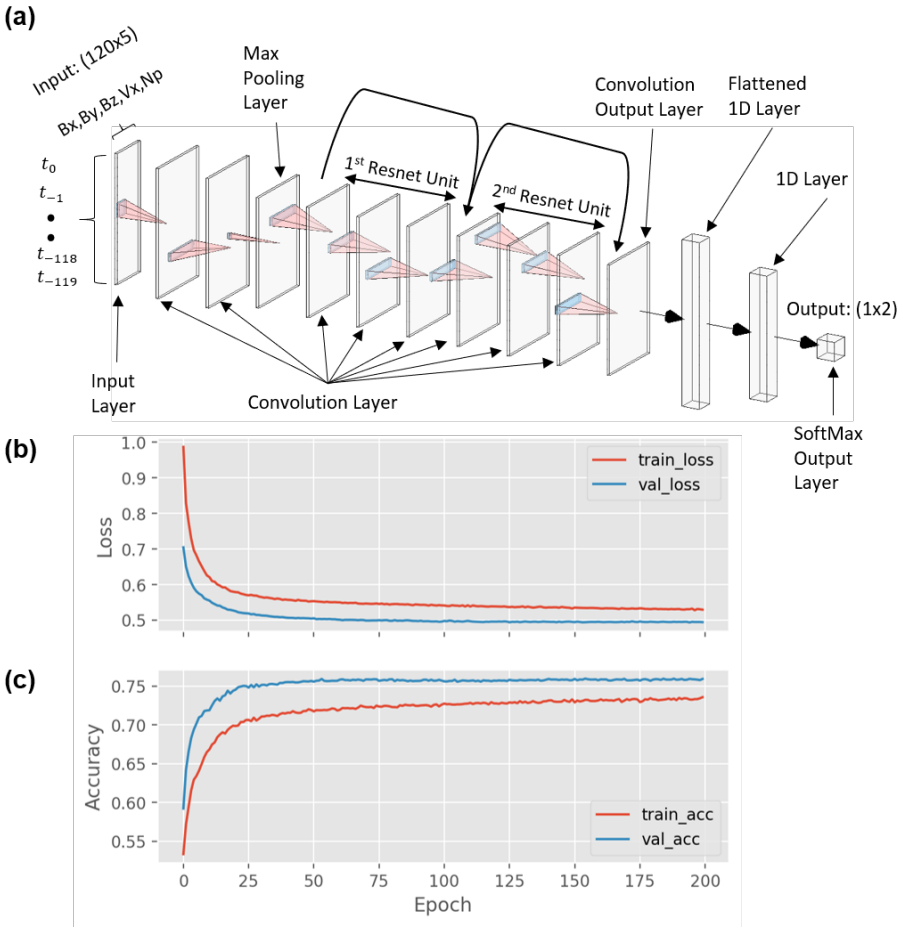

Figure 5.2: (a) A schematic of ResNet CNN architecture with two ResNet Units for multivariate time series processing of solar wind & IMF data. The input layer takes a 2D input array with 120 × 5 elements and the output layer renders probability estimates. The output layer has two nodes, one for the substorm class and the other for the non-substorm class. (Note that the layer dimensions are shown in log scale.) Each polyhedron between the adjacent convolution layers represent the mapping of a previous layer to the next through a two-dimensional convolution. (b) Loss and (c) accuracy curves of the model training on training (red curve) and validation (blue curve) data sets. An Epoch is a complete iteration over the entire training data.

taken from the two-hours period preceeding this interval. The actual onset times identified by SuperMAG are indicated by the dashed red lines for the TP and FN categories and the probabilities associated with each forecast are annotated in the bottom panels.

In the TP example, the model forecasted a potential onset for the time period covering 1230

UT and 1330 UT with a high degree of confidence ($P_{onset} = 0.80$) and an onset was indeed identified in SuperMAG SML index ∼0115 UT, confirming the prediction. A drop in SML index further confirms substorm activity during this period. The input to the model are solar wind and IMF parameters between 1030 UT and 1229 UT; Bz was predominantly negative and Vx was ∼ -600 km/s during this period. Moving to the FP case, the model forecasts a substorm onset between 1800 and 1900 UT and the interval preceding the prediction (1600 - 1759 UT) was dominated with a weak negative Bz. It is interesting to note that while the onset detection criteria (Equations 5.1-5.4) do not find any onset in this time period, a closer examination reveals a drop in the SML index, perhaps associated with a minor substorm or a psuedo-onset. This event failed to satisfy all four criteria formulated by Newell and Gjerloev [2011a] and was therefore classified as a non-onset, whereas our model forecast an onset during this interval based on the input solar wind and IMF conditions. This event shows the challenges associated with accurately identifying actual substorm onsets from the SML dataset and separating them from pseudo-onsets and minor geomagnetic disturbances. While the SML-based onset list is the most comprehensive and continuous dataset available, it has certain limitations and uncertainties which propagate into the model. We must be clear that our model is trained to predict substorm onsets as specified by the criteria of Newell and Gjerloev [2011a]. In the FN case, Bz was mostly weak negative with short periods of positive Bz and Vx was ∼ - 440 km/s during the input interval (1930-2129 UT). While our model failed to forecast an onset detected by SuperMAG ∼2210 UT in this case, it is important to note that P_{onset} was 0.48 indicating higher uncertainty in the model for this prediction. Finally, in the TN example, the model successfully forecasted a period without any substorm activity between 1500 and 1600 UT with a high degree of confidence ($P_{onset} = 0.11$) and the same is confirmed by the SML index. In summary, two important features can be observed from the figure, firstly, a negative IMF Bz has a significant impact on the forecasts and, secondly, the prediction probability (indicated by P_{onset}) is higher for successful predictions

compared to the FN case. These features will be analyzed further in the next sections.

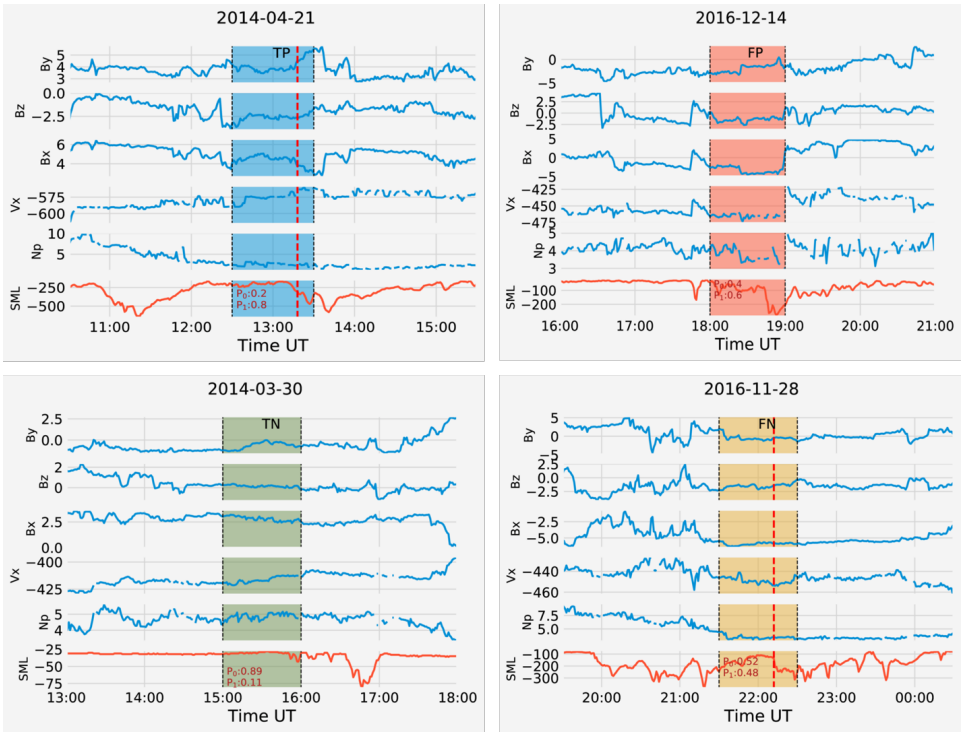

Figure 5.3: Example model predictions, clockwise from top left are True Positive (TP), False Positive (FP), False Negative (FN) and True Negative (TN) predictions. In each figure, the top three panels show IMF By, Bz and Bx, respectively, the fourth and fifth panels show the solar wind velocity and number density, and the sixth panel presents the SML index. The dashed black lines and/or the shaded regions mark the prediction interval and the dashed red lines indicate actual onset time provided by SuperMAG. The probabilities associated with each forecast are shown in the bottom panel. See text for details.

5.3.2 Model Performance

We used the model to forecast a large number of intervals between 1997 and 2017 and the evaluation metrics are summarized in Table 5.1. The "# intervals" column in the table indicates the number of forecast intervals used during training, validation and testing. For example, 21236 non-substorm and substorm intervals (a total of 42472 data points) were used to train the model, whereas 4607 intervals of each class were used for testing. We can note

from the table that the model achieves a F1-score of 0.74 for both the classes on the test data. The model evaluation metrics listed in Table 5.1 are based on setting the P_{onset} threshold to 0.5, i.e., we expect the model forecasted a substorm onset if $P_{onset} > 0.5$ and a non-substorm otherwise. We will now analyze the impact of systematically varying this threshold between 0 and 1 on the model performance, using a Receiver Operating Characteristic (ROC) curve. The ROC curve is created by plotting the recall against the false positive rate at various threshold levels and serves as a useful tool for evaluating binary classifiers. We plot the ROC curve for our model in Figure 5.4a, the threshold value of 0.5 is marked by the "x" symbol. As we increase the threshold, the recall increases, however, this is accompanied by an increase in the false positive rate. There are certain advantages and disadvantages of choosing a certain threshold and the choice is therefore best left to the end user. In comparison, the ROC curve of a model that makes a prediction based on a random guess is indicated by the diagonal dotted black line. In other words, the further the solid black curve is from the diagonal line, the better the model is at discriminating between onsets and non-onsets. Overall, our model achieves a ROC area of 0.82 which is a measure of the separability between the onset and non-onset classes.

After training, our model achieves an accuracy of $\sim$ 75% and the remaining 25% of the events are mis-classified. Now we separately examine the distributions of P_{onset} for both the onset and non-onset classes to further understand model performance. Such an analysis will provide insights into the confidence of a forecast. For example, a higher P_{onset} (> 0.85) shows that the model is very confident of the forecast compared to a lower value. Figure 5.4b shows histograms of P_{onset} for both the onset (purple) and non-onset (green) classes. In this figure, we use a threshold of 0.5 (dashed black line) to forecast an onset. So for the non-onset class (i.e., no subsequent substorm) when $P_{onset} < 0.5$, the model's forecast is correct and is categorized as a TN event. Likewise, when $P_{onset} \geq 0.5$ for an onset class (i.e.,

Table 5.1: Model performance for training, validation, and test datasets.

Prediction for training Data

Class Label	Precision	Recall	F1-Score	# Intervals
0 (non-substorm)	0.77	0.70	0.73	21,236
1 (substorm)	0.72	0.79	0.75	21,236

Prediction for Validation Data

Class Label	Precision	Recall	F1-Score	# Intervals
0 (non-substorm)	0.74	0.80	0.77	4,496
1 (substorm)	0.78	0.73	0.75	4,496

Prediction for Test Data

Class Label	Precision	Recall	F1-Score	# Intervals
0 (non-substorm)	0.74	0.75	0.74	4,607
1 (substorm)	0.75	0.73	0.74	4,607

subsequent substorm) it is categorized as a TP event. On the other hand, $P_{onset} < 0.5$ for an onset class makes the event FN whereas $P_{onset} > 0.5$ for a non-onset class make it FP. All four categories are marked in the figure. We note that the model can predict large number of substorm and non-substorm events with high confidence as reflected by the two peaks in the purple ($P_{onset} > 0.8$) and green curves ($P_{onset} < 0.15$), respectively. However, we find that there are a considerable number of non-substorm events mis-classified as onsets (FPs) by the model (green curve in regions where $P_{onset} > 0.5$) and a similar albeit less prominent feature is observed for FNs. We will further analyze this behavior in later sections and analyze the origin of this problem in greater detail.

We have so far examined the overall performance of the model forecasts and now we analyze its dependence on the change in geomagnetic activity, binned by the maximum drop in SML index during the prediction horizon interval of 60 minutes (Δ_{SML}). In Figure 5.5, we show the number of forecasts (panel a) and P_{onset} (panel b), individually for each prediction category (TP, FP, TN and FN) for different Δ_{SML} bins. It can be seen that when the maximum drop

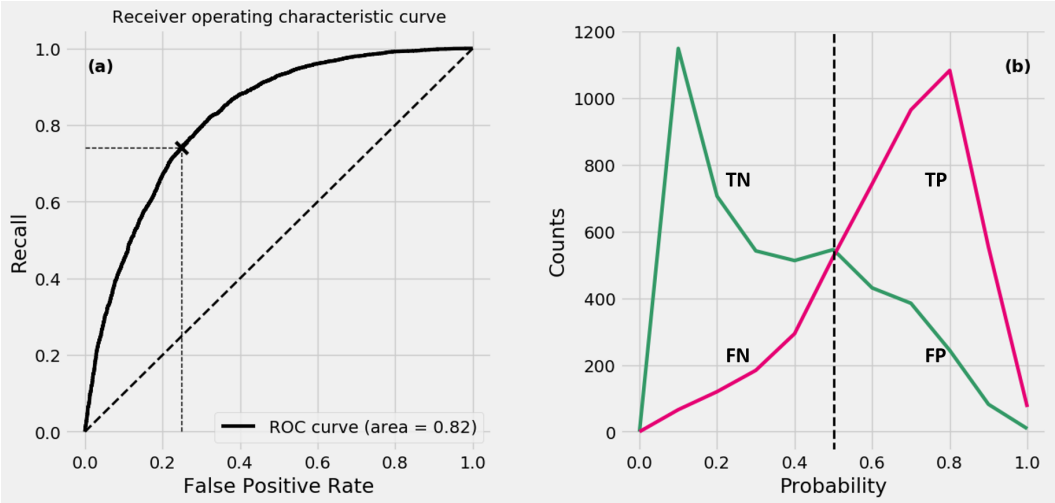

Figure 5.4: (a) Receiver operating characteristic (ROC) curve for the forecasts. The 0.5 threshold is marked by the "x" sign. The dotted blue line represents the ROC curve of a model that makes a prediction based on a random guess. (b) Histograms of predicted probability of substorms, P_{onset}, forecasted for both onset (maroon) and non-onset (green) classes.

in SML during the one hour forecast interval is less than 100 (corresponding to the -100 to 0 bin), the maximum forecasts belong to the TN category, whereas a noticeable number from the FP and TP categories are observed as well. Furthermore, the number of TPs increases while the number of TNs decreases with Δ_{SML}. This higher number of TNs in the first bin can be attributed to the fact that lower Δ_{SML} periods are usually quiet with very few onsets, and the increase in the number of onsets with Δ_{SML} accounts for the higher TPs in those bins. Panel (b) shows a plot of P_{onset} which is indicative of the confidence assigned to the forecast. A very high (low) P_{onset} suggests the model is confident in its forecast of an onset (no-onset). However, an intermediate value of P_{onset} between 0.35 and 0.65 typically is indicative of increased uncertainty in the predictions. It can be concluded from the figure that uncertainty in the model while forecasting onsets (non-onsets) is higher when $|\Delta_{SML}|$ is low (high). Another key feature to note is that the maximum number of FPs occur when the drop in SML is less than 100 nT, and moreover, the model is not very confident in predicting

onsets in this range. We will analyze this behavior further and discuss its impact on model predictions in the discussion section.

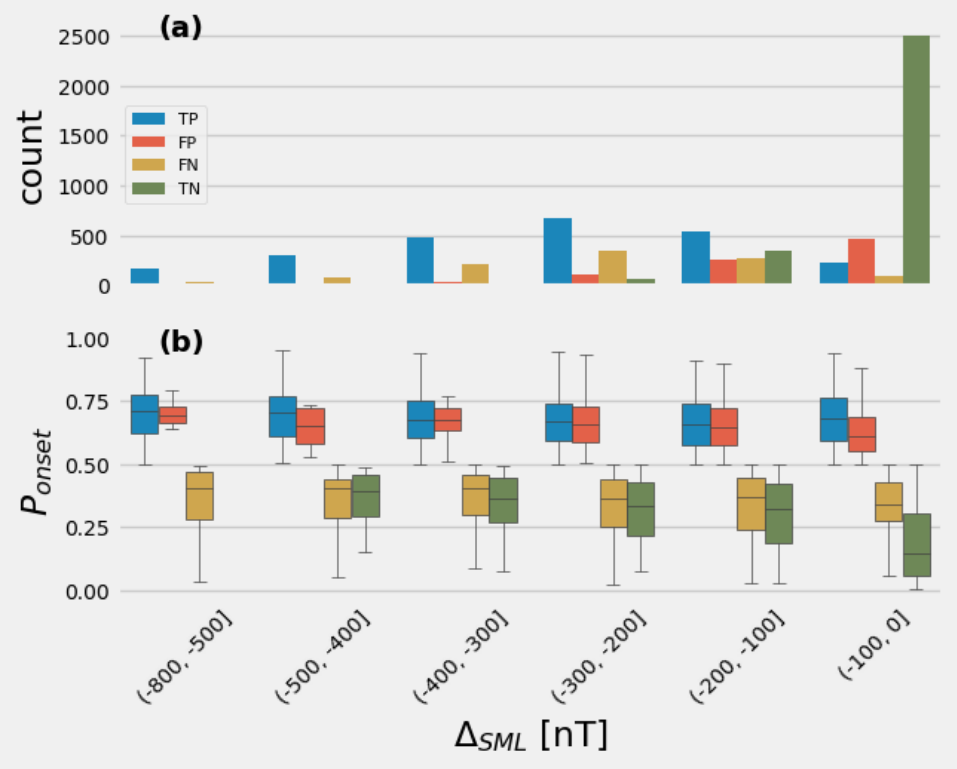

Figure 5.5: Variability in model predictions with Δ_{SML}: (a) distribution of all the 4 forecast categories (TP, FP, FN, TN) versus Δ_{SML} bins, and (b) variability of P_{onset} for the four forecast categories versus Δ_{SML}. Each box presents the quartiles (minimum, first quartile, median, third quartile, and maximum) of P_{onset} and values beyond $\pm$ 1.5 $\times$ (interquartile range) are discarded as outliers

.

5.3.3 Overlap in the Input Parameters

We now examine the behavior of input parameters to understand their influence on model performance. Of particular interest is IMF Bz which is expected to have the maximum impact on substorm onsets [Caan et al., 1977; Lyons, 1995; Lyons et al., 1997]. In Figure 5.6, we present a plot of Bz with respect to the prediction time for each of the four prediction

categories (TP, FP, FN, TN), in other words, ΔT_{pred} indicates the time IMF Bz was measured relative to the prediction time. For example, if the prediction time is 1200 UT, then ΔT_{pred} is -60 minutes for a Bz value at 1100 UT. The solid lines in the figure indicate median values whereas the shaded regions mark the 25^{th} and 75^{th} percentile range of IMF Bz. While there is significant variance in Bz for all the four forecast categories, certain strong patterns emerge for each of them. It can be noted that the input IMF Bz turns increasingly southward for the TP category as one moves closer to the prediction time ($\Delta T_{pred} = 0$). In contrast, IMF Bz turns increasingly northward closer to the prediction time for the TN category. Clearly, there is a sharp distinction in the behavior of Bz between the TP and TN categories and such distinguishing features are expected to improve the model performance. It is further interesting to note that the trend in IMF Bz for the FP (FN) categories is similar to the TP (TN) categories, albeit slightly weaker. This suggests that our model associates onsets with a preceding interval of southward IMF. More importantly, the similarity in IMF Bz trend between TP and FP (as well as TN and FN) categories suggests that the errors in model prediction could be associated with an overlap in input parameters between the onset and non-onset classes. We will now explore the degree of overlap in the input IMF and solar wind parameters further through Principal Component Analysis (PCA).

Each class label has an associated 2D array with 600 elements (120 by 5) and it is not possible to fully visualize such high dimensional data. We therefore use Principal Component Analysis (PCA) techniques to reduce the dimensions of the 2D input arrays, while preserving as much variation in the data as possible, and visualize them in a new coordinate system as shown in Figure 5.7. Panel (a) shows percent explained variance vs. number of principal components and Panels (b)-(d) show the two classes projected onto the first three principal components. In the transformed coordinate system, the first three principal components alone can explain about 65% of the variance in the original input data. As seen from panels

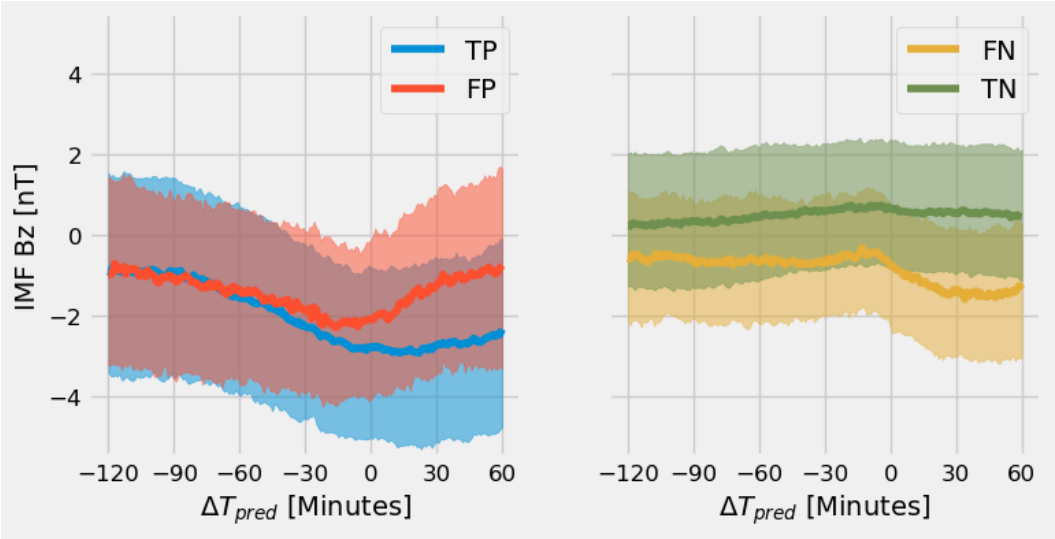

Figure 5.6: Variability in IMF Bz with respect to prediction time for the four forecast categories. Solid lines indicate median values and the shaded region indicates the 25th to 75th percentile values. Left panel shows true positive (blue) and false positive (orange) categories and right panel shows the true negative (green) and false negative categories (yellow). See text for details.

(b) - (d), the two classes are strongly overlapped with each other in the reduced 3-D space. Admittedly, we cannot rule out the possibility that the two classes could be more separable through the other principal components that contain the remaining 35% variance. However, the significant overlap between the two classes suggests that large number of substorm and non-substorm events have very similar solar wind and IMF conditions in their 120 minutes of time history intervals prior to the prediction times. This is also apparent from the strong overlap in IMF Bz for the four forecast categories shown in Figure 5.6.

The strong overlap revealed by the PCA analysis shown in Figure 5.7 is for all substorm categories. However we found that the amount of overlap varies when the substorm level is considered – specifically, there is less overlap between substorm and non-substorm events when smaller substorms, as characterized by Δ_{SML}, are discarded (results not shown). Here we show how the deep learning model performs for different levels of substorms. Intuitively we would expect the larger substorms to be detected more easily than the smaller ones.

Figure 5.7e shows the recall versus substorm level thresholded by Δ_{SML}. As expected, the model performance improves for increasing substorm levels. For example, the recall is about 75% when all substorms are considered and it reaches $\sim 95\%$ for substorms with $\Delta_{SML} \geq 700$. The decrease in recall for smaller substorms correlates with more PCA overlap between the two classes (there are a few potential explanations for this finding. See Section 4.4 for a detailed discussion on the impact of solar wind/IMF overlap and other factors on model performance).

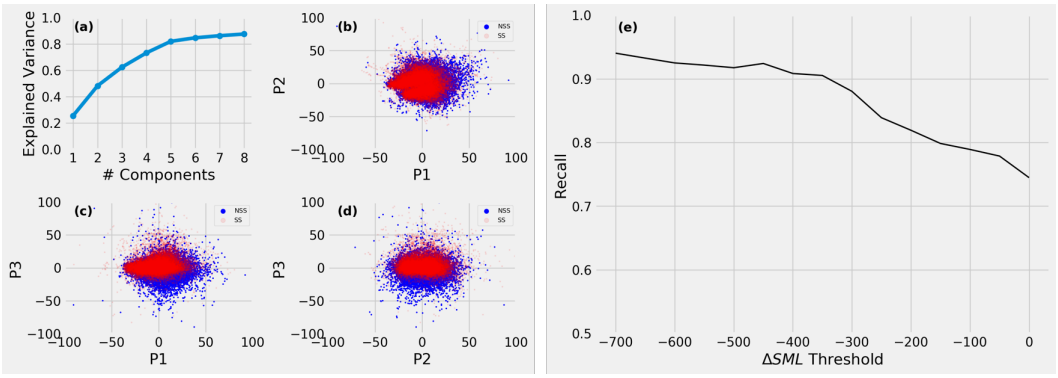

Figure 5.7: Principal component analysis of the input 2D arrays of substorm and non-substorm events : (a) Percent explained variance versus number of principal components, (b) scatter plot of first two principal components, (c) scatter plot of first and third principal components, (d) scatter plot of second and third principal components, and (e) variation in recall versus substorm levels thresholded by Δ_{SML}.

5.3.4 Input Parameter Importance

Deep learning models generally perform better than traditional machine learning models when the dataset is large and the relationship between the input data and output labels are complex. However, deep learning models, or any artificial neural networks in general, are known to be difficult for human interpretation because the features generated in the last hidden layer (i.e., the layer just before the output) cannot be directly related to the input features. In our application it is important to have some type of model interpretability which

we can relate to our physical understanding of drivers of substorm onsets. To overcome the black box nature of deep learning models, we take the backward stepwise feature selection procedure which is often used in linear regression to rank the input parameter importance. The assumption here is that if a certain input parameter is important in triggering substorms, it should also be an important feature for deep learning models to predict substorm onset. Such an approach was previously used by Weigel et al. [2003] to determine the importance of different parameters in predicting ground magnetic field and its time derivative. Table 5.2 lists the performance metrics (precision, recall, and F1-score) of the ResNet CNN model for different combinations of input parameters. We can see that Bz and Vx are the most important factors on the model performance such that Bz influences both precision and recall while Vx influences mostly the recall. This is apparent when each of the five features is used as input individually or is dropped from the full model that uses all the five features. The implications of the parameter importance are discussed in more detail later.

5.3.5 Baseline Comparison

We compare the performance of our model with the methodology described in Lyons et al. [1997] that nowcast substorm onset. A rigorous set of quantitative rules (listed below) were proposed to determine if a substorm is triggered at a given time (t_{on}) based on the variations in IMF Bz 30 minutes prior to the onset (i.e.,$t_{on} - 30$ to t_{on}).

$$N_{B_Z(t_{on}-30:t_{on})<0} >= 22 \tag{5.6}$$

$$B_Z(t_{on} + \Delta_t) - B_Z(t_{on}) >= 0.375nT/min \tag{5.7}$$

$$\frac{B_Z(t_{on} : t_{on} + 10\Delta_t)}{10\Delta_t} >= 0.175nT/min \tag{5.8}$$

Table 5.2: Parameter ranking. Precision and recall of onsets and non-onsets when different IMF and solar wind parameters are given as inputs to the model.

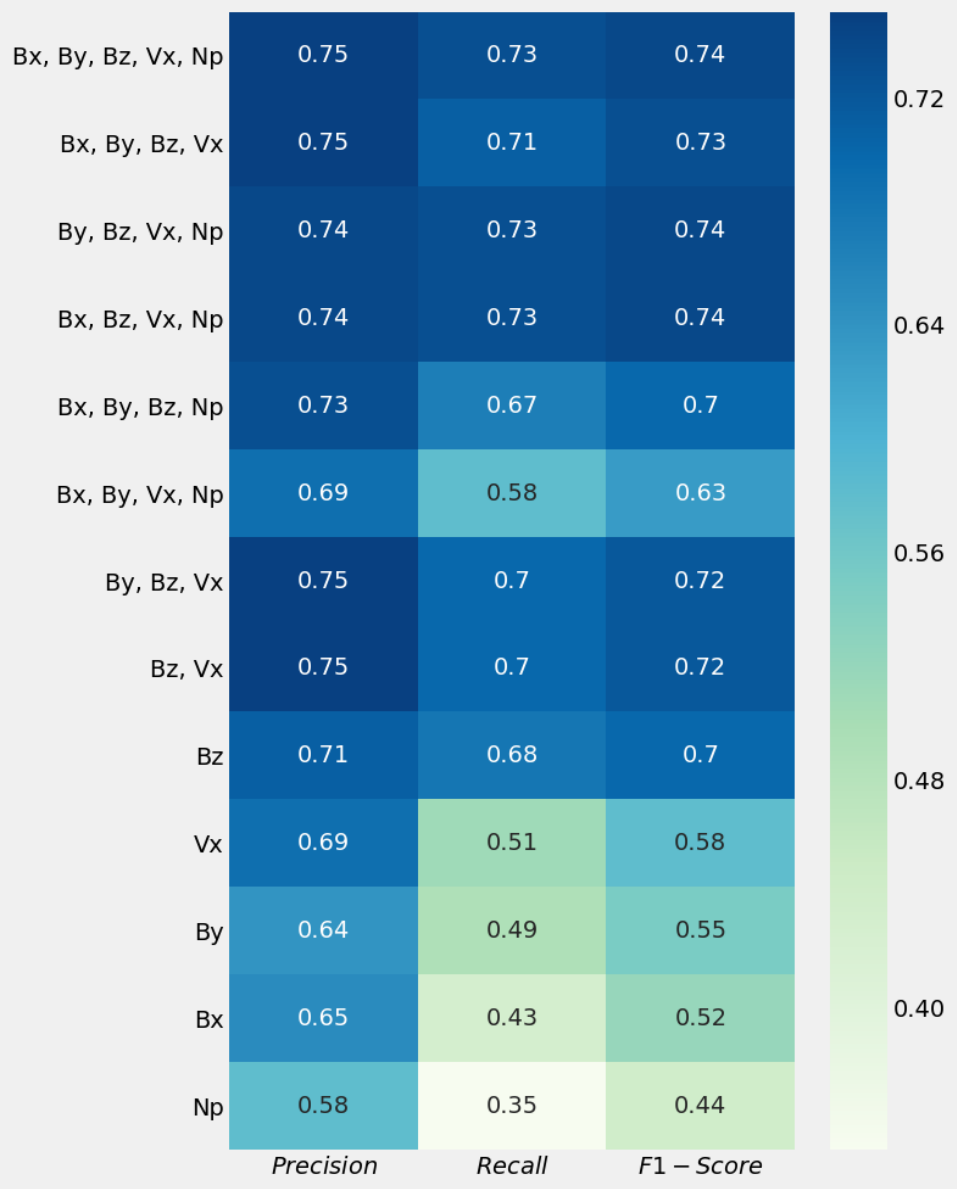

$$B_Z(t_{on} + \Delta_t : t_{on} + 3\Delta_t) >= B_Z(t_{on}) + 0.15nT \tag{5.9}$$

$$B_Z(t_{on} + 3\Delta_t : t_{on} + 10\Delta_t) >= B_Z(t_{on}) + 0.45nT \tag{5.10}$$

Equations 5.6 through 5.10 represent the criteria proposed by Lyons et al. [1997]. Equation 5.6 quantifies the criterion that IMF must be southward for at least 22 of the preceding 30 minutes, representing the growth phase requirement. The remaining equations (5.7 to 5.10) quantify the criteria for triggering the onset, a rapid and sustained northward turning of IMF Bz. We find that the Lyons et al. [1997] model can correctly identify ∼21% of the substorms listed in the SuperMAG database. Previous studies [Morley and Freeman, 2007; Wild et al., 2009; Newell and Liou, 2011] applied the same criteria on other datasets such as those from POLAR UVI [Liou, 2010] and IMAGE [Frey et al., 2004], and found that all the criteria are satisfied only by a small subset ($< 30\%$) of substorm events, similar to our study. It should be emphasized that the Lyons et al. [1997] model was developed for a different purpose, namely, to study the triggering mechanisms of substorms and it has since then been extremely valuable in improving our understanding of substorms. However, from a space weather prediction perspective, there are very few tools/methods available to forecast the onset of a substorm [Tanaka et al., 2015] and we believe our model will serve this purpose.

5.3.6 Solar Wind-Magnetosphere Coupling Function

While it is difficult to interpret the features captured by any deep-learning based model, modulating the input features and understanding their influence on the prediction can provide some useful insights. Next, we analyze the impact of using different solar wind-magnetosphere coupling functions as inputs to our model.

Table 5.3 shows performance metrics of the model (precision, recall, and F1-score) when different coupling functions with 120 minutes of time history are given as model inputs. We found that using $d\Phi/dt$ which is indicative of the rate magnetic flux opened at the magnetopause [Newell et al., 2007] as input to our model gives the best performance in predicting substorm onsets (F1-score = 0.73) compared to other coupling functions. The most successful implementation of the model, which uses the raw solar wind and IMF features (i.e. Bx, By, Bz, Vx, Np) as input features, achieves an F1-score of 0.74, and thus, performs slightly better than the other models that use coupling functions as features. Furthermore, providing $d\Phi/dt$ as input to the model in addition to the raw solar wind and IMF features doesn't improve the model performance any further. These results suggest that our model is able to replicate the behavior of the coupling functions which quantify certain aspects of solar wind - magnetosphere interactions, from the input solar wind and IMF parameters.

5.4 Discussion

In this study, we presented the first deep learning based approach to forecast the occurrence probability of substorm onsets over the next 60 minutes. The model was shown to achieve 72±2% precision and 77±4% recall rates and an ROC area of 0.83 (Figure 5.4a). We further showed that a majority of the false positives are associated with small substorms ($|\Delta_{SML}| < 100nT$). The errors in model prediction can be attributed to a strong overlap in input parameters between the onset and non-onset classes as demonstrated by PCA in Figure 5.7. Finally, we found that Bz and Vx have the most significant impact on model performance. In this section, we further analyze our findings and compare them with observations from previous studies.

Table 5.3: Precision, Recall, and F-Score of the model when different coupling functions are given as model inputs. The value of each metric is given in the form of mean ± std., where the mean and standard deviation are computed by training the model repeatedly on 10 different training/test/validation sets.

Model Inputs	Precision	Recall	F1-Score
$V_x\ B_T$	0.67 ± 0.03	0.65 ± 0.06	0.65 ± 0.03
$E_{KL} = V_x\ B_T\ sin^2(\frac{\theta_c}{2})$ [Kan and Lee, 1979]	0.71 ± 0.03	0.71 ± 0.05	0.71 ± 0.01
$E_{TL} = N_p^{\frac{1}{2}}\ V_x^2\ B_T\ sin^6(\frac{\theta_c}{2})$ [Temerin and Li, 2006]	0.72 ± 0.03	0.68 ± 0.04	0.70 ± 0.01
$\frac{d\Phi_{MP}}{dt} = V_x^{\frac{4}{3}}\ B_T^{\frac{2}{3}}\ sin^{\frac{8}{3}}(\frac{\theta_c}{2})$ [Newell et al., 2007]	0.72 ± 0.03	0.75 ± 0.04	0.73 ± 0.01
B_x, B_y, B_z, V_x, N_p	0.72 ± 0.02	0.77 ± 0.04	0.74 ± 0.01
B_x, B_y, B_z, V_x, N_p, $\frac{d\Phi_{MP}}{dt}$	0.72 ± 0.02	0.78 ± 0.04	0.74 ± 0.01

5.4.1 Comparison with previous approaches

Some studies used neural networks to predict auroral indices over the next few minutes using solar wind and IMF as inputs [Hernandez et al., 1993; Gleisner and Lundstedt, 1997; Gavrishchaka and Ganguli, 2001], and provided a mechanism to forecast substorm. While these studies serve as excellent starting points, there are uncertainties and inaccuracies associated with using auroral indices (such as AE) as a proxy for identifying substorm activity [Kullen et al., 2009]. More recently, Luo et al. [2013] developed empirical models of auroral indices and showed that predicting short term variations is more challenging than predicting the long term average trends. Furthermore, Barkhatov et al. [2017] used an Elman artificial neural network to make a short-term forecast of the AL index, and showed that taking into account the 2-3 hour history of solar wind kinetic energy loading the magnetosphere significantly improves the accuracy of the model. In this study, we build on these approaches, by developing a model that directly forecasts the occurrence probability of a substorm onset, with a higher prediction horizon of 60 minutes. In agreement with these studies, we find that incorporating the history of solar wind and IMF into the model, indicating the growth phase of the substorm, is crucial for making accurate forecasts. Furthermore, our analysis shows that the deep learning based approach is capable of capturing complex interactions between the solar wind and magnetosphere and can serve as an alternative to those approaches that are based on coupling functions. These results are supported by an early study [Weigel et al., 2003], which successfully showed that a neural network can be used to develop a "data-derived" non-linear coupling function to predict ground magnetic field and its time derivative at different local times using solar wind and IMF over a 3 hour period as inputs.

5.4.2 External triggering of substorms

The epoch analysis presented in Figure 5.6 shows that a crucial factor driving the model's predictions is the trend in IMF Bz. If Bz starts turning increasingly negative ∼60 minutes prior to the prediction time, the model is more likely to forecast the occurrence of a substorm onset. This behavior suggests the model is capturing the growth phase of the substorm during which energy from the solar wind is accumulated in the magnetotail, a widely accepted condition necessary for triggering a substorm [McPherron et al., 1973; Lyons, 1995; Henderson et al., 1996; Lyons et al., 1997; Russell, 2000; Freeman and Morley, 2009; Johnson and Wing, 2014].

A few studies [Caan et al., 1977; Lyons, 1995; Lyons et al., 1997; Russell, 2000] postulated another condition necessary to trigger a substorm, namely, a sharp northward turning of IMF Bz close to or coinciding with the onset. However, the ability of our model to accurately forecast (up to one hour ahead) substorm onset without any IMF or solar wind input close to the actual onset time strongly suggests that the second condition may not always be necessary to trigger an onset. Moreover, the epoch analysis doesn't show a strong trend indicative of IMF northward turning immediately prior to the onset. Our findings suggest that the behavior of a majority of substorm onsets is in agreement with another set of studies [Henderson et al., 1996; Morley and Freeman, 2007; Freeman and Morley, 2009; Newell and Liou, 2011; Johnson and Wing, 2014], which argued that initial elevated solar wind driving conditions is the only necessary condition for triggering a substorm, and the northward turning of IMF Bz is coincidentally rather than causally related to onsets [Morley and Freeman, 2007; Freeman and Morley, 2009].

5.4.3 Input Parameter Importance

Determining the roles of different IMF and solar wind parameters in triggering a substorm has been a subject of interest for several decades [McPherron et al., 1973; Caan et al., 1977; Troshichev et al., 1986; Petrukovich et al., 2000; Newell et al., 2013, 2016]. In this study, we modulated the inputs given to our machine learning model to quantify the influence of different parameters in forecasting substorm onsets. We found IMF Bz, Vx and IMF By had the most significant influence on the forecasts (in the same order), and including them as inputs improved the accuracy of the forecasts whereas dropping them reduced it, as shown in Table 5.2.

A southward IMF Bz was expected to be a significant factor because the magnetic flux accumulation that occurs during substorm growth phase via dayside magnetic reconnection is well known to occur during southward IMF Bz. In our analysis IMF By ranked third in importance. While not as impactful as Bz, under dominant By conditions open flux can still be added to the magnetosphere via dayside reconnection [Sandholt et al., 1998] and thus contribute to the growth phase of a substorm. Several earlier studies have confirmed the role of By in driving substorms, especially when Bz is positive and cannot contribute to the growth phase significantly [Troshichev et al., 1986; Petrukovich et al., 2000; Wild et al., 2009; Lee et al., 2010].

Our model ranks Vx as the second most influential factor in forecasting substorms. This is in good agreement with Li et al. [2007]; Luo et al. [2013]; Newell et al. [2016] who showed that while the Bz component of IMF plays an important role in modulating magnetospheric dynamics, the role of solar wind velocity is more important than is usually assumed. Furthermore, we confirm the result reported by Li et al. [2007] that number density by itself is the least significant factor influencing substorm electrodynamics (Table 5.2). Recent observa-

tions [Tanskanen, 2009; Newell et al., 2013] also showed that higher Vx is directly correlated with increased substorm activity. Moreover, Vx has been a component of many solar wind - magnetosphere coupling functions that estimate the dayside magnetopause merging, in fact, 17 out of 20 coupling functions listed in [Newell et al., 2007] include Vx. This suggests higher Vx can increase the open flux transportation to the magnetotail, and thus, facilitate substorm growth phase. Beyond the role of Vx in modulating dayside merging, MHD simulation studies of [Goodrich et al., 2007; Pulkkinen et al., 2007] show that higher solar wind speed makes the magnetotail much more unstable, which may also trigger more substorms.

5.4.4 Impact of Solar Wind/IMF Overlap on Model Performance

An important observation from Figure 5.5 is that the forecasts belonging to the false positive and true negative classes are most apparent when $|\Delta_{SML}|$ is less than 200 nT, when the geomagnetic activity is relatively low. However, during periods of dynamic geomagnetic activity (higher $|\Delta_{SML}|$), the number of TN and FP forecasts drops significantly and the TP forecasts dominate over the other classes. In other words, the FP forecasts occur during similar conditions as the TN forecasts and this behavior can be attributed to the degree of overlap between the onset and non-onset classes (Figure 5.7a). While the lower Δ_{SML} bins are predominantly associated with quiet conditions (no onsets) they still had a notable number of "minor" substorms or pseudo-onset, increasing the number of FPs and the uncertainty in the model. One such example is seen in the top-right panel of Figure 5.3 where our model predicts an onset but the SML index only shows a small disturbance or perhaps a pseudo-onset. This uncertainty in forecasting "minor" substorms is further confirmed by a drop in P_{onset} (Figure 5.5) when $|\Delta_{SML}| <$ -200 nT as well as the increase in recall with $|\Delta_{SML}|$ threshold (Figure 5.7b).

The performance of our model relies on the assumption that a recent history of solar wind and IMF can determine the dynamics of magnetic substorms. However, the distinction in solar wind and IMF conditions prior to non-substorm intervals, pseudo-onset and minor substorms is not sharp [Kullen and Karlsson, 2004]. The lack of a clear and sharp differentiating factor in solar wind and IMF prior to the two classes (substorm and non-substorm) indicates the existence of an overlap between the classes (observed in the PCA analysis shown in Figure 7) and such an overlap can reduce the performance of any machine model [Batista et al., 2004]. There are also other assumptions pertaining to the input data and the model architecture, violation of which will affect the mode performance. For example, similar to other approaches such as Magnetohydrodynamics (MHD) and time series based models, our model is developed on the assumption that an upstream point measurements can fully represent the solar wind and IMF conditions across the entire magnetopause. However, such a situation might not be completely valid because of the uncertainties in point measurements [Petrukovich et al., 2000]. Another assumption is that the ResNet model will capture all of the dynamics of the magnetosphere. In principle, a neural network could fully capture the dynamics, but this may not be possible in practice. One motivation for using a deep neural network, such as the one in this study, is that it provides better performance than a shallow neural network even though both are "universal approximators" [Hornik et al., 1989; Cybenko, 1989]. It is also important to note that the performance of our model is also coupled with the substorm onset list derived using the SML index and any uncertainties or shortcomings in the list may propagate into the model. Nonetheless, the SML based onset list is the most comprehensive and continuous dataset available, and is ideally suitable for training a deep learning model.

While a majority of substorms are associated with southward IMF Bz or increased solar wind driving [McPherron et al., 1973; Lyons, 1995; Kullen and Karlsson, 2004; Newell et al., 2016], several studies have reported observations of substorms even during northward Bz intervals

[Lee et al., 2010; Petrukovich et al., 2000; Miyashita et al., 2011]. The presence of such intervals, albeit in fewer number, further reduces the model performance. Such substorms were suggested to be driven by factors not related to recent history of solar wind and IMF. For example, magnetosphere can take several hours to release the excess energy which may have been supplied during a previous southward IMF interval [Akasofu, 1975; Lee et al., 2010; Kullen and Karlsson, 2004; Miyashita et al., 2011]. In such cases, the 120 minutes of time history is not enough and considering longer time history may help fully capture the state of the system. Another factor is the small-scale spatial variability in IMF during weak solar wind driving conditions which may lead to small regions of southward IMF that can supply energy through localized reconnection regions [Petrukovich et al., 2000; Kullen and Karlsson, 2004].

In summary, we find that while the recent history of solar wind and IMF can be used to forecast a majority substorm onsets, the significant overlap in solar wind and IMF conditions prior to minor substorms and non-onsets reduces the model performance. Other factors, such as the implicit model assumptions and the lack of information on the internal state of the magnetosphere [McPherron et al., 2008], may be additional factors that reduce the model performance.

5.5 Conclusions and Summary

In this paper, we presented the first deep learning based approach to forecast the onset of a magnetic substorm, as identified by the SuperMAG SML index. A ResNet convolutional neural network architecture was developed to predict the occurrence probability of an onset over the next one hour by using the 120-minute history of solar wind and IMF parameters (Vx, Np, Bx, By, Bz) prior to onset as inputs to the model. The model was trained on

a dataset consisting of substorm onset intervals derived from the list of onsets compiled by SuperMAG between 1997 and 2017, as well as an equal number of non-onset intervals during the same time period. We further split the entire data into three subsets: training (70%), validation (15%) and test (15%) and the model achieved 72±2% precision and 77±4% recall rates on the test set. These precision and recall rates show that our model is able to accurately forecast the occurrence of a majority of substorm onsets without any solar wind or IMF input close to the actual onset time. This observation suggests that the majority of substorms are not externally triggered by Bz northward turning. To analyze the influence of different parameters on the forecasts, we modulated the input IMF and solar wind parameters provided to the model and found that IMF Bz and solar wind velocity (Vx) have the most significant influence and provide maximum predictive power. Finally, principal component analysis reveals that small substorms share very similar solar wind and IMF time history conditions with non-substorms, suggesting the inputs provided to the model may not be sufficient by themselves to forecast all substorms, and so other factors such as internal magnetospheric instability are at play.

Acknowledgments

We thank the National Science Foundation for support under grants AGS-1341918, AGS-1259508 and AGS-1552247. B. S. R. Kunduri thanks and acknowledges the support of NSF under grants AGS-1822056 and AGS-1839509. The authors acknowledge Advanced Research Computing at Virginia Tech for providing computational resources and technical support that have contributed to the results reported within this paper. URL: http://www.arc.vt.edu. We gratefully acknowledge the SuperMAG collaborators (http://supermag.jhuapl.edu/info/?page=acknowledgement. The SML index and the substorm onset datasets are available from http://supermag.jhuapl.edu/substorms/. We also wish to acknowledge the use of the NASA/GFSC Space Physics Data Facility's OMNIWeb

and CDAWeb service. The solar wind and IMF data used in this study can be obtained from https://cdaweb.gsfc.nasa.gov/index.html/. The majority of analysis and visualization were completed with the help of free, open-source software tools such as matplotlib [Hunter, 2007], IPython [Pérez and Granger, 2007], pandas [McKinney, 2010], and others [Millman and Aivazis, 2011].

Chapter 6

Conclusions and Future Work

The purpose of this research has been to investigate the driving influences of electrodynamics in the mid- and high- latitude regions of the ionosphere. In chapter 2, we examined the IMF By influence on reverse convection during extreme northward IMF. We analyzed an interval when the RISR-N radar made measurements in the high latitude noon sector while the IMF turned from duskward to strongly northward. We found that the high-latitude plasma convection can have dual flow responses with different lag times to strong dynamic IMF conditions that involve IMF By rotation. Similar observations were reported by [Eriksson et al., 2017] using measurements from SuperDARN radars. Such phenomena are rarely observed and are not predicted by the antiparallel or component reconnection models applied to quasi-static conditions. Our analysis suggested that the difference in lag times is consistent with the propagation delay expected for mapping electric fields along the magnetic field from two separate reconnection sites on the magnetopause, namely, poleward of the cusp and at the magnetopause subsolar point. More case studies, perhaps involving SuperDARN radars in conjunction with multiple spacecraft, are needed to corroborate the existence of dual- and multi-site reconnection geometries.

In Chapters 3 & 4, we investigated the driving influences of subauroral flows by first deriving statistical patterns of the nightside subauroral (52° - 60°) convection under quiet to moderately disturbed conditions using data from six mid-latitude SuperDARN radars distributed across the continental United States. These climatological patterns are organized

by magnetic latitude, magnetic local time, month, season, Kp, and the IMF clock angle. Comparison with the quiet-time neutral wind patterns has shown that the local F region neutral wind dynamo does not account for the observed sense of convection in the premidnight sector. Considering the role of ionospheric conductivity, our analysis of Kp and IMF influences suggested that penetration electric field could be the dominant driver of convection in the dusk sector while the neutral wind effect may dominate in the dawn sector. An immediate extension of this work is to examine the response of subauroral flows to sudden IMF Bz southward (northward) turning preceded by a sustained IMF Bz+ (Bz-) under quiet conditions. This can be achieved through case studies using coordinated measurements of plasma drifts and neutral winds from SuperDARN and Fabry–Perot interferometer (FPI), respectively. Carrying out such analysis will allow us to separate the influences of the neutral wind and penetration electric fields on subauroral convection. Note that "quiet" conditions are preferred because, under geomagnetically disturbed conditions, distinguishing the penetration effect from the disturbance dynamo effect in the subauroral region can be difficult since both processes can exist simultaneously with similar plasma flow signatures.

In Chapter 5, we examined the driving influences of magnetic substorms using a machine learning approach. We built the first deep learning-based approach to predict the onset of substorms using the 120-minute history of solar wind and IMF parameters (Vx, Np, Bx, By, Bz). Our model has been trained and tested on a dataset derived from the SuperMAG list of magnetic substorm onsets and correctly predicts substorms ∼75% of the time. In contrast, an earlier prediction algorithm [Lyons et al., 1997] correctly identified only ∼21% of the substorms when applied to the same dataset. This is a good first step toward the larger goal of predicting substorm onset occurrence in real time. However, parameters other than solar wind and IMF also need to be explored to further improve the prediction accuracy. Our principal component analysis shows a significant degree of overlap in the solar

wind and IMF parameters prior to both substorm and non-substorm intervals, suggesting that solar wind and IMF alone may not be sufficient to forecast all substorms, and preconditioning of the magnetotail may be an important factor. This is further corroborated by our observation that, after an extensive amount of model tuning with variants of recently published deep learning architectures, no model had a clear advantage over the others in terms of prediction accuracy when only the solar wind & IMF parameters were used as predictors. Therefore, a logical extension of this work is to include parameters that characterize conditions in the magnetotail, such as dipolarizations, which can be identified from GOES magnetometer data. The challenge is that such measurements are not continuous and thus would reduce the number of substorm events we could use for model training. One possible (but computationally expensive) solution would be to extract those parameters from MHD model runs.

In summary, we investigated the driving influences of (1) plasma convection in the polar cap region under dynamic IMF conditions, (2) subauroral convection under geomagnetically quiet to moderately disturbed conditions, and (3) magnetic substorms in the auroral region. We proposed a dual-site reconnection geometry for explaining unusual behavior of plasma convection in the polar cap region observed under dynamic IMF conditions, which was inconsistent with the predictions of steady-state reconnection models. We provided compelling evidence that penetration of high-latitude convection electric field is a significant factor in driving subauroral plasma drifts and can in fact dominate the neutral wind dynamo. Finally, making use of the latest machine learning techniques, we showed that external factors, such as the solar wind and IMF, are not sufficient by themselves to forecast all substorms, and that preconditioning of the magnetotail may be an important factor.

Below we provide suggestions for future directions that one could take to make use of the research findings presented in this dissertation:

1. In the event study presented in Chapter 2, our time-lagged correlation analysis revealed that the IMF By influence acted on a lag time which was 10 min faster than that of the Bz component. We demonstrated that this difference in lag time is consistent with the propagation delay expected for mapping electric fields along the magnetic field from two separate reconnection sites on the magnetopause: antiparallel reconnection with the Bz component poleward of the cusp and component reconnection with the By component in the vicinity of the magnetopause nose. However, this study raises important questions such as "how does the reconnection geometry evolve from a single site to dual or multiple sites?" and "What are the conditions that contribute to differences in reconnection geometry under dynamic IMF conditions compared to steady-state conditions?". We suggest carrying out a global MHD modeling study of this event to elucidate the precise manner in which the reconnection geometry changes during periods of strong dynamic IMF.

2. The persistent penetration of high-latitude electric field into the subauroral region has not yet been fully tested and needs to be validated using first-principle models in combination with observations. The role of ionospheric conductivity in modulating the relative dominance of penetration electric field and neutral wind dynamo is also poorly understood. Therefore, it is necessary to use coupled Magnetosphere-Ionosphere-Thermosphere models, such as LFM-TIEGCM-RCM, to simulate subauroral ionospheric convection during geomagnetically quiet conditions and to compare the results with longitudinally extended observations from SuperDARN. This will allow us to quantify the relative contributions of penetration electric field and neutral winds in driving quiet-time subauroral convection and to determine the ionospheric conductivity effect in modulating the two drivers. Such a modeling study might also provide explanations for the latitudinal variation of zonal flow speed between 18 and

2 MLT in winter, which is the most striking feature presented in Chapters 3 & 4.

3. The twin Van Allen Probes satellites in the inner magnetosphere have entered their seventh year of operation since launch in 2012, and have produced a sizeable database of electric drift measurements. This provides a good opportunity to carry out a comprehensive study of plasma drifts observations in the coupled inner magnetosphere – subauroral ionosphere system using the Van Allen Probes electric drift measurements in conjunction with the SuperDARN radar observations of subauroral drifts. Since the inner magnetosphere and the subauroral ionosphere are coupled via geomagnetic field lines, we would expect a similar plasma convection patterns in the two regions. However, any significant difference could be due to local factors, in either the subauroral ionosphere or the inner magnetosphere, whose effects are not fully mapped along the magnetic field lines.

4. The time-series deep learning approach to substorm prediction presented in Chapter 5 can be extended to dynamic prediction of other physical phenomena such as plasma convection and Birkeland currents. Many empirical models have been developed for characterizing the steady-state patterns of plasma convection and Birkeland currents. However, there isn't yet a model that makes time-series predictions for evolving patterns while accounting for the past history of the solar wind and IMF. We would expect that taking this direction would significantly improve the space weather prediction of these phenomena and their impacts.

Results from this research have been published in the Journal of Geophysical Research: Space Physics [Maimaiti et al., 2017, 2018, 2019a] and Space Weather [Maimaiti et al., 2019b]. Four co-authored papers have been published in the Journal of Geophysical Research: Space Physics [Clauer et al., 2016; Kunduri et al., 2018b; Lin et al., 2019] and Geophysical Research

Letters [Eriksson et al., 2017] on topics related to this research.

Bibliography

S.-I. Akasofu. The development of the auroral substorm. *Planetary and Space Science*, 12 (4):273 – 282, 1964. ISSN 0032-0633. doi: https://doi.org/10.1016/0032-0633(64)90151-5. URL http://www.sciencedirect.com/science/article/pii/0032063364901515.

S.-I. Akasofu. The roles of the north-south component of the interplanetary magnetic field on large-scale auroral dynamics observed by the dmsp satellite. *Planetary and Space Science*, 23(10):1349 – 1354, 1975. ISSN 0032-0633. doi: https://doi.org/10.1016/0032-0633(75)90030-6.

S.-I. Akasofu, S. Chapman, and C.-I Meng. The polar electrojet. *Journal of Atmospheric and Terrestrial Physics*, 27(11):1275 – 1305, 1965. ISSN 0021-9169. doi: https://doi.org/10.1016/0021-9169(65)90087-5. URL http://www.sciencedirect.com/science/article/pii/0021916965900875.

H. Alfven. On the electric field theory of magnetic storms and aurorae. *Tellus*, 7(1):50–64, 1955. doi: 10.1111/j.2153-3490.1955.tb01140.x. URL https://onlinelibrary.wiley.com/doi/abs/10.1111/j.2153-3490.1955.tb01140.x.

J. A Van Allen. Observation of high intensity radiation by satellites 1958 alpha and gamma. *Journal of Jet Propulsion*, 28(9):588–592, 1958. doi: 10.2514/8.7396. URL https://doi.org/10.2514/8.7396.

James A. Van Allen and Louis A. Frank. Radiation around the earth to a radial distance of 107,400 km. *Nature*, 183(4659):430–434, 1959. ISSN 1476-4687. doi: 10.1038/183430a0. URL https://doi.org/10.1038/183430a0.

V. Angelopoulos. The themis mission. *Space Science Reviews*, 141(1):5, Apr 2008. ISSN 1572-9672. doi: 10.1007/s11214-008-9336-1.

Vassilis Angelopoulos, James P. McFadden, Davin Larson, Charles W. Carlson, Stephen B. Mende, Harald Frey, Tai Phan, David G. Sibeck, Karl-Heinz Glassmeier, Uli Auster, Eric Donovan, Ian R. Mann, I. Jonathan Rae, Christopher T. Russell, Andrei Runov, Xu-Zhi Zhou, and Larry Kepko. Tail reconnection triggering substorm onset. *Science*, 321(5891): 931–935, 2008. ISSN 0036-8075. doi: 10.1126/science.1160495.

W. I. Axford and C. O. Hines. A unifying theory of high-latitude geophysical phenomena and geomagnetic storms. *Canadian Journal of Physics*, 39(10):1433–1464, 1961. doi: 10.1139/p61-172. URL http://dx.doi.org/10.1139/p61-172.

Hasan Bahcivan, Roland Tsunoda, Michael Nicolls, and Craig Heinselman. Initial ionospheric observations made by the new resolute incoherent scatter radar and comparison to solar wind imf. *Geophysical Research Letters*, 37(15):n/a–n/a, 2010. ISSN 1944-8007. doi: 10.1029/2010GL043632. URL http://dx.doi.org/10.1029/2010GL043632. L15103.

D. N. Baker. The inner magnetosphere: A review. *Surveys in Geophysics*, 16(3):331–362, May 1995. ISSN 1573-0956. doi: 10.1007/BF01044572. URL https://doi.org/10.1007/BF01044572.

D. N. Baker, T. I. Pulkkinen, V. Angelopoulos, W. Baumjohann, and R. L. McPherron. Neutral line model of substorms: Past results and present view. *Journal of Geophysical Research: Space Physics*, 101(A6):12975–13010, 1996. doi: 10.1029/95JA03753.

D. N. Baker, P. J. Erickson, J. F. Fennell, J. C. Foster, A. N. Jaynes, and P. T. Verronen. Space weather effects in the earth's radiation belts. *Space Science Reviews*, 214(1):17, Dec 2017. ISSN 1572-9672. doi: 10.1007/s11214-017-0452-7. URL https://doi.org/10.1007/s11214-017-0452-7.

J. B. H. Baker, R. A. Greenwald, J. M. Ruohoniemi, K. Oksavik, J. W. Gjerloev, L. J. Paxton, and M. R. Hairston. Observations of ionospheric convection from the wallops superdarn radar at middle latitudes. *Journal of Geophysical Research: Space Physics*, 112 (A1):n/a–n/a, 2007. ISSN 2156-2202. doi: 10.1029/2006JA011982. URL http://dx.doi.org/10.1029/2006JA011982. A01303.

K. B. Baker and S. Wing. A new magnetic coordinate system for conjugate studies at high latitudes. *Journal of Geophysical Research: Space Physics*, 94(A7):9139–9143, 1989. doi: 10.1029/JA094iA07p09139. URL https://agupubs.onlinelibrary.wiley.com/doi/abs/10.1029/JA094iA07p09139.

N. A. Barkhatov, V. G. Vorob'ev, S. E. Revunov, and O. I. Yagodkina. Effect of solar dynamics parameters on the formation of substorm activity. *Geomagnetism and Aeronomy*, 57(3):251–256, May 2017. doi: 10.1134/S0016793217030021.

J. Bartels, N. H. Heck, and H. F. Johnston. The three-hour-range index measuring geomagnetic activity. *Terrestrial Magnetism and Atmospheric Electricity*, 44(4):411–454, 1939. doi: 10.1029/TE044i004p00411. URL https://onlinelibrary.wiley.com/doi/abs/10.1029/TE044i004p00411.

Gustavo E. A. P. A. Batista, Ronaldo C. Prati, and Maria Carolina Monard. A study of the behavior of several methods for balancing machine learning training data. *SIGKDD Explor. Newsl.*, 6(1):20–29, June 2004. ISSN 1931-0145. doi: 10.1145/1007730.1007735. URL http://doi.acm.org/10.1145/1007730.1007735.

Vladimir Belakhovsky, Vyacheslav Pilipenko, Mark Engebretson, Yaroslav Sakharov, and Vasily Selivanov. Impulsive disturbances of the geomagnetic field as a cause of induced currents of electric power lines. *J. Space Weather Space Clim.*, 9:A18, 2019. doi: 10.1051/swsc/2019015. URL https://doi.org/10.1051/swsc/2019015.

Kristian Birkeland. *The Norwegian aurora polaris expedition, 1902-1903*, volume 1. Christiania,H. Aschelhoug„ 1908. URL https://www.biodiversitylibrary.org/item/57262. https://www.biodiversitylibrary.org/bibliography/17857 — Vol.I issued in 2 pts., each with t.-p., and paged continuously. — v.1. On the cause of magnetic storms and the origin of terrestrial magnetism, by Kr. Birkeland.

M. Blanc and A.D. Richmond. The ionospheric disturbance dynamo. *Journal of Geophysical Research: Space Physics*, 85(A4):1669–1686, 1980. ISSN 2156-2202. doi: 10.1029/JA085iA04p01669. URL http://dx.doi.org/10.1029/JA085iA04p01669.

M. Blanc, P. Amayenc, P. Bauer, and C. Taieb. Electric field induced drifts from the french incoherent scatter facility. *Journal of Geophysical Research*, 82(1):87–97, 1977. ISSN 2156-2202. doi: 10.1029/JA082i001p00087. URL http://dx.doi.org/10.1029/JA082i001p00087.

Mariusz Bojarski, Davide Del Testa, Daniel Dworakowski, Bernhard Firner, Beat Flepp, Prasoon Goyal, Lawrence D. Jackel, Mathew Monfort, Urs Muller, Jiakai Zhang, Xin Zhang, Jake Zhao, and Karol Zieba. End to end learning for self-driving cars, 2016.

Antoine Bordes, Sumit Chopra, and Jason Weston. Question answering with subgraph embeddings. In *Proceedings of the 2014 Conference on Empirical Methods in Natural Language Processing (EMNLP)*, pages 615–620, Doha, Qatar, October 2014. Association for Computational Linguistics. doi: 10.3115/v1/D14-1067. URL https://www.aclweb.org/anthology/D14-1067.

Joseph E Borovsky and Juan Alejandro Valdivia. The earth's magnetosphere: A systems science overview and assessment. *Surveys in geophysics*, 39(5):817–859, 2018.

Joseph E. Borovsky and Kateryna Yakymenko. Substorm occurrence rates, substorm recurrence times, and solar wind structure. *Journal of Geophysical Research: Space*

Physics, 122(3):2973–2998, 2017. doi: 10.1002/2016JA023625. URL https://agupubs.onlinelibrary.wiley.com/doi/abs/10.1002/2016JA023625.

M. J. Buonsanto and O. G. Witasse. An updated climatology of thermospheric neutral winds and f region ion drifts above millstone hill. *Journal of Geophysical Research: Space Physics*, 104(A11):24675–24687, 1999. ISSN 2156-2202. doi: 10.1029/1999JA900345. URL http://dx.doi.org/10.1029/1999JA900345.

M. J. Buonsanto, J. C. Foster, and D. P. Sipler. Observations from millstone hill during the geomagnetic disturbances of march and april 1990. *Journal of Geophysical Research: Space Physics*, 97(A2):1225–1243, 1992. ISSN 2156-2202. doi: 10.1029/91JA02428. URL http://dx.doi.org/10.1029/91JA02428.

M. J. Buonsanto, M. E. Hagan, J. E. Salah, and B. G. Fejer. Solar cycle and seasonal variations in f region electrodynamics at millstone hill. *Journal of Geophysical Research: Space Physics*, 98(A9):15677–15683, 1993. ISSN 2156-2202. doi: 10.1029/93JA01187. URL http://dx.doi.org/10.1029/93JA01187.

J. L. Burch, P. H. Reiff, R. W. Spiro, R. A. Heelis, and S. A. Fields. Cusp region particle precipitation and ion convection for northward interplanetary magnetic field. *Geophysical Research Letters*, 7(5):393–396, 1980. ISSN 1944-8007. doi: 10.1029/GL007i005p00393. URL http://dx.doi.org/10.1029/GL007i005p00393.

W. J. Burke, M. C. Kelley, R. C. Sagalyn, M. Smiddy, and S. T. Lai. Polar cap electric field structures with a northward interplanetary magnetic field. *Geophysical Research Letters*, 6(1):21–24, 1979. ISSN 1944-8007. doi: 10.1029/GL006i001p00021. URL http://dx.doi.org/10.1029/GL006i001p00021.

R. G. Burnside, J. C. G. Walker, R. A. Behnke, and C. A. Gonzales. Polarization electric fields in the nighttime f layer at arecibo. *Journal of Geophysical Research: Space Physics*,

88(A8):6259–6266, 1983. ISSN 2156-2202. doi: 10.1029/JA088iA08p06259. URL http://dx.doi.org/10.1029/JA088iA08p06259.

Michael N. Caan, Robert L. McPherron, and Christopher T. Russell. Characteristics of the association between the interplanetary magnetic field and substorms. *Journal of Geophysical Research: Space Physics*, 82(29):4837–4842, 1977. doi: 10.1029/JA082i029p04837.

E. Camporeale. The challenge of machine learning in space weather: Nowcasting and forecasting. *Space Weather*, 17(8):1166–1207, 2019. doi: 10.1029/2018SW002061. URL https://agupubs.onlinelibrary.wiley.com/doi/abs/10.1029/2018SW002061.

L. A. Carpenter and V. W. J. H. Kirchhoff. Comparison of high-latitude and mid-latitude ionospheric electric fields. *Journal of Geophysical Research*, 80(13):1810–1814, 1975. ISSN 2156-2202. doi: 10.1029/JA080i013p01810. URL http://dx.doi.org/10.1029/JA080i013p01810.

M. O. Chandler, S. A. Fuselier, M. Lockwood, and T. E. Moore. Evidence of component merging equatorward of the cusp. *Journal of Geophysical Research: Space Physics*, 104 (A10):22623–22633, 1999. ISSN 2156-2202. doi: 10.1029/1999JA900175. URL http://dx.doi.org/10.1029/1999JA900175.

M. Chandorkar, E. Camporeale, and S. Wing. Probabilistic forecasting of the disturbance storm time index: An autoregressive gaussian process approach. *Space Weather*, 15(8): 1004–1019, 2017. doi: 10.1002/2017SW001627. URL https://agupubs.onlinelibrary.wiley.com/doi/abs/10.1002/2017SW001627.

G. Chisham, M. Lester, S. E. Milan, M. P. Freeman, W. A. Bristow, A. Grocott, K. A. McWilliams, J. M. Ruohoniemi, T. K. Yeoman, P. L. Dyson, R. A. Greenwald, T. Kikuchi, M. Pinnock, J. P. S. Rash, N. Sato, G. J. Sofko, J.-P. Villain,

and A. D. M. Walker. A decade of the super dual auroral radar network (superdarn): scientific achievements, new techniques and future directions. *Surveys in Geophysics*, 28(1):33–109, 2007. ISSN 1573-0956. doi: 10.1007/s10712-007-9017-8. URL http://dx.doi.org/10.1007/s10712-007-9017-8.

François Chollet et al. Keras. https://keras.io, 2015.

C. Robert Clauer, Zhonghua Xu, M. Maimaiti, J. Michael Ruohoneimi, Wayne Scales, Michael D. Hartinger, Michael J. Nicolls, Stephen Kaeppler, Frederick D. Wilder, and Ramon E. Lopez. Investigation of a rare event where the polar ionospheric reverse convection potential does not saturate during a period of extreme northward imf solar wind driving. *Journal of Geophysical Research: Space Physics*, 121(6):5422–5435, 2016. ISSN 2169-9402. doi: 10.1002/2016JA022557. URL http://dx.doi.org/10.1002/2016JA022557. 2016JA022557.

L. B. N. Clausen, J. B. H. Baker, J. M. Ruohoniemi, R. A. Greenwald, E. G. Thomas, S. G. Shepherd, E. R. Talaat, W. A. Bristow, Y. Zheng, A. J. Coster, and S. Sazykin. Large-scale observations of a subauroral polarization stream by midlatitude superdarn radars: Instantaneous longitudinal velocity variations. *Journal of Geophysical Research: Space Physics*, 117(A5):n/a–n/a, 2012. ISSN 2156-2202. doi: 10.1029/2011JA017232. URL http://dx.doi.org/10.1029/2011JA017232. A05306.

Lasse B. N. Clausen and Hannes Nickisch. Automatic classification of auroral images from the oslo auroral themis (oath) data set using machine learning. *Journal of Geophysical Research: Space Physics*, 123(7):5640–5647, 2018. doi: 10.1029/2018JA025274.

E. D. P. Cousins and S. G. Shepherd. A dynamical model of high-latitude convection derived from superdarn plasma drift measurements. *Journal of Geophysical Research: Space*

Physics, 115(A12):n/a–n/a, 2010. ISSN 2156-2202. doi: 10.1029/2010JA016017. URL http://dx.doi.org/10.1029/2010JA016017. A12329.

S. W. H. Cowley. A qualitative study of the reconnection between the earth's magnetic field and an interplanetary field of arbitrary orientation. *Radio Science*, 8(11):903–913, 1973. ISSN 1944-799X. doi: 10.1029/RS008i011p00903. URL http://dx.doi.org/10.1029/RS008i011p00903.

S. W. H. Cowley. Comments on the merging of nonantiparallel magnetic fields. *Journal of Geophysical Research*, 81(19):3455–3458, 1976. ISSN 2156-2202. doi: 10.1029/JA081i019p03455. URL http://dx.doi.org/10.1029/JA081i019p03455.

N. U. Crooker. Dayside merging and cusp geometry. *Journal of Geophysical Research: Space Physics*, 84(A3):951–959, 1979. ISSN 2156-2202. doi: 10.1029/JA084iA03p00951. URL http://dx.doi.org/10.1029/JA084iA03p00951.

N. U. Crooker. Mapping the merging potential from the magnetopause to the ionosphere through the dayside cusp. *Journal of Geophysical Research: Space Physics*, 93(A7):7338–7344, 1988. ISSN 2156-2202. doi: 10.1029/JA093iA07p07338. URL http://dx.doi.org/10.1029/JA093iA07p07338.

G. Crowley, D. J. Knipp, K. A. Drake, J. Lei, E. Sutton, and H. Lühr. Thermospheric density enhancements in the dayside cusp region during strong by conditions. *Geophysical Research Letters*, 37(7), 2010. doi: 10.1029/2009GL042143. URL https://agupubs.onlinelibrary.wiley.com/doi/abs/10.1029/2009GL042143.

Y. Le Cun, B. Boser, J. S. Denker, R. E. Howard, W. Habbard, L. D. Jackel, and D. Henderson. Handwritten digit recognition with a back-propagation network. In David S. Touretzky, editor, *Advances in Neural Information Processing Systems 2*, pages 396–404. Morgan Kaufmann Publishers Inc., San Francisco, CA, USA, 1990. ISBN 1-55860-100-7.

G. Cybenko. Approximation by superpositions of a sigmoidal function. *Mathematics of Control, Signals and Systems*, 2(4):303–314, Dec 1989. ISSN 1435-568X. doi: 10.1007/BF02551274. URL https://doi.org/10.1007/BF02551274.

F. Darrouzet, J. de Keyser, and V. Pierrard. *The Earth's Plasmasphere: A CLUSTER and IMAGE Perspective*. Springer New York, 2009. ISBN 9781441913234. URL https://books.google.com/books?id=d2vuugSeSWgC.

T. Neil Davis and Masahisa Sugiura. Auroral electrojet activity index ae and its universal time variations. *Journal of Geophysical Research (1896-1977)*, 71(3):785–801, 1966. doi: 10.1029/JZ071i003p00785.

S. de Larquier, P. Ponomarenko, A. J. Ribeiro, J. M. Ruohoniemi, J. B. H. Baker, K. T. Sterne, and M. Lester. On the spatial distribution of decameter scale subauroral ionospheric irregularities observed by superdarn radars. *Journal of Geophysical Research: Space Physics*, 118(8):5244–5254, 2013. ISSN 2169-9402. doi: 10.1002/jgra.50475. URL http://dx.doi.org/10.1002/jgra.50475.

Michael Denton and Joseph Borovsky. The superdense plasma sheet in the magnetosphere during high-speed-stream-driven storms: Plasma transport timescales. *Journal of Atmospheric and Solar-Terrestrial Physics*, 71:1045–1058, 07 2009. doi: 10.1016/j.jastp.2008.04.023.

Pedro Domingos. A few useful things to know about machine learning. *Commun. ACM*, 55 (10):78–87, October 2012. ISSN 0001-0782. doi: 10.1145/2347736.2347755. URL http://doi.acm.org/10.1145/2347736.2347755.

John C. Dorelli, Amitava Bhattacharjee, and Joachim Raeder. Separator reconnection at earth's dayside magnetopause under generic northward interplanetary magnetic field

conditions. *Journal of Geophysical Research: Space Physics*, 112(A2), 2007. doi: 10.1029/2006JA011877. URL https://agupubs.onlinelibrary.wiley.com/doi/abs/10.1029/2006JA011877.

Douglas P. Drob, John T. Emmert, John W. Meriwether, Jonathan J. Makela, Eelco Doornbos, Mark Conde, Gonzalo Hernandez, John Noto, Katherine A. Zawdie, Sarah E. McDonald, Joe D. Huba, and Jeff H. Klenzing. An update to the horizontal wind model (hwm): The quiet time thermosphere. *Earth and Space Science*, 2(7):301–319, 2015. ISSN 2333-5084. doi: 10.1002/2014EA000089. URL http://dx.doi.org/10.1002/2014EA000089. 2014EA000089.

J. W. Dungey. Interplanetary magnetic field and the auroral zones. *Phys. Rev. Lett.*, 6: 47–48, Jan 1961. doi: 10.1103/PhysRevLett.6.47. URL http://link.aps.org/doi/10.1103/PhysRevLett.6.47.

JW Dungey. The structure of the exosphere, or adventures in velocity space. *Geophysics, The Earth's Environment*, 1963.

R. C. Elphic, M. F. Thomsen, J. E. Borovsky, and D. J. McComas. Inner edge of the electron plasma sheet: Empirical models of boundary location. *Journal of Geophysical Research: Space Physics*, 104(A10):22679–22693, 1999. doi: 10.1029/1999JA900213. URL https://agupubs.onlinelibrary.wiley.com/doi/abs/10.1029/1999JA900213.

J. T. Emmert, B. G. Fejer, and D. P. Sipler. Climatology and latitudinal gradients of quiet time thermospheric neutral winds over millstone hill from fabry-perot interferometer measurements. *Journal of Geophysical Research: Space Physics*, 108(A5):n/a–n/a, 2003. ISSN 2156-2202. doi: 10.1029/2002JA009765. URL http://dx.doi.org/10.1029/2002JA009765. 1196.

J. T. Emmert, M. L. Faivre, G. Hernandez, M. J. Jarvis, J. W. Meriwether, R. J. Niciejewski, D. P. Sipler, and C. A. Tepley. Climatologies of nighttime upper thermospheric winds measured by ground-based fabry-perot interferometers during geomagnetically quiet conditions: 1. local time, latitudinal, seasonal, and solar cycle dependence. *Journal of Geophysical Research: Space Physics*, 111(A12):n/a–n/a, 2006. ISSN 2156-2202. doi: 10.1029/2006JA011948. URL http://dx.doi.org/10.1029/2006JA011948. A12302.

S. Eriksson, M. Maimaiti, J. B. H. Baker, K. J. Trattner, D. J. Knipp, and F. D. Wilder. Dual e × b flow responses in the dayside ionosphere to a sudden imf by rotation. *Geophysical Research Letters*, 44(13):6525–6533, 2017. doi: 10.1002/2017GL073374. URL https://agupubs.onlinelibrary.wiley.com/doi/abs/10.1002/2017GL073374.

Donald H. Fairfield. Average and unusual locations of the earth's magnetopause and bow shock. *Journal of Geophysical Research (1896-1977)*, 76(28):6700–6716, 1971. doi: 10.1029/JA076i028p06700. URL https://agupubs.onlinelibrary.wiley.com/doi/abs/10.1029/JA076i028p06700.

H. I. Fawaz, G. Forestier, J. Weber, L. Idoumghar, and P.-A. Muller. Deep learning for time series classification: a review. *Data Mining and Knowledge Discovery*, pages 1–47, 2019.

B. G. Fejer. F region plasma drifts over arecibo: Solar cycle, seasonal, and magnetic activity effects. *Journal of Geophysical Research: Space Physics*, 98(A8):13645–13652, 1993. ISSN 2156-2202. doi: 10.1029/93JA00953. URL http://dx.doi.org/10.1029/93JA00953.

B. G. Fejer, M. Blanc, and A. D. Richmond. Post-storm middle and low-latitude ionospheric electric fields effects. *Space Science Reviews*, 206(1):407–429, Mar 2017. ISSN 1572-9672. doi: 10.1007/s11214-016-0320-x. URL https://doi.org/10.1007/s11214-016-0320-x.

Y. I. Feldstein and Yu. I. Galperin. The auroral luminosity structure in the high-latitude upper atmosphere: Its dynamics and relationship to the large-scale struc-

ture of the earth's magnetosphere. *Reviews of Geophysics*, 23(3):217–275, 1985. doi: 10.1029/RG023i003p00217. URL https://agupubs.onlinelibrary.wiley.com/doi/abs/10.1029/RG023i003p00217.

Kostas Florios, Ioannis Kontogiannis, Sung-Hong Park, Jordan A Guerra, Federico Benvenuto, D Shaun Bloomfield, and Manolis K Georgoulis. Forecasting solar flares using magnetogram-based predictors and machine learning. *Solar Physics*, 293(2):28, 2018.

M. Förster and S. Haaland. Interhemispheric differences in ionospheric convection: Cluster edi observations revisited. *Journal of Geophysical Research: Space Physics*, 120(7):5805–5823, 2015. doi: 10.1002/2014JA020774. URL https://agupubs.onlinelibrary.wiley.com/doi/abs/10.1002/2014JA020774.

M. Förster, G. Paschmann, S. E. Haaland, J. M. Quinn, R. B. Torbert, H. Vaith, and C. A. Kletzing. High-latitude plasma convection from cluster edi: variances and solar wind correlations. *Annales Geophysicae*, 25(7):1691–1707, 2007. doi: 10.5194/angeo-25-1691-2007. URL https://www.ann-geophys.net/25/1691/2007/.

M. Förster, S. E. Haaland, G. Paschmann, J. M. Quinn, R. B. Torbert, H. Vaith, and C. A. Kletzing. High-latitude plasma convection during northward imf as derived from in-situ magnetospheric cluster edi measurements. *Annales Geophysicae*, 26(9):2685–2700, 2008. doi: 10.5194/angeo-26-2685-2008. URL http://www.ann-geophys.net/26/2685/2008/.

Richard Fozzard, Gary Bradshaw, and Louis Ceci. A connectionist expert system that actually works. In *Advances in neural information processing systems*, pages 248–255, 1989.

M. P. Freeman and S. K. Morley. A minimal substorm model that explains the observed statistical distribution of times between substorms. *Geophysical Research Letters*, 31(12), 2004. doi: 10.1029/2004GL019989.

M. P. Freeman and S. K. Morley. No evidence for externally triggered substorms based on superposed epoch analysis of imf bz. *Geophysical Research Letters*, 36(21), 2009. doi: 10.1029/2009GL040621.

Mervyn P. Freeman, Colin Forsyth, and I. Jonathan Rae. The influence of substorms on extreme rates of change of the surface horizontal magnetic field in the u.k. *Space Weather*, 0, 2019. doi: 10.1029/2018SW002148.

H. U. Frey, S. B. Mende, V. Angelopoulos, and E. F. Donovan. Substorm onset observations by image-fuv. *Journal of Geophysical Research: Space Physics*, 109(A10), 2004. doi: 10.1029/2004JA010607.

T.J. Fuller-Rowell, G.H. Millward, A.D. Richmond, and M.V. Codrescu. Storm-time changes in the upper atmosphere at low latitudes. *Journal of Atmospheric and Solar-Terrestrial Physics*, 64(12):1383 – 1391, 2002. ISSN 1364-6826. doi: https://doi.org/10.1016/S1364-6826(02)00101-3. URL http://www.sciencedirect.com/science/article/pii/S1364682602001013. Equatorial Aeronomy.

S. A. Fuselier, K. J. Trattner, and S. M. Petrinec. Cusp observations of high- and low-latitude reconnection for northward interplanetary magnetic field. *Journal of Geophysical Research: Space Physics*, 105(A1):253–266, 2000. ISSN 2156-2202. doi: 10.1029/1999JA900422. URL http://dx.doi.org/10.1029/1999JA900422.

S. A. Fuselier, K. J. Trattner, and S. M. Petrinec. Antiparallel and component reconnection at the dayside magnetopause. *Journal of Geophysical Research: Space Physics*, 116(A10): n/a–n/a, 2011. ISSN 2156-2202. doi: 10.1029/2011JA016888. URL http://dx.doi.org/10.1029/2011JA016888. A10227.

Valeriy V. Gavrishchaka and Supriya B. Ganguli. Optimization of the neural-network geomagnetic model for forecasting large-amplitude substorm events. *Journal of Geophysical*

Research: Space Physics, 106(A4):6247–6257, 2001. doi: 10.1029/2000JA900137. URL https://agupubs.onlinelibrary.wiley.com/doi/abs/10.1029/2000JA900137.

J. W. Gjerloev. The supermag data processing technique. *Journal of Geophysical Research: Space Physics*, 117(A9), 2012. doi: 10.1029/2012JA017683.

H. Gleisner and H. Lundstedt. Response of the auroral electrojets to the solar wind modeled with neural networks. *Journal of Geophysical Research: Space Physics*, 102(A7):14269–14278, 1997. doi: 10.1029/96JA03068. URL https://agupubs.onlinelibrary.wiley.com/doi/abs/10.1029/96JA03068.

H. Gleisner, H. Lundstedt, and P. Wintoft. Predicting geomagnetic storms from solar-wind data using time-delay neural networks. *Annales Geophysicae*, 14(7):679–686, 1996. doi: 10.1007/s00585-996-0679-1. URL https://www.ann-geophys.net/14/679/1996/.

Xavier Glorot and Yoshua Bengio. Understanding the difficulty of training deep feedforward neural networks. In Yee Whye Teh and Mike Titterington, editors, *Proceedings of the Thirteenth International Conference on Artificial Intelligence and Statistics*, volume 9 of *Proceedings of Machine Learning Research*, pages 249–256, Chia Laguna Resort, Sardinia, Italy, 13–15 May 2010. PMLR.

C. C. Goodrich, T. I. Pulkkinen, J. G. Lyon, and V. G. Merkin. Magnetospheric convection during intermediate driving: Sawtooth events and steady convection intervals as seen in lyon-fedder-mobarry global mhd simulations. *Journal of Geophysical Research: Space Physics*, 112(A8), 2007. doi: 10.1029/2006JA012155. URL https://agupubs.onlinelibrary.wiley.com/doi/abs/10.1029/2006JA012155.

J. T. Gosling, M. F. Thomsen, S. J. Bame, R. C. Elphic, and C. T. Russell. Plasma flow reversals at the dayside magnetopause and the origin of asymmetric polar cap convection.

Journal of Geophysical Research: Space Physics, 95(A6):8073–8084, 1990. ISSN 2156-2202. doi: 10.1029/JA095iA06p08073. URL http://dx.doi.org/10.1029/JA095iA06p08073.

J. T. Gosling, M. F. Thomsen, S. J. Bame, R. C. Elphic, and C. T. Russell. Observations of reconnection of interplanetary and lobe magnetic field lines at the high-latitude magnetopause. *Journal of Geophysical Research: Space Physics*, 96(A8):14097–14106, 1991. ISSN 2156-2202. doi: 10.1029/91JA01139. URL http://dx.doi.org/10.1029/91JA01139.

R. A. Greenwald, K. B. Baker, R. A. Hutchins, and C. Hanuise. An hf phased-array radar for studying small-scale structure in the high-latitude ionosphere. *Radio Science*, 20(1): 63–79, 1985. ISSN 1944-799X. doi: 10.1029/RS020i001p00063. URL http://dx.doi.org/10.1029/RS020i001p00063.

Raymond A. Greenwald, Kjellmar Oksavik, Philip J. Erickson, Frank D. Lind, J. Michael Ruohoniemi, Joseph B. H. Baker, and Jesper W. Gjerloev. Identification of the temperature gradient instability as the source of decameter-scale ionospheric irregularities on plasmapause field lines. *Geophysical Research Letters*, 33(18):n/a–n/a, 2006. ISSN 1944-8007. doi: 10.1029/2006GL026581. URL http://dx.doi.org/10.1029/2006GL026581. L18105.

Robin Gubby and John Evans. Space environment effects and satellite design. *Journal of Atmospheric and Solar-Terrestrial Physics*, 64(16):1723 – 1733, 2002. ISSN 1364-6826. doi: https://doi.org/10.1016/S1364-6826(02)00122-0. Space Weather Effects on Technological Systems.

M. S. Gussenhoven, D. A. Hardy, and N. Heinemann. Systematics of the equatorward diffuse auroral boundary. *Journal of Geophysical Research: Space Physics*, 88(A7):5692–5708, 1983. doi: 10.1029/JA088iA07p05692. URL https://agupubs.onlinelibrary.wiley.com/doi/abs/10.1029/JA088iA07p05692.

S. E. Haaland, G. Paschmann, M. Förster, J. M. Quinn, R. B. Torbert, C. E. McIlwain, H. Vaith, P. A. Puhl-Quinn, and C. A. Kletzing. High-latitude plasma convection from cluster edi measurements: method and imf-dependence. *Annales Geophysicae*, 25(1):239–253, 2007. doi: 10.5194/angeo-25-239-2007. URL https://www.ann-geophys.net/25/239/2007/.

M. R. Hairston and R. A. Heelis. Model of the high-latitude ionospheric convection pattern during southward interplanetary magnetic field using de 2 data. *Journal of Geophysical Research: Space Physics*, 95(A3):2333–2343, 1990. doi: 10.1029/JA095iA03p02333. URL https://agupubs.onlinelibrary.wiley.com/doi/abs/10.1029/JA095iA03p02333.

D. A. Hardy, L. K. Schmitt, M. S. Gussenhoven, F. J. Marshall, H. C. Yeh, T. L. Schumaker, A. Hube, and J. Pantazis. Precipitating electron and ion detectors (SSJ/4) for the block 5D/flights 6-10 DMSP (Defense meteorological satellite program) satellites: Calibration and data presentation. *Rep. AFGL-TR-84-0317*, pages Air Force Geophys. Lab., Bedford, Mass., 1984.

D. A. Hardy, M. S. Gussenhoven, and E. Holeman. A statistical model of auroral electron precipitation. *Journal of Geophysical Research: Space Physics*, 90(A5):4229–4248, 1985. doi: 10.1029/JA090iA05p04229. URL https://agupubs.onlinelibrary.wiley.com/doi/abs/10.1029/JA090iA05p04229.

David A. Hardy, M. S. Gussenhoven, and D. Brautigam. A statistical model of auroral ion precipitation. *Journal of Geophysical Research: Space Physics*, 94(A1):370–392, 1989. doi: 10.1029/JA094iA01p00370. URL https://agupubs.onlinelibrary.wiley.com/doi/abs/10.1029/JA094iA01p00370.

R.M. Harper and J.C.G. Walker. Comparison of electrical conductivities in the e-and f-regions of the nocturnal ionosphere. *Planetary and Space Science*, 25(2):197 – 199, 1977.

ISSN 0032-0633. doi: https://doi.org/10.1016/0032-0633(77)90026-5. URL http://www.sciencedirect.com/science/article/pii/0032063377900265.

Kaiming He, Xiangyu Zhang, Shaoqing Ren, and Jian Sun. Deep residual learning for image recognition. *2016 IEEE Conference on Computer Vision and Pattern Recognition (CVPR)*, Jun 2016. doi: 10.1109/cvpr.2016.90. URL http://dx.doi.org/10.1109/CVPR.2016.90.

R. A. Heelis and W. R. Coley. East-west ion drifts at mid-latitudes observed by dynamics explorer 2. *Journal of Geophysical Research: Space Physics*, 97(A12):19461–19469, 1992. ISSN 2156-2202. doi: 10.1029/92JA01840. URL http://dx.doi.org/10.1029/92JA01840.

R. A. Heelis and M. R. Hairston. Studies of ionospheric dynamics utilizing data from dmsp. *Rep. GL-TR-90-0047*, pages 39, Geophys. Lab., Hanscom AFB, Mass., 1990.

Verena Heidrich-Meisner and Robert F. Wimmer-Schweingruber. Chapter 16 - solar wind classification via k-means clustering algorithm. In Enrico Camporeale, Simon Wing, and Jay R. Johnson, editors, *Machine Learning Techniques for Space Weather*, pages 397 – 424. Elsevier, 2018. ISBN 978-0-12-811788-0. doi: https://doi.org/10.1016/B978-0-12-811788-0.00016-0. URL http://www.sciencedirect.com/science/article/pii/B9780128117880000160.

Moritz Helmstaedter, Kevin L Briggman, Srinivas C Turaga, Viren Jain, H Sebastian Seung, and Winfried Denk. Connectomic reconstruction of the inner plexiform layer in the mouse retina. *Nature*, 500(7461):168, 2013.

M. G. Henderson, G. D. Reeves, R. D. Belian, and J. S. Murphree. Observations of magnetospheric substorms occurring with no apparent solar wind/imf trigger. *Journal of Geophysical Research: Space Physics*, 101(A5):10773–10791, 1996. doi: 10.1029/96JA00186.

J. P. Heppner and N. C. Maynard. Empirical high-latitude electric field models. *Journal of Geophysical Research: Space Physics*, 92(A5):4467–4489, 1987. ISSN 2156-2202. doi: 10.1029/JA092iA05p04467. URL http://dx.doi.org/10.1029/JA092iA05p04467.

J. V. Hernandez, T. Tajima, and W. Horton. Neural net forecasting for geomagnetic activity. *Geophysical Research Letters*, 20(23):2707–2710, 1993. doi: 10.1029/93GL02848. URL https://agupubs.onlinelibrary.wiley.com/doi/abs/10.1029/93GL02848.

G. Hinton, L. Deng, D. Yu, G. E. Dahl, A. Mohamed, N. Jaitly, A. Senior, V. Vanhoucke, P. Nguyen, T. N. Sainath, and B. Kingsbury. Deep neural networks for acoustic modeling in speech recognition: The shared views of four research groups. *IEEE Signal Processing Magazine*, 29(6):82–97, Nov 2012. doi: 10.1109/MSP.2012.2205597.

R. H. Holzworth and C.-I. Meng. Mathematical representation of the auroral oval. *Geophysical Research Letters*, 2(9):377–380, 1975. ISSN 1944-8007. doi: 10.1029/GL002i009p00377. URL http://dx.doi.org/10.1029/GL002i009p00377.

R. B. Horne, S. A. Glauert, N. P. Meredith, D. Boscher, V. Maget, D. Heynderickx, and D. Pitchford. Space weather impacts on satellites and forecasting the earth's electron radiation belts with spacecast. *Space Weather*, 11(4):169–186, 2013. doi: 10.1002/swe.20023.

Kurt Hornik, Maxwell Stinchcombe, and Halbert White. Multilayer feedforward networks are universal approximators. *Neural Networks*, 2(5):359 – 366, 1989. ISSN 0893-6080. doi: https://doi.org/10.1016/0893-6080(89)90020-8. URL http://www.sciencedirect.com/science/article/pii/0893608089900208.

Chao-Song Huang, G. J. Sofko, A. V. Koustov, D. A. Andre, J. M. Ruohoniemi, R. A. Greenwald, and M. R. Hairston. Evolution of ionospheric multicell convection during northward

interplanetary magnetic field with |bz /by | > 1. *Journal of Geophysical Research: Space Physics*, 105(A12):27095–27107, 2000. ISSN 2156-2202. doi: 10.1029/2000JA000163. URL http://dx.doi.org/10.1029/2000JA000163.

Chao-Song Huang, Stanislav Sazykin, Jorge L. Chau, Naomi Maruyama, and Michael C. Kelley. Penetration electric fields: Efficiency and characteristic time scale. *Journal of Atmospheric and Solar-Terrestrial Physics*, 69(10):1135 – 1146, 2007. ISSN 1364-6826. doi: https://doi.org/10.1016/j.jastp.2006.08.016. URL http://www.sciencedirect.com/science/article/pii/S1364682607000636. Storm-Time Penetration Electric Fields and their Effects: Magnetospheric and Ionospheric Perspectives.

J. D. Hunter. Matplotlib: A 2d graphics environment. *Computing In Science & Engineering*, 9(3):90–95, 2007. doi: 10.1109/MCSE.2007.55.

Egor A Illarionov and Andrey G Tlatov. Segmentation of coronal holes in solar disc images with a convolutional neural network. *Monthly Notices of the Royal Astronomical Society*, 481(4):5014–5021, Oct 2018. ISSN 1365-2966. doi: 10.1093/mnras/sty2628. URL http://dx.doi.org/10.1093/mnras/sty2628.

Toshihiko Iyemori. Storm-time magnetospheric currents inferred from mid-latitude geomagnetic field variations. *Journal of geomagnetism and geoelectricity*, 42(11):1249–1265, 1990. doi: 10.5636/jgg.42.1249.

R. K. Jaggi and R. A. Wolf. Self-consistent calculation of the motion of a sheet of ions in the magnetosphere. *Journal of Geophysical Research*, 78(16):2852–2866, 1973. ISSN 2156-2202. doi: 10.1029/JA078i016p02852. URL http://dx.doi.org/10.1029/JA078i016p02852.

Jay R. Johnson and Simon Wing. External versus internal triggering of substorms: An

information-theoretical approach. *Geophysical Research Letters*, 41(16):5748–5754, 2014. doi: 10.1002/2014GL060928.

J. R. Kan and L. C. Lee. Energy coupling function and solar wind-magnetosphere dynamo. *Geophysical Research Letters*, 6(7):577–580, 1979. doi: 10.1029/GL006i007p00577. URL https://agupubs.onlinelibrary.wiley.com/doi/abs/10.1029/GL006i007p00577.

Fazle Karim, Somshubra Majumdar, Houshang Darabi, and Samuel Harford. Multivariate lstm-fcns for time series classification. *arXiv preprint arXiv:1801.04503*, 2018.

Z. Kaymaz. Imp 8 magnetosheath field comparisons with models. *Annales Geophysicae*, 16 (4):376–387, Apr 1998. ISSN 1432-0576. doi: 10.1007/s00585-998-0376-3. URL https://doi.org/10.1007/s00585-998-0376-3.

M. C. Kelley, B. G. Fejer, and C. A. Gonzales. An explanation for anomalous equatorial ionospheric electric fields associated with a northward turning of the interplanetary magnetic field. *Geophysical Research Letters*, 6(4):301–304, 1979. ISSN 1944-8007. doi: 10.1029/GL006i004p00301. URL http://dx.doi.org/10.1029/GL006i004p00301.

M.C. Kelley. *The Earth's Ionosphere: Plasma Physics and Electrodynamics*. ISSN. Elsevier Science, 2009. ISBN 9780080916576. URL https://books.google.com/books?id=3GlWQnjBQNgC.

M.C. Kelley and R.A. Heelis. *The Earth's Ionosphere: Plasma Physics and Electrodynamics*. International geophysics series. Academic Press, 1989. ISBN 9780124040120. URL https://books.google.com/books?id=-1eIoCUUZuoC.

Michael C. Kelley, Jonathan J. Makela, Jorge L. Chau, and Michael J. Nicolls. Penetration of the solar wind electric field into the magnetosphere/ionosphere system. *Geophysical*

Research Letters, 30(4):n/a–n/a, 2003. ISSN 1944-8007. doi: 10.1029/2002GL016321. URL http://dx.doi.org/10.1029/2002GL016321. 1158.

L. Kepko, R. L. McPherron, O. Amm, S. Apatenkov, W. Baumjohann, J. Birn, M. Lester, R. Nakamura, T. I. Pulkkinen, and V. Sergeev. Substorm current wedge revisited. *Space Science Reviews*, 190(1):1–46, Jul 2015. doi: 10.1007/s11214-014-0124-9. URL https://doi.org/10.1007/s11214-014-0124-9.

Diederik P Kingma and Jimmy Ba. Adam: A method for stochastic optimization. *arXiv preprint arXiv:1412.6980*, 2014.

M. G. Kivelson and C. T. Russell. *Introduction to Space Physics*. Cambridge University Press, April 1995.

Alex Krizhevsky, Ilya Sutskever, and Geoffrey E. Hinton. Imagenet classification with deep convolutional neural networks. *Commun. ACM*, 60(6):84–90, May 2017. ISSN 0001-0782. doi: 10.1145/3065386. URL http://doi.acm.org/10.1145/3065386.

A. Kullen and T. Karlsson. On the relation between solar wind, pseudobreakups, and substorms. *Journal of Geophysical Research: Space Physics*, 109(A12), 2004. doi: 10.1029/2004JA010488.

A. Kullen, S. Ohtani, and T. Karlsson. Geomagnetic signatures of auroral substorms preceded by pseudobreakups. *Journal of Geophysical Research: Space Physics*, 114(A4), 2009. doi: 10.1029/2008JA013712.

B. S. R. Kunduri, J. B. H. Baker, J. M. Ruohoniemi, L. B. N. Clausen, A. Grocott, E. G. Thomas, M. P. Freeman, and E. R. Talaat. An examination of inter-hemispheric conjugacy in a subauroral polarization stream. *Journal of Geophysical Research: Space Physics*, 117

(A8):n/a–n/a, 2012. ISSN 2156-2202. doi: 10.1029/2012JA017784. URL http://dx.doi.org/10.1029/2012JA017784. A08225.

B. S. R. Kunduri, J. B. H. Baker, J. M. Ruohoniemi, E. G. Thomas, S. G. Shepherd, and K. T. Sterne. Statistical characterization of the large-scale structure of the subauroral polarization stream. *Journal of Geophysical Research: Space Physics*, 122(6):6035–6048, 2017. ISSN 2169-9402. doi: 10.1002/2017JA024131. URL http://dx.doi.org/10.1002/2017JA024131. 2017JA024131.

B. S. R. Kunduri, J. B. H. Baker, J. M. Ruohoniemi, N. Nishitani, K. Oksavik, P. J. Erickson, A. J. Coster, S. G. Shepherd, W. A. Bristow, and E. S. Miller. A new empirical model of the subauroral polarization stream. *Journal of Geophysical Research: Space Physics*, 0 (0), 2018a. doi: 10.1029/2018JA025690. URL https://agupubs.onlinelibrary.wiley.com/doi/abs/10.1029/2018JA025690.

B. S. R. Kunduri, J. B. H. Baker, J. M. Ruohoniemi, S. Sazykin, K. Oksavik, M. Maimaiti, P. J. Chi, and M. J. Engebretson. Recent developments in our knowledge of inner magnetosphere-ionosphere convection. *Journal of Geophysical Research: Space Physics*, 0(ja), 2018b. doi: 10.1029/2018JA025914. URL https://agupubs.onlinelibrary.wiley.com/doi/abs/10.1029/2018JA025914.

Yann LeCun, Yoshua Bengio, and Geoffrey Hinton. Deep learning. *nature*, 521(7553):436, 2015. doi: 10.1038/nature14539.

D.-Y. Lee, K.-C. Choi, S. Ohtani, J. H. Lee, K. C. Kim, K. S. Park, and K.-H. Kim. Can intense substorms occur under northward imf conditions? *Journal of Geophysical Research: Space Physics*, 115(A1), 2010. doi: 10.1029/2009JA014480.

Wei-Meng Lee. *Supervised Learning—Classification Using Logistic Regression*, chapter 7, pages 151–175. John Wiley & Sons, Ltd, 2019. ISBN 9781119557500. doi: 10.

1002/9781119557500.ch7. URL https://onlinelibrary.wiley.com/doi/abs/10.1002/9781119557500.ch7.

Solène Lejosne and F. S. Mozer. Typical values of the electric drift e x b/b2 in the inner radiation belt and slot region as determined from van allen probe measurements. *Journal of Geophysical Research: Space Physics*, 121(12):12,014–12,024, 2016. ISSN 2169-9402. doi: 10.1002/2016JA023613. URL http://dx.doi.org/10.1002/2016JA023613. 2016JA023613.

Solène Lejosne and F. S. Mozer. Magnetic activity dependence of the electric drift below l = 3. *Geophysical Research Letters*, 45(9):3775–3782, 2018. doi: 10.1029/2018GL077873. URL https://agupubs.onlinelibrary.wiley.com/doi/abs/10.1029/2018GL077873.

Xinlin Li, Kap Soo Oh, and M. Temerin. Prediction of the al index using solar wind parameters. *Journal of Geophysical Research: Space Physics*, 112(A6), 2007. doi: 10.1029/2006JA011918.

Maxwell W. Libbrecht and William Stafford Noble. Machine learning applications in genetics and genomics. *Nature Reviews Genetics*, 16:321 EP –, May 2015. URL https://doi.org/10.1038/nrg3920. Review Article.

Dong Lin, Wenbin Wang, Wayne A. Scales, Kevin Pham, Jing Liu, Binzheng Zhang, Viacheslav Merkin, Xueling Shi, Bharat Kunduri, and Maimaitirebike Maimaiti. Saps in the 17 march 2013 storm event: Initial results from the coupled magnetosphere-ionosphere-thermosphere model. *Journal of Geophysical Research: Space Physics*, 124(7):6212–6225, 2019. doi: 10.1029/2019JA026698. URL https://agupubs.onlinelibrary.wiley.com/doi/abs/10.1029/2019JA026698.

K. Liou, P. T. Newell, and C.-I Meng. Seasonal effects on auroral particle acceleration and precipitation. *Journal of Geophysical Research: Space Physics*, 106(A4):5531–5542, 2001.

doi: 10.1029/1999JA000391. URL https://agupubs.onlinelibrary.wiley.com/doi/abs/10.1029/1999JA000391.

Kan Liou. Polar ultraviolet imager observation of auroral breakup. *Journal of Geophysical Research: Space Physics*, 115(A12), 2010. doi: 10.1029/2010JA015578.

M. Lockwood and S. W. H. Cowley. Comment on "a statistical study of the ionospheric convection response to changing interplanetary magnetic field conditions using the assimilative mapping of ionospheric electrodynamics techniqu e" by a.j. ridley et al. *Journal of Geophysical Research: Space Physics*, 104(A3):4387–4391, 1999. ISSN 2156-2202. doi: 10.1029/1998JA900145. URL http://dx.doi.org/10.1029/1998JA900145.

C. A. Loewe and G. W. Prölss. Classification and mean behavior of magnetic storms. *Journal of Geophysical Research: Space Physics*, 102(A7):14209–14213, 1997. doi: 10.1029/96JA04020. URL https://agupubs.onlinelibrary.wiley.com/doi/abs/10.1029/96JA04020.

T. M. Loto'aniu, H. J. Singer, J. V. Rodriguez, J. Green, W. Denig, D. Biesecker, and V. Angelopoulos. Space weather conditions during the galaxy 15 spacecraft anomaly. *Space Weather*, 13(8):484–502, 2015. doi: 10.1002/2015SW001239. URL https://agupubs.onlinelibrary.wiley.com/doi/abs/10.1002/2015SW001239.

J. G. Luhmann, R. J. Walker, C. T. Russell, N. U. Crooker, J. R. Spreiter, and S. S. Stahara. Patterns of potential magnetic field merging sites on the dayside magnetopause. *Journal of Geophysical Research: Space Physics*, 89(A3):1739–1742, 1984. ISSN 2156-2202. doi: 10.1029/JA089iA03p01739. URL http://dx.doi.org/10.1029/JA089iA03p01739.

H. Lühr, M. Rother, W. Köhler, P. Ritter, and L. Grunwaldt. Thermospheric up-welling in the cusp region: Evidence from champ observations. *Geophysical Research Letters*, 31(6),

2004. doi: 10.1029/2003GL019314. URL https://agupubs.onlinelibrary.wiley.com/doi/abs/10.1029/2003GL019314.

Hermann Lühr, Chao Xiong, and Nils Olsen. Near-earth magnetic field effects of large-scale magnetospheric currents. *Space Science Reviews*, 07 2016. doi: 10.1007/s11214-016-0267-y.

A. T. Y. Lui. A synthesis of magnetospheric substorm models. *Journal of Geophysical Research: Space Physics*, 96(A2):1849–1856, 1991. doi: 10.1029/90JA02430.

A. T. Y. Lui. Current disruption in the earth's magnetosphere: Observations and models. *Journal of Geophysical Research: Space Physics*, 101(A6):13067–13088, 1996. doi: 10.1029/96JA00079.

A. T. Y. Lui. Tutorial on geomagnetic storms and substorms. *IEEE Transactions on Plasma Science*, 28(6):1854–1866, Dec 2000. ISSN 0093-3813. doi: 10.1109/27.902214.

H. Lundstedt and P. Wintoft. Prediction of geomagnetic storms from solar wind data with the use of a neural network. *Annales Geophysicae*, 12(1):19–24, 1994. doi: 10.1007/s00585-994-0019-2. URL https://www.ann-geophys.net/12/19/1994/.

Bingxian Luo, Xinlin Li, M. Temerin, and Siqing Liu. Prediction of the au, al, and ae indices using solar wind parameters. *Journal of Geophysical Research: Space Physics*, 118(12):7683–7694, 2013. doi: 10.1002/2013JA019188.

L. R. Lyons. A new theory for magnetospheric substorms. *Journal of Geophysical Research: Space Physics*, 100(A10):19069–19081, 1995. doi: 10.1029/95JA01344.

L. R. Lyons, G. T. Blanchard, J. C. Samson, R. P. Lepping, T. Yamamoto, and T. Moretto. Coordinated observations demonstrating external substorm triggering. *Journal of Geophysical Research: Space Physics*, 102(A12):27039–27051, 1997. doi: 10.1029/97JA02639.

M. Maimaiti, J. M. Ruohoniemi, J. B. H. Baker, C. R. Clauer, Michael J. Nicolls, and Marc R. Hairston. Risr-n observations of the imf by influence on reverse convection during extreme northward imf. *Journal of Geophysical Research: Space Physics*, 122(3):3707–3720, 2017. doi: 10.1002/2016JA023612. URL https://agupubs.onlinelibrary.wiley.com/doi/abs/10.1002/2016JA023612.

M. Maimaiti, J. M. Ruohoniemi, J. B. H. Baker, and A. J. Ribeiro. Statistical study of nightside quiet time midlatitude ionospheric convection. *Journal of Geophysical Research: Space Physics*, 123(3):2228–2240, 2018. doi: 10.1002/2017JA024903. URL https://agupubs.onlinelibrary.wiley.com/doi/abs/10.1002/2017JA024903.

M. Maimaiti, J. B. H. Baker, J. M. Ruohoniemi, and B. Kunduri. Morphology of nightside subauroral ionospheric convection: Monthly, seasonal, kp, and imf dependencies. *Journal of Geophysical Research: Space Physics*, 124(6):4608–4626, 2019a. doi: 10.1029/2018JA026268. URL https://agupubs.onlinelibrary.wiley.com/doi/abs/10.1029/2018JA026268.

M. Maimaiti, B. Kunduri, J. M. Ruohoniemi, J. B. H. Baker, and Leanna L. House. A deep learning-based approach to forecast the onset of magnetic substorms. *Space Weather*, n/a (n/a), 2019b. doi: 10.1029/2019SW002251. URL https://agupubs.onlinelibrary.wiley.com/doi/abs/10.1029/2019SW002251.

Naomi Maruyama, Stanislav Sazykin, Robert W. Spiro, David Anderson, Adela Anghel, Richard A. Wolf, Frank R. Toffoletto, Timothy J. Fuller-Rowell, Mihail V. Codrescu, Arthur D. Richmond, and George H. Millward. Modeling storm-time electrodynamics of the low-latitude ionosphere–thermosphere system: Can long lasting disturbance electric fields be accounted for? *Journal of Atmospheric and Solar-Terrestrial Physics*, 69(10):1182 – 1199, 2007. ISSN 1364-6826. doi: https://doi.org/10.1016/j.jastp.2006.08.020. URL

http://www.sciencedirect.com/science/article/pii/S1364682607000673. Storm-Time Penetration Electric Fields and their Effects: Magnetospheric and Ionospheric Perspectives.

D.J. McComas, S.J. Bame, P. Barker, W.C. Feldman, J.L. Phillips, P. Riley, and J.W. Griffee. Solar wind electron proton alpha monitor (swepam) for the advanced composition explorer. *Space Science Reviews*, 86(1-4):563–612, 1998. ISSN 0038-6308. doi: 10.1023/A:1005040232597. URL http://dx.doi.org/10.1023/A%3A1005040232597.

Ryan M. McGranaghan, Anthony J. Mannucci, Brian Wilson, Chris A Mattmann, and Richard Chadwick. New capabilities for prediction of high-latitude ionospheric scintillation: A novel approach with machine learning. *Space Weather*, 16(11):1817–1846, 2018. doi: 10.1029/2018SW002018. URL https://agupubs.onlinelibrary.wiley.com/doi/abs/10.1029/2018SW002018.

Wes McKinney. Data structures for statistical computing in python. In Stéfan van der Walt and Jarrod Millman, editors, *Proceedings of the 9th Python in Science Conference*, pages 51 – 56. SciPy Conference, 2010.

R. L. McPherron, C. T. Russell, and M. P. Aubry. Satellite studies of magnetospheric substorms on august 15, 1968: 9. phenomenological model for substorms. *Journal of Geophysical Research: Space Physics*, 78(16):3131–3149, 1973. doi: 10.1029/JA078i016p03131.

Robert L. McPherron. Magnetospheric substorms. *Reviews of Geophysics*, 17(4):657–681, 1979. doi: 10.1029/RG017i004p00657. URL https://agupubs.onlinelibrary.wiley.com/doi/abs/10.1029/RG017i004p00657.

Robert L. McPherron and Xiangning Chu. Relation of the auroral substorm to the substorm current wedge. *Geoscience Letters*, 3(1):12, Apr 2016. ISSN 2196-4092. doi: 10.1186/s40562-016-0044-5. URL https://doi.org/10.1186/s40562-016-0044-5.

Robert L. McPherron, James M. Weygand, and Tung-Shin Hsu. Response of the earth's magnetosphere to changes in the solar wind. *Journal of Atmospheric and Solar-Terrestrial Physics*, 70(2):303 – 315, 2008. ISSN 1364-6826. doi: https://doi.org/10.1016/j.jastp.2007.08.040. Recent Observations and Simulations of the Sun-Earth System.

Michel Menvielle, Toshihiko Iyemori, Aurélie Marchaudon, and Masahito Nosé. Geomagnetic indices. In *Geomagnetic observations and models*, pages 183–228. Springer, 2011.

Ronald T. Merrill, M.W. McElhinny, and P.L. McFadden. *The Magnetic Field of the Earth: Paleomagnetism, the Core, and the Deep Mantle*. International geophysics series. Academic Press, 1998. ISBN 9780124912465. URL https://books.google.com/books?id=96APl4nK9lIC.

K. Jarrod Millman and Michael Aivazis. Python for scientists and engineers. *Computing in Science & Engineering*, 13(2):9–12, March-April 2011. doi: 10.1109/MCSE.2011.36.

Tom Michael Mitchell. *The discipline of machine learning*, volume 9. Carnegie Mellon University, School of Computer Science, Machine Learning …, 2006.

Y. Miyashita, Y. Kamide, K. Liou, C.-C. Wu, A. Ieda, N. Nishitani, S. Machida, Y. Saito, and T. Mukai. Successive substorm expansions during a period of prolonged northward interplanetary magnetic field. *Journal of Geophysical Research: Space Physics*, 116(A9), 2011. doi: 10.1029/2011JA016719.

T. E. Moore, M.-C. Fok, and M. O. Chandler. The dayside reconnection x line. *Journal of Geophysical Research: Space Physics*, 107(A10):SMP 26–1–SMP 26–7, 2002. ISSN 2156-2202. doi: 10.1029/2002JA009381. URL http://dx.doi.org/10.1029/2002JA009381. 1332.

S. K. Morley and M. P. Freeman. On the association between northward turnings of the

interplanetary magnetic field and substorm onsets. *Geophysical Research Letters*, 34(8), 2007. doi: 10.1029/2006GL028891.

D.L. Murr and W.J. Hughes. The coherence between the imf and high-latitude ionospheric flows: The dayside magnetosphere–ionosphere low-pass filter. *Journal of Atmospheric and Solar-Terrestrial Physics*, 69(3):223 – 233, 2007. ISSN 1364-6826. doi: https://doi.org/10.1016/j.jastp.2006.07.019. URL http://www.sciencedirect.com/science/article/pii/S1364682606002628. Global Aspects of Magnetosphere-Ionosphere Coupling.

P.T. Newell and J. W. Gjerloev. Evaluation of supermag auroral electrojet indices as indicators of substorms and auroral power. *Journal of Geophysical Research: Space Physics*, 116(A12), 2011a. doi: 10.1029/2011JA016779.

P.T. Newell and J. W. Gjerloev. Substorm and magnetosphere characteristic scales inferred from the supermag auroral electrojet indices. *Journal of Geophysical Research: Space Physics*, 116(A12), 2011b. doi: 10.1029/2011JA016936.

P.T. Newell and Kan Liou. Solar wind driving and substorm triggering. *Journal of Geophysical Research: Space Physics*, 116(A3), 2011. doi: 10.1029/2010JA016139.

P.T. Newell, T. Sotirelis, K. Liou, C. I. Meng, and F. J. Rich. A nearly universal solar wind-magnetosphere coupling function inferred from 10 magnetospheric state variables. *Journal of Geophysical Research: Space Physics*, 112(A1), 2007. doi: 10.1029/2006JA012015.

P.T. Newell, J. W. Gjerloev, and E. J. Mitchell. Space climate implications from substorm frequency. *Journal of Geophysical Research: Space Physics*, 118(10):6254–6265, 2013. doi: 10.1002/jgra.50597. URL https://agupubs.onlinelibrary.wiley.com/doi/abs/10.1002/jgra.50597.

P.T. Newell, K. Liou, J.W. Gjerloev, T. Sotirelis, S. Wing, and E.J. Mitchell. Substorm

probabilities are best predicted from solar wind speed. *Journal of Atmospheric and Solar-Terrestrial Physics*, 146:28 – 37, 2016. ISSN 1364-6826. doi: https://doi.org/10.1016/j.jastp.2016.04.019. URL http://www.sciencedirect.com/science/article/pii/S1364682616301195.

A. Nishida. The earth's dynamic magnetotail. *Space Science Reviews*, 91(3):507–577, Feb 2000. ISSN 1572-9672. doi: 10.1023/A:1005223124330. URL https://doi.org/10.1023/A:1005223124330.

Atsuhiro Nishida. Coherence of geomagnetic dp 2 fluctuations with interplanetary magnetic variations. *Journal of Geophysical Research*, 73(17):5549–5559, 1968. ISSN 2156-2202. doi: 10.1029/JA073i017p05549. URL http://dx.doi.org/10.1029/JA073i017p05549.

Norichika Nishitani, John Ruohoniemi, Mark Lester, Joseph Baker, A. Koustov, Simon Shepherd, Gareth Chisham, Tomoaki Hori, Evan Thomas, Roman Makarevich, Aurélie Marchaudon, Pavlo Ponomarenko, James Wild, Stephen Milan, William Bristow, John Devlin, Ethan Miller, Raymond Greenwald, Tadahiko Ogawa, and T. Kikuchi. Review of the accomplishments of mid-latitude super dual auroral radar network (superdarn) hf radars. *Progress in Earth and Planetary Science*, 6, 12 2019. doi: 10.1186/s40645-019-0270-5.

T. P. O'Brien. Seaes-geo: A spacecraft environmental anomalies expert system for geosynchronous orbit. *Space Weather*, 7(9), 2009. doi: 10.1029/2009SW000473.

K. Oksavik, R. A. Greenwald, J. M. Ruohoniemi, M. R. Hairston, L. J. Paxton, J. B. H. Baker, J. W. Gjerloev, and R. J. Barnes. First observations of the temporal/spatial variation of the sub-auroral polarization stream from the superdarn wallops hf radar. *Geophysical Research Letters*, 33(12):n/a–n/a, 2006. ISSN 1944-8007. doi: 10.1029/2006GL026256. URL http://dx.doi.org/10.1029/2006GL026256. L12104.

W. P. Olson and K. A. Pfitzer. A quantitative model of the magnetospheric magnetic field. *Journal of Geophysical Research (1896-1977)*, 79(25):3739–3748, 1974. doi: 10.1029/JA079i025p03739. URL https://agupubs.onlinelibrary.wiley.com/doi/abs/10.1029/JA079i025p03739.

Vladimir O. Papitashvili and Frederick J. Rich. High-latitude ionospheric convection models derived from defense meteorological satellite program ion drift observations and parameterized by the interplanetary magnetic field strength and direction. *Journal of Geophysical Research: Space Physics*, 107(A8):SIA 17–1–SIA 17–13, 2002. doi: 10.1029/2001JA000264. URL https://agupubs.onlinelibrary.wiley.com/doi/abs/10.1029/2001JA000264.

E. N. Parker. Dynamics of the interplanetary gas and magnetic fields. *The Astrophysical Journal*, 128:664, 10 1958. doi: 10.1086/146579.

G.K. Parks. Magnetosphere. In Gerald R. North, John Pyle, and Fuqing Zhang, editors, *Encyclopedia of Atmospheric Sciences (Second Edition)*, pages 309 – 315. Academic Press, Oxford, second edition edition, 2015. ISBN 978-0-12-382225-3. doi: https://doi.org/10.1016/B978-0-12-382225-3.00211-5.

Fernando Pérez and Brian E. Granger. IPython: a system for interactive scientific computing. *Computing in Science and Engineering*, 9(3):21–29, May 2007. ISSN 1521-9615. doi: 10.1109/MCSE.2007.53. URL http://ipython.org.

Steven Michael Petrinec. On the magnetic field configuration of the magnetosheath. *Terrestrial, Atmospheric & Oceanic Sciences*, 24(2):265 – 272, 2013. ISSN 10170839. URL http://login.ezproxy.lib.vt.edu/login?url=http://search.ebscohost.com/login.aspx?direct=true&db=a9h&AN=87347406&scope=site.

A. A. Petrukovich, W. Baumjohann, R. Nakamura, T. Mukai, and O. A. Troshichev. Small

substorms: Solar wind input and magnetotail dynamics. *Journal of Geophysical Research: Space Physics*, 105(A9):21109–21117, 2000. doi: 10.1029/2000JA900057.

Z. Y. Pu, C. J. Xiao, X. G. Zhang, Z. Y. Huang, S. Y. Fu, Z. X. Liu, M. W. Dunlop, Q. G. Zong, C. M. Carr, H. Réme, I. Dandouras, A. Fazakerley, T. Phan, T. L. Zhang, H. Zhang, and X. G. Wang. Double star tc-1 observations of component reconnection at the dayside magnetopause: a preliminary study. *Annales Geophysicae*, 23(8):2889–2895, 2005. doi: 10.5194/angeo-23-2889-2005. URL http://www.ann-geophys.net/23/2889/2005/.

M.I. Pudovkin. *Physics of Magnetospheric Substorms: A Review*, pages 17–27. American Geophysical Union (AGU), 1991. ISBN 9781118663981. doi: 10.1029/GM064p0017. URL https://agupubs.onlinelibrary.wiley.com/doi/abs/10.1029/GM064p0017.

T. I. Pulkkinen, C. C. Goodrich, and J. G. Lyon. Solar wind electric field driving of magnetospheric activity: Is it velocity or magnetic field? *Geophysical Research Letters*, 34(21), 2007. doi: 10.1029/2007GL031011. URL https://agupubs.onlinelibrary.wiley.com/doi/abs/10.1029/2007GL031011.

Patricia H. Reiff, James L. Burch, and Robert W. Spiro. Cusp proton signatures and the interplanetary magnetic field. *Journal of Geophysical Research: Space Physics*, 85(A11): 5997–6005, 1980. ISSN 2156-2202. doi: 10.1029/JA085iA11p05997. URL http://dx.doi.org/10.1029/JA085iA11p05997.

J. P. Reistad, N. Østgaard, K. M. Laundal, A. Ohma, K. Snekvik, P. Tenfjord, A. Grocott, K. Oksavik, S. E. Milan, and S. Haaland. Observations of asymmetries in ionospheric return flow during different levels of geomagnetic activity. *Journal of Geophysical Research: Space Physics*, 123(6):4638–4651, 2018. doi: 10.1029/2017JA025051. URL https://agupubs.onlinelibrary.wiley.com/doi/abs/10.1029/2017JA025051.

A. J. Ribeiro, J. M. Ruohoniemi, J. B. H. Baker, L. B. N. Clausen, S. de Larquier, and R. A. Greenwald. A new approach for identifying ionospheric backscatter in midlatitude superdarn hf radar observations. *Radio Science*, 46(4):n/a–n/a, 2011. ISSN 1944-799X. doi: 10.1029/2011RS004676. URL http://dx.doi.org/10.1029/2011RS004676. RS4011.

A. J. Ribeiro, J. M. Ruohoniemi, J. B. H. Baker, L. B. N. Clausen, R. A. Greenwald, and M. Lester. A survey of plasma irregularities as seen by the midlatitude blackstone superdarn radar. *Journal of Geophysical Research: Space Physics*, 117(A2):n/a–n/a, 2012. ISSN 2156-2202. doi: 10.1029/2011JA017207. URL http://dx.doi.org/10.1029/2011JA017207. A02311.

A. J. Ribeiro, J. M. Ruohoniemi, P. V. Ponomarenko, L. B. N. Clausen, J. B. H. Baker, R. A. Greenwald, K. Oksavik, and S. de Larquier. A comparison of superdarn acf fitting methods. *Radio Science*, 48(3):274–282, 2013. ISSN 1944-799X. doi: 10.1002/rds.20031. URL http://dx.doi.org/10.1002/rds.20031.

A. D. Richmond, S. Matsushita, and J. D. Tarpley. On the production mechanism of electric currents and fields in the ionosphere. *Journal of Geophysical Research*, 81(4):547–555, 1976. ISSN 2156-2202. doi: 10.1029/JA081i004p00547. URL http://dx.doi.org/10.1029/JA081i004p00547.

A. D. Richmond, M. Blanc, B. A. Emery, R. H. Wand, B. G. Fejer, R. F. Woodman, S. Ganguly, P. Amayenc, R. A. Behnke, C. Calderon, and J. V. Evans. An empirical model of quiet-day ionospheric electric fields at middle and low latitudes. *Journal of Geophysical Research: Space Physics*, 85(A9):4658–4664, 1980. ISSN 2156-2202. doi: 10.1029/JA085iA09p04658. URL http://dx.doi.org/10.1029/JA085iA09p04658.

A. J. Ridley, Gang Lu, C. R. Clauer, and V. O. Papitashvili. A statistical study of the ionospheric convection response to changing interplanetary magnetic field conditions

using the assimilative mapping of ionospheric electrodynamics technique. *Journal of Geophysical Research: Space Physics*, 103(A3):4023–4039, 1998. ISSN 2156-2202. doi: 10.1029/97JA03328. URL http://dx.doi.org/10.1029/97JA03328.

A. J. Ridley, G. Crowley, and C. Freitas. An empirical model of the ionospheric electric potential. *Geophysical Research Letters*, 27(22):3675–3678, 2000. doi: 10.1029/1999GL011161. URL https://agupubs.onlinelibrary.wiley.com/doi/abs/10.1029/1999GL011161.

Brian D. Ripley. *Pattern recognition and neural networks /*. Cambridge University Press,, Cambridge ;, 1996.

H. Rishbeth. The f-layer dynamo. *Planetary and Space Science*, 19(2):263 – 267, 1971. ISSN 0032-0633. doi: http://dx.doi.org/10.1016/0032-0633(71)90205-4. URL http://www.sciencedirect.com/science/article/pii/0032063371902054.

H. Rishbeth. The ionospheric e-layer and f-layer dynamos - a tutorial review. *Journal of Atmospheric and Solar-Terrestrial Physics*, 59(15):1873 – 1880, 1997. ISSN 1364-6826. doi: http://dx.doi.org/10.1016/S1364-6826(97)00005-9. URL http://www.sciencedirect.com/science/article/pii/S1364682697000059.

G. Rostoker, S.-I. Akasofu, J. Foster, R.A. Greenwald, Y. Kamide, K. Kawasaki, A.T.Y. Lui, R.L. McPherron, and C.T. Russell. Magnetospheric substorms—definition and signatures. *Journal of Geophysical Research: Space Physics*, 85(A4):1663–1668, 1980. doi: 10.1029/JA085iA04p01663. URL https://agupubs.onlinelibrary.wiley.com/doi/abs/10.1029/JA085iA04p01663.

Gordon Rostoker. Geomagnetic indices. *Reviews of Geophysics*, 10(4):935–950, 1972. doi: 10.1029/RG010i004p00935. URL https://agupubs.onlinelibrary.wiley.com/doi/abs/10.1029/RG010i004p00935.

David E. Rumelhart, Geoffrey E. Hinton, and Ronald J. Williams. Learning representations by back-propagating errors. *Nature*, 323(6088):533–536, 1986. ISSN 1476-4687. doi: 10.1038/323533a0. URL https://doi.org/10.1038/323533a.

J. M. Ruohoniemi and K. B. Baker. Large-scale imaging of high-latitude convection with super dual auroral radar network hf radar observations. *Journal of Geophysical Research: Space Physics*, 103(A9):20797–20811, 1998. ISSN 2156-2202. doi: 10.1029/98JA01288. URL http://dx.doi.org/10.1029/98JA01288.

J. M. Ruohoniemi and R. A. Greenwald. The response of high-latitude convection to a sudden southward imf turning. *Geophysical Research Letters*, 25(15):2913–2916, 1998. ISSN 1944-8007. doi: 10.1029/98GL02212. URL http://dx.doi.org/10.1029/98GL02212.

J. M. Ruohoniemi and R. A. Greenwald. Dependencies of high-latitude plasma convection: Consideration of interplanetary magnetic field, seasonal, and universal time factors in statistical patterns. *Journal of Geophysical Research: Space Physics*, 110(A9):n/a–n/a, 2005. ISSN 2156-2202. doi: 10.1029/2004JA010815. URL http://dx.doi.org/10.1029/2004JA010815. A09204.

C. T. Russell. How northward turnings of the imf can lead to substorm expansion onsets. *Geophysical Research Letters*, 27(20):3257–3259, 2000. doi: 10.1029/2000GL011910.

Stuart J. Russell and Peter. Norvig. *Artificial intelligence :*. Prentice Hall series in artificial intelligence. Prentice Hall„ Upper Saddle River, N.J. :, 3rd ed. edition, c2010.

D S. Evans and M S. Greer. Polar orbiting environmental satellite space environment monitor-2 instrument descriptions and archive data documentation. *NOAA Tech. Memo. 1.4*, 01 2004. Space Environ. Lab., Boulder, Colorado.

A. L. Samuel. Some studies in machine learning using the game of checkers. *IBM Journal of Research and Development*, 3(3):210–229, July 1959. doi: 10.1147/rd.33.0210.

Per Even Sandholt, Charles J. Farrugia, Jøran Moen, and Stanley W. H. Cowley. Dayside auroral configurations: Responses to southward and northward rotations of the interplanetary magnetic field. *Journal of Geophysical Research: Space Physics*, 103(A9):20279–20295, 1998. doi: 10.1029/98JA01541. URL https://agupubs.onlinelibrary.wiley.com/doi/abs/10.1029/98JA01541.

L. Scherliess, B. G. Fejer, J. Holt, L. Goncharenko, C. Amory-Mazaudier, and M. J. Buonsanto. Radar studies of midlatitude ionospheric plasma drifts. *Journal of Geophysical Research: Space Physics*, 106(A2):1771–1783, 2001. doi: 10.1029/2000JA000229. URL https://agupubs.onlinelibrary.wiley.com/doi/abs/10.1029/2000JA000229.

C. Senior and M. Blanc. Convection in the inner magnetosphere - Model predictions and data. *Annales Geophysicae*, 5:405–420, December 1987.

Catherine Senior and Michel Blanc. On the control of magnetospheric convection by the spatial distribution of ionospheric conductivities. *Journal of Geophysical Research: Space Physics*, 89(A1):261–284, 1984. ISSN 2156-2202. doi: 10.1029/JA089iA01p00261. URL http://dx.doi.org/10.1029/JA089iA01p00261.

Catherine Senior, Jean-Claude Cerisier, Adalbjorn Thorolfsson, and Mark Lester. Propagation in the ionosphere of convection changes following a sharp interplanetary magnetic field by transition. *Journal of Geophysical Research: Space Physics*, 107(A10): SMP 20–1–SMP 20–9, 2002. ISSN 2156-2202. doi: 10.1029/2001JA005078. URL http://dx.doi.org/10.1029/2001JA005078. 1316.

S. G. Shepherd. Altitude-adjusted corrected geomagnetic coordinates: Definition and functional approximations. *Journal of Geophysical Research: Space Physics*, 119(9):7501–7521,

2014. doi: 10.1002/2014JA020264. URL https://agupubs.onlinelibrary.wiley.com/doi/abs/10.1002/2014JA020264.

George L. Siscoe. Energy coupling between regions 1 and 2 birkeland current systems. *Journal of Geophysical Research: Space Physics*, 87(A7):5124–5130, 1982. ISSN 2156-2202. doi: 10.1029/JA087iA07p05124. URL http://dx.doi.org/10.1029/JA087iA07p05124.

C.W. Smith, J. L'Heureux, N.F. Ness, M.H. Acuña, L.F. Burlaga, and J. Scheifele. The ace magnetic fields experiment. *Space Science Reviews*, 86(1-4):613–632, 1998. ISSN 0038-6308. doi: 10.1023/A:1005092216668. URL http://dx.doi.org/10.1023/A%3A1005092216668.

D. J. Southwood. The role of hot plasma in magnetospheric convection. *Journal of Geophysical Research*, 82(35):5512–5520, 1977. ISSN 2156-2202. doi: 10.1029/JA082i035p05512. URL http://dx.doi.org/10.1029/JA082i035p05512.

E.C. Stone, A.M. Frandsen, R.A. Mewaldt, E.R. Christian, D. Margolies, J.F. Ormes, and F. Snow. The advanced composition explorer. *Space Science Reviews*, 86(1):1–22, Jul 1998. ISSN 1572-9672. doi: 10.1023/A:1005082526237. URL https://doi.org/10.1023/A:1005082526237.

GA Stringer, I Heuten, C Salazar, and B Stokes. Artificial neural network (ann) forecasting of energetic electrons at geosynchronous orbit. *GEOPHYSICAL MONOGRAPH-AMERICAN GEOPHYSICAL UNION*, 97:291–296, 1996.

M. Sugiura. Hourly values of equatorial dst for the igy. *Ann. Int. Geophys. Yr.*, 35, 1 1964.

M. Sugiura and S. Chapman. *The average morphology of geomagnetic storms with sudden commencement*. Abhandlungen der Akademie der Wissenschaften in Göttingen. Math.-

phys. Kl. Sonderh. Vandenhoeck & Ruprecht, 1960. URL https://books.google.com/books?id=-zfmmQEACAAJ.

Ilya Sutskever, Oriol Vinyals, and Quoc V. Le. Sequence to sequence learning with neural networks. In *Proceedings of the 27th International Conference on Neural Information Processing Systems - Volume 2*, NIPS'14, pages 3104–3112, Cambridge, MA, USA, 2014. MIT Press. URL http://dl.acm.org/citation.cfm?id=2969033.2969173.

T. Tanaka, D. Kitao, Y. Sato, Y. Tanaka, and D. Ikeda. Forecasting auroral substorms from observed data with a supervised learning algorithm. In *2015 IEEE 11th International Conference on e-Science*, pages 284–287, 2015. doi: 10.1109/eScience.2015.48.

E. I. Tanskanen. A comprehensive high-throughput analysis of substorms observed by image magnetometer network: Years 1993–2003 examined. *Journal of Geophysical Research: Space Physics*, 114(A5), 2009. doi: 10.1029/2008JA013682. URL https://agupubs.onlinelibrary.wiley.com/doi/abs/10.1029/2008JA013682.

K. F. Tapping. Recent solar radio astronomy at centimeter wavelengths: The temporal variability of the 10.7-cm flux. *Journal of Geophysical Research: Atmospheres*, 92(D1): 829–838, 1987. doi: 10.1029/JD092iD01p00829. URL https://agupubs.onlinelibrary.wiley.com/doi/abs/10.1029/JD092iD01p00829.

K. F. Tapping. The 10.7 cm solar radio flux (f10.7). *Space Weather*, 11(7):394–406, 2013. doi: 10.1002/swe.20064. URL https://agupubs.onlinelibrary.wiley.com/doi/abs/10.1002/swe.20064.

M. Temerin and Xinlin Li. Dst model for 1995–2002. *Journal of Geophysical Research: Space Physics*, 111(A4), 2006. doi: 10.1029/2005JA011257. URL https://agupubs.onlinelibrary.wiley.com/doi/abs/10.1029/2005JA011257.

O. Theobald. *Machine Learning for Absolute Beginners: A Plain English Introduction*. Machine Learning for Beginners. Independently Published, 2018. ISBN 9781549617218. URL https://books.google.com/books?id=PGNzswEACAAJ.

E. G. Thomas and S. G. Shepherd. Statistical patterns of ionospheric convection derived from mid-latitude, high-latitude, and polar superdarn hf radar observations. *Journal of Geophysical Research: Space Physics*, 123(4):3196–3216, 2018. doi: 10.1002/2018JA025280. URL https://agupubs.onlinelibrary.wiley.com/doi/abs/10.1002/2018JA025280.

K. J. Trattner, S. A. Fuselier, and S. M. Petrinec. Location of the reconnection line for northward interplanetary magnetic field. *Journal of Geophysical Research: Space Physics*, 109(A3):n/a–n/a, 2004. ISSN 2156-2202. doi: 10.1029/2003JA009975. URL http://dx.doi.org/10.1029/2003JA009975. A03219.

K. J. Trattner, S. A. Fuselier, S. M. Petrinec, T. K. Yeoman, C. Mouikis, H. Kucharek, and H. Reme. Reconnection sites of spatial cusp structures. *Journal of Geophysical Research: Space Physics*, 110(A4):n/a–n/a, 2005. ISSN 2156-2202. doi: 10.1029/2004JA010722. URL http://dx.doi.org/10.1029/2004JA010722. A04207.

Daniel Sáez Trigueros, Li Meng, and Margaret Hartnett. Face recognition: From traditional to deep learning methods, 2018.

O. A. Troshichev, A. L. Kotikov, B. D. Bolotinskaya, and V. G. Andrezen. Influence of the imf azimuthal component on magnetospheric substorm dynamics. *Journal of geomagnetism and geoelectricity*, 38(11):1075–1088, 1986. doi: 10.5636/jgg.38.1075.

Vytenis M. Vasyliunas. *Mathematical Models of Magnetospheric Convection and its Coupling to the Ionosphere*, pages 60–71. Springer Netherlands, Dordrecht, 1970. ISBN 978-94-010-3284-1. doi: 10.1007/978-94-010-3284-1_6. URL https://doi.org/10.1007/978-94-010-3284-1_6.

Vytenis M. Vasyliunas. *The Interrelationship of Magnetospheric Processes*, pages 29–38. Springer Netherlands, Dordrecht, 1972. ISBN 978-94-010-2896-7. doi: 10.1007/978-94-010-2896-7_3. URL https://doi.org/10.1007/978-94-010-2896-7_3.

J. Šafránková, Z. Němeček, Š. Dušík, L. Přech, D. G. Sibeck, and N. N. Borodkova. The magnetopause shape and location: a comparison of the interball and geotail observations with models. *Annales Geophysicae*, 20(3):301–309, 2002. doi: 10.5194/angeo-20-301-2002. URL https://www.ann-geophys.net/20/301/2002/.

R. H. Wand and J. V. Evans. The penetration of convection electric fields to the latitude of millstone hill (Λ=56°). *Journal of Geophysical Research: Space Physics*, 86(A7):5809–5814, 1981a. ISSN 2156-2202. doi: 10.1029/JA086iA07p05809. URL http://dx.doi.org/10.1029/JA086iA07p05809.

Ronald H. Wand and John V. Evans. Seasonal and magnetic activity variations of ionospheric electric fields over millstone hill. *Journal of Geophysical Research: Space Physics*, 86 (A1):103–118, 1981b. ISSN 2156-2202. doi: 10.1029/JA086iA01p00103. URL http://dx.doi.org/10.1029/JA086iA01p00103.

Zhiguang Wang, Weizhong Yan, and Tim Oates. Time series classification from scratch with deep neural networks: A strong baseline. In *2017 International joint conference on neural networks (IJCNN)*, pages 1578–1585. IEEE, 2017.

Lihang Wei, Qiuzhen Zhong, Ruilin Lin, Jingjing Wang, Siqing Liu, and Yong Cao. Quantitative prediction of high-energy electron integral flux at geostationary orbit based on deep learning. *Space Weather*, 16(7):903–916, 2018. doi: 10.1029/2018SW001829. URL https://agupubs.onlinelibrary.wiley.com/doi/abs/10.1029/2018SW001829.

R. S. Weigel, A. J. Klimas, and D. Vassiliadis. Solar wind coupling to and predictability of

ground magnetic fields and their time derivatives. *Journal of Geophysical Research: Space Physics*, 108(A7), 2003. doi: 10.1029/2002JA009627.

D. R. Weimer. Improved ionospheric electrodynamic models and application to calculating joule heating rates. *Journal of Geophysical Research: Space Physics*, 110(A5):n/a–n/a, 2005. ISSN 2156-2202. doi: 10.1029/2004JA010884. URL http://dx.doi.org/10.1029/2004JA010884. A05306.

D. R. Weimer, D. M. Ober, N. C. Maynard, M. R. Collier, D. J. McComas, N. F. Ness, C. W. Smith, and J. Watermann. Predicting interplanetary magnetic field (imf) propagation delay times using the minimum variance technique. *Journal of Geophysical Research: Space Physics*, 108(A1), 2003. doi: 10.1029/2002JA009405. URL https://agupubs.onlinelibrary.wiley.com/doi/abs/10.1029/2002JA009405.

Willard W. White, George L. Siscoe, Gary M. Erickson, Zerefsan Kaymaz, Nelson C. Maynard, Keith D. Siebert, Bengt U. Ö Sonnerup, and Daniel R. Weimer. The magnetospheric sash and the cross-tail s. *Geophysical Research Letters*, 25(10):1605–1608, 1998. ISSN 1944-8007. doi: 10.1029/98GL50865. URL http://dx.doi.org/10.1029/98GL50865.

J. A. Wild, E. E. Woodfield, and S. K. Morley. On the triggering of auroral substorms by northward turnings of the interplanetary magnetic field. *Annales Geophysicae*, 27(9): 3559–3570, 2009. doi: 10.5194/angeo-27-3559-2009.

P. Wintoft and H. Lundstedt. Prediction of daily average solar wind velocity from solar magnetic field observations using hybrid intelligent systems. *Physics and Chemistry of the Earth*, 22(7):617 – 622, 1997. ISSN 0079-1946. doi: https://doi.org/10.1016/S0079-1946(97)00186-9. URL http://www.sciencedirect.com/science/article/pii/S0079194697001869. Low-Altitude Investigation of Dayside Magnetospheric Boundary Processes.

Jian-Guo Wu and Henrik Lundstedt. Geomagnetic storm predictions from solar wind data with the use of dynamic neural networks. *Journal of Geophysical Research: Space Physics*, 102(A7):14255–14268, 1997. doi: 10.1029/97JA00975. URL https://agupubs.onlinelibrary.wiley.com/doi/abs/10.1029/97JA00975.

Chao Xiong, Hermann Lühr, and Bela G. Fejer. Global features of the disturbance winds during storm time deduced from champ observations. *Journal of Geophysical Research: Space Physics*, 120(6):5137–5150, 2015. doi: 10.1002/2015JA021302. URL https://agupubs.onlinelibrary.wiley.com/doi/abs/10.1002/2015JA021302.

H.-C. Yeh, J. C. Foster, F. J. Rich, and W. Swider. Storm time electric field penetration observed at mid-latitude. *Journal of Geophysical Research: Space Physics*, 96(A4):5707–5721, 1991. ISSN 2156-2202. doi: 10.1029/90JA02751. URL http://dx.doi.org/10.1029/90JA02751.

Shun-Rong Zhang, John M. Holt, and Mary McCready. High latitude convection based on long-term incoherent scatter radar observations in north america. *Journal of Atmospheric and Solar-Terrestrial Physics*, 69(10):1273 – 1291, 2007. ISSN 1364-6826. doi: https://doi.org/10.1016/j.jastp.2006.08.017. URL http://www.sciencedirect.com/science/article/pii/S1364682607000739. Storm-Time Penetration Electric Fields and their Effects: Magnetospheric and Ionospheric Perspectives.

Yun Zou and Nozomu Nishitani. Study of mid-latitude ionospheric convection during quiet and disturbed periods using the superdarn hokkaido radar. *Advances in Space Research*, 54 (3):473 – 480, 2014. ISSN 0273-1177. doi: https://doi.org/10.1016/j.asr.2014.01.011. URL http://www.sciencedirect.com/science/article/pii/S0273117714000295. Recent Advances in Equatorial, Low- and Mid-Latitude Mesosphere, Thermosphere-Ionosphere System Studies.

Appendices

Appendix A

Supporting Information for Chapter 4

A.1 Introduction

This supporting information provides a figure that shows the histograms of IMF bias vector clock angles (i.e. 60-min stable IMF clock angle intervals) for the 8 IMF clock angle bins in Figure 4.8 in the manuscript, as well as a complete set of figures (A.2-A.10) showing subauroral convection patterns calculated for winter, equinox, and summer under 8 different IMF clock angle conditions for the region between 52° and 60° magnetic latitudes.

A.2 Supplementary Figures

Figure A.1 shows the histograms of IMF bias vector clock angles (i.e. 60-min stable IMF clock angle intervals) for the 8 IMF clock angle bins in Figure 4.8. It can be seen that the distribution of data over the 8 IMF clock angle bins is not balanced with the number of data points in IMF By bins having ∼3 times of those of IMF Bz.

Figures A.2-A.10 below show subauroral convection patterns (2-D, zonal, and meridional vectors) calculated for winter, equinox, and summer under 8 different IMF clock angle conditions for the region between 52° and 60° magnetic latitudes.

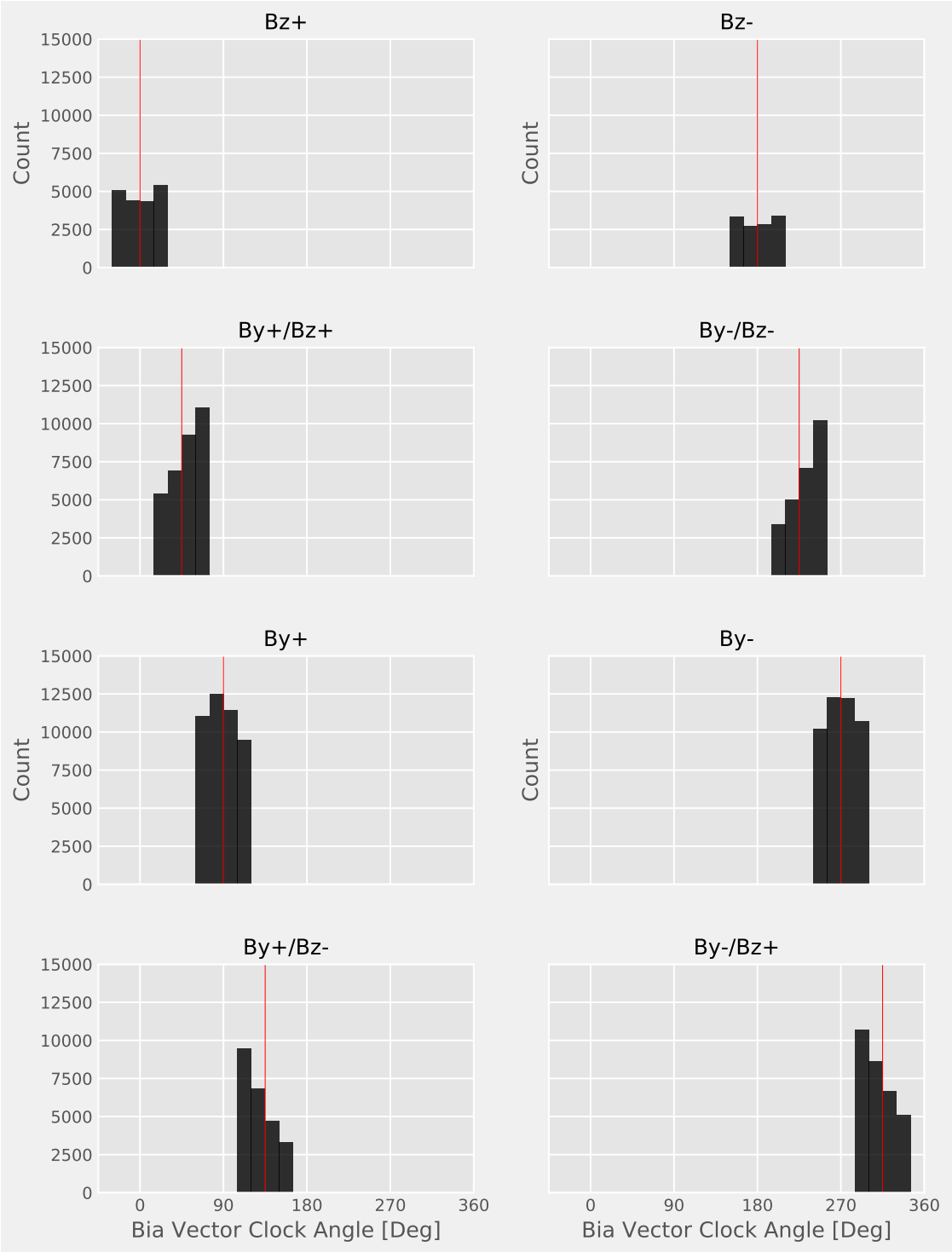

Figure A.1: Histograms of IMF bias vector clock angles for the 8 IMF clock angle bins in Figure 4.8.

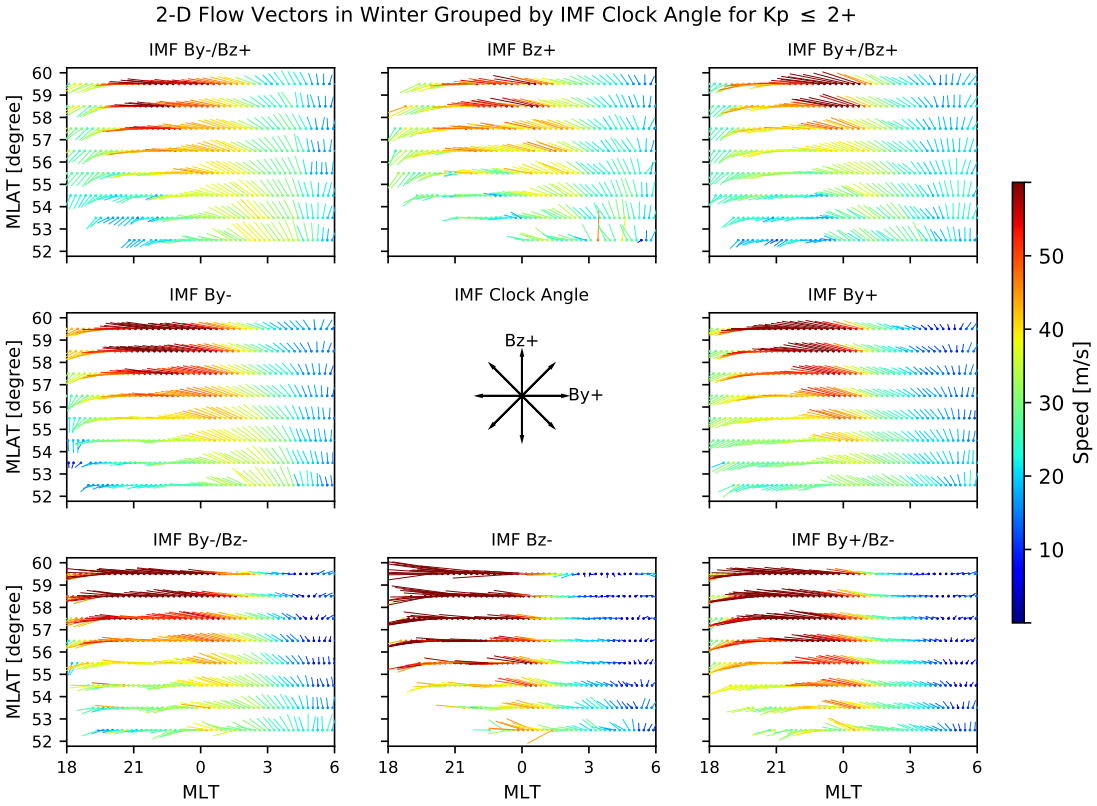

Figure A.2: Two-dimensional quiet-time (Kp $\leq$ 2+) subauroral convection patterns calculated for winter under 8 different IMF clock angle conditions for the region between 52° and 60° magnetic latitudes. (Figure 4.8 in the manuscript)

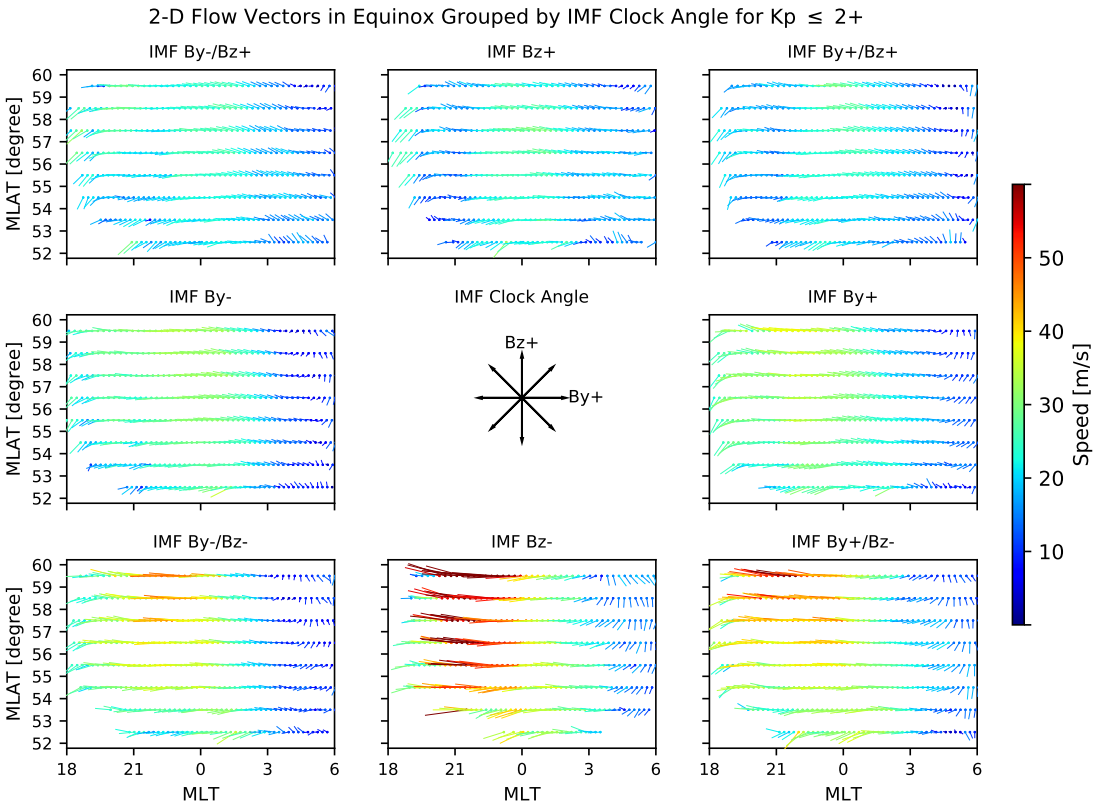

Figure A.3: Two-dimensional quiet-time (Kp $\leq$ 2+) subauroral convection patterns calculated for equinox under 8 different IMF clock angle conditions for the region between 52° and 60° magnetic latitudes.

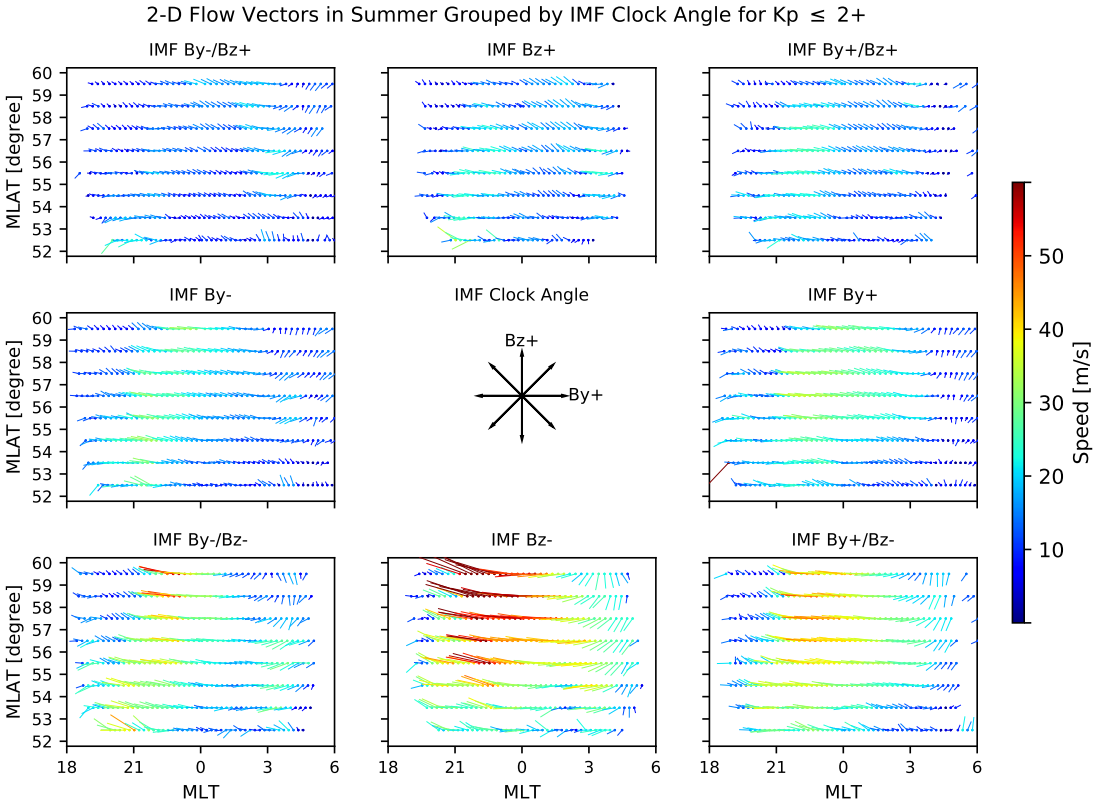

Figure A.4: Two-dimensional quiet-time (Kp $\leq$ 2+) subauroral convection patterns calculated for summer under 8 different IMF clock angle conditions for the region between 52° and 60° magnetic latitudes.

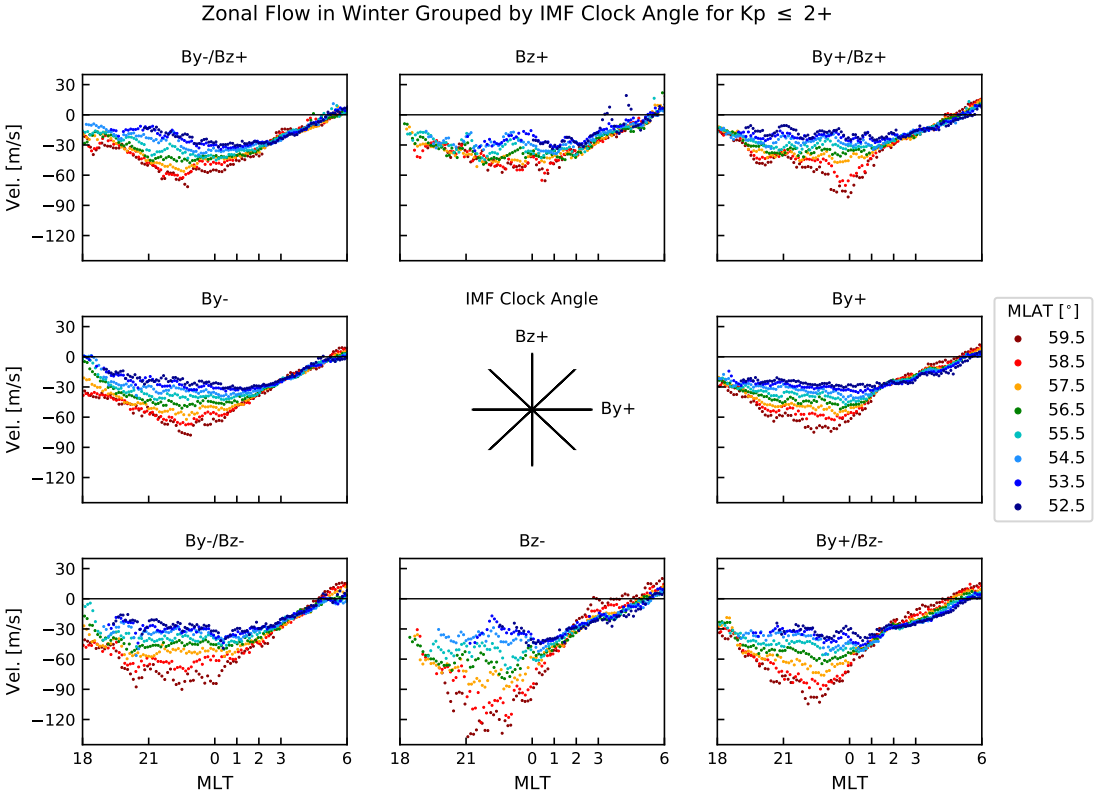

Figure A.5: Fitted zonal velocities (positive eastward) by magnetic latitude versus MLT in winter for 8 IMF clock angle bins. Note that extra tick marks were placed at every 1 hour between 3 - 6 MLT to aid in comparing the distinct IMF By influence on subauroral zonal flows. (Figure 4.9 in the manuscript)

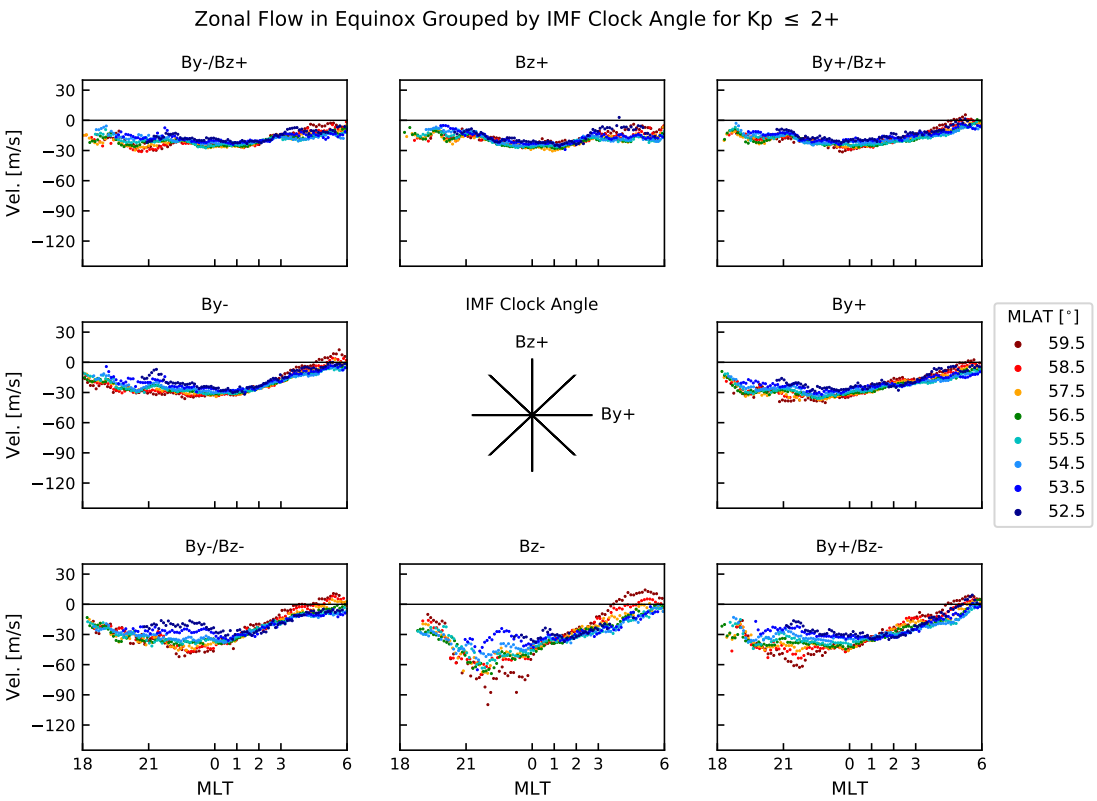

Figure A.6: Fitted zonal velocities (positive eastward) by magnetic latitude versus MLT in equinox for 8 IMF clock angle bins.

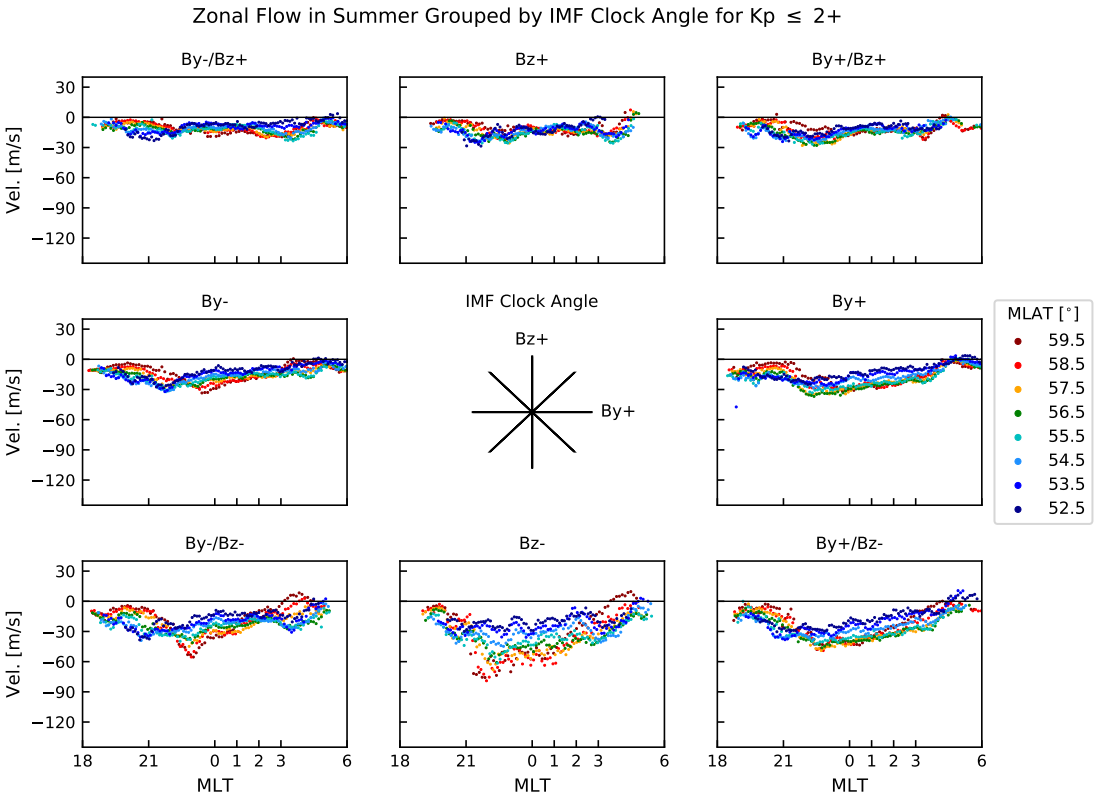

Figure A.7: Fitted zonal velocities (positive eastward) by magnetic latitude versus MLT in summer for 8 IMF clock angle bins.

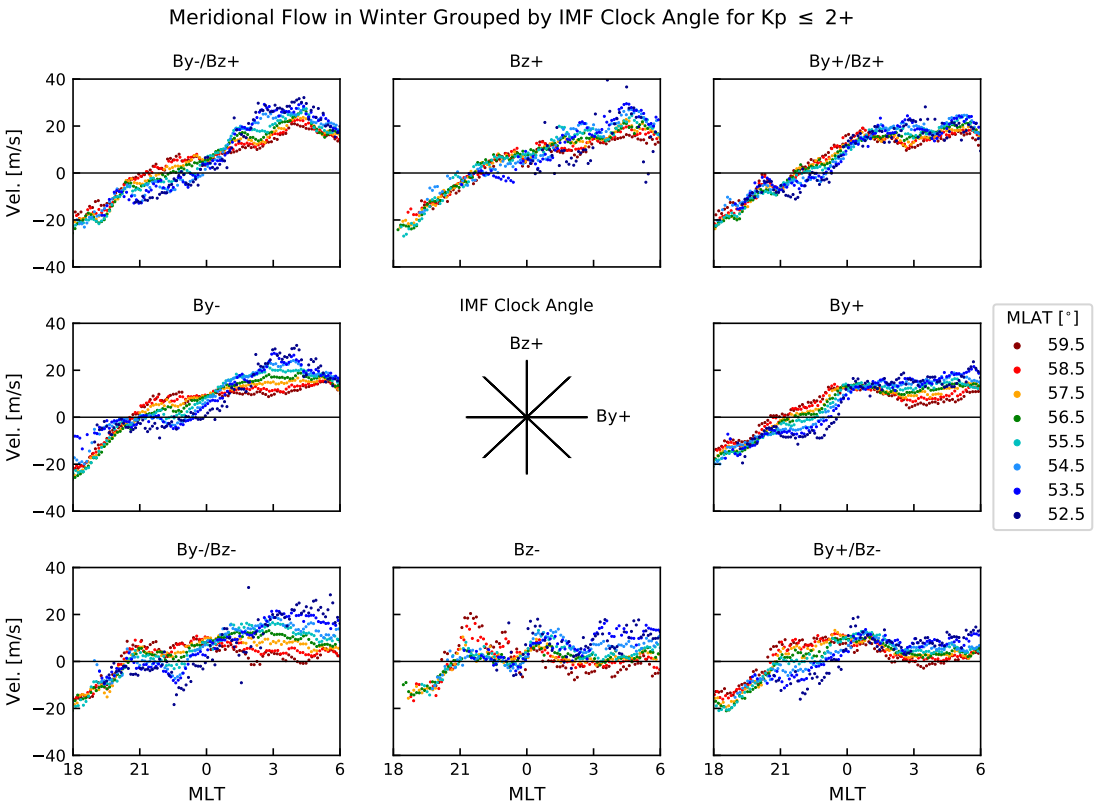

Figure A.8: Fitted meridional velocities (positive eastward) by magnetic latitude versus MLT in winter for 8 IMF clock angle bins. (Figure 4.10 in the manuscript)

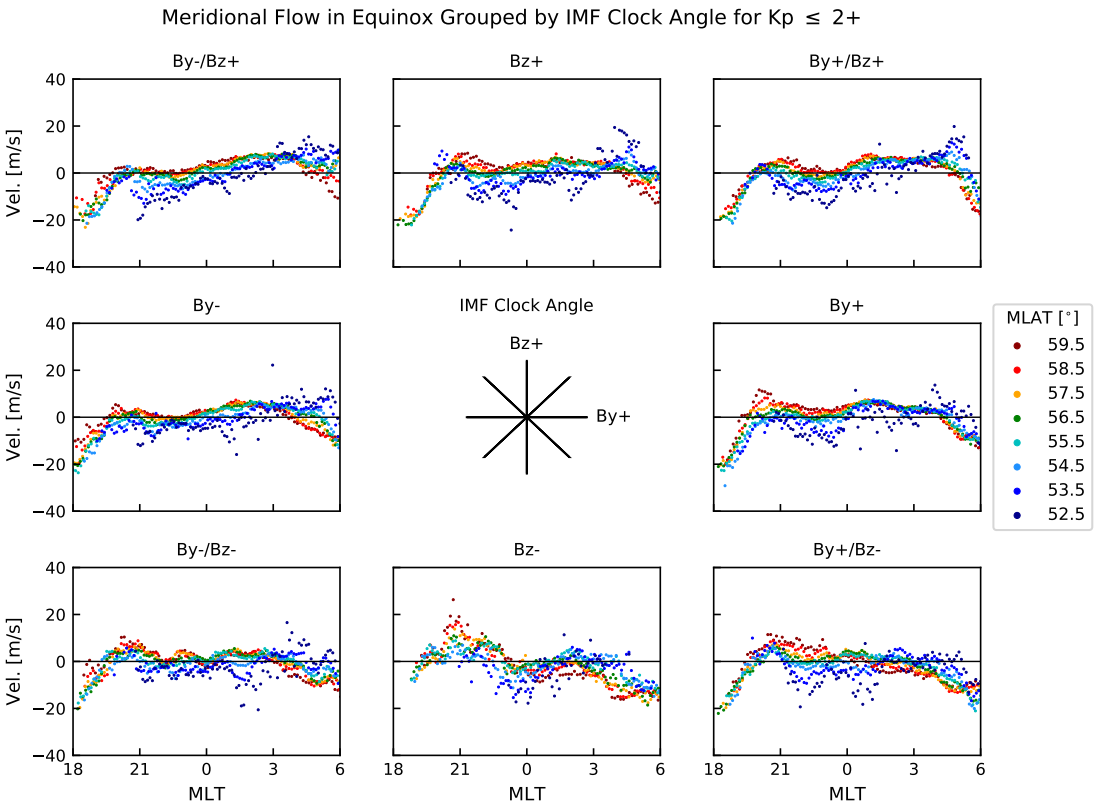

Figure A.9: Fitted meridional velocities (positive eastward) by magnetic latitude versus MLT in equinox for 8 IMF clock angle bins.

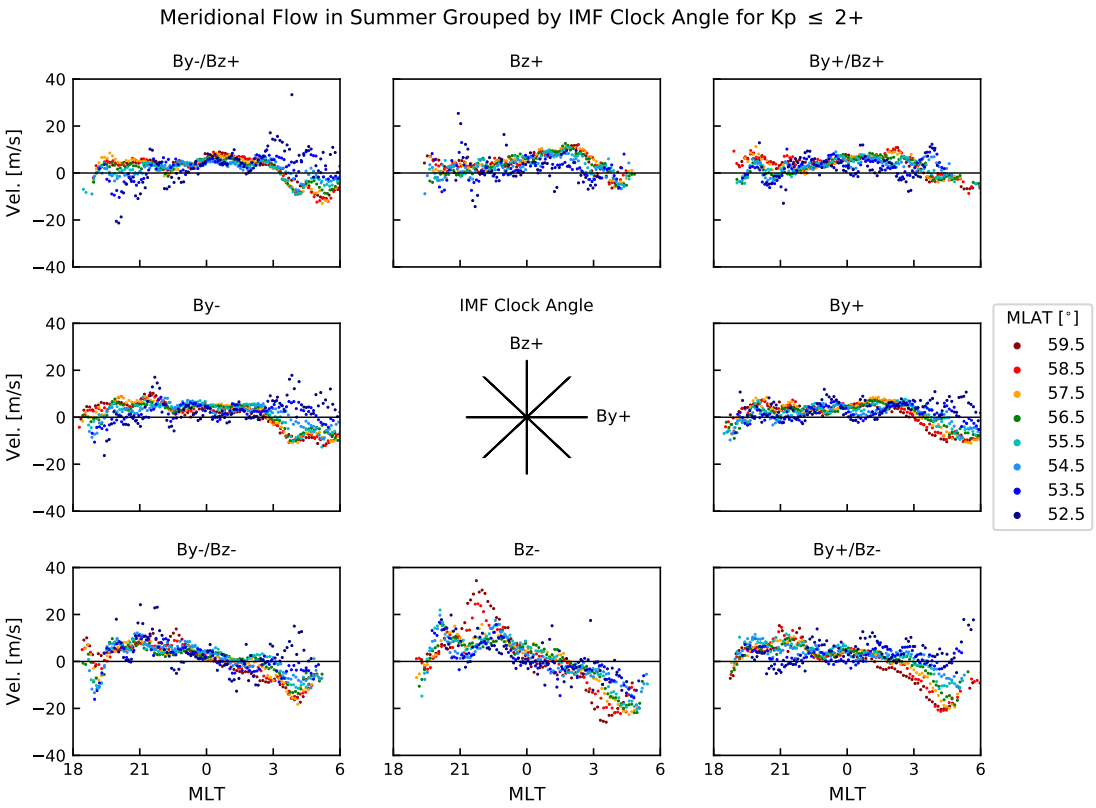

Figure A.10: Fitted meridional velocities (positive eastward) by magnetic latitude versus MLT in summer for 8 IMF clock angle bins.